THE FUNDAMENTAL SCIENCE OF NITROGEN-DOPING OF NIOBIUM SUPERCONDUCTING CAVITIES

A Dissertation

Presented to the Faculty of the Graduate School

of Cornell University

in Partial Fulfillment of the Requirements for the Degree of

Doctor of Philosophy

by

Daniel Alfred Gonnella

August 2016

THE FUNDAMENTAL SCIENCE OF NITROGEN-DOPING OF NIOBIUM SUPERCONDUCTING CAVITIES

Daniel Alfred Gonnella, Ph.D.

Cornell University 2016

Doping of niobium superconducting RF cavities with impurities has been demonstrated to have the ability to significantly improve the cryogenic efficiency of the accelerating structures. Doping SRF cavities with nitrogen is a relatively simple additional step to cavity preparation that can make drastic improvements in a cavity's intrinsic quality factor, Q_0. Nitrogen-doping consists of treating SRF cavities at high temperatures in a low nitrogen-atmosphere. This leads to two important effects: an improvement in Q_0 at low fields, and the presence of an "anti-Q slope" in which the cryogenic efficiency of doped cavities actually improves at higher fields. After its initial discovery, nitrogen-doping showed real promise but many fundamental scientific questions remained about the process. Nitrogen-doped cavities consistently quenched at lower fields than un-doped cavities, cooling the cavities through their critical temperature slowly led to poor performance, and the mechanism behind the Q_0 improvement was not well understood. This dissertation focuses on addressing these issues. Single-cell 1.3 GHz cavities were prepared with different nitrogen-dopings and their effects studied systematically. It was found that nitrogen-doping drastically lowers the mean free path of the RF penetration layer of the niobium, leading to a lowering of the temperature-dependent BCS resistance, R_{BCS}, at low fields. Theoretical work to predict the anti-Q slope was compared with experimental results to more fundamentally understand the na-

ture of the field dependence of R_{BCS}. Nitrogen-doped cavities were found to have a much larger sensitivity of residual resistance from trapped magnetic flux than un-doped cavities. Fast cool downs with large spatial temperature gradients through T_c were found to more efficiently expel magnetic flux. The full dependence of this sensitivity to trapped magnetic flux was studied as a function of changing mean free path and found to be in good agreement with theoretical predictions. The nature of the low-field quench in nitrogen-doped cavities was also studied with high power pulsed measurements and found to be related to a lowering of the lower critical field, B_{c1} due to lowering of the mean free path. Finally, five cryomodule tests were carried out on nitrogen-doped 9-cell cavities to understand how the cryomodule environment affects the performance of doped cavities. This is the first demonstration that environmental factors can be controlled to achieve high Q_0 of more than 2.7×10^{10} at 16 MV/m and 2.0 K in a cryomodule, meeting and exceeding the specification for LCLS-II. The work presented here represents a significant leap forward in the understanding of the underlying science behind nitrogen-doped cavities and demonstrates their readiness for use in future particle accelerators.

BIOGRAPHICAL SKETCH

Dan was born and raised in Rochester, NY. In 2007 he began studies in Physics and Mathematics and Clarkson University. A summer research position at Cornell in 2009 gave Dan his first foray into accelerator physics. In 2011, he started his graduate studies at Cornell University in the SRF group. He graduated in 2016.

To my fellow graduate students: Nick Valles, Sam Posen, Daniel "Tex" Hall, and James Maniscalco who have been not only great coworkers but also fantastic friends.

ACKNOWLEDGEMENTS

The work presented here would never have been possible without the help of many of the faculty, scientists, technical staff, and graduate students that I have worked with over the past five years.

I am most thankful for having a fantastic advisor in Matthias Liepe. Matthias has not only been a wonderful mentor from a scientific stand-point, but the genuine concern he has for his students' well being truly sets him apart. I'm happy to count him as a friend in addition to a mentor. He provided an environment in which I was able to thrive over the past five years.

I have had the great opportunity to discuss my work with many esteemed Cornell faculty members on a weekly basis at our SRF meetings. Insight from Georg Hoffstaetter, Hasan Padamsee, and Don Hartill has been invaluable as I carried out the experiments for this dissertation. I was also very lucky to be a part of the LCLS-II High Q Project which allowed me to work closely with colleagues from Fermilab, JLab, and SLAC. I am especially thankful for having the opportunity to work with Anna Grassellino and Alex Romanenko at Fermilab and to be included in a few of their experiments as part of our collaboration.

My day to day life was made better thanks to my fellow graduate students Yi Xie, Nick Valles, Sam Posen, Dan Hall, James Maniscalco, Pete Koufalis, and Ryan Porter from helping out with my experiments to many lunch breaks with lively conversations and board games to pass the time. I was very lucky to learn from the students older than me and to be able to pass that knowledge on to those below me.

I've had the opportunity to mentor many undergraduate students during my time at Cornell. Matt Zotta, Ryan French, Nicolai Giedraitis, Arielle Balthazard, and Waverly Gorman participated in the CLASSE REU and SRCCS pro-

grams which gave me the chance to pass on my knowledge and also to have a helping hand during my summers. I was only able to complete many summer experiments quickly thanks to their help.

There are many members of the scientific and technical staff at both Newman and Wilson labs that significantly helped me over the past few years. I would especially like to thank chemistry room leaders Terri Gruber and Holly Conklin, John Kaufman for running the furnace, Peter Quigley, Vivian Ho, and Vadim Veshcherevich for helping during HTC testing, cyogenic experts Colby Shore, Dan Sabol, Dwight Widger, and Eric Smith, drafters Tim O'Connell and Matt Rifenburg, engineers Brendan Elmore and Ben Bullock, scientists Fumio Furuta, Mingqi Ge, and Ralf Eichhorn, machinists Neil Alexander, Randy Miller, Shawn Clark, Mark Howser, and John Kaminski, welder Brian Clasby, and Greg Kulina and Paul Bishop, who keep things running in the Newman basement. I'd also like to thank James Sears for his invaluable expertise around the lab and for including me on many SCUBA diving trips around New York state.

I am deeply thankful for the friends that I have made during my time in both undergraduate and graduate school. Outside of the lab I've gotten to know a number great people in the physics department. I especially want to mention Greg Stiehl, Summer Saraf, Evan MacQuarrie, Ed Lochocki, and Kevin McDermott. I also would not have made it to graduate school without the support of my friends from Clarkson, especially Kathryn O'Leary, Josh Lamontagne, Brendan Wiedow, and Steve Haluska.

I would also like to thank my family who has helped me in many ways from a young age, through college, and graduate school. I especially want to thank my parents Al and Gina and my Grandma for supporting me and pushing me to succeed.

Finally I would like to thank my girlfriend Lindsay who helped me to stay motivated to finish this dissertation so I could get out to California and escape the snow quickly. Also it has been wonderful to have the best thesis-writing-buddy, Espresso, our 8-pound mini-dachshund.

TABLE OF CONTENTS

LIST OF TABLES

LIST OF FIGURES

LIST OF ABBREVIATIONS

BCP	Buffer Chemical Polish
BCS	Bardeen, Cooper and Schrieffer
CBP	Centrifugal Barrel Polish
EP	Electro-polish
ERL	Energy Recovery Linac
FEL	Free Electron Laser
FNAL	Fermilab National Accelerator Laboratory
GL	Ginzburg-Landau
HOM	Higher-Order Mode
HPR	High-Pressure Rinse
HTC	Horizontal Test Cryomodule
ILC	International Linear Collider
LCLS	Linac Coherent Light Source
LCLS-II	Linac Coherent Light Source II
LHC	Large Hadron Collider
LINAC	Linear Accelerator
LLRF	Low-level RF
MLC	Main-Linac Cryomodule
PLL	Phase-locked loop
RF	Radio Frequency
RRR	Residual Resistivity Ratio
SLAC	SLAC National Accelerator Laboratory
SRF	Superconducting Radio Frequency
TE	Transverse Electric
TJNAF	Thomas Jefferson National Accelerator Facility
TM	Transverse Magnetic
UHV	Ultra-High Vacuum
VEP	Vertical Electro-polish
XFEL	X-Ray Free Electron Laser

LIST OF SYMBOLS

B	Magnetic flux density
$B_c(0)$	Critical magnetic field at 0 K
B_{c_1}	Lower critical magnetic field
B_{c_2}	Upper critical magnetic field
B_{pk}	Peak (maximal) surface magnetic field
B_{sh}	Superheating field
$c = 299\,792\,458$ m/s	The speed of light in free space
D	Electric flux density
$e = 2.71828\ldots$	Euler's number
E	Electric field intensity
E_{acc}	Accelerating electric Field
$E_g \equiv 2\Delta(0)/(k_B T_c)$	Normalized energy gap of a superconductor
E_{pk}	Peak (maximal) surface electric field
$E_S \equiv \Delta(0)/(k_B T_c)$	Normalized energy gap of one electron in a Cooper pair used in SRIMP calculations
f	Frequency of electromagnetic wave
G	Geometry factor of RF structure
H	Magnetic field intensity
i	Imaginary unit, $\sqrt{-1}$
$\Im$	Imaginary part
k	Wavenumber
$k_B = 1.38 \times 10^{-23}$ J/K	Boltzmann constant
K	Kelvin (SI unit of temperature)
ℓ_{tr}	Normal conducting electron's mean free path
m	Mass (usually of the electron)
n	Density of electron gas
P_{diss}	Dissipated power
$q = 1.60217657 \times 10^{-19}$ C	Charge of the electron
Q	Quality Factor
Q_0	Intrinsic Q of a resonator
Q_{ext}	External Q, generally of a coupler

Q_L	Loaded Q of resonator and coupler
(R/Q)	Shunt impedance (monopole) [Ω]
$(R/Q)_\perp$	Transverse shunt impedance [Ω/cm^{2m}]
$(R/Q)'_\perp$	Transverse shunt impedance [Ω]
R_0	Residual resistance
R_{BCS}	BCS resistance
R_s	Surface resistance
$\mathfrak{R}$	Real part
S	Fermi surface area
$S_F \equiv 4\pi(3\pi^2 n)^{2/3}$	Fermi surface normalization factor
t	Time
$t \equiv T/T_c$	Normalized temperature
T	Temperature
T_c	Critical temperature of a superconductor
U	Stored energy
v	Velocity
v_F	Fermi velocity
V	Voltage
$\beta = v/c$	Velocity normalized to the speed of light
β	Coefficient relating Δf and $\Delta\lambda$
γ	Relativistic Lorentz factor
$\gamma = 0.57721\ldots$	Euler-Masheroni constant
γ_c	Electronic specific heat coefficient
Γ	Gamma function
δ	Skin-depth of a conductor
$\Delta(0)$	Half the binding energy of a Cooper pair
Δf	Frequency shift
$\Delta\lambda$	Change in penetration depth
ϵ	(Complex) Permittivity of material
$\epsilon_0 \equiv 1/\left(\mu_0 \cdot c^2\right)$ $= 8.9\ldots \times 10^{-12}$ F/m	Permittivity of free space
ε	Electronic charge in CGS units (esu)

$\zeta(s)$	Euler-Riemann zeta function
η	(Complex) Wave impedance
θ	Polar angle
κ_{GL}	Ginzburg-Landau parameter
λ_{GL}	Ginzburg-Landau penetration depth
λ_L	London Penetration depth at 0 K
λ_{tr}	Argument to Gor′kov χ function
μ	(Complex) Permeability of material
$\mu_0 \equiv 4\pi \times 10^{-7}$ N/A^2	Permeability of free space
ν	Frequency of electromagnetic wave
ξ_0	BCS coherence length
ξ_{GL}	Ginzburg-Landau penetration depth
ξ_S	Coherence length used in SRIMP
$\pi \equiv \tau/2 \approx 3.14159\ldots$	Ratio of a circle's circumference to its diameter
ρ	Electrical resistivity
σ	Electrical conductivity
$\tau = 6.283185\ldots$	The ratio of circle's circumference to radius
ϕ	Azimuthal angle
χ	Gor′kov χ function
ψ	Digamma function, derivative of Γ
ω	Angular frequency
$\hbar = 1.0546 \times 10^{-34}$ J·s	Reduced Planck's Constant

CHAPTER 1

INTRODUCTION

Particle accelerators are machines which use electromagnetic fields to control particle beams for use in scientific applications. Over the last 100 years, they have been at the forefront of scientific exploration having many applications from high energy physics, to study new particles and probe the underlying physics of our world [Aa12], to light sources which serve as a tool for disciplines outside of physics such as biology and chemistry [DPE05, Gal14], to small scale applications for industry and the medical field [HS10, Sab13]. Particle accelerators operate by accelerating and controlling a charged particle beam to use in collision experiments (such as at the Large Hadron Collider at Cern) or to generate x-rays (such as at the Linac Coherent Light Source at SLAC).

The most common tool for accelerating the particle beams are radio frequency cavities. These cavities store electromagnetic energy which can then be given to the particle beams as they pass through the cavity. RF cavities come in two varieties: normal conducting (typically made of copper) and superconducting (typically made of niobium). Superconducting RF (SRF) cavities provide many benefits over normal conducting cavities in terms of the RF power required for operation, however they bring with them significant cryogenic costs due to the need to operate at near absolute-zero temperatures. New proposed accelerators require the use of many cavities which leads to significant costs in terms of operation of both the RF and cyrogenic plants.

Up until recently, the cryogenic load from SRF cavities was typically not a significant portion of the operational costs of accelerators. This was mostly because of the operation of the cavities at low accelerating fields to minimize the

cryogenic power required for operation or the use of a pulsed-mode in which the cavities are only "turned on" when particle beams are passing through in machines with only a few cavities. As the limits of modern accelerators continue to be advanced however, a new regime has been reached in which operation at higher accelerating fields is desirable. This necessitates the need for improvement of the cryogenic efficiency of the SRF cavities.

This dissertation focuses on studying a new cavity preparation technique known as nitrogen-doping [GRS+13]. By heat treating SRF cavities in a low pressure nitrogen atmosphere, nitrogen atoms will diffuse into the niobium bulk and majorly alter the underlying physics of the system. This impurity doping has enabled the cryogenic efficiency of these accelerating structures to be drastically improved, which brings forward the chance to apply this technology to future accelerators and continue pushing the limits of modern accelerator technology.

1.1 Organization of this Dissertation

This dissertation begins in Chapter 2 with an introduction to the theories of superconductivity to introduce the framework for the later experimental work. This theoretical presentation is followed by a discussion on SRF cavities and typical cavity performance. Chapter 3 gives an overview of how SRF cavities are typically prepared and tested, including the theoretical basis for measuring cavity performance. Doping of SRF cavities with impurities is introduced in Chapter 4. This includes a discussion of previous work, outlines a list of open scientific questions, and gives an overview of the cavities prepared at Cornell. Chapter 5 studies the impact of nitrogen-doping on the temperature-dependent BCS resistance. This includes understanding how nitrogen diffuses into nio-

bium and how R_{BCS} is affected at both low and high fields. Chapter 6 studies the other component of surface resistance, the temperature-independent residual resistance, R_{res}. This focuses on how ambient magnetic field and cool down conditions affect R_{res} in doped cavities. The nature of the reduced quench fields in nitrogen-doped cavities is studied in Chapter 7. Finally, Chapter 8 looks at how nitrogen-doped cavities perform in realistic cryomodule environments. The dissertation concludes in Chapter 9 with a summary and outlook for the future.

CHAPTER 2

SRF BACKGROUND

This chapter will focus on the theoretical background to the physics of SRF cavities. It begins with a brief introduction to the theory of superconductivity, beginning with the London equations and a description of Ginzburg-Landau theory. Next a discussion on surface resistance under RF is presented. Following this, a summary of all the necessary material parameters that are used in this dissertation and their definitions is presented. Finally, this chapter ends with a brief introduction to SRF cavities.

2.1 Introduction to Superconductivity

Superconductivity was first discovered experimentally in 1911 by Kamerlingh Onnes [Onn11]. By cooling certain materials below a critical temperature, T_c, he discovered that the resistance under DC current dropped to zero. This phenomenon has been used in many modern applications [SML04] and enabled an entire new regime of particle accelerators to be built, using both superconducting cavities for acceleration [ABB+00] but also superconducting magnets [Sch91], able to reach significantly higher fields than in normal conducting magnets.

In addition to zero resistance under DC fields, superconductors perfectly expel magnetic field, an effect known as the Meissner effect [MO33]. If the superconductor is placed in a weak magnetic field, it acts as a dimagnet and generates screening currents on the surface resulting in flux expulsion from the bulk. This allows the interior of the superconductor to remain in the Meissner

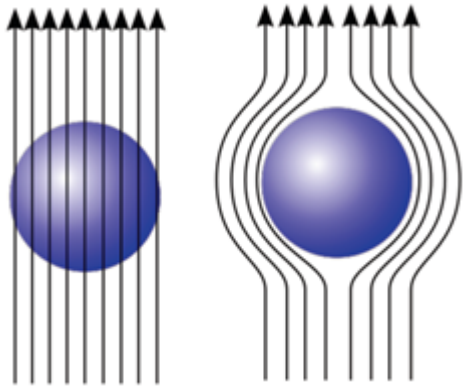

Figure 2.1: Meissner Effect - below T_c magnetic field is perfectly screened from the bulk [Mei16].

state, a state in which magnetic flux is completely absent. Figure 2.1 shows a schematic example of the Meissner effect with a superconducting sphere placed in a magnetic field above and below T_c.

Superconductors can generally be broken into two categories: Type-I and Type-II. High temperature superconductors (HTSCs) are a subset of Type-II characterized by significantly higher T_c, as high as 203 K [Sax12] and are often made of complex ceramics. The earliest superconductors discovered were Type-I. The exact distinction between Type-I and Type-II will be discussed in great depth later. In broad terms, Type-I superconductors can exist either in the Meissner or normal conducting state, while Type-II superconductors can also exist in a mixed state in which the bulk is superconducting but normal conducting lines or vortices are present. This dissertation focuses on cavities made of niobium which is a weakly to moderate Type-II superconductor, depending on the purity of the niobium.

2.1.1 Theories of Superconductivity

There are several theories devoted to understanding the physics of superconductors. The physics of superconductivity was first motivated by the London equations, developed by the London brothers in 1935 [LL35]. A theory aimed at explaining superconductivity in depth was proposed b V.L. Ginzburg and L.D. Landau in 1950 as a phenomenological theory based on the theory of phase transitions. Ginzburg-Landau theory looks at the macroscopic behavior of superconductors without examining the microscopic behavior [GL50]. In 1957, a theory published by Bardeen, Cooper, and Schrieffer (BCS theory) explained the microscopic details of superconductivity [BCS57]. Finally, in 1959, L.P. Gor'kov showed that the Ginzburg-Landau equations could be derived from the microscopic BCS theory [Gor59].

The following derivation of the London equations and GL theory follow the formalism presented in [Tin04].

The London Equations

Based on the experimental discovery of superconductivity, the London brothers began the theoretical study of superconductivity in 1935 [LL35]. They presented two equations to govern the microscopic electric and magnetic fields in a superconductor. These so called "London Equations" can be motivated from a quantum mechanical argument. F. London noted that in the absence of a magnetic field the ground state would have zero net momentum with the canonical momentum

$$\mathbf{p} = m\mathbf{v} + \frac{-e\mathbf{A}}{mc}, \tag{2.1}$$

with m the electron mass. Then the local average velocity is

$$\langle \mathbf{v}_s \rangle = \frac{-e\mathbf{A}}{mc}. \tag{2.2}$$

Denoting the number density of ground state electrons as n_s, the current density $\mathbf{J}_s$ can be calculated as

$$\mathbf{J}_s = n_s e \langle \mathbf{v}_s \rangle = \frac{-n_s e^2 \mathbf{A}}{mc} = \frac{-\mathbf{A}}{\Lambda c}, \tag{2.3}$$

with

$$\Lambda = \frac{4\pi\lambda_L^2}{c^2} = \frac{m}{n_s e^2}, \tag{2.4}$$

where λ_L is a penetration depth of the field into the material, the implications of which will be discussed momentarily. Taking the time derivative of both sides leads to the first London equation

$$\mathbf{E} = \frac{\partial}{\partial t} \left(\Lambda \mathbf{J}_s \right). \tag{2.5}$$

Equation 2.5 gives the perfect conductivity of a superconductor, now with n_s the density of superconducting electrons. By taking the curl of Equation 2.5 one obtains the second London equation

$$\mathbf{H} = -c\nabla \times \left(\Lambda \mathbf{J}_s \right), \tag{2.6}$$

which when combined with Maxwell's equations leads to

$$\nabla^2 \mathbf{H} = \frac{\mathbf{H}}{\lambda_L^2}. \tag{2.7}$$

Equation 2.7 implies that a magnetic field will be exponentially screened from the interior of a superconductor with penetration depth λ_L, known as the London penetration depth[1].

[1] λ_L is a constant for materials. For example, clean niobium has $\lambda_L = 39$ nm [Tin04].

Ginzburg-Landau Theory

Now with a firm basis in London theory, it is worth discussing the macroscopic Ginzburg-Landau (GL) theory. GL theory introduces a pseudowavefunction, $\psi(\mathbf{r})$ as a complex order parameter. $|\psi(\mathbf{r})|^2$ represents the local density of superconducting electrons, $n_s(\mathbf{r})$ in London theory. If one assumes that ψ is small and varies slowly in space, the free energy density f can be expanded as a series:

$$f = f_{n0} + \alpha|\psi|^2 + \frac{\beta}{2}|\psi|^4 + \frac{1}{2m^*}\left|\left(\frac{\hbar}{i}\nabla - \frac{e^*}{c}\mathbf{A}\right)\psi\right|^2 + \frac{h^2}{8\pi}, \tag{2.8}$$

with series expansion coefficients α and β and an effective charge and mass of the electrons e^* and m^*, respectively. The goal of GL theory is to minimize Equation 2.8. If $\psi = 0$, this reduces to the free energy of the normal conducting state, $f_n = f_{n0} + h^2/8\pi$. If one assumes that there are no fields and ψ is slowly changing then

$$f_s - f_n = \alpha|\psi|^2 + \frac{1}{2}\beta|\psi|^4, \tag{2.9}$$

which is valid near T_c where $|\psi|^2 \rightarrow 0$. β must be positive in order for Equation 2.9 to make sense. Depending on the sign of α, two cases arise: if α is positive, the minimum free energy is at $|\psi|^2 = 0$, whereas if α is negative, the minimum occurs when

$$|\psi|^2 = |\psi_\infty|^2 \equiv -\frac{\alpha}{\beta}. \tag{2.10}$$

Substituting this into Equation 2.9 gives

$$f_s - f_n = \frac{-\alpha}{2\beta}. \tag{2.11}$$

This suggests that $\alpha(T)$ must change sign from positive to negative at T_c. Taylor expanding in T then gives

$$\alpha(T) = \alpha'(t - 1), \tag{2.12}$$

with $t = T/T_c$ and $\alpha' > 0$. Then $|\psi|^2$ takes the form

$$|\psi|^2 \propto (1 - t) \tag{2.13}$$

for T near $\mathrm{T_c}$.

Taking variational derivatives of Equation 2.8 and minimizing the derivative gives the GL equations

$$\alpha\psi + \beta|\psi|^2\psi + \frac{1}{2m^*}\left(\frac{\hbar}{i}\nabla - \frac{e^*}{c}\mathbf{A}\right)^2 \psi = 0 \tag{2.14}$$

and

$$\mathbf{J} = \frac{e^*\hbar}{2m^*i}(\psi^*\nabla\psi - \psi\nabla\psi^*) - \frac{e^{*2}}{m^*c}\psi^*\psi\mathbf{A}. \tag{2.15}$$

The temperature dependency of the penetration depth can be calculated from GL theory and given by

$$\lambda_{GL} = \sqrt{\frac{\beta}{e^2|\alpha|}} = \sqrt{\frac{\beta}{e^2|\alpha'|}} \cdot \frac{1}{\sqrt{1-t}}. \tag{2.16}$$

It is useful to define a characteristic length, ξ_{GL} as

$$\xi_{GL} = \frac{1}{\sqrt{2|\alpha|}} = \frac{1}{\sqrt{2|\alpha'|}} \cdot \frac{1}{\sqrt{1-t}}. \tag{2.17}$$

It is then useful to define the temperature independent GL parameter

$$\kappa_{GL} \equiv \frac{\lambda_{GL}}{\xi_{GL}} = \sqrt{\frac{2\beta}{e^2}}. \tag{2.18}$$

Superconductors are separated into the two categories by the GL parameter, κ_{GL}. Type-I superconductors are those with $\kappa_{GL} < 1/\sqrt{2}$ and Type-II are those with $\kappa_{GL} > 1/\sqrt{2}$. .

The difference between the two types of superconductors can be understood in terms of energy. When an external magnetic field is applied to a superconductor, the free energy is raised as supercurrents flow near the surface to screen

the bulk from the field. For a normal conducting vortex of size ξ to form in the bulk, the free energy in the region λ away from the vortex would be decreased while the energy would be increased in the now normal conducting volume. In Type-I superconductors, with large ξ compared to λ, the energy cost is more expensive than the benefit. However, in Type-II, the opposite holds true and there exists an external field at which it becomes energetically favorable for a normal conducting core to form in the bulk. The magnetic flux contained in a single normal conducting vortex core is quantized with each core containing $\phi_0 \approx 2.07 \times 10^{-15}$ Wb [DN61]. A discussion on the theories of critical fields and the quantitative differences between Type-I and Type-II superconductors will be presented in Chapter 7.

The Pippard Approximation

In 1953, A.B. Pippard introduced what is now known as the BCS coherence length, ξ_0, by developing a superconducting model that took into account non-local effects on the electron interactions. He argued that the superconducting wave function should have a characteristic length scale which could be estimated by an uncertainty-principle argument. Only electrons around $k_B T_c$ of the Fermi energy can affect dynamics near T_c and they have momentum $\Delta p \approx k_B T_c / v_F$, with v_F, the Fermi velocity. Then by the uncertainty principle

$$\Delta x \gtrsim \frac{\hbar}{\Delta p} \approx \frac{\hbar v_F}{k_B T_c}, \tag{2.19}$$

which leads to the definition of the BCS coherence length

$$\xi_0 = \frac{\hbar v_F}{k_B T_c}. \tag{2.20}$$

If one assumes that a pure material has a BCS coherence length, ξ_0, then impurities that introduce scattering (lowering the mean free path of the material,

ℓ) will modify the coherence length and lead to an effective coherence length [Pip53]

$$\frac{1}{\xi_{eff}} = \frac{1}{\xi_0} + \frac{1}{\ell}. \tag{2.21}$$

The penetration depth can also then be calculated as the mean free path changes as

$$\lambda_{eff}(\ell) = \lambda_L \sqrt{1 + \frac{\xi_0}{\ell}}, \tag{2.22}$$

for sufficiently large values of mean free path.

BCS Theory

In 1956, L.N. Cooper showed that electrons near the Fermi surface formed an instability in the presence of a weak attractive potential. This potential led to the pairing of electrons into what is now known as Cooper pairs [Coo56]. In 1957, building on this work, Cooper along with J. Bardeen and J.R. Schrieffer developed a complete microscopic theory of superconductivity. This BCS theory, as it is now known, describes superconductivity from the interactions of electrons and phonons in a vibrating crystal lattice structure [BCS57].

The presence of an energy gap, E_g, between the ground state and the quasiparticle excitations of the system was first suggested in 1946 by J.G. Daunt and K. Mendelssohn [DM46]. BCS theory directly leads to a prediction of an energy gap, the energy required to break a Cooper pair. This energy can be calculated as

$$E_g(T = 0) = 2\Delta(T = 0) = 2.528 k_B T_c, \tag{2.23}$$

in agreement with experimental findings.

It is also important to note that the GL coherence length can be calculated

from BCS theory using λ_L, ξ_0, and the mean free path [OMFB79] as

$$\xi_{GL} = \frac{0.739}{\sqrt{\xi_0^{-2} + \frac{0.882}{\xi_0 \ell}}}. \tag{2.24}$$

The GL penetration depth can be calculated in a similar manner as

$$\lambda_{GL} = \frac{\lambda_L}{\sqrt{2}} \sqrt{1 + \frac{0.882\xi_0}{\ell}}. \tag{2.25}$$

BCS theory predicts a resistance under RF electromagnetic fields, known as the BCS resistance, R_{BCS}. As the temperature decreases, the fraction of electrons paired in Cooper pairs increases and R_{BCS} decreases quickly. An approximation of the surface resistance due to BCS theory in the dirty limit ($\ell \ll \xi_0$) is

$$R_{BCS} = A\frac{f^2}{T} \exp\left(\frac{-\Delta}{k_B T}\right), \tag{2.26}$$

where f is the frequency, T is the temperature, k_B is the Boltzmann constant, Δ half the energy required to break a cooper pair, and A is a constant that depends on material properties such as the mean free path [PKH98].

The BCS resistance can more accurately be calculated from BCS theory using a code called SRIMP which solves the BCS equations [Hal70]. The qualitative behavior of R_{BCS}'s dependence on material properties can then be observed. Figure 2.2a shows how R_{BCS} changes as the energy gap (normalized to $k_B T_c$) changes. Increasing $\Delta / k_B T_c$ results in an exponential decrease in R_{BCS}. Additionally, Figure 2.2b shows how R_{BCS} changes as mean free path changes. R_{BCS} is minimized at low mean free path corresponding to $\ell \approx \xi/2$. A detailed study of the effect of mean free path on R_{BCS} in SRF cavities to find the optimal mean free path which minimizes R_{BCS} will be presented in Chapter 5.

From BCS theory, R_s can be calculated for a given frequency as a function of temperature. An example of this is shown for niobium at 1.3 GHz in Figure 2.3

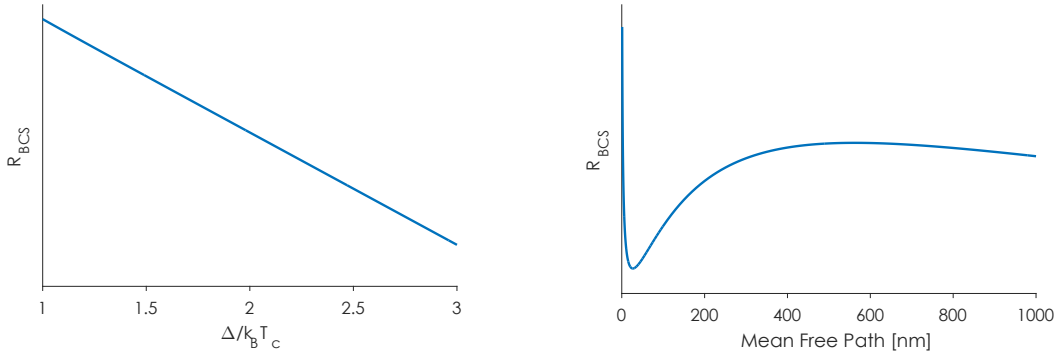

(a) Change in R_{BCS} as a function of energy gap. Larger Δ/k_BT_c leads to an exponential decrease in R_{BCS}.

(b) Change in R_{BCS} as a function of mean free path. A minimum in R_{BCS} is present at $\ell \approx \xi/2$.

Figure 2.2: Change in R_{BCS} due to changing material properties calculated by SRIMP [Hal70].

in addition to R_s for copper for comparison. Copper's resistance is relatively constant below 10 K at ~10 mΩ [Mat79]. Above T_c, niobium has a surface resistance on the same order as copper, however below T_c, R_s drops exponentially as the temperature is decreased. At very low temperatures, the temperature dependent R_{BCS} drops to zero and R_s falls to the temperature independent residual resistance, R_{res}. R_{res} will be discussed in detail in Chapter 6 and is is typically a few nΩ's.

2.2 Material Parameters

So far several material parameters have been discussed which are important for the remainder of this dissertation. First is the critical temperature of the superconductor, denoted T_c. T_c is the temperature at which the phase transition between the normal and superconducting states occurs and is 9.2 K for clean niobium [FSS66]. Second is the energy gap, E_g, which is the energy cost re-

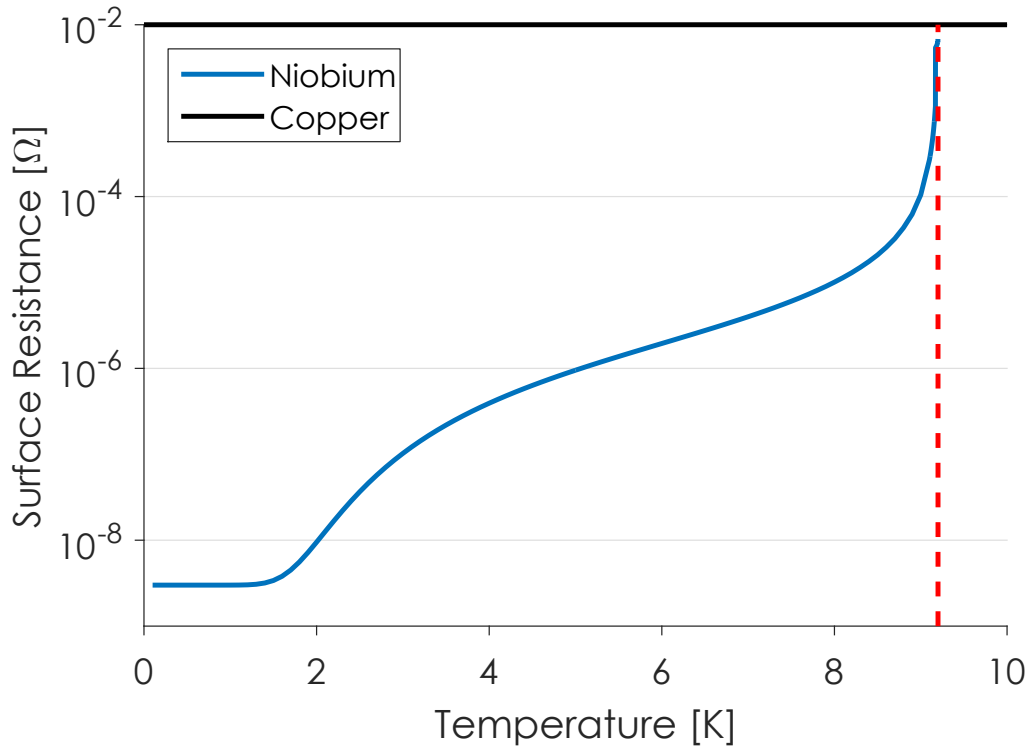

Figure 2.3: Surface resistance versus temperature for niobium and copper at 1.3 GHz calculated from BCS theory with SRIMP [Hal70]. Near T_c, niobium's R_s approaches that of copper's while at low temperatures it can reach as low as a few nΩ's, limited by the temperature independent residual resistance, R_{res}.

quired to break a cooper pair. In this dissertation it is usually denoted as half the energy gap and normalized to $k_B T_c$ and is thus denoted $\Delta/k_B T_c$. The London penetration depth, denoted λ_L is the length over which external magnetic field decays exponentially into the superconducting bulk. For clean niobium it is 39 nm [MM65]. The BCS coherence length, denoted ξ_0 is roughly the size of the cooper pairs and normal conducting vortices if they appear in the superconductor. In clean niobium it is 38 nm [MM65]. The mean free path, denoted ℓ, is the average distance an electron travels in a material in between hitting scattering sites. The mean free path can be used to calculate the "dirty" penetration depth and coherence length values from Equation 2.22 and Equation 2.24. Fi-

Variable	Name	Clean Nb Value[1]
T_c	Critical temperature	9.2 K
Δ/k_BT_c	$\frac{1}{2}$ the energy gap[2]	1.81
λ_L	London penetration depth	39 nm
ξ_0	Clean coherence length	38 nm
ℓ	Mean free path	$> 1\ \mu$m
κ_{GL}	GL parameter	~1

[1] Clean niobium means high RRR niobium with large mean free path.
[2] Normalized to k_BT_C.

Table 2.1: Summary of material parameters used in this dissertation. Values obtained from [FSS66, MM65, NM75].

nally, the GL parameter, κ_{GL}, is defined as the ratio of the GL penetration depth to the GL coherence length. For clean niobium, $\kappa_{GL} \approx 1$. A summary of these material parameters and their values in clean niobium is presented in Table 2.1.

2.3 Introduction to SRF Cavities

Superconducting RF cavities (SRF) are the dominant driving force in modern accelerators. Cavities can be thought of as modified waveguides so the physics of them can be derived from the physics of waveguides as in [PKH98]. Maxwell's equations in vacuum will yield the wave equation

$$\left(\nabla^2 - \frac{1}{c^2}\frac{\partial^2}{\partial t^2}\right)\begin{pmatrix}\mathbf{E}\\ \mathbf{H}\end{pmatrix} = 0 \tag{2.27}$$

Then if it is assumed that the fields take the form

$$\mathbf{E}(x,t) = \mathbf{E}(\rho,t)e^{i(kz-\omega t)} \tag{2.28}$$

$$\mathbf{H}(x,t) = \mathbf{H}(\rho,t)e^{i(kz-\omega t)}, \tag{2.29}$$

with ω the RF frequency and k the wave number,

$$\nabla_{\perp}^2 + \left(\frac{\omega^2}{c^2} - k^2\right)\begin{pmatrix} \mathbf{E} \\ \mathbf{H} \end{pmatrix} = 0, \tag{2.30}$$

with the operator $\nabla_{\perp}^2 = \nabla^2 - \frac{\partial^2}{\partial z^2}$. Here $\mathbf{H}$ is the magnetic field intensity related to $\mathbf{B}$ by $\mathbf{B} = \mu\mathbf{H}$. Additionally, the boundary conditions imposed at the perfectly conducting wall are given by

$$\hat{n} \times \mathbf{E} = 0, \quad \hat{n} \cdot \mathbf{H} = 0. \tag{2.31}$$

The solutions to the eigenvalue Equation 2.30 form an orthogonal set with eigenvalues $\gamma^2 = \omega^2/c^2 - k^2$.

Consider the case of a cylindrical pill-box cavity - a cylindrical structure (radius R) of finite length of length (d). The solutions to the eigenvalue equation are Bessel functions. The modes are classified by the name TM_{mnp} with m, n, and p representing the number of times E_z changes sign in the ϕ, ρ, and z directions, respectively. The lowest frequency TM mode is

$$E_z = E_0 J_0\left(\frac{2.405\rho}{R}\right)e^{-i\omega t} \tag{2.32}$$

$$H_{\phi} = -i\frac{E_0}{\eta}J_1\left(\frac{2.405\rho}{R}\right)e^{-i\omega t}, \tag{2.33}$$

with J_0 and J_1 the zeroth and first order Bessel functions respectively, ρ the distance from the center of the pillbox, and $\eta = \sqrt{\frac{\mu_0}{\epsilon_0}}$. The resonant frequency is given by

$$\omega_{010} = \frac{2.405c}{R}. \tag{2.34}$$

While the cavities discussed in this dissertation are more complicated than a pillbox cavity, the main ideas provide a good intuition for the physics inside more complicated accelerating structures that use a TM_{010} mode. An illustration

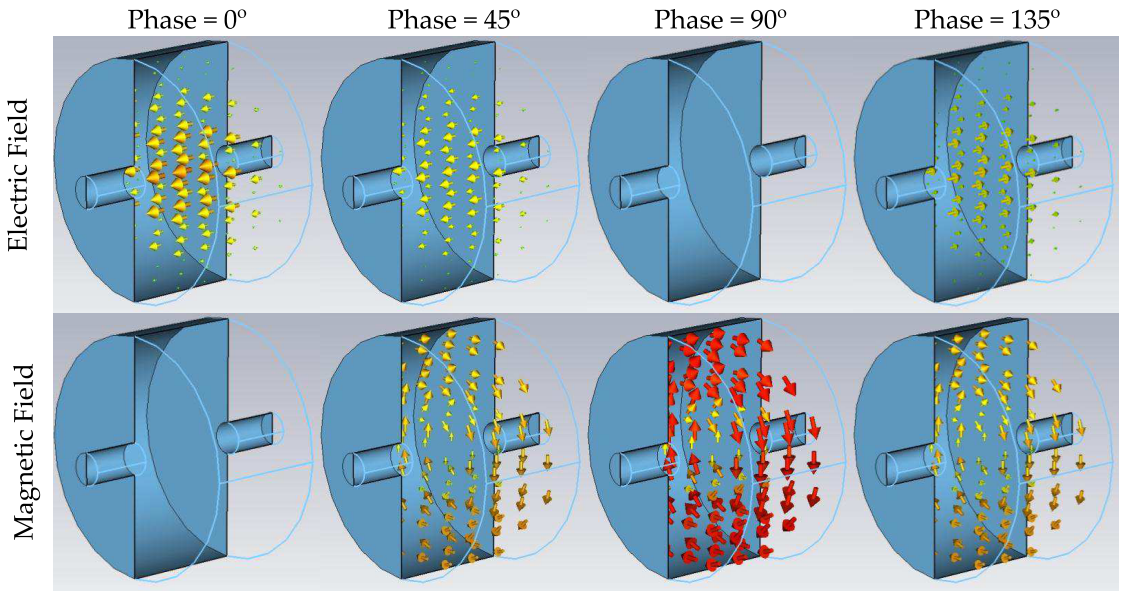

Figure 2.4: Time evolution of the electric and magnetic fields for the TM010 mode of a pillbox cavity with beam tubes. Image from [Val13]

of the TM_{010} mode in a pillbox cavity for different phases is shown in Figure 2.4. The TM modes have an electric field component that points along the longitudinal axis, allowing energy to be transferred to charged particles that pass through the structure along this axis. If a relativistic electron passes through the cavity on axis ($\rho = 0$), it will experience an accelerating voltage V given by

$$V = \Re\left\{\int \mathbf{E}(\rho = 0, z)e^{i(\omega_0 z/c+\phi)}dz\right\}, \tag{2.35}$$

for some arbitrary phase, ϕ.

An important figure of merit for accelerating structures is the accelerating electric field (E_{acc}) that the electron sees defined by

$$E_{acc} = \frac{V_{max}}{d}, \tag{2.36}$$

where V_{max} is the maximum accelerating voltage, maximized by proper choice of ϕ.

While this derivation is for perfect conductors, true cavities (including SRF

cavities) have a finite conductivity, i.e. a non-zero surface resistance. This leads to a dissipated power in the cavity walls and to the definition of the quality factor, Q_0, another important figure of merit for cavities

$$Q_0 \equiv \frac{\omega U}{P_{diss}}, \tag{2.37}$$

with U the stored energy in the cavity and P_{diss} the dissipated power in the cavity walls.

2.3.1 Surface Resistance in SRF Cavities

As discussed in the previous sections, the physics of superconductivity is well described by GL and BCS theory. While under DC currents, superconductors show a zero resistance due to screening of unpaired electrons by the Cooper pairs. However, under AC currents and the finite inertia of the Cooper pairs, this screening is imperfect, leading to a small but not negligible resistance. This resistance is typically denoted the surface resistance, R_s. The following derivation follows the formalism presented in [PKH98]. From R_s, the dissipated power P_{diss} in the wall of the superconductor per unit area can be calculated

$$P_{diss} = \frac{1}{2} R_s \int_S |\mathbf{H}|^2 ds, \tag{2.38}$$

with $\mathbf{H}$ the RF magnetic field. P_{diss} is related to the quality factor of a resonator by Equation 2.37. The total energy in the resonator is given by

$$U = \frac{1}{2} \mu_0 \int_V |\mathbf{H}|^2 dv. \tag{2.39}$$

Then Equation 2.37 can be written

$$Q_0 = \frac{\omega_0 \mu_0 \int_V |\mathbf{H}|^2 dv}{R_s \int_S |\mathbf{H}|^2 ds}. \tag{2.40}$$

Property	TESLA[1]	TESLA[2]	Cornell ERL[1]	CEBAF
f [GHz]	1.3	1.3	1.3	1.5
E_{pk}/E_{acc}	1.88	2.00	1.76	1.81
B_{pk}/E_{acc} [mT/MVm^{-1}]	4.28	4.26	4.08	4.4
G [Ω]	278	270	272	255
R_a/Q_0 [Ω][3]	105	1036	116	102
$E_{pk}/\sqrt{U}$ [MVm^{-1}/ $\sqrt{\text{J}}$]	15.1	5.53	14.7	17.6

[1] Single-cell cavities.
[2] 9-cell cavities.
[3] In this dissertation, the accelerator definition of R_a/Q_0 is used.

Table 2.2: Cavity shapes used in this dissertation and their parameters. Values were calculated by V. Shemelin for single-cell cavities with long beam pipes using SLANS [MY91] and first presented in [Pos15b].

It is useful to define the geometry factor, G

$$G = \frac{\omega_0 \mu_0 \int_V |\mathbf{H}|^2 dv}{\int_S |\mathbf{H}|^2 ds}, \tag{2.41}$$

so that R_s can be written as

$$R_s = \frac{G}{Q_0}. \tag{2.42}$$

G depends only on the shape of the cavity and can be calculated from EM codes for a given cavity shape. Important constants for the cavity shapes used in this dissertation are given in Table 2.2. These parameters were calculated using SLANS [MY91] for the various cavity shapes.

In SRF cavities, typically the BCS resistance, R_{BCS}, is only one component of the total surface resistance, R_s. An additional temperature independent term has been shown to play a role, denoted the residual resistance, R_{res}. R_{res} becomes increasingly important at low temperature as R_{BCS} drops to zero. R_{res} is made up of contributions to R_s not coming from BCS theory and not dependent on temperature. These contributions can be for example from oxides, hydrides, and trapped magnetic flux. The effects of trapped magnetic flux will be dis-

cussed in great detail in Chapter 6. The total surface resistance can then be written

$$R_s(T, B) = R_{BCS}(T, B) + R_{res}(B), \tag{2.43}$$

in which it is important to note that both components can depend on the magnitude of the RF field applied, B. Recall that the exact BCS resistance at low surface fields can be calculated from codes as was discussed in section 2.1.1.

It is useful to look at how R_s breaks up for a typical SRF cavity. Figure 2.5 shows the measured R_s (in gray), R_{BCS} (in light blue), and R_{res} (in dark blue) for a 1.3 GHz TESLA shape cavity [ABB+00] as a function of temperature at low fields. At high temperatures (near 4.2 K), R_s is dominated by R_{BCS}. However, as the temperature is decreased, R_{BCS} becomes less important, eventually dropping to near zero at 1.5-1.6 K. At low temperature R_s is dominated by R_{res}. It is also important to note that in the intermediate temperature regime (~2 K), R_{BCS} and R_{res} are on the same order and play equally important roles in the total R_s.

2.3.2 Typical Cavity Performance

Cavity performance is typically quantified by E_{acc} and Q_0 measurements. Typically these performance tests consist of measuring Q_0 versus temperature at low field, Q_0 versus E_{acc} at different temperatures, and resonance frequency versus temperature near T_c. To give context to the performance that will be discussed later in this dissertation, it is useful to look at how a typically prepared cavity performs. The following are examples from a 1.3 GHz TESLA shaped cavity prepared with the standard, high performance cavity preparation[2] [GRS+13]

[2]Surface preparation with electropolishing to be discussed in full detail in Chapter 3.

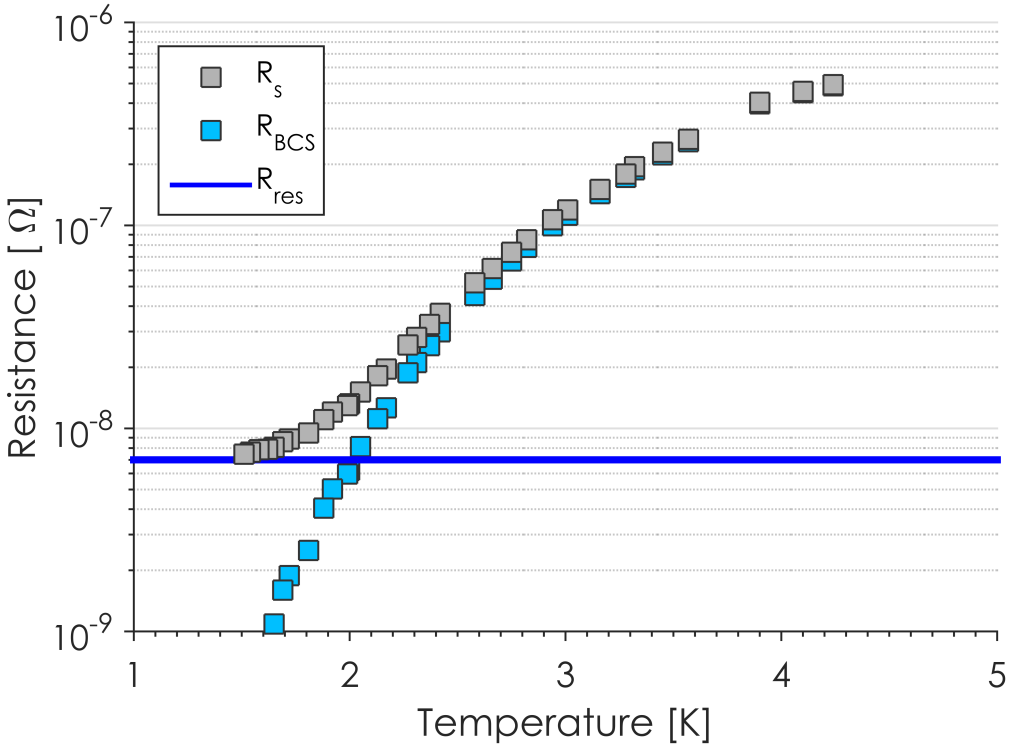

Figure 2.5: Example of how surface resistance (R_s, shown in gray) splits into BCS resistance (R_{BCS}, shown in light blue) and residual resistance (R_{res}, shown in dark blue). Data measured at low fields on a 1.3 GHz niobium cavity prepared with electropolishing and 48 hour 120°C heat treatment.

prior to the development of nitrogen-doping.

Due to the (roughly) exponential behavior of R_s with temperature, Q_0 increases exponentially as the temperature is decreased. An example of a Q_0 versus 1/temperature plot for an SRF cavity is shown in Figure 2.6. Q_0 at high temperature (4.2 K) is on the order of 6×10^8. As the temperature is decreased, Q_0 increases exponentially (linearly with $1/T$ on a logarithmic scale) reaching nearly 8×10^{10}, corresponding to ~3.5 nΩ of surface resistance. This linear relationship between $1/T$ and log Q_0 is in agreement with BCS theory and Equation 2.26. It is not unusual for cavities prepared with modern techniques to reach Q_0's as high as 1×10^{11}.

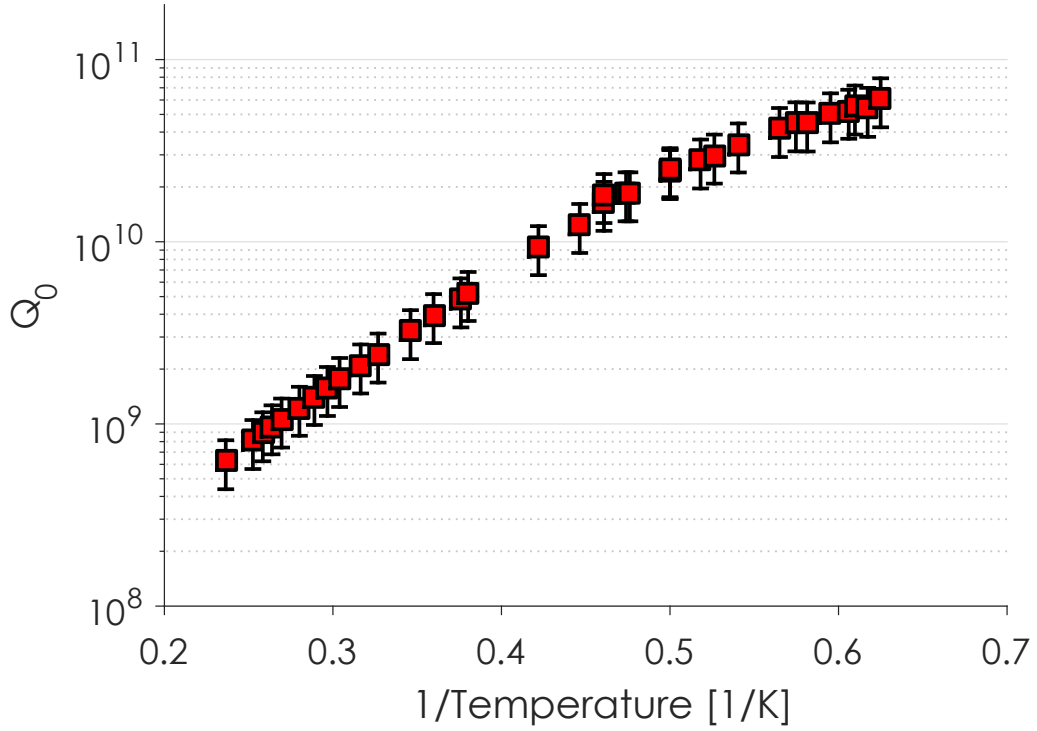

Figure 2.6: Typical Q_0 versus inverse temperature for a cavity prepared with electropolishing. Q_0 increases linearly on a logarithmic scale with $1/T$ as predicted by BCS theory and Equation 2.26. At low temperature (large $1/T$), R_{res} dominates and Q_0 deviates from the linear behavior.

Cavities prepared with electropolishing display a very characteristic Q_0 versus E_{acc} curve that can be divided into three regions [PKH98]. An example Q_0 versus E_{acc} for a cavity at 2.0 K, the typical operating temperature of SRF cavities, is shown in Figure 2.7. The three distinct regions are

1. Low field Q slope (LFQS): below 5 MV/m, Q_0 increases as E_{acc} is increased (shown in red in Figure 2.7).
2. Medium field Q slope (MFQS): between 5 and ~25 MV/m, the Q_0 decreases slowly as E_{acc} is increased (shown in blue in Figure 2.7).
3. High field Q slope (HFQS): above 25 MV/m the Q_0 decreases quickly as

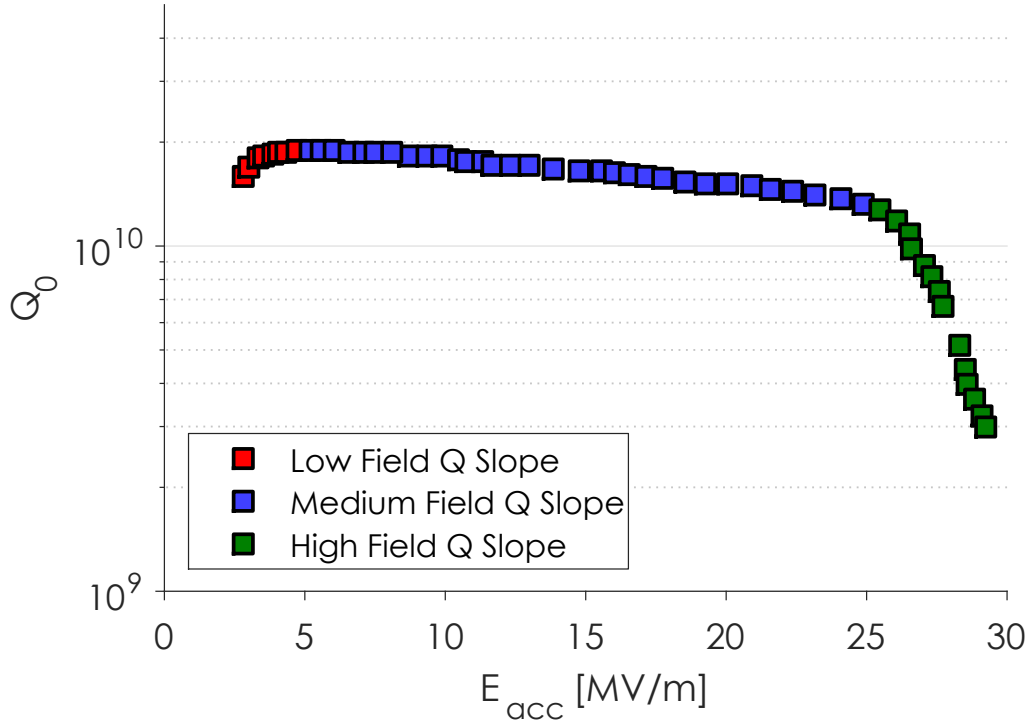

Figure 2.7: Typical Q_0 versus E_{acc} for a cavity prepared with electropolishing. Q_0 increases with increasing E_{acc} between 0 and 5 MV/m (low field Q slope); Q_0 decreases slowly with increasing E_{acc} between 5 and 25 MV/m (medium field Q slope); Q_0 decreases quickly with increasing E_{acc} above 25 MV/m (high field Q slope). Data courtesy of FNAL [GRS+13].

E_{acc} is increased (shown in green in Figure 2.7).

Typically standard preparation methods can yield cavities that reach 2×10^{10} at 2.0 K.

It has been shown that the HFQS can be eliminated in electropolished cavities by the use of a 120°C heat treatment for 48 hours [Cio04]. Cavities without this heat treatment typically are limited to fields < 30 MV/m whereas those that receive it can typically reach higher fields, in some cases more than 40 MV/m. In well prepared cavities, the fundamental limit in SRF cavities reached is usu-

ally a quench, the point at which the cavity becomes normal conducting due to high magnetic fields on the surface above the superconductor's critical field or due to excessive heating causing the cavity to heat above T_c. However, some cavities may quench earlier due to defects in the material.

As was discussed above, cavities are resonators and thus have a resonant frequency where they optimally store energy. This resonance frequency is heavily dependent on temperature, especially near the critical temperature, T_c. Recall from Equation 2.16 that the penetration depth changes with temperature. As the penetration depth increases near T_c, the cavity effectively gets larger as the field penetrates further into the walls. This change results in a shift in resonance frequency that can be measured. An example of the shift in resonance frequency for a cavity between 7.5 and 9.2 K is shown in Figure 2.8. As the temperature is increased, the frequency decreases significantly, on the order of 5 kHz between liquid helium temperatures and T_c and can be used to extract material parameters, see section 3.4.

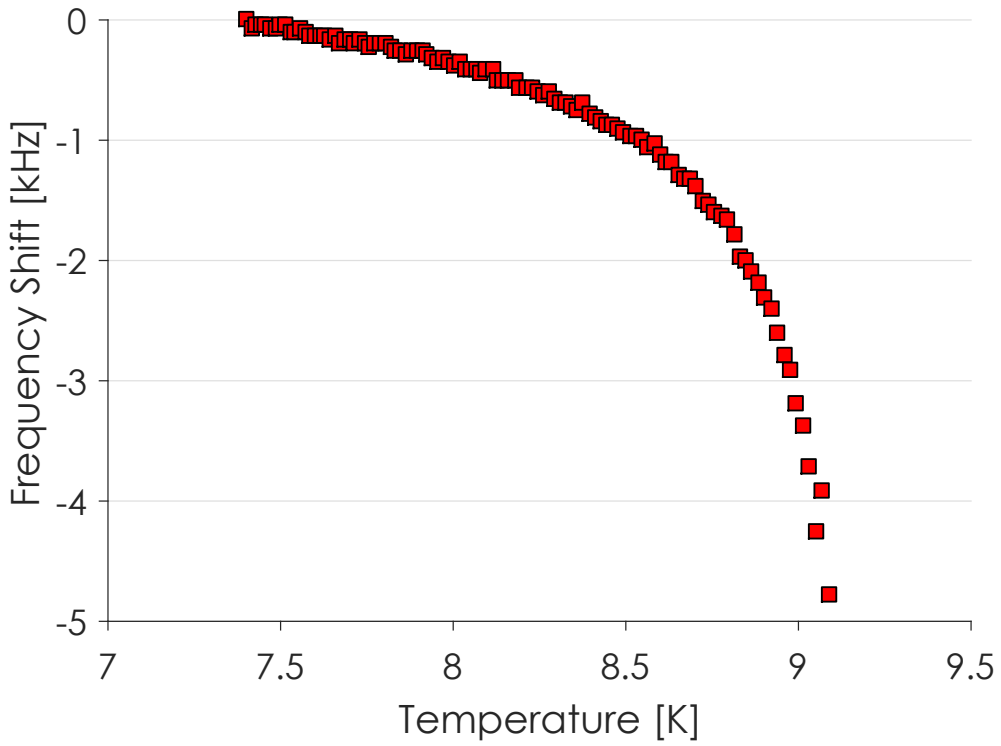

Figure 2.8: Example of cavity resonance frequency shift in the region of 7.5 to 9.2 K.

CHAPTER 3

SRF CAVITY TESTING

This chapter discusses the preparation and CW testing of SRF cavities. It begins with a discussion of how cavities are prepared, including fabrication, chemistry, degassing, cleaning, assembly on the test stand, and test preparation. Next a discussion on the RF measurement methods, based on the formalism presented in [PKH98] is given. Third, an introduction to the Cornell temperature mapping system is presented including techniques for finding cavity quench location using the system. Finally, this chapter ends with a brief discussion on extraction of material properties from RF data.

3.1 Cavity Preparation

Niobium SRF cavities are manufactured from high purity niobium sheets (cavities discussed in this dissertation were, for the most part, produced with RRR 320 material from Tokyo Denkai). The sheets, which are typically 3 mm thick, are pressed into half cell "cups" and welded together with an electron beam welder. The cavities discussed here mostly come in two configurations: single-cell cavities used primarily for R&D purposes in vertical tests, and 9-cell cavities which are used for production-style R&D in vertical tests and full cryomodule tests.

After fabrication, the cavities undergo a variety of processes to clean the surface and prepare for use. Usually this begins with a chemical etch using either a buffer chemical polish (BCP) [PKH98] or an electropolish (EP) [FHG+12] to re-

Cathode	Aluminum >99.5%
Stir-tube	PVDF
Paddles	PVDF
Seals	FEP enacpsulated O-ring
End Group	PTFE, HDPE
Electrolyte	24 liters/9-cell
Electrolyte Composition	10:1 (H_2S0_4:HF)
Maximum Use	9 g/L dissolved Nb
Current	80-120 A
Voltage	12 V
Temperature	15-19°C
Stir Frequency	~0-2 Hz
EP Removal Rate (Avg.)	~0.2 μm/min

Table 3.1: Cornell VEP Parameters

move the damaged layer from the surface caused by cavity fabrication. Previous experience has shown that ~100 μm is typicall sufficient to remove the damaged layer. BCP consists of mixture of hydrofluoric acid (HF), nitric acid, and phosphoric acid. During EP, a current is applied to the cavity through an electrolyte containing a mixture of HF and sulfuric acid. At Cornell, a vertical electropolish (VEP) system is used which has been shown to produce similar results as horizontal EP [FHG+12]. Figure 3.1 shows a 9-cell and single-cell cavity on the Cornell VEP system along with a schematic of the process. The exact details of VEP system are shown in Table 3.1 [Fur16]. Immediately after bulk chemical etching, the cavity is cleaned in an ultrasonic bath and rinsed on a high pressure rinse stand (HPR) to remove any acid residue. This HPR consists of spraying deionized water at approximately 1000 psi on the inside of the cavity.

While EP typically produces a smoother surface than BCP, it can result in a higher uptake of hydrogen into the niobium. In order to remove this hydrogen, cavities prepared with EP are degassed in an Ultra-high vacuum (UHV) furnace. This degas typically lasts a few hours and takes place between 650 and 800°C.

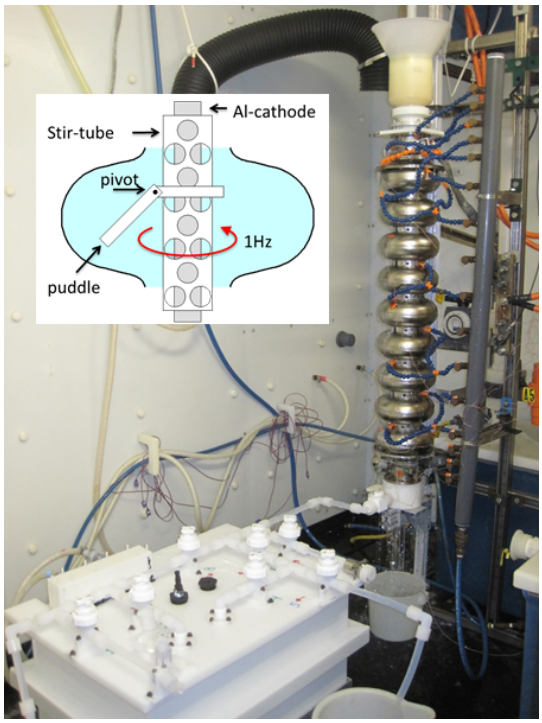

(a) Picture of a 9-cell cavity on the VEP setup along with a schematic of the VEP process.

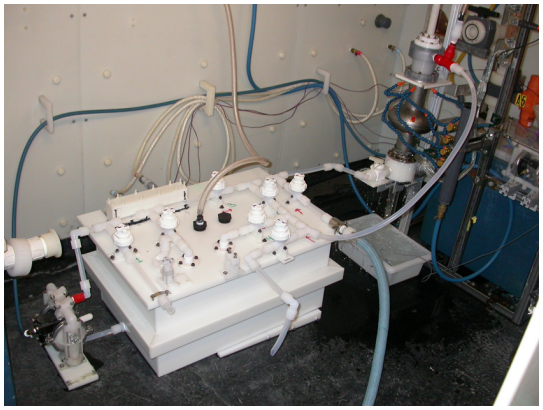

(b) Picture of a single-cell cavity on the VEP setup.

Figure 3.1: Cornell vertical electropolish (VEP) setup for 9-cell and single-cell cavities. Images from [Fur16]

A picture of the Cornell UHV furnace is shown in Figure 3.2a.

Occasionally bulk material removal is done with a centrifugal barrel polish (CBP) instead of EP. This is done in a tumbler such as the one shown in Figure 3.2b and consists of filling the cavity with polishing media (usually made of wood, ceramic, or plastic) and tumbling the cavity for many hours. This produces a mirror-like finish but requires a small amount of additional etching before testing to remove residual, embedded polishing media.

After degassing in the UHV furnace, the cavity is brought into a class 10 clean room to be assembled. The cavity is given another HPR to clean any contaminants prior to assembly. After this HPR, the top plate connection is made to

(a) Picture of the Cornell T-M vacuum furnace.

(b) Picture of the Cornell tumbler for centrifugal barrel polishing (CBP).

Figure 3.2: Cornell UHV furnace and tumbler.

one of cavity flanges with an indium seal (Figure 3.3). This top plate contains a weakly coupled ($Q_{ext} \sim 10^{13}$) antenna for measuring the transmitted power (P_t). The power sampled with the P_t antenna is proportional to the stored energy in the cavity and is thus a way of measuring the fields in the cavity. The cavity is then given a final HPR (Figure 3.4a) to remove any remaining contaminants, allowed to dry and then assembled on the test stand (Figure 3.4b). The test stand contains a variable RF input coupler which can adjust the coupling between $\sim 10^8$ and $\sim 10^{11}$ and is used to excite fields inside the cavity. After assembly, the test stand vacuum system, including the cavity, is pumped down using a scroll pump and oil-free turbomolecular pump operating through a mass flow controller to control the pump down rate. A schematic of the test stand used is shown in Figure 3.5a.

After assembly and pump down, the cavity is leak checked and the insert is prepared for testing. This includes attachment of the forward and transmitted power cables to the cavity, and setting up the instrumentation used: a helium level stick for measuring helium level, cernox temperature sensors, flux-

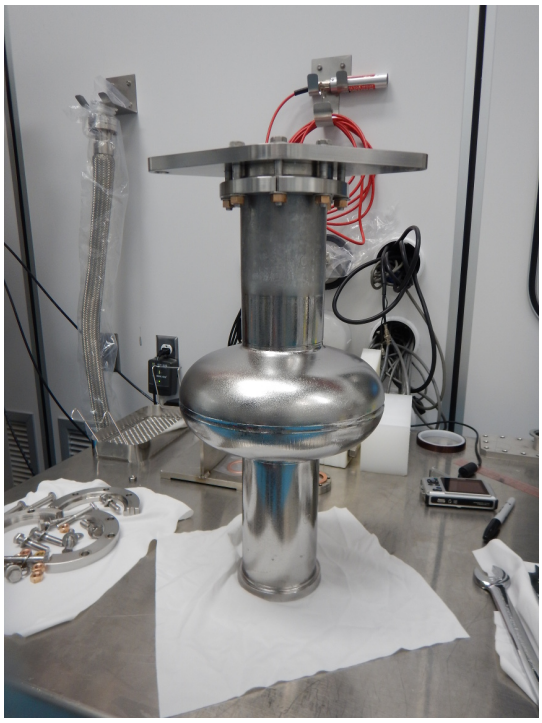

(a) Picture of a single-cell cavity assembled with the top plate.

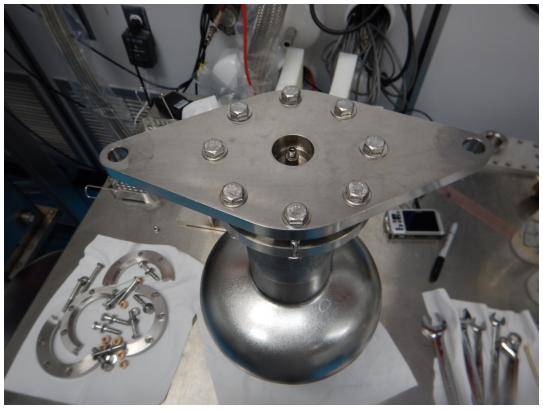

(b) Picture of the top plate on a single-cell cavity. P_t probe is connected with an SMA connector.

Figure 3.3: Single-cell cavity assembled with the top plate prior to HPR.

gate magnetometers for measuring ambient magnetic fields, and a heater for assisting in warm up and a slow cool down system. The slow cool down system consists of a series of resistors that serve to warm up helium gas as it passes in order to control the rate of cool down. This system typically can produce cool downs with rates as slow as 10 min/K and temperature gradients of < 0.1 K across a cavity cell. The insert is then placed into one of the cryogenic test dewars which are located in pits carved out of a reinforced concrete floor for radiation shielding as seen in Figure 3.6. A 90 ton shielding block is placed over the pit prior to testing for additional shielding. Immediately prior to testing, the dewar is filled with liquid helium to cool the cavity below T_c.

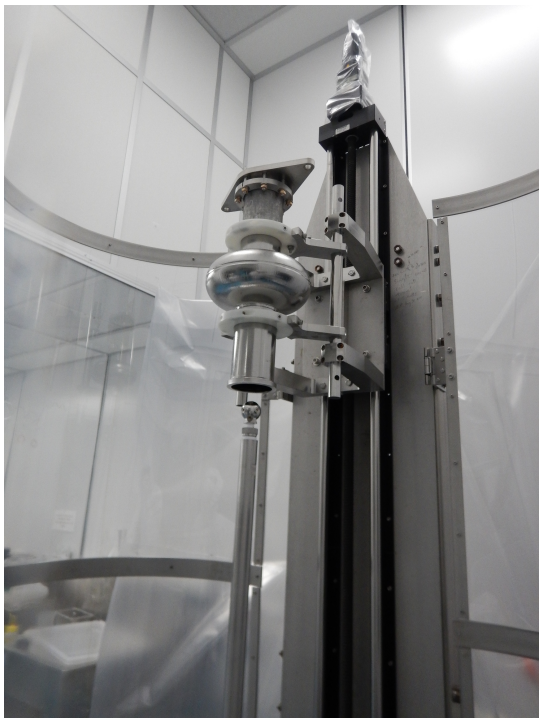

(a) Picture of a single-cell cavity on the high pressure rinse stand (HPR).

(b) Picture of a cavity being assembled on the single-cell test insert.

Figure 3.4: Single-cell cavity HPR and assembly on the test insert.

3.2 CW Cavity Testing

The most important figures of merit for an SRF cavity are the Q_0 and E_{acc}, Q_0 being a measure of the cryogenic efficiency of the cavity, and E_{acc} a measure of the accelerating strength. Usually a Q_0 vs E_{acc} curve is measured to quantify a cavity's performance. To obtain this curve, RF power is applied to the cavity near the resonance frequency through the RF input power coupler. The forward (P_f) and reverse (P_{rev}) powers are sampled using directional couplers and measured with power meters. The fields in the cavity are sampled with the transmitted power (P_t) coupler and measured with a power meter. In order to "lock" the drive RF power on the cavity's resonance, a phase lock loop (PLL) is used by mixing P_f and P_t and using them as phase feedback for the signal generator. A

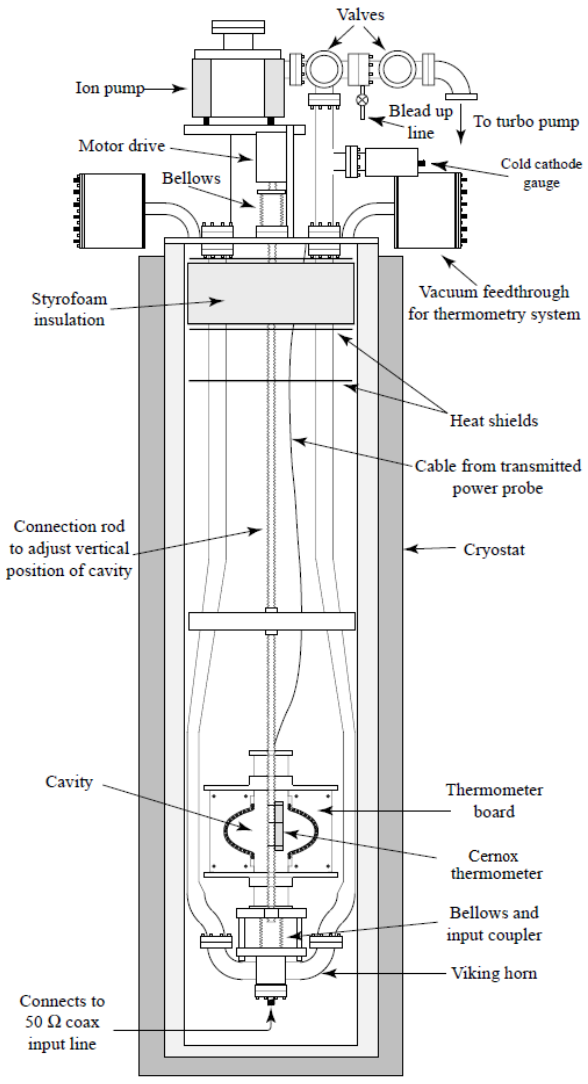

(a) Schematic representation of the test stand adapted from [Kno97] The space within the cryostat is filled with liquid helium during testing.

(b) Picture of the test stand after cavity assembly.

Figure 3.5: Single-cell cavity test stand for CW cavity testing.

Figure 3.6: The Cornell vertical test facility consisting of three dewars of varying size. Shown in the picture are the two smaller test pits.

schematic of the PLL and RF system is shown in Figure 3.7.

The following derivation is based on [PKH98]. The intrinsic quality factor, Q_0, is related to the resonance frequency, ω, the stored energy, U, and the dissipated power, P_{diss}, in the cavity walls by

$$Q_0 = \frac{\omega U}{P_{diss}}. \tag{3.1}$$

In addition to the dissipated power in the cavity walls, some power leaves via the input and transmitted power couplers. Therefore we can define a "loaded" quality factor

$$Q_L = \frac{\omega U}{P_{tot}}, \tag{3.2}$$

where P_{tot} is defined as the total power losses in the system,

$$P_{tot} = P_{diss} + P_e + P_t, \tag{3.3}$$

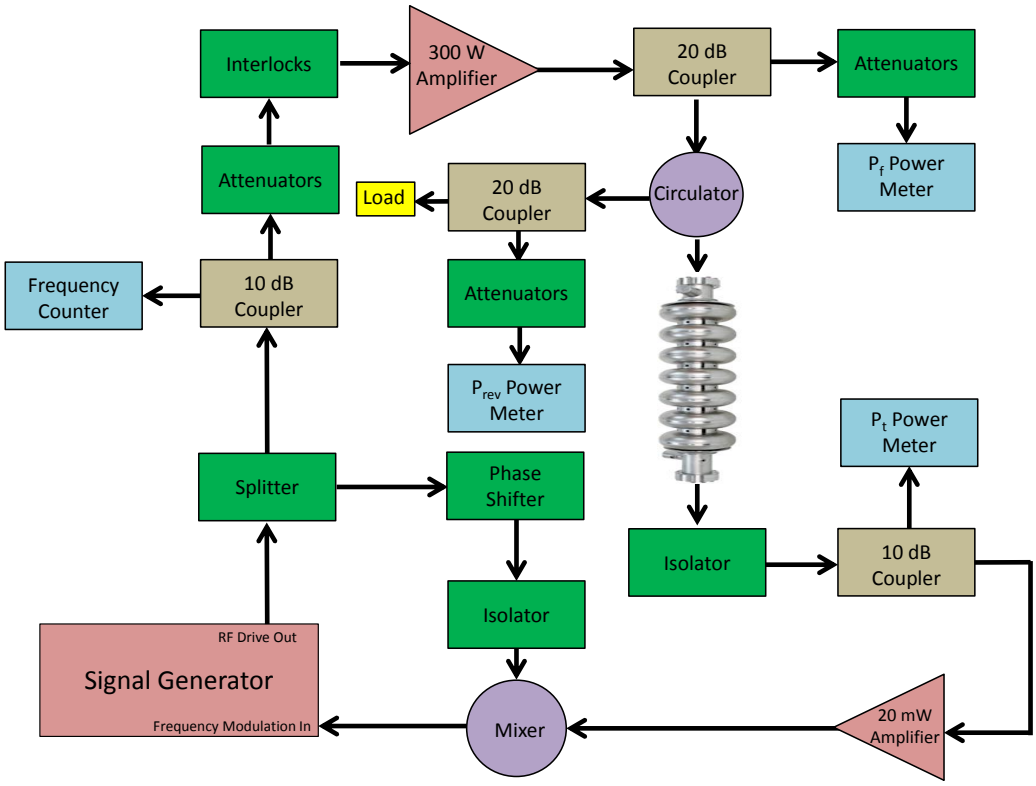

Figure 3.7: A schematic of the RF system used for CW testing. Drive frequency is locked to the cavity resonance via a phase lock loop (PLL).

where P_e is the power leaving through the input coupler and P_t is the transmitted power.

When the power is turned off, the stored energy will decay according to the differential equation

$$\frac{dU}{dt} = -P_{tot} = -\frac{\omega U}{Q_L}. \tag{3.4}$$

The solution to this equation is

$$U = U_0 \exp\left(\frac{-\omega t}{Q_L}\right), \tag{3.5}$$

where U_0 is the stored energy at $t = 0$. We can therefore define a time constant at which the energy in the cavity decays

$$\tau_L = \frac{Q_L}{\omega}. \tag{3.6}$$

A measurement of this decay time directly leads to a measurement of Q_L. Because we are interested in finding the intrinsic quality factor of the cavity Q_0, it is useful to define the quality factors of the couplers by

$$\frac{P_{tot}}{\omega U} = \frac{P_{diss} + P_e + P_t}{\omega U}, \tag{3.7}$$

$$\frac{1}{Q_L} = \frac{1}{Q_0} + \frac{1}{Q_e} + \frac{1}{Q_t}, \tag{3.8}$$

where

$$Q_e \equiv \frac{\omega U}{P_e} \tag{3.9}$$

and

$$Q_t \equiv \frac{\omega U}{P_t}. \tag{3.10}$$

Equation 3.8 can be rewritten by defining

$$\beta_e \equiv \frac{Q_0}{Q_e} \tag{3.11}$$

and

$$\beta_t \equiv \frac{Q_0}{Q_t}, \tag{3.12}$$

so that

$$\frac{1}{Q_L} = \frac{1}{Q_0}(1 + \beta_e + \beta_t) \approx \frac{1}{Q_0}(1 + \beta_e), \tag{3.13}$$

as the transmitted power probe is only weakly coupled ($Q_t \gg Q_0$) so $\beta_t \ll 1$. This coupling strength is defined as $\beta \equiv Q_0/Q_e$. Therefore by measuring the coupling parameter β along with the decay constant τ_L, the intrinsic quality factor, Q_0 can be calculated.

On resonance and in steady state, the dissipated power is related to the forward power by [PKH98]

$$P_{diss} = \frac{4\beta}{(1+\beta)^2} P_f. \tag{3.14}$$

During a cavity test, P_f, ω, τ_L, and β are measured. Therefore, Equation 3.13 can be used to find Q_0 and Equation 3.1 and Equation 3.14 can be used to calculate the stored energy, U. For a given cavity geometry, $E_{acc}/\sqrt{U}$ is a constant that can be calculated from computer codes and then used to find E_{acc}.

In summary, P_f, P_t, and the total reverse power, P_{rev} are measured with power meters, τ_L is measured by taking a decay curve of either P_{rev} or P_t, ω is measured with a frequency counter. β remains to be calculated. The term reflected power, P_r is reserved for the steady state value of the reverse power when the cavity is on resonance.

A schematic of a typical P_{rev} trace is shown in Figure 3.8 [Val13]. Under full reflection, when the drive is not locked to the cavity, $P_{rev} = P_i$, and the incident power can be read from the power meter. When the drive power is locked to the cavity, P_{rev} drops and the cavity is filled with energy. After some time P_{rev} reaches its steady state value of P_r and can be read by the power meter. Immediately after turning the RF power off, $P_{rev} = P_e$, and the emitted power can be measured by the power meter. P_{rev} then decays with decay constant τ_L.

With these measurements of P_i, P_r, and P_e, β can be calculated in two ways [PKH98]:

$$\beta_e = \frac{1}{2\sqrt{\frac{P_f}{P_e}} - 1} \tag{3.15}$$

and

$$\beta_r = \frac{1 \pm \sqrt{P_r/P_i}}{1 \mp \sqrt{P_r/P_i}}. \tag{3.16}$$

If $\beta > 1$, the cavity is over-coupled ($Q_0 > Q_e$) and the upper sign is used. If $\beta < 1$, the cavity is under-coupled ($Q_0 < Q_e$) and the lower sign is used[1]. Equation 3.15

[1] β's significantly larger than 1 can lead to additional losses in the coupler. In order to minimize this all Q_0's measured in this dissertation were measured at $\beta \approx 0.5$.

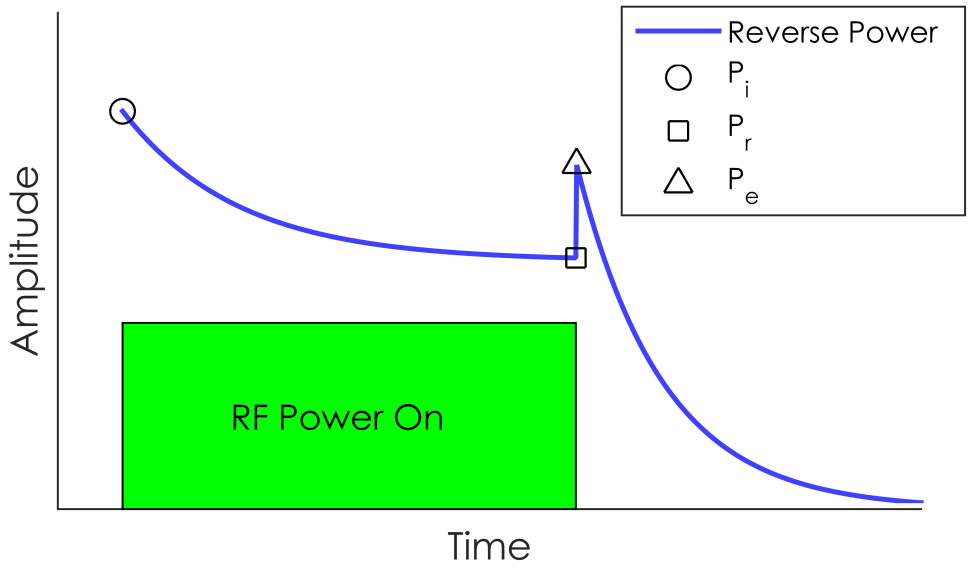

Figure 3.8: Typical reverse power, P_{rev}, trace shown schematically. The "RF Power On" box represents when the forward power is on and locked to the cavity resonance frequency. Incident, steady state reflected, and emitted power are shown. Image modified from [Val13].

is used to measure if the cavity is over-coupled or under-coupled and then β_e and β_r are averaged to find the β used in the above equations for Q_0[2].

After a measurement of a single Q_0 vs E_{acc} point, the now calibrated P_t measured on the power meter can be used to determine the accelerating field, E_{acc}, and simplify the measurement. For this, the constants U/P_t and $E_{acc}/\sqrt{P_t}$ are used with the steady state value of P_t to determine U and E_{acc} directly. Measurement errors on both E_{acc} and Q_0 are approximately 10% and are primarily from systematic errors. The random errors between points are typically much smaller[3].

[2] A discrepancy of more than 20% between β_e and β_r is indicative of a problem with the measurement.

[3] Random errors are larger at low fields where power is low and typically are on the order of 5%.

3.3 Temperature Mapping and Quench Detection

Temperature mapping (T-map) is a useful tool for diagnosing cavity performance. A T-map is an array of temperature sensors placed around the outside surface of a cavity and used to measure temperature changes due to heating caused by the RF field with spatial resolution [LMN72, Pie80, Mul84, Kno97]. It is a useful tool for locating "hot spots" on the cavity during operation which can be indicative of a defect. Additionally, it is useful for identifying locations of higher surface resistance, increased global surface resistance, and regions associated with the cavity quench. These regions can then be inspected optically using a telescope and mirror.

The T-map system at Cornell was first developed by Knobloch in 1997 [Kno97] for 1.5 GHz CEBAF cavities and modified by Posen in 2012 [PGH+12] for 1.3 GHz TESLA cavities. Figure 3.9 shows two pictures of the current Cornell system. It consists of 38 printed circuit boards each with 17 Allen-Bradley carbon resistors. These resistors are highly sensitive to changes in temperature in the region that SRF cavities operate. The resistors are mounted on pogo sticks to ensure good thermal contact with the cavity surface. They are driven by a 3 μA current and the voltage drop across them is read by a National Instruments multiplexer. By calibrating the Allen-Bradley resistors with a cernox sensor in the bath, a real temperature can be read over the cavity with a spatial resolution of ~1 cm^2. The temperature resolution of the T-Map is ~0.2 mK.

The T-map resistors are arranged at locations around the cavity such that they sample the regions of highest magnetic field, where one would expect the highest RF losses to appear. There is extensive coverage near the equator and

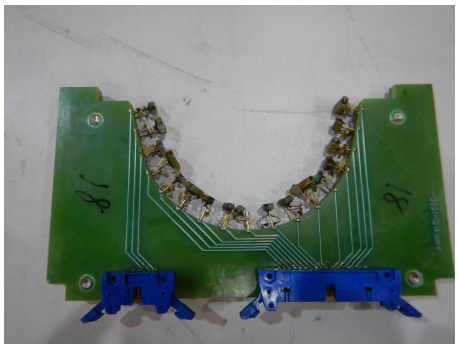

(a) A single TMap board consisting of 17 resistors.

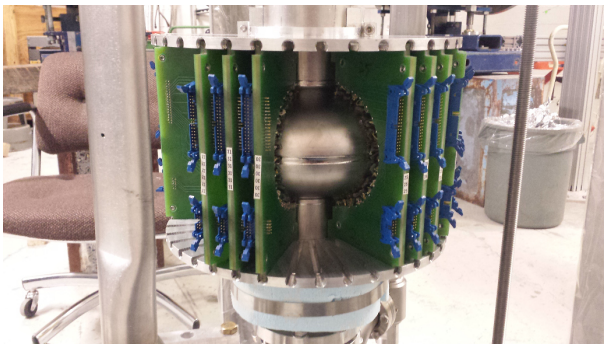

(b) A single-cell cavity with the partially assembled TMap.

Figure 3.9: The single-cell temperature mapping (TMap) system which consists of 38 boards each with 17 resistors.

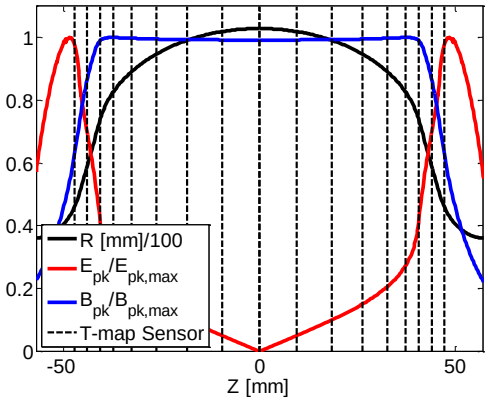

Figure 3.10: Distribution of the 17 T-map sensors on each board compared with the ERL cavity shape and its surface fields. The TESLA shape is similar. Image from [Pos15b].

minimal coverage near the irises. Figure 3.10 shows the electric and magnetic field distributions in a Cornell ERL cavity shape along with the locations of each of the 17 resistors for a given board. The TESLA shape field distribution is similar to the ERL shape.

The T-map can also be used as a means of quench detection. When an SRF cavity quenches, the quench location becomes normal conducting. This drastic increase in temperature will be expressed on the T-map as a large drop in voltage across the resistors in the quench region. With the cavity partly normal

conducting, the stored energy is lost and the cavity will cool down and become superconducting again. This results in the voltage reading across a T-map resistor returning to its original steady state value. A schematic drawing of this effect is shown in Figure 3.11a. The width of the dip in voltage is the length of time that the given resistor is "warm." The data acquistion system is able to read approximately two boards at a time at a 750 Hz rate. Therefore by reading over many quenches, a full picture of the cavity quench can be obtained. The center of the quench should be located at the resistors that show the widest drop as in Figure 3.11a. An example of this for a cavity quenching at a single defect is shown in Figure 3.11b. The quench was centered at board 13, resistor 10, which is very close to the equator and the region of highest magnetic field for TESLA cavities.

3.4 Extraction of Material Properties

The extraction of material properties from RF measurements is an important tool for understanding cavity performance and its relation to the cavity's preparation. Here I will discuss fitting two independent sets of data, Q_0 versus temperature, and resonance frequency versus temperature to extract energy gap, critical temperature, mean free path, and residual resistance. A full description of the methods including analysis of errors on results can be found in [Val13, MPL14].

BCS theory can be used to calculate the BCS resistance or penetration depth for a given set of material parameters, frequency, and temperature. A code written by Halbritter, SRIMP, can be used to do this calculation [Hal70]. Adapted by

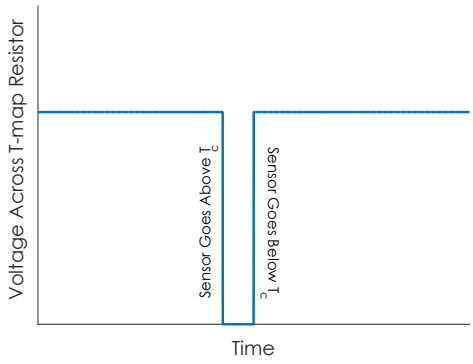

(a) A schematic of the voltage drop across a T-map resistor during a quench. When the resistor warms up above T_c, the voltage drops. As the cavity and resistor cool down after the quench, the voltage increases again. The width of the drop is the "warm duration."

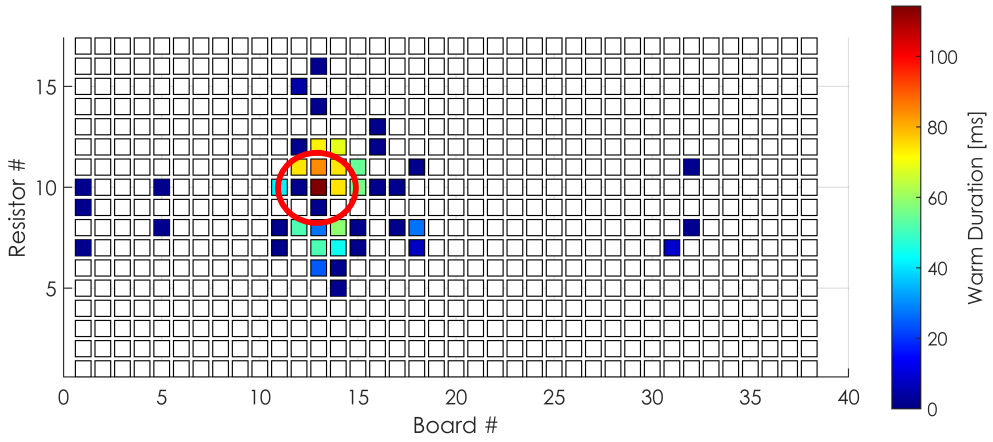

(b) An example of quench detection using the T-map. The quench location is circled in red.

Figure 3.11: Use of the T-map system for quench detection on a single-cell cavity.

Valles, SRIMP can be used to fit material parameters to surface resistance versus temperature or change in penetration depth versus temperature data [Val13]. Fitting of surface resistance versus temperature is fairly straight forward: After cooling to 4.2 K, Q_0 is measured at low fields ($E_{acc} \sim 2$ MV/m) as the temperature is lowered to the lowest reachable temperature every ~0.1 K. At Cornell this is usually 1.5 to 1.6 K. As discussed in subsection 2.3.1, Equation 2.42 can

be used to calculate R_s from Q_0. Because SRIMP calculates R_{BCS}, R_{res} needs to be subtracted from the R_s versus temperature data in order to fit. Typically, R_{res} and energy gap (normalized to $k_B T_c$ and denoted $\Delta/k_B T_c$) are fit to the R_s versus temperature data. An example of this fitting is shown in Figure 3.12a.

In the temperature range in which R_s is typically measured (1.6 to 4.2 K), R_s is sensitive to $\Delta/k_B T_c$ and R_{res} but not sensitive to T_c or mean free path (ℓ). T_c can be directly measured as the cavity is warmed up or cooled down by tracking the resonance frequency with a network analyzer. Just above T_c, the Q observed on the network analyzer will be much lower than just below T_c (the resonance curve will be much wider). In addition to R_{BCS}, SRIMP can calculate the penetration depth as discussed above. By tracking resonance frequency of the cavity, the change in resonance frequency can be converted to change in penetration depth by

$$\lambda(T) - \lambda(T_0) = \frac{1}{\beta}\left[f(T) - f(T_0)\right], \tag{3.17}$$

in which λ is the penetration depth, T is the temperature, T_0 is the starting temperature, f is the resonance frequency of the cavity, and $\beta = 12.4\,\mathrm{kHz}/\mu\mathrm{m}$ [Cio04]. In the region of 6 to 9.2 K, change in penetration depth is very sensitive to the mean free path and T_c. As T_c is measured directly, change in penetration depth is fit for mean free path while holding $\Delta/k_B T_c$ constant. An example of this fitting is shown in Figure 3.12b.

In summary, the typical process for extraction of mean free path (ℓ), T_c, energy gap ($\Delta/k_B T_c$), and residual resistance R_{res} is:

1. Measure T_c directly using a network analyzer.
2. Fit change in penetration depth versus temperature (in the range of 6-

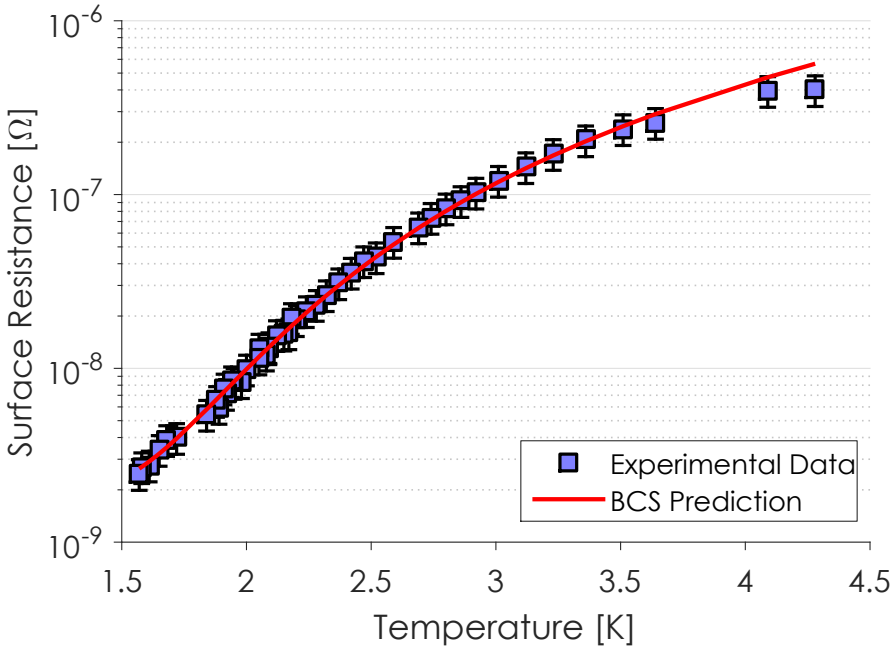

(a) Example fitting of surface resistance versus temperature in the range of 1.66 to 4.2 K.

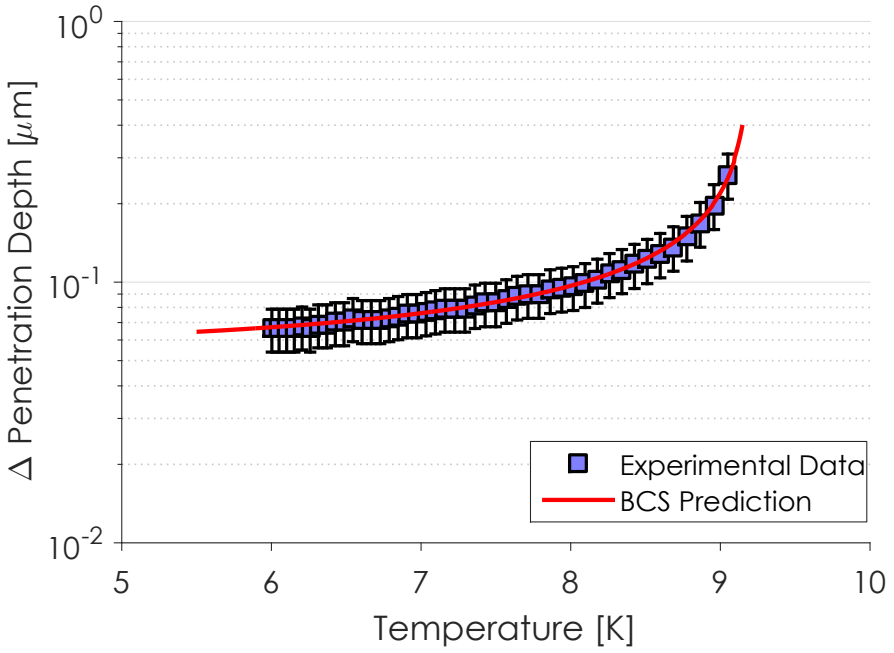

(b) Example fitting of change in penetration depth versus temperature in the range of 6 to 9.2 K.

Figure 3.12: Example fitting of cavity data with SRIMP [Hal70].

9.2 K) for ℓ holding T_c, $\Delta/k_B T_c$, and R_{res} constant.

3. Fit R_s versus temperature (in the range of 1.6-4.2 K) for $\Delta/k_B T_c$ and R_{res} holding T_c and ℓ constant.
4. Iterate this process again by using the extracted parameters from R_s vs T fitting to again fit $\Delta\lambda$ vs T and vice versa.

CHAPTER 4

INTRODUCTION TO DOPING OF NIOBIUM WITH IMPURITIES

This chapter presents an introduction to doping of niobium SRF cavities with impurities in order to improve the cavity's quality factor at usable temperatures and accelerating gradients. It begins with a discussion on the need for reaching higher Q's for future accelerators and the current state of the art prior to the work presented in this dissertation. Then the discovery of the anti-Q slope is discussed from measurements at both Thomas Jefferson National Accelerator Facility (TJNAF) in which the anti-Q slope was observed on an SRF cavity after high temperature heat treatment and Fermilab National Accelerator Laboratory (FNAL) where nitrogen-doping was first used and its effects discovered. Following this is an introduction to the dopings carried out at Cornell for this dissertation. A typical doping protocol and the doping setup is discussed and then an outline of all cavities prepared and tested is given. Finally, this chapter concludes with a brief discussion on 9-Cell work completed at Cornell.

4.1 The Need for High Q

Modern accelerators such as the Cornell Electron Storage Ring (CESR), the Large Hadron Collider (LHC), and many others operate their SRF cavities in continuous wave (CW) mode, meaning there is always electromagnetic energy stored in them. Due to the large cryogenic load that this operation produces, these machines typically run only a few cavities at low accelerating voltages. This type of operation is acceptable since the machines are typically circular, giving many passes for the particle beam to be accelerated to full energy. Other machines such as the Continuous Electron Beam Accelerator Facility (CEBAF) do

operate between these two regimes, with many cavities in CW operation. However, due to the large cryogenic cost of operating the cavities in CW, the maximum accelerating gradient in CEBAF must be limited. New machines however such as the European X-Ray Free Electron Laser (EXFEL) are constructed as a single linac, giving the beam only one pass through the cavities to reach the final energy. This requires the use of many cavities operating at high gradients. In order to offset the drastic cryogenic cost that this would require in CW operation, the cavities are typically operated in pulsed mode. This means that cavities are "turned on" just before the beam enters to provide acceleration and "turned off" just after the beam exits. Because of this pulsed operation, specifications for cavity intrinsic quality factors, Q_0, are modest and well within the currently achievable range. For example, the EXFEL has a Q_0 specification of $1{\times}10^{10}$ at 22 MV/m and 2.0 K. An example of the state-of-the-art in SRF cavity performance as of 2013 is shown in Figure 4.1. This cavity received a preparation similar to the EXFEL recipe [SIM+13] which was accepted as the standard cavity preparation technique to reach high Q. It was treated with a bulk electropolish (EP), degas at 800°C in vacuum for 3 hours, followed by a 48 hour 120°C bake. It is typical for cavities of this preparation to reach Q_0's of $2{\times}10^{10}$ at 16 MV/m and 2.0 K with quench fields above 30 MV/m. Between 5 and 25 MV/m there is typically a medium field Q slope (MFQS) in which the Q_0 decreases as the accelerating field is increased. This preparation was more than suitable for machines like the EXFEL and the International Linear Collider (ILC) (specifications for these machines are also shown in Figure 4.1).

In general, the largest cryogenic load that can be supported by a single cryoplant is 5 kW with a wall plug power consumption of 5 MW. The cryogenic

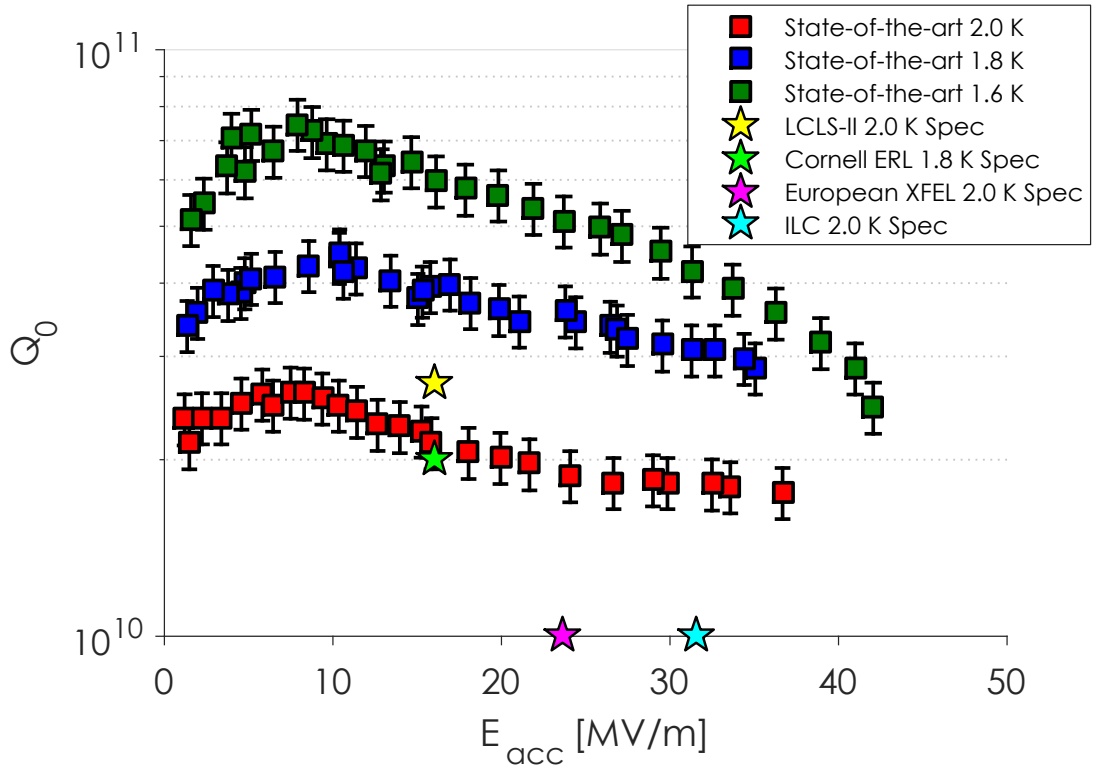

Figure 4.1: Q_0 versus E_{acc} of a 1.3 GHz single-cell cavity prepared with standard preparation techniques (800°C degas in vacuum, EP, 48 hour 120°C bake). Also shown are the machine specifications for LCLS-II, the Cornell ERL, the EXFEL, and the ILC.

power consumed by an SRF cavity linac can be calculated as

$$P_{cryo} = \frac{V_{acc} E_b}{2R/Q \times Q_0}, \tag{4.1}$$

with E_b the beam energy and V_{acc} the operating accelerating voltage of the cavities [LK06]. Figure 4.2 shows the cryogenic power as a function of accelerating voltage in the cavities for TESLA shaped 9-cell cavities and a required beam energy of 5 GeV. Cryogenic power increases linearly with the accelerating voltage. For example, the highest gradient one could operate cavities with $Q_0 = 2 \times 10^{10}$ would be ~10 MV/m. In order to operate at higher gradients, higher Q_0 must be achieved in the cavities.

New machines such as the proposed Cornell Energy Recovery Linac (ERL)

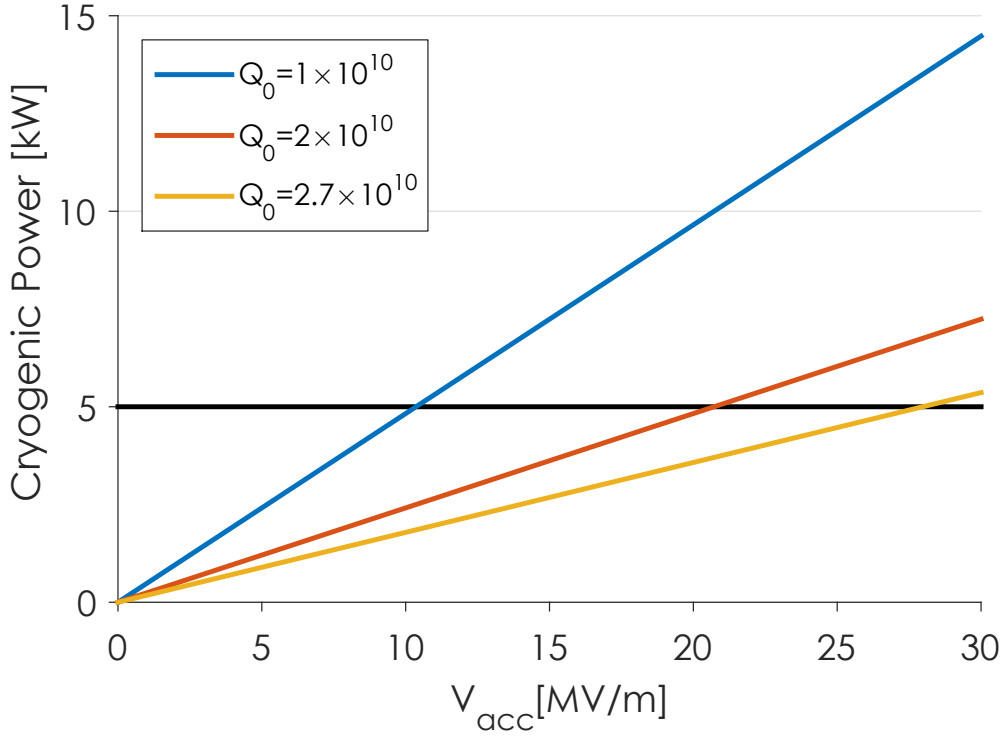

Figure 4.2: Cryogenic power versus accelerating voltage. P_{cryo} increases linearly with V_{acc}. Typically, the largest cryoplant available can support a cryogenic load of 5 kW.

and the SLAC Linac Coherent Light Source II (LCLS-II) also require operation in CW mode, but at higher gradients in order to reach the design beam energy with fewer cavities. Unlike in earlier machines such as the LHC, the use of many cavities results in the cryogenic power consumption becoming the main limiting cost factor for operation. The cryogenic load on the system is significantly higher than in previous machines and emphasizes the need for the highest possible Q_0's achievable in the cavities. For example, Figure 4.3 shows a total cost estimate (linac construction plus 10 year operation cost) as a function of the accelerating field in the cavities for LCLS-II and contains most of the linac construction costs (including cavity fabrication, RF station equipment, etc.) and the operating costs (RF power, cryogenic power). This estimate was obtained from

[Lie16]. LCLS-II specifications call for operation at 16 MV/m to reach a beam energy of 4.7 GeV. Two estimates are shown, both at 2.0 K, the first for cavities operating at 2.0×10^{10}, a reasonable Q_0 to obtain with well-established cavity preparation techniques. The jump observed in cost at ~15 MV/m is due to the requirements of a second cryo-compressor unit. This shows that in order to operate at 2.0 K and 16 MV/m more than one cryoplant would be necessary to operate the machine. However, if the cavity Q_0 could be increased to 2.7×10^{10}, this limitation is staved off until more than 20 MV/m and results in an overall lower cost. Because of this, a Q_0 specification of 2.7×10^{10} was chosen for LCLS-II. As can be seen from Figure 4.1, the standard EXFEL preparation does not produce cavities good enough to reach this very ambitious specification. Instead, a new cavity preparation technique needed to be employed.

4.2 Impurity Doping: Discovery of the Anti-Q Slope

As is evident from Figure 4.1, SRF cavities prepared with standard preparation techniques (i.e. EP+120°C bake), show a medium field Q slope between 5 and 25 MV/m. This MFQS limits the Q_0 at medium fields in which operation is crucial for new machines such as LCLS-II and the Cornell ERL. However, doping of the niobium with impurities such as nitrogen has recently been shown to eliminate this MFQS and lead to an anti-Q slope in which the Q_0 increases between 5 and 25 MV/m instead of decreases. This section will explore the work done at Jefferson Lab and Fermilab that led to the discovery of this phenomenon.

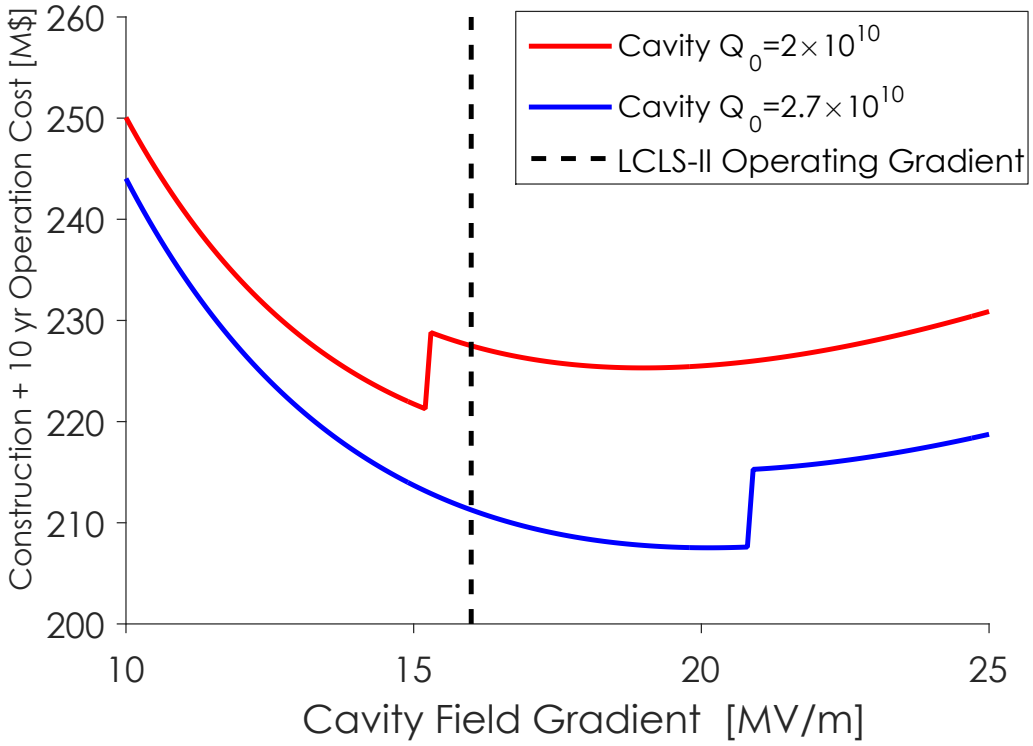

Figure 4.3: Estimate of the total cost of LCLS-II for cavities operating at Q_0's of 2.0×10^{10} and 2.7×10^{10} as a function of operating gradient. Estimate based on [Lie16].

4.2.1 Titanium-Doping at Jefferson Lab

The presence of an anti-Q slope caused by high temperature treatment was first observed at Thomas Jefferson National Accelerator Facility (TJNAF) by Dhakal et. al. [DCM+13]. A large grain 1.5 GHz single-cell cavity was first treated with a buffer chemical polish (BCP) and tested (results shown in Figure 4.4 in blue). It reached a Q_0 of ~2×10^{10} at 2.0 K. Following the baseline test, the cavity was given a heat treatment at 1400°C and re-tested (results shown in Figure 4.4 in green). It was found that an anti-Q slope appeared in which the Q_0 increased with field to a maximum of 5×10^{10} at 2.0 K and 90 mT (~20 MV/m). The temperature dependent BCS resistance was significantly reduced by ~24% and the

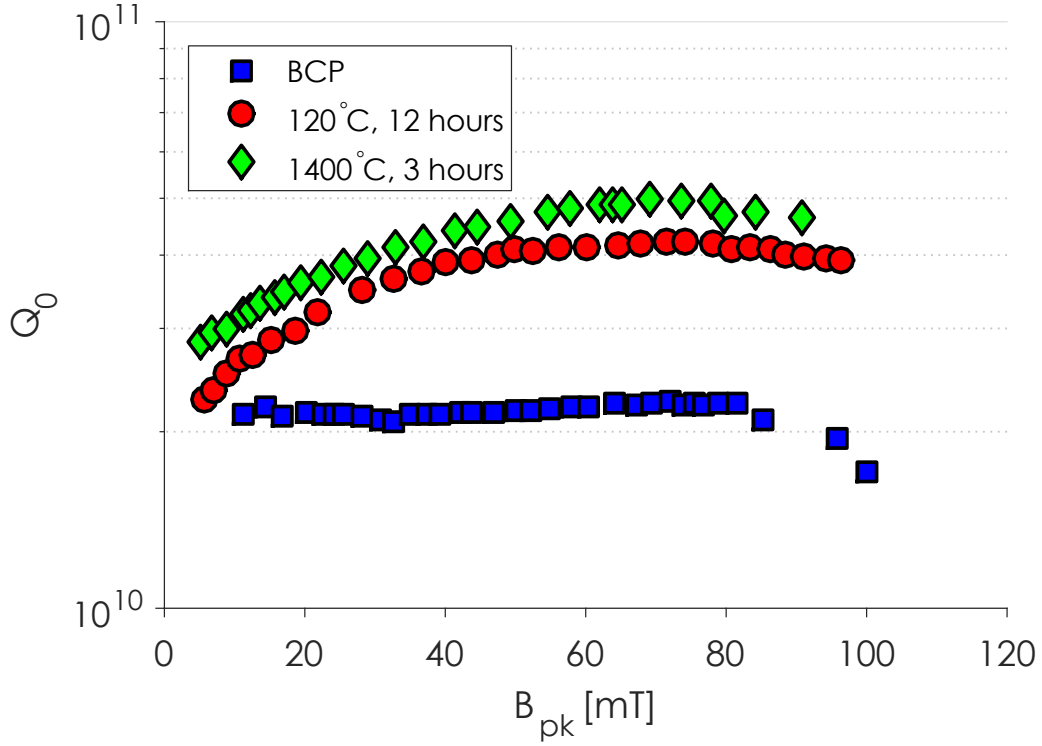

Figure 4.4: Q_0 versus B_{pk} at 2.0 K for a large grain 1.5 GHz cavity treated first with BCP, second after heat treatment at 1400°C for 3 hours, and thrid after 120°C heat treatment for 12 hours. Data courtesy of TJNAF and first published in [DCM+13].

temperature independent residual resistance was lowered to ~1 nΩ. Following the test of the cavity at 1400°C, it was given a low temperature heat treatment at 120°C for 12 hours and tested (results shown in Figure 4.4 in red). The anti-Q slope was still present however the residual resistance of the cavity increased, leading to a slightly lower Q_0 with a maximum of ~4×10^{10}.

Samples treated with the cavity at 1400°C were also analyzed to find the concentrations of carbon, nitrogen, hydrogen, and titanium in the niobium. It was found that concentrations of carbon, nitrogen, and oxygen were all increased after the heat treatment. A titanium-oxide phase also formed within the first micron of the surface. This data suggests that a doping of the niobium with

Cavity ID	Type	Treatment	Final EP [μm]	Highest Q_0 at 2 K[1]
AES016	Large-grain EP	1000°C 1 h with ~2×10^{-2} Torr N_2	**80**	$(7.4\pm1.4)\times10^{10}$, 40 mT
AES003	Fine-grain BCP	1000°C 10 min with ~2×10^{-2} Torr N_2	**10**, 60	$(4.1\pm0.6)\times10^{10}$, 50 mT
ACC005	Fine-grain EP	1000°C 1 h with ~2×10^{-2} Torr N_2	20, 40, **80**	$(4.2\pm0.13)\times10^{10}$, 70 mT
NR005	Fine-grain EP	800°C 10 min with ~2×10^{-2} Torr N_2	**5**, 15	$(5.3\pm0.85)\times10^{10}$, 70 mT

[1] Corresponding to material removal in bold and located at B_{pk} given.

Table 4.1: Summary of nitrogen-dopings carried out at FNAL presented in [GRS+13].

impurities occurred, leading to the improved performance.

4.2.2 Nitrogen-Doping at Fermilab

The use of nitrogen as a dopant in SRF cavities was first done by Grassellino et. al. at FNAL [GRS+13]. In an attempt to form niobium nitride (a superconductor with a T_c of 16 K), the FNAL team treated four single-cell 1.3 GHz cavities in a UHV furnace at high temperatures (800-1000°C) for some time (10 minutes to 1 hour) with 20 mTorr of N_2 gas. A summary of these treatments is shown in Table 4.1. This doping consisted of treating the cavities in a UHV furnace

Immediately after heat treatment in the nitrogen atmosphere, the cavities showed very poor Q_0's, on the order of ~10^7. Grassellino suggests that this poor performance is a result of lossy phases of NbN forming on the surface and thus gave each cavity an additional material removal after treatment ranging

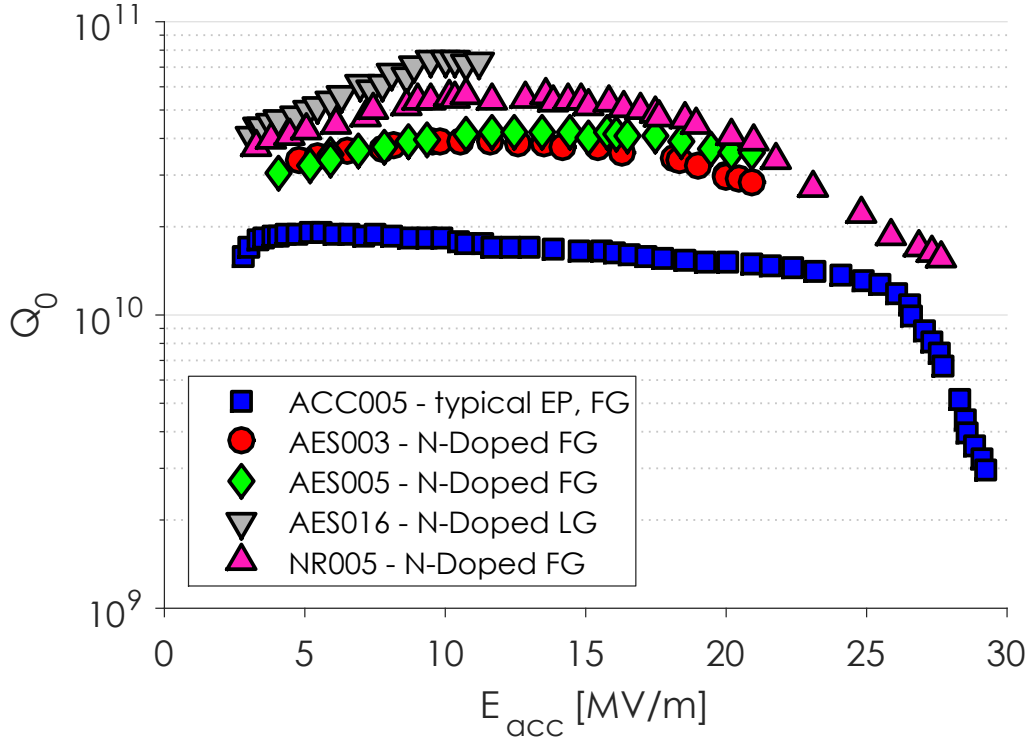

Figure 4.5: Q_0 versus E_{acc} at 2.0 K for five 1.3 GHz cavities to demonstrate the discovery of nitrogen-doping at FNAL. ACC005 represents a cavity prepared with standard preparation techniques while the other four show cavities treated with nitrogen-doping. Low field Q_0 is increased and the MFQS disappears and is replaced with an anti-Q slope. Data courtesy of FNAL and first presented in [GRS+13].

between 5 and 80 μm. After this material removal, rather than reverting back to performance expected from a standard EP surface, all four cavities showed a drastic improvement in Q_0, reaching as high as 7.4×10^{10} at 2.0 K. The highest Q_0 achieved is also given in Table 4.1. Additionally, a plot of Q_0 versus E_{acc} for these four cavities plus a standard prepared cavity is shown in Figure 4.5 in which it is clear that performance was significantly altered by the heat treatment in the nitrogen atmosphere.

This process of heat treating niobium cavities in a nitrogen-atmosphere defined a new cavity preparation technique, now known as "nitrogen-doping" in

which nitrogen diffuses into the niobium at the surface layer. Four important conclusions can be drawn from the data shown in Table 4.1 and Figure 4.5:

1. The amount of material removal to reach the best Q_0 at 2.0 K was heavily dependent on the temperature and the length of time the cavity was exposed to nitrogen in the furnace: cavities with longer doping times and higher doping temperatures required significantly more material removal to reach optimal performance compared with cavities that were doped for shorter times. This may be indicative of an "optimal" level of nitrogen-doping to maximize the benefits.
2. The low field Q_0 is significantly higher for all of the nitrogen-doped cavities than for the standard cavity at low fields.
3. The medium field Q slope is completely absent between 5 and 20 MV/m in the doped cavities and is replaced with an anti-Q slope in which the Q_0 increases as the accelerating field is increased.
4. All four nitrogen-doped cavities quenched at lower fields than the cavity with standard preparation and all but NR005 quenched at significantly lower fields (as low as 10 MV/m).

These initial discoveries of a significant improvement in Q_0 at 2.0 K due to nitrogen-doping open up the door to reaching previously inaccessibly high values of Q_0 for future machines. While nitrogen-doping was very encouraging, many technical details were not well understood and much work remained to be done before the technology could be applied to a large scale accelerator.

4.2.3 Concern About Cool Down Dynamics

While the potential for reaching previously unheard of high Q_0's by use of nitrogen-doping is very promising, a new phenomenon arose regarding how cavities are cooled below T_c before testing. Romanenko et. al. discovered that the speed of cool down of nitrogen-doped cavities significantly impacted their performance. Faster cool down (starting the cool down from a higher temperature) led to much better Q_0's than slow cool down [RGMS14a]. An example of this is shown in Figure 4.6a. The benefits of nitrogen-doping were only possible with fast cool downs. Moreover, they observed a similar effect on standard EP+120°C bake cavities, however the effect was not nearly as significant (Figure 4.6b).

The change in Q_0 observed was directly attributed to the temperature independent residual resistance component of the surface resistance. Romanenko et. al. also claims that this change is due to more efficient magnetic flux expulsion during fast cool down than in slow cool down. They explain this by a superconducting barrier that sweeps through the cavity during a fast cool down, pushing magnetic flux out of the cavity in a fast cool down. In a slow cool down, small regions of superconductivity form and encircle regions of normal conductivity, effectively trapping magnetic flux there. While the cool down rate was changed, so too were other parameters such as spatial temperature gradients which are difficult to decouple from the cool down rate. Initially it was not clear which parameters directly related to flux expulsion efficiency.

The difference in how the two cavities reacted to cool down rate is striking and may be indicative of the cavity preparation technique affecting the efficiency of flux expulsion or the total additional residual resistance from a given

amount of trapped flux. Romanenko et. al. cite that the doped cavity and EP+120°C bake cavity have very different mean free paths: ℓ~2 nm for EP+120°C baked niobium and ℓ~40 nm for nitrogen-doped niobium. This suggests that the differences in mean free paths may lead to differences in flux expulsion efficiency and/or RF losses from trapped magnetic flux. The exact dependency on mean free path was studied in depth as part of this dissertation and is presented in Chapter 6.

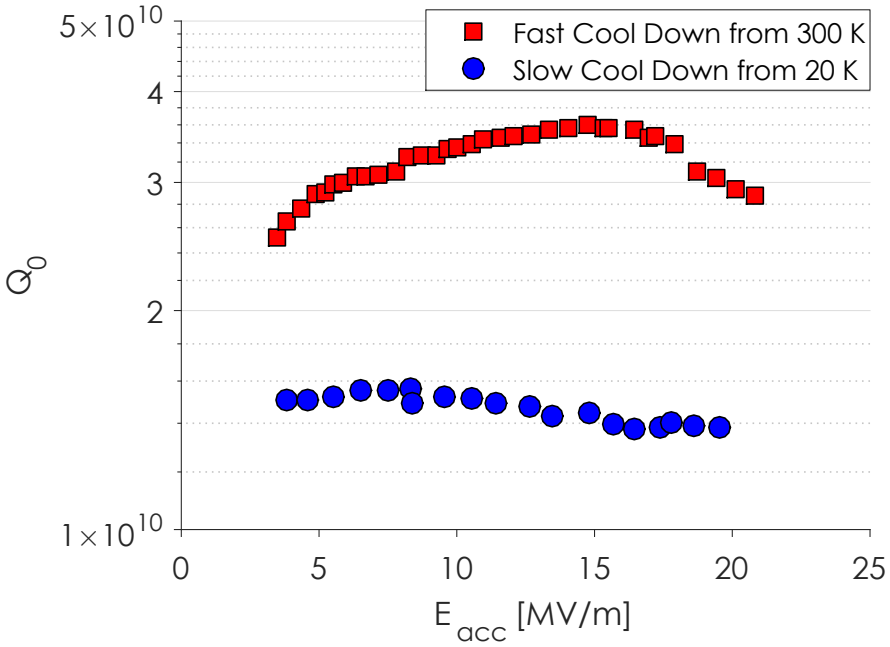

(a) For a nitrogen-doped cavity.

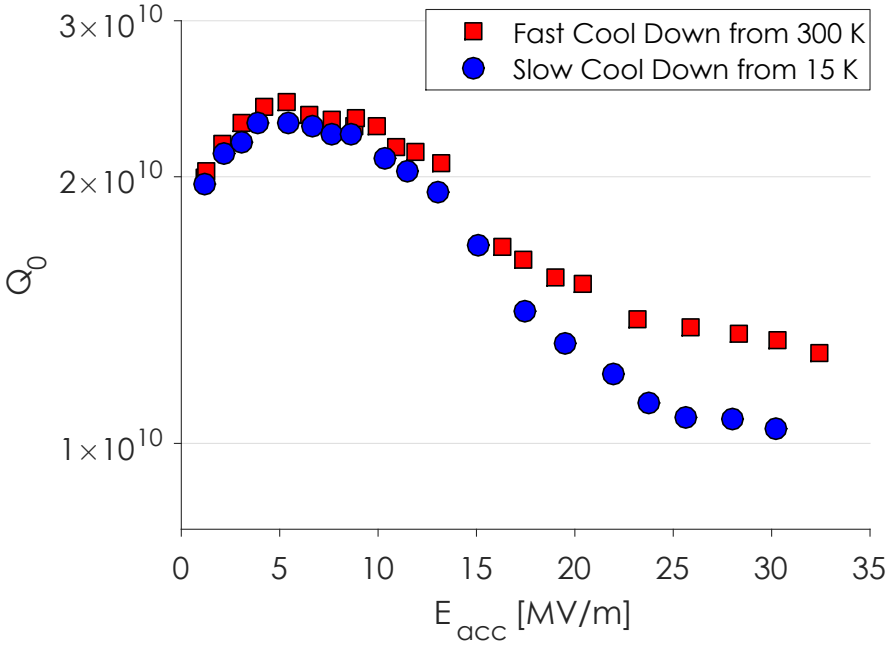

(b) For an EP+120°C bake cavity.

Figure 4.6: Effect of cool down speed on the Q_0 versus E_{acc} at 2.0 K of a nitrogen-doped 1.3 GHz cavity and an EP+120°C bake cavity. Data courtesy of FNAL and first published in [RGMS14a].

4.3 Open Questions

After the initial discovery of impurity doping of niobium SRF cavities, good cavity performance was able to be reliably achieved, but many important scientific questions remained about the mechanisms behind the improved cavity performance. This dissertation focuses on answering the following essential questions in a systematic way.

1. What causes nitrogen-doped cavities to have higher Q_0 at low fields than un-doped cavities? (See subsection 5.3.1)
2. What causes the anti-Q slope, allowing nitrogen-doped cavities to reach significantly higher Q_0 at medium fields than un-doped cavities? (see subsection 5.3.2)
3. Why are nitrogen-doped cavities more susceptible to losses from magnetic flux than un-doped cavities? (see Chapter 6)
4. Why do nitrogen-doped cavities typically quench at lower fields than un-doped cavities? (see Chapter 7)
5. Can performance of nitrogen-doped cavities be maintained in a cryomodule environment? (see Chapter 8)

4.4 Nitrogen-Doping at Cornell: An Overview

In order to further study the mechanics of doping SRF cavities with impurities such as nitrogen, a research program was developed at Cornell. This program consisted of studying:

1. Single-cell cavities for fundamental research on the mechanism behind nitrogen-doping and its effect on Q performance.
2. 9-cell cavities to test the scaling of nitrogen-doping up to cavities ready for use in an accelerator.
3. Full cryomodule tests to understand the effects of assembling nitrogen-doped cavities in a cryomodule and to study the impact of the cryomodule environment on Q_0 in order to demonstrate readiness for LCLS-II.

This dissertation focuses primarily on points 1 and 3. 9-cell cavities tested vertically will be discussed briefly in this section.

4.4.1 Typical Doping Protocol/Setup

Doping of SRF cavities is typically done in an Ultra-High Vacuum (UHV) furnace. At Cornell this is done in a T-M Vacuum Products Inc. Super Series Vacuum Furnace, model PRFM 24/60-14MCX. The furnace can comfortably hold one 9-Cell ILC shaped cavity or three single-cell cavities. It can reach a maximum temperature of 1450°C and typically reached vacuums on the order of 1×10^{-7} during cavity heat treatments at 800°C. An example of three single-cell cavities in the Cornell UHV furnace is shown in Figure 4.7. A typical doping consists of five steps:

1. Bulk material removal, typically with EP (or VEP at Cornell) of 100-200 μm.
2. Degas at 800°C in a UHV furnace in vacuum for 3 hours. (All cavities are loosely capped with niobium foil on each flange during the heat treatment)

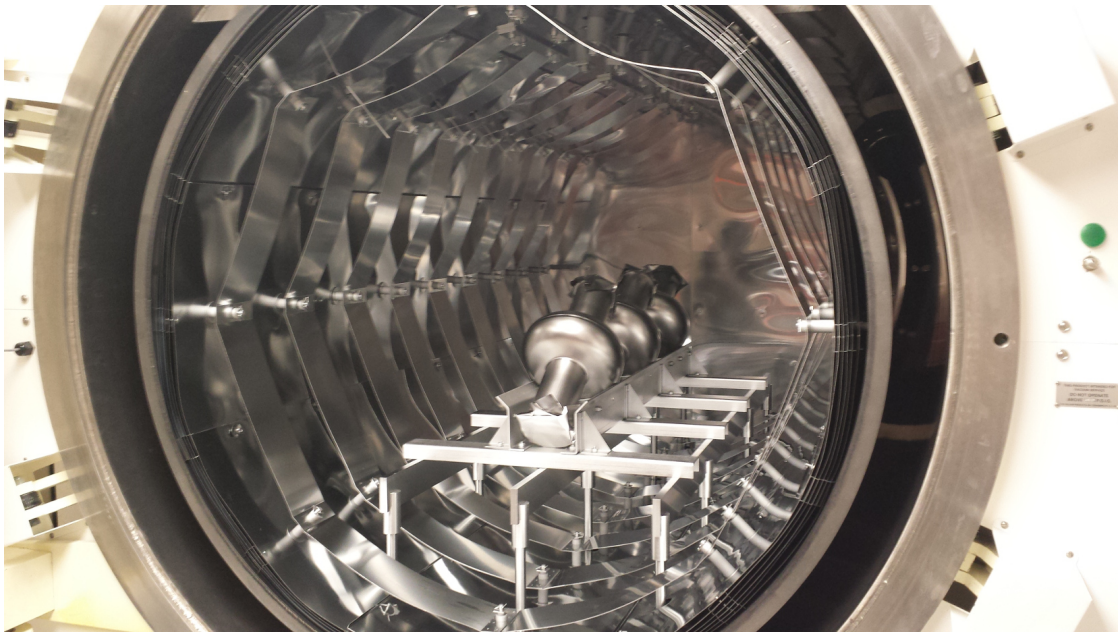

Figure 4.7: The Cornell UHV furnace with three single-cell ILC shaped cavities after a nitrogen-doping.

3. Doping at 700-1000°C in furnace in some mTorr of N_2 gas (typically 2-30 minutes).
4. Anneal at the same temperature as doping in vacuum (typically 0-30 minutes).
5. Final material removal, typically with EP of at least 5 μm.

Steps 1 and 2 are standard cavity preparation techniques to clean the cavity surface after fabrication and to remove hydrogen implanted in the material by the large amounts of chemistry. Hydrogen has been shown to significantly degrade the performance of SRF cavities [PKH98, RBCG13].

During nitrogen-doping, the pressure of the nitrogen gas in the furnace will change dramatically as nitrogen is absorbed into the niobium. The pressure quoted as the doping pressure for the remainder of this dissertation is the maximum pressure reached during the doping (usually right after gas injection).

Diffusion occurs faster as the temperature is increased [CR80], i.e. the pressure drops much faster. This behavior is well understood and is discussed in depth in the context of a nitrogen-diffusion simulation in subsection 5.2.1. An example pressure versus time plot is shown in Figure 4.8 during which time three cavities were nitrogen-doped. After the degas step, nitrogen gas was injected to ~38 mTorr and then to ~58 mTorr. The total doping time was 20 minutes. It is clear that during the doping, the nitrogen pressure drops as nitrogen is absorbed by the niobium. This corresponds to an uptake of ~47 Torr-liters of nitrogen at 800°C per cavity. The uptake of nitrogen by the furnace itself is negligible compared with the uptake by the cavities (see inset of Figure 4.8).

4.4.2 Single-Cell Cavities Prepared and Tested

This dissertation will focus on 11 single-cell cavities doped with various gases and given a variety of final material removal after doping (5 individual cavities were used and reset in between preparations with VEP). These cavities were 1.3 GHz ILC shape [ABB+00] single-cells and were fabricated at Cornell with fine grain RRR 320 material from Tokyo Denkai and are shown in Figure 4.9. Nine of the 11 preparations were doped with nitrogen, one with argon, and the last one with helium. The exact recipes for each of these dopings is summarized in Table 4.2.

Of the nitrogen-doped cavities prepared and tested, five were doped at 800°C in 60 mTorr of N_2 for 20 minutes followed by a 30 minute anneal in vacuum. Two heavy nitrogen-dopings were carried out, the first at 900°C in 60 mTorr of N_2 for 20 minutes followed by a 30 minute anneal in vacuum, and

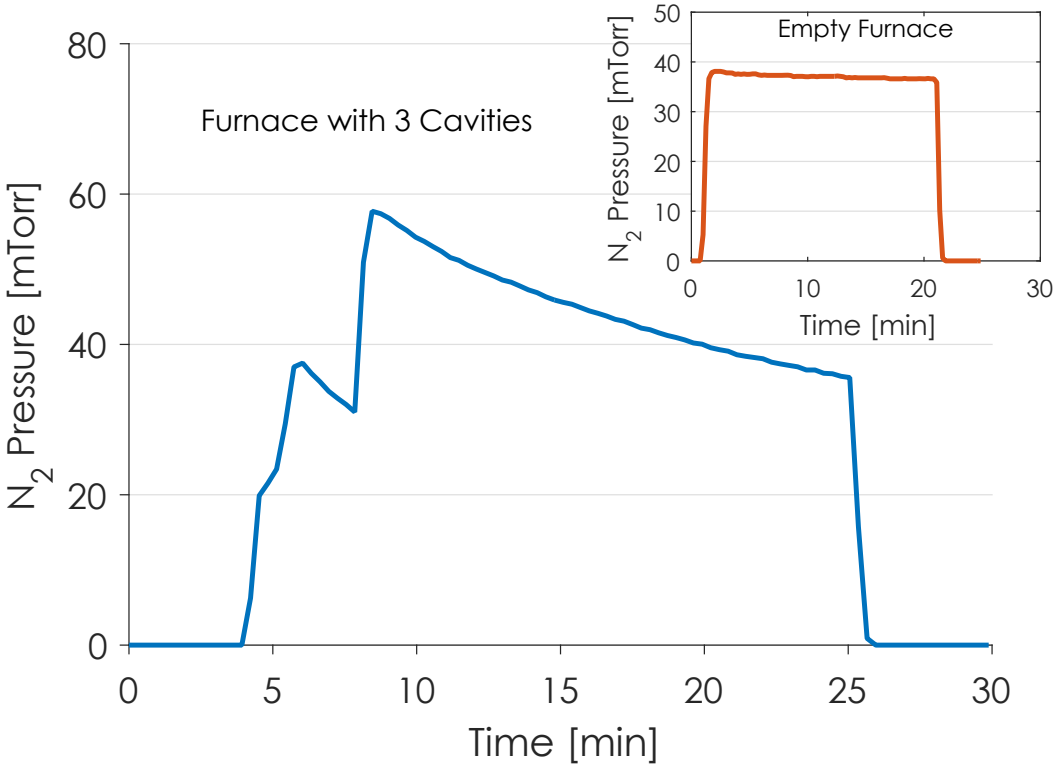

Figure 4.8: Nitrogen pressure versus time during a typical nitrogen-doping. Doping was completed at 800°C with three single-cell cavities in the furnace. Nitrogen gas is injected at the 4 minute mark to ~38 mTorr and again at 7 minutes up to ~58 mTorr. The pressure drops as nitrogen is absorbed by the cavities. At the 25 minute mark, the remaining nitrogen gas is pumped out and the furnace returns to vacuum. The inset shows a similar doping with no cavities in the furnace. Nitrogen uptake by the furnace itself is negligible.

the second at 990°C in 20 mTorr of N_2 for 5 minutes with no anneal. Finally, two light dopings were completed, one at 600°C and one at 700°C. These cavities were tested in a variety of ways to study their performance, which will be presented and analyzed in detail in the following chapters.

Cavity Name	Preparation	Doping Gas	Doping Temperature [°C]	Doping Pressure [mTorr]	Doping Time [min]	Annealing Time [min]	Final VEP (total) [μm]
LT1-1	1	N_2	800	60	20	30	18
LT1-1	2	Ar	800	60	20	30	0
LT1-1	3	He	400	20	2	0	0
LT1-2	1	N_2	800	60	20	30	6
LT1-2	2	N_2	900	60	20	30	6, 12, 18
LT1-3	1	N_2	800	60	20	30	12
LT1-3	2	N_2	990	20	5	0	5
LT1-4	1	N_2	800	60	20	30	24
LT1-4	2	N_2	600	20	40	0	0
LT1-4	3	N_2	700	20	40	0	0
LT1-5	1	N_2	800	60	20	30	30, 40

Table 4.2: Summary of Single-Cell Cavity Dopings

Figure 4.9: Single-cell cavities constructed at Cornell for doping studies

4.4.3 9-Cell Performance at Cornell

In addition to single-cell cavities, five 9-cell cavities were also prepared. These cavities were 1.3 GHz ILC shaped constructed by AES. The doping parameters for these five cavities are summarized in Table 4.3. All 9-cell cavities were doped at 800°C. The first three received a heavy doping for 20 minutes with a 30 minute anneal in 60 mTorr of N_2. The last two cavities were given a light doping for only 2 minutes in 20 mTorr of N_2 with a 6 minute anneal. As part of the LCLS-II High Q Project, after vertical testing some of these cavities went into the Cornell HTC, the Fermilab HTS, and the LCLS-II prototype cryomodules.

This dissertation will focus primarily on single-cell cavities for fundamental studies however for completeness the Q_0 vs E_{acc} performance for these five 9-cell cavities is shown in Figure 4.10. All of the 9-cell cavities met the LCLS-II 2.0 K Q_0 spec of 2.7×10^{10}. Four of the five cavities met the accelerating field specification of 16 MV/m except for AES029 which quenched at 15 MV/m. These five cavities reached an average Q_0 of 3×10^{10} and an average quench field of

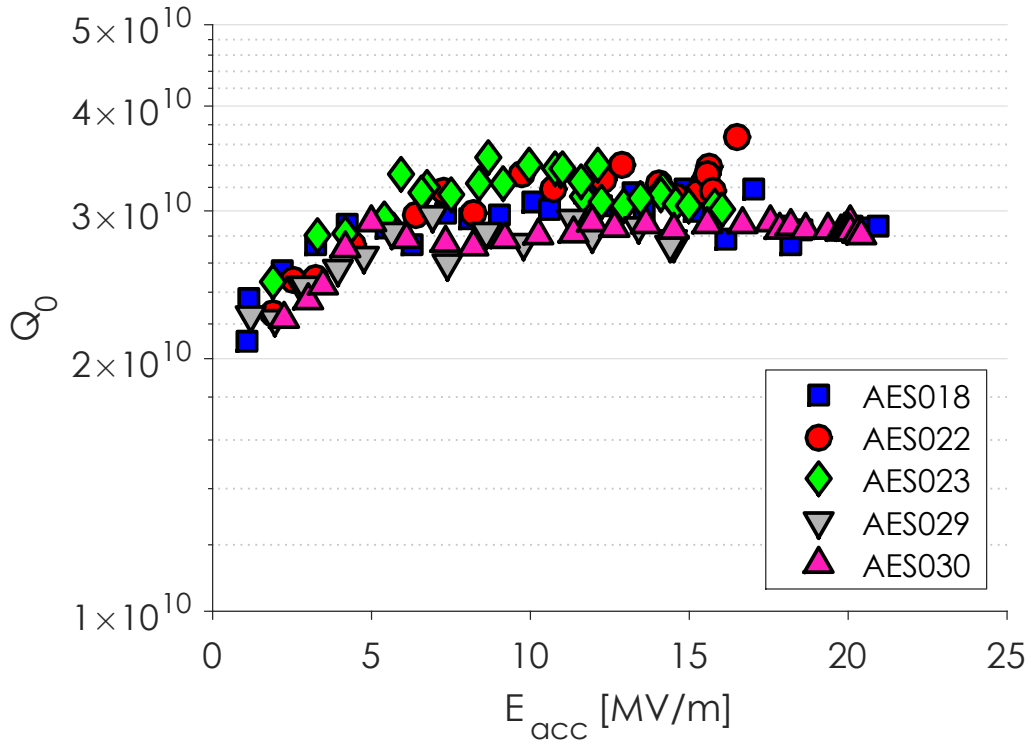

Figure 4.10: Q_0 versus E_{acc} at 2.0 K for 1.3 GHz 9-cell cavities prepared with nitrogen-doping and tested at Cornell. The cavity preparations are summarized in Table 4.3.

17 MV/m, well exceeding the LCLS-II specifications.

Cavity Name	AES018	AES022	AES023	AES029	AES030
Doping Temperature [°C]	800	800	800	800	800
Doping Pressure [mTorr]	60	60	60	20	20
Doping Time [min]	20	20	20	2	2
Annealing Time [min]	30	30	30	6	6
Final VEP [μm]	14, 24	14	17, 27	27	26
Final Q_0 (16 MV/m, 2 K)	3.2×10^{10}	3.4×10^{10}	3.0×10^{10}	2.7×10^{10}	3.0×10^{10}
Quench Field [MV/m]	21	17	16	15	17

Table 4.3: Summary of 9-Cell Cavity Dopings and Performance

CHAPTER 5

BCS RESISTANCE STUDIES

This chapter focuses on studies of the temperature dependent BCS resistance (R_{BCS}) in doped cavities. First a discussion on how doping with impurities affects material properties is presented including the extracted material properties for all the doped cavities tested for this dissertation. Next a diffusion model of nitrogen into niobium is presented and compared with sample analysis using SIMS and data from the doping runs in the ultra-high vacuum (UHV) furnace. Following this an in-depth discussion on the changes in R_{BCS} due to doping is presented. This includes a look at how mean free path is affected leading to changes in low-field R_{BCS} and a study of the field dependence of R_{BCS} in the anti-Q slope region to better understand the cause of the anti-Q slope. Five different methods of fitting R_{BCS} versus E_{acc} are presented based on BCS theory and theories presented by Xiao and Gurevich. Finally, the chapter concludes with the beginnings of a discussion on optimal doping level to minimize R_{BCS}. This will be combined with studies in the next chapter to present a full optimization of the doping parameter space.

5.1 Change in Material Properties from Doping

For the doping studies discussed in this chapter, five single-cell cavities were used, constructed by Cornell as discussed in Chapter 4. These five cavities were given a variety of dopings with nitrogen, amounting to a total of 10 different tests of varying doping level. The cavities and their preparation number (corresponding to the preparations outlined in Table 4.2) are summarized in Table 5.1.

Cavity	Preparation[1]	Final VEP [μm]	T_c [K]	Δ/k_BT_c	Mean Free Path [nm]	R_{BCS} 5 MV/m [nΩ][2]	R_{BCS} 16 MV/m [nΩ][2]	R_{res} 5 MV/m [nΩ][3]	R_{res} 16 MV/m [nΩ][3]	Quench Field [MV/m]
LT1-1	1	18	9.3 ± 0.1	1.88 ± 0.01	39 ± 12	6.4	5.5	2.4	2.4	18
LT1-2	1	6	9.3 ± 0.1	1.87 ± 0.01	19 ± 6	5.0	3.0	1.8	3.6	16
LT1-3	1	12	9.3 ± 0.1	1.91 ± 0.01	34 ± 10	6.2	4.1	1.3	1.7	33
LT1-4	1	24	9.2 ± 0.1	1.89 ± 0.01	47 ± 14	8.1	6.3	1.8	2.1	34
LT1-5	1	30	9.2 ± 0.1	1.88 ± 0.01	60 ± 18	9.2	7.9	1.3	1.3	26
LT1-5	1	40	9.2 ± 0.1	1.94 ± 0.01	214 ± 64	9.3	9.7	2.05	2.1	18
LT1-2	2	6	9.2 ± 0.1	1.94 ± 0.01	17 ± 5	5.3	4.4[4]	4.0	4.1[4]	9
LT1-2	2	12	9.2 ± 0.1	1.90 ± 0.01	13 ± 4	6.0	N/A	1.9	N/A	12
LT1-2	2	18	9.1 ± 0.1	2.01 ± 0.01	6 ± 2	6.8	N/A	2.2	N/A	15
LT1-3	2	5	9.1 ± 0.1	2.05 ± 0.01	4 ± 1	6.2	5.3[4]	4.1	3.1[4]	9

[1] Preparations defined in Table 4.2.
[2] Errors on R_{BCS} are ~ 10%.
[3] Errors on R_{res} are ~ 10%.
[4] R_{BCS} and R_{res} presented just below quench field.

Table 5.1: Summary of Nitrogen-Doped Single-Cell Cavity Material Properties

Doping with impurities can cause a change in the material properties of the niobium. These changing material properties (T_c, energy gap, and mean free path) will directly lead to a change in R_{BCS} as R_{BCS} is heavily dependent on material properties (approximated by Equation 2.26). These material properties can be extracted via fitting using BCS theory as outlined in section 3.4. These methods were used to extract T_c, energy gap (normalized to T_c and expressed as Δ/k_BT_c), and mean free path (ℓ) for all ten cavity preparations. Additionally the temperature independent residual resistance was extracted for optimal cool downs (a full discussion on R_{res} is presented in the next chapter, including a discussion on optimal cool down conditions). From the total surface resistance (R_s) at 2.0 K and R_{res}, R_{BCS} at 2.0 K was extracted. A summary of these material properties and resistances at 5 and 16 MV/m are also presented in Table 5.1. It can be seen that the material property most strongly affected by doping is the mean free path. Roughly speaking, stronger doping leads to lower mean free paths. This will be discussed further in the following sections.

5.2 Nitrogen Diffusion Model and Sample Analysis

In order to more systematically study how niobium changes after nitrogen-doping, a nitrogen-diffusion model was developed and nitrogen-doped niobium samples were analyzed using secondary ion mass spectroscopy (SIMS). These two studies allow for a theoretical prediction of nitrogen concentration in niobium to be obtained and compared with experimental results.

5.2.1 Diffusion Model

The diffusion model developed was based on the methods outline in [CR80] in which diffusion of nitrogen into niobium was calculated. There are two important regions to take into consideration: the nitride layer that forms on the surface of the niobium and the doped layer in which nitrogen is interstitial in the niobium. The model is a result of solving Fick's second law under the correct boundary conditions.

The concentration of nitrogen in the nitride, c_n, can be expressed as

$$c_n = C_n'' - (C_n'' - C_n(\infty)) \operatorname{erf}\left(x/\left(2\sqrt{D_n t}\right)\right), \tag{5.1}$$

with x the distance into the niobium. Diffusion constants and concentration constants are defined in Table 5.2. The concentration of nitrogen in the niobium, c_m, can be expressed as

$$c_m = C_m' + \left(\frac{(C_m'' - C_m')}{\operatorname{erfc}\left(\gamma_n \sqrt{D_n/D_m}\right)} \operatorname{erfc}\left(x/\left(2\sqrt{D_m t}\right)\right)\right). \tag{5.2}$$

The thickness of the the nitride layer can be expressed as

$$\xi_n = 2\gamma_n \sqrt{D_n t}, \tag{5.3}$$

or

$$\xi_n = 2\gamma_m \sqrt{D_m t}, \tag{5.4}$$

leading to the definition

$$\frac{D_n}{D_m} = \left(\frac{\gamma_m}{\gamma_n}\right)^2 = \phi. \tag{5.5}$$

Equation 5.2 leads to a direct calculation of the concentration of nitrogen in niobium at a distance x into the material for a given doping temperature T and time t. In addition to calculating the nitrogen diffusion using the Equation 5.2,

the annealing step after doping was implemented by solving the diffusion equation numerically assuming the initial concentration profile from the doping step and that the nitride layer acts as the source. Because the furnace does not cool instantly, an additional annealing will occur as the furnace is cooled. This was modeled using the numerical method described above for the anneal, taking into account the true furnace temperature and its effect on the diffusion coefficients.

There are three important conclusions to draw:

1. The concentration of nitrogen just below the NbN layer only depends on the temperature, T.
2. For a given doping temperature, depth of the nitrogen-doped layer increases as $\sqrt{t}$. This means if the doping time is doubled the depth of the doped layer will only increase by a factor of $\sqrt{2}$. The maximum concentration does not change with time, only the depth of the doping layer changes.
3. Concentration of nitrogen in niobium is completely independent of the pressure in the furnace. This is due to the process being diffusion limited rather than source limited. It is likely that at extremely low or high pressures this model may deviate from reality but in the range that nitrogen-doping typically is done for SRF cavities (10's of mTorr of N_2 gas), pressure should not play a role.

Figure 5.1 shows a nitrogen concentration profile for a standard doping at 800°C for 20 minutes with a 30 minute anneal and a heavy doping at 990°C for 5 minutes. Both dopings lead to doped layers approximately 80 μm thick, with

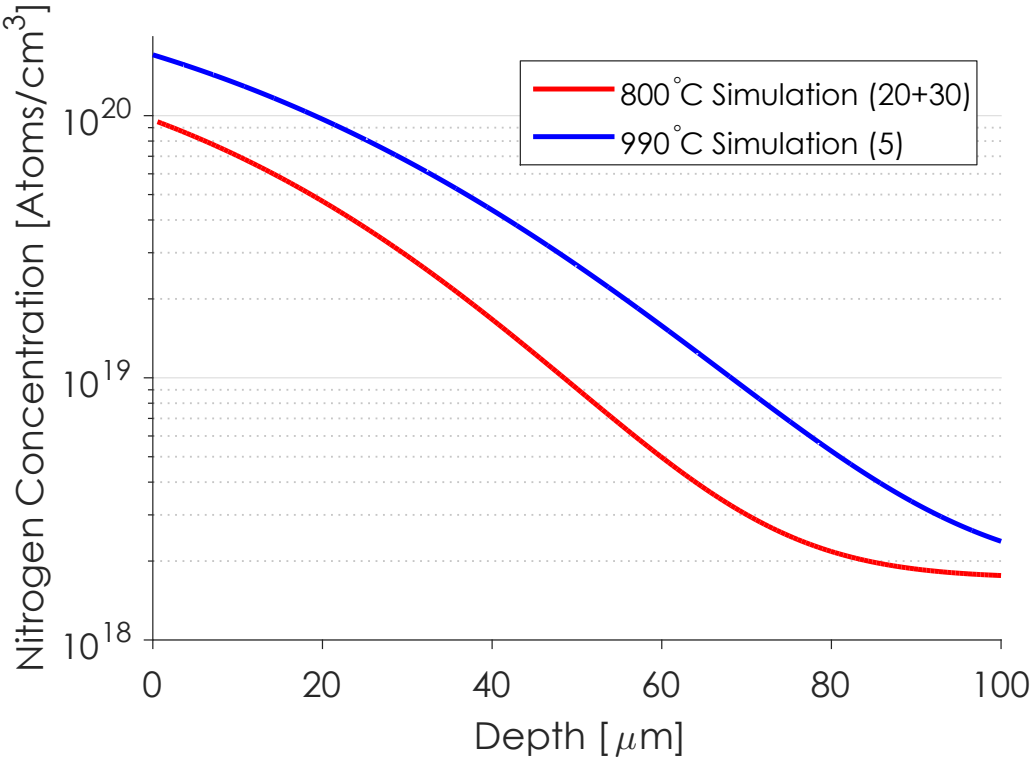

Figure 5.1: Interstitial nitrogen concentration as a function of depth into the niobium as predicted by the diffusion simulation for material doped at 800°C for 20 minutes with a 30 minute anneal and material doped at 990°C for 5 minutes. The nitride layer, which is ~1 μm thick, is not shown.

the 990°C having a higher concentration near the surface. This calculation will be compared to measured data on samples in the next section.

In addition to comparing the concentration of nitrogen predicted by the simulation with experimental results, another check on the viability of the model is if the pressure drop observed in the furnace can be calculated correctly. While absolute pressure does not affect nitrogen concentration in the niobium, the change of the pressure in the furnace can be found by calculating the amount of nitrogen uptake by a cavity. The change in nitrogen mass per unit area can be

Constant	Definition	Value at 800°C	Temperature Dependence
C'_m	Initial concentration of N in Nb	$0.04^1 \mathrm{kg/m^3}$	Temp-independent
C''_m	Saturation concentration of N in Nb	$2.2037\ \mathrm{kg/m^3}$	$\exp(-2.4828 + 0.00305028T)$
$C_n(\infty)$	Initial concentration of N in nitride	0	Temp-independent
C''_n	Saturation concentration of N in nitride	$1095.5\ \mathrm{kg/m^3}$	Temp-independent
γ_n	Proportionality constant for nitride thickness	0.0182	$0.014 + \exp(-0.0107T)$
D_n	N diffusion constant in the nitride	$7.41\times10^{-14}\ \mathrm{m^2/s}$	$2.1 \times 10^{-8} \exp\left(-1.12 \times 10^5/(8.314T)\right)$
D_m	N diffusion constant in Nb	$1.34\times10^{-13}\ \mathrm{m^2/s}$	$4.8 \times 10^{-9} \exp\left(-1.12 \times 10^4/T\right)$

[1] Value obtained from SIMS results presented later.

Table 5.2: Nitrogen diffusion constants and their temperature dependencies for use in the diffusion model. Values obtained from [CR80] unless otherwise noted. Temperature T should be in kelvin.

expressed as

$$\left(\frac{\Delta m}{A}\right)_{\text{total}} = \left[2\left(C_n' - C_m''\right)\gamma_n\sqrt{D_n} + \frac{2\sqrt{D_n}\left(C_n'' - C_n'\right)\left(1 - \exp\left(-\gamma_n^2\right)\right)}{\sqrt{\pi}\,\text{erf}\left(\gamma_n\right)} + \frac{2\sqrt{D_m}\left(C_m'' - C_m'\right)\exp\left(-\gamma_n^2\phi\right)}{\sqrt{\pi}\,\text{erfc}\left(\gamma_n\sqrt{\phi}\right)}\right]. \tag{5.6}$$

The change in pressure of a furnace with cold volume V_1 and warm volume V_2 can then be calculated if loaded with a cavity of surface area A_c using the ideal gas law,

$$\Delta P = -R \cdot \left(\frac{\Delta m}{A}\right) \cdot \frac{A_c}{28 \times 10^{-3}\ \text{mol/kg}} \cdot \left(\frac{V_1}{293\ \text{K}} + \frac{V_2}{T}\right)^{-1}, \tag{5.7}$$

where R is the universal gas constant and T the warm temperature of the furnace in kelvin. For the same doping as presented in Figure 5.1, the change in pressure was calculated and is shown in Figure 5.2. Also shown is the measured pressure drop data from a furnace run with the same doping parameters. It is clear that the prediction from the theory is very close to the measured values in the furnace.

5.2.2 SIMS Analysis

Secondary ion mass spectroscopy (SIMS) is a technique that can be used for sample analysis to measure elemental composition of a material. It is done by sputtering the surface of a metal with a focused ion beam and analyzing the ejected secondary ions. SIMS is highly sensitive to measuring concentrations of nitrogen in niobium specifically, making it a prime candidate for analyzing nitrogen-doped samples. Two preparations were analyzed using SIMS on 1 cm

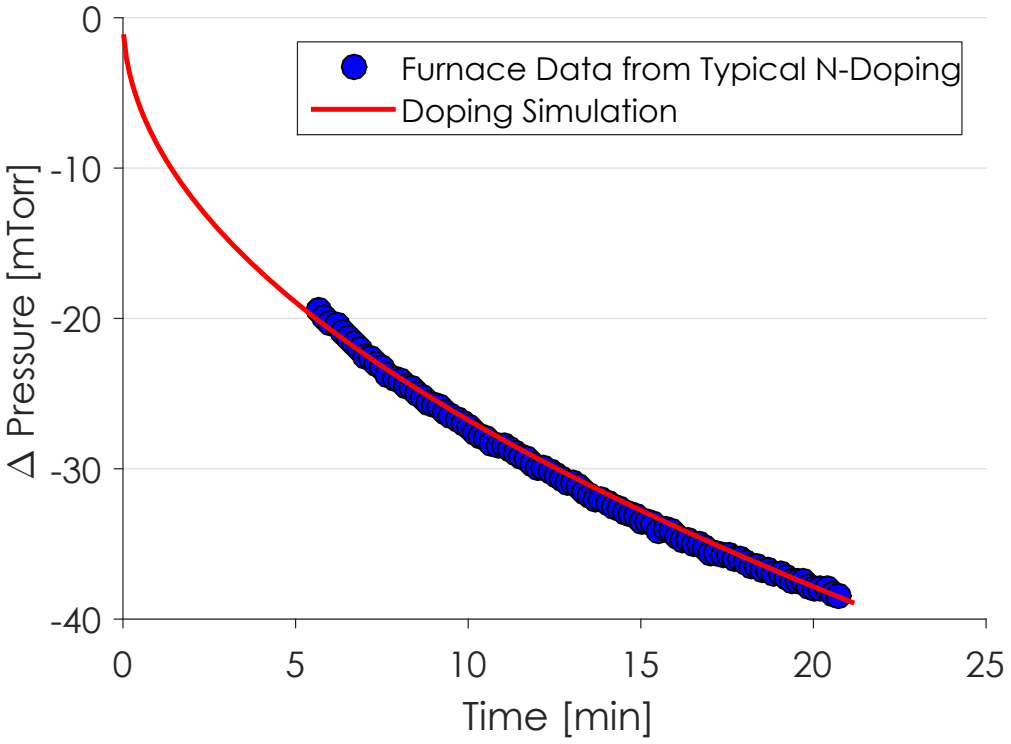

Figure 5.2: Change in pressure in the UHV furnace during a typical doping as predicted by the diffusion simulation and compared with experimental data from a doping run.

square niobium samples made from the same RRR 320 material the cavities were manufactured from. The two preparations were

1. 150 μm BCP, heat treatment at 800°C for 3 hours in vacuum, 20 minutes in 60 mTorr of N_2 at 800°C, 30 minutes in vacuum at 800°C.
2. 150 μm BCP, heat treatment at 800°C for 3 hours in vacuum, 5 minutes in 20 mTorr of N_2 at 990°C.

Note that these two preparations were identical to some of the single-cell cavities. Figure 5.3 shows the results from SIMS measurements on these two samples. For reference, typical background levels of nitrogen are ~2×10^{18} atoms/cm^3 for the SIMS technology used.

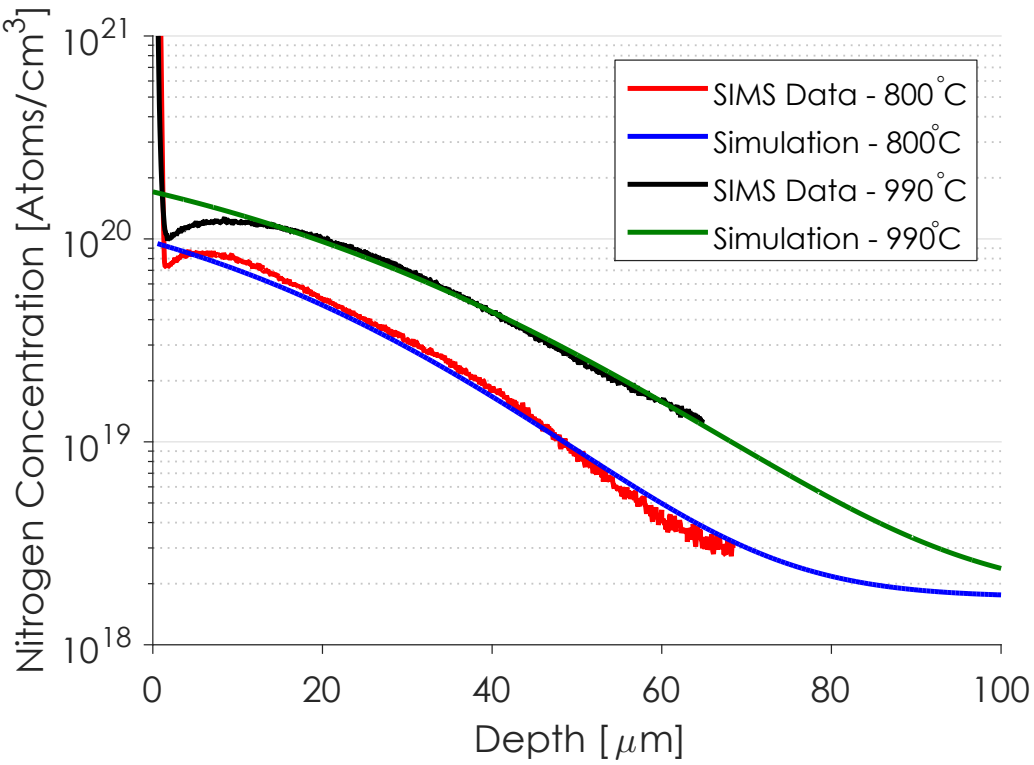

Figure 5.3: Nitrogen concentration in two nitrogen-doped samples as measured with SIMS. The red curve was from a sample doped at 800°C while the black was from as sample doped at 990°C. Also shown is the prediction from the nitrogen diffusion simulation. For the sample doped at 990°C, the diffusion constant D_m was modified from the value in Table 5.2 by fitting to the SIMS data.

It can be seen from Figure 5.3 that the nitrogen concentration of the doped samples is significantly higher than the background level, as one would intuitively expect. There are two important regions of note. Firstly, in the first couple microns, the nitrogen concentration is significantly larger than the rest of the material (more than an order of magnitude higher). This is due to a nitride layer forming on the surface of the material which is inherently lossy to RF as it is not a good phase of NbN. This is why the final step before testing for nitrogen-doped SRF cavities is a light EP, to remove this nitride layer. Secondly, there is a region between a few microns and 60-70 μm in which the concentration

of nitrogen is higher than standard "clean" niobium. This region is the doped region where nitrogen-doped cavities are typically operating. It is also important to note that the concentration of nitrogen is changing slowly with respect to the depth of the RF penetration layer (~40 nm). Additionally, as material is removed (etched) from the surface, the concentration of nitrogen generally decreases. There is an initial small increase in concentration in the first few microns below the nitride layer.

Another check on the accuracy of the nitrogen diffusion model is to compare its predictions with measurements on samples using SIMS. Also shown in Figure 5.3 are the predictions from the diffusion simulation for materials doped in the same way. It is clear that the diffusion model and the SIMS measurement are in very good agreement, lending additional credibility to the accuracy of the diffusion model for samples doped both at 800°C and 990°C.

The nitrogen concentration in niobium can be used to calculate the mean free path. Mean free path is related to the normal conducting electrical resistivity of the material via

$$\ell = \frac{\sigma}{\Delta\rho}, \tag{5.8}$$

with σ =0.37×10^{-15} Ω·m^2 [GK68]. Other values of σ have also been presented in [SES10]. $\Delta\rho$ is the increase in resistivity due to the nitrogen impurities in the niobium and can be related to the nitrogen concentration as

$$\Delta\rho = \left[5.2 \times 10^{-8}\Omega \cdot \text{ m}\right] \cdot c', \tag{5.9}$$

where c' is the atomic percentage of nitrogen in the niobium [PKH98]. Equations 5.8 and 5.9 can then be used to calculate the mean free path from the nitrogen concentration in niobium from SIMS data or from the nitrogen diffusion simulation. This was done for the SIMS analysis on the same treated at 800°C and is

shown in Figure 5.4 along with the nitrogen concentration as a function of depth into the sample. Also shown in Figure 5.4 is data from the six single-cell cavities given the same nitrogen-doping as the sample. For these points, mean free path was extracted via RF measurements as shown in Table 5.1. The overall trend closely follows the calculated mean free path from SIMS, with more removal leading to higher mean free paths however there is a consistent offset. This is most likely due to errors in the amount of removal and in the conversion factor between mean free path and $\Delta\rho$, σ, which has been shown to have different values in the literature (changes in σ by less than 20% result in very good agreement between RF extracted mean free path and SIMS results). As will be seen in the next section, the extracted mean free path values agree very closely with low field predictions from BCS theory, lending additional credibility to their values.

It is clear from the SIMS analysis and this calculation that as the nitrogen concentration is increased, mean free path of the surface layer decreases quite significantly. In regions typically used in doped cavities (5 μm on the heavily doped end), the mean free path is as low as tens of nanometers, significantly lower than that of clean niobium which has a mean free path on the order of $\sim$1 μm. This change in mean free path is consistent with the lowering shown in Table 5.1 and will strongly impact R_{BCS} as discussed in the following of this chapter.

5.3 Effect of Doping on R_{BCS}

Predictions from the nitrogen diffusion model and sample analysis using SIMS clearly point to a strongly changed mean free path as a result of nitrogen-

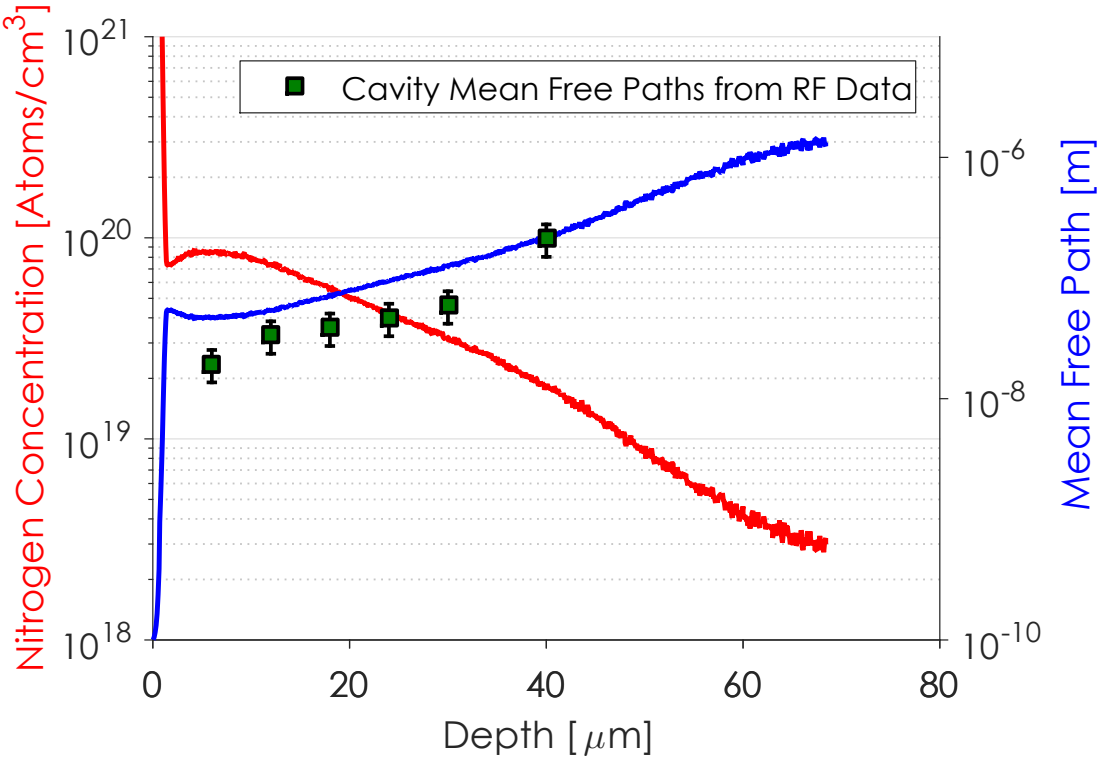

Figure 5.4: Nitrogen concentration from SIMS on the nitrogen-doped sample treated at 800°C along with the computed mean free path from nitrogen concentration and equations 5.8 and 5.9. Also shown are mean free paths for the single-cell cavities that received the same nitrogen-doping as the sample.

doping. This change in mean free path, one of the vital material properties in BCS theory, will result in a significant change in the BCS resistance. It is likely that these changing material properties lead to the two important effects observed in doped cavities: higher Q_0 at low fields and an anti-Q slope resulting in very high Q_0 in the medium field region.

5.3.1 Change in Mean Free Path from Doping

R_{BCS} has a complex dependence on mean free path as was illustrated in Figure 2.2b. R_{BCS} is minimized at mean free paths of roughly half the coherence length. Figure 5.5 shows the measured R_{BCS} at low fields and 2.0 K for each of the ten cavities versus their extracted mean free path and normalized for differences in Δ/k_BT_c via

$$R_{BCS,norm} = \frac{\exp\left(-\frac{\Delta_m}{k_BT_c}\cdot\frac{T_{c,m}}{T}\right)}{\exp\left(-\frac{\bar{\Delta}}{k_BT_c}\cdot\frac{\bar{T_c}}{T}\right)}\cdot R_{BCS}, \tag{5.10}$$

with $\frac{\Delta_m}{k_BT_c}$ the measured Δ/k_BT_c , $\frac{\bar{\Delta}}{k_BT_c}$ the average Δ/k_BT_c , $T_{c,m}$ the measured T_c, $\bar{T_c}$ the average T_c, and T the experimental temperature. Also shown is the prediction from BCS theory as calculated by SRIMP for the average material properties. It is clear that the cavities' R_{BCS} agrees very well with the R_{BCS} prediction and the minimum observed in the experimental data agrees very well with the prediction of a minimum R_{BCS} at $\ell \approx \xi_0/2 \approx 20$ nm.

This data shows concretely that nitrogen-doping directly leads to a lowering of the mean free path. This lowering of the mean free path in turn leads to a lowering of the BCS resistance at low fields. Q_0 is higher at low fields in doped cavities due to the mean free paths being closer to the optimal value of minimized R_{BCS}.

The relative anti-Q slope is also maximized at $\ell \lesssim 20$ nm. This can be seen in Figure 5.6 in which R_{BCS} (5 MV/m)/R_{BCS} (16 MV/m) versus mean free path is shown. This quantity gives a rough estimate of the strength of the anti-Q slope. For cavities that did not reach 16 MV/m due to quench, the ratio is computed at the highest obtainable field. The maximum observed at $\ell \approx 20$ nm is most likely caused by the two cavities at very small mean free paths did not reach

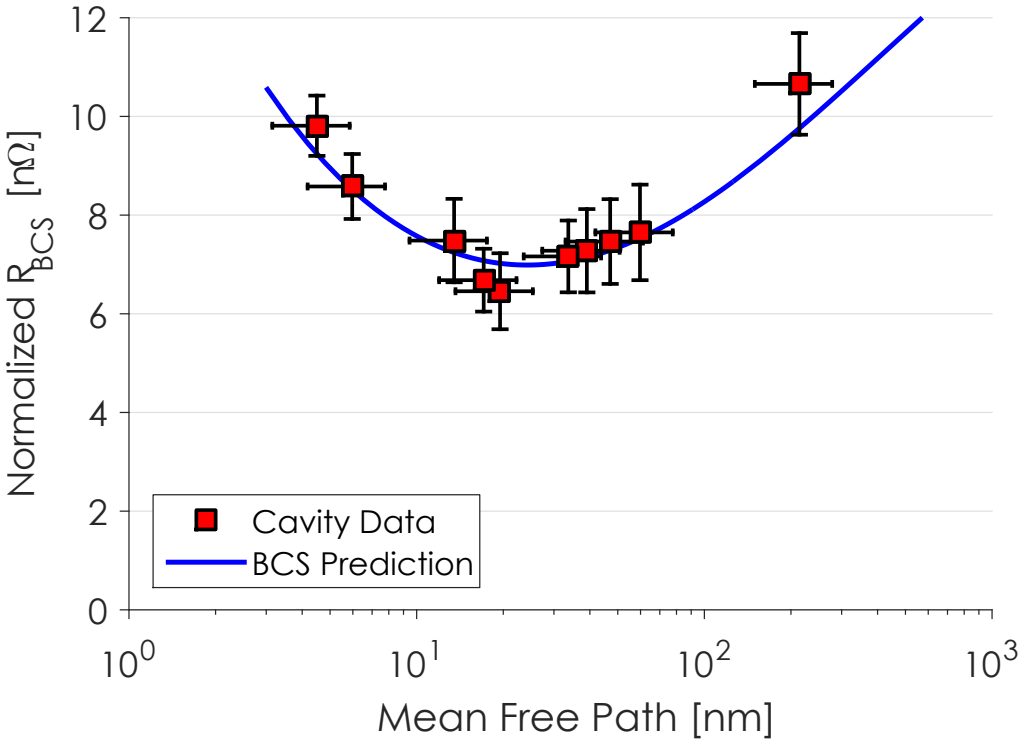

Figure 5.5: 2.0 K R_{BCS} at low fields normalized via Equation 5.10 for differences in Δ/k_BT_c versus mean free path for the ten nitrogen-doped cavities. Low field R_{BCS} experimental data agrees well with the prediction from BCS theory (λ_L = 39 nm and ξ_0 = 38 nm were used). Higher Q_0 in nitrogen-doped cavities at low fields is a result of the lowering of the mean free path pushing the material closer to the minimum.

high enough fields to see the full benefit of the anti-Q slope. There is however a general trend of lower mean free paths leading to larger anti-Q slope, an effect which will be studied in great detail in the following sections.

5.3.2 Field Dependence of R_{BCS}

In addition to the improvement in Q_0 at low fields in nitrogen-doped cavities, a field dependence is also observed in the form of an anti-Q slope in which the Q_0 of doped cavities increases as the field is increased between 5 and 20 MV/m.

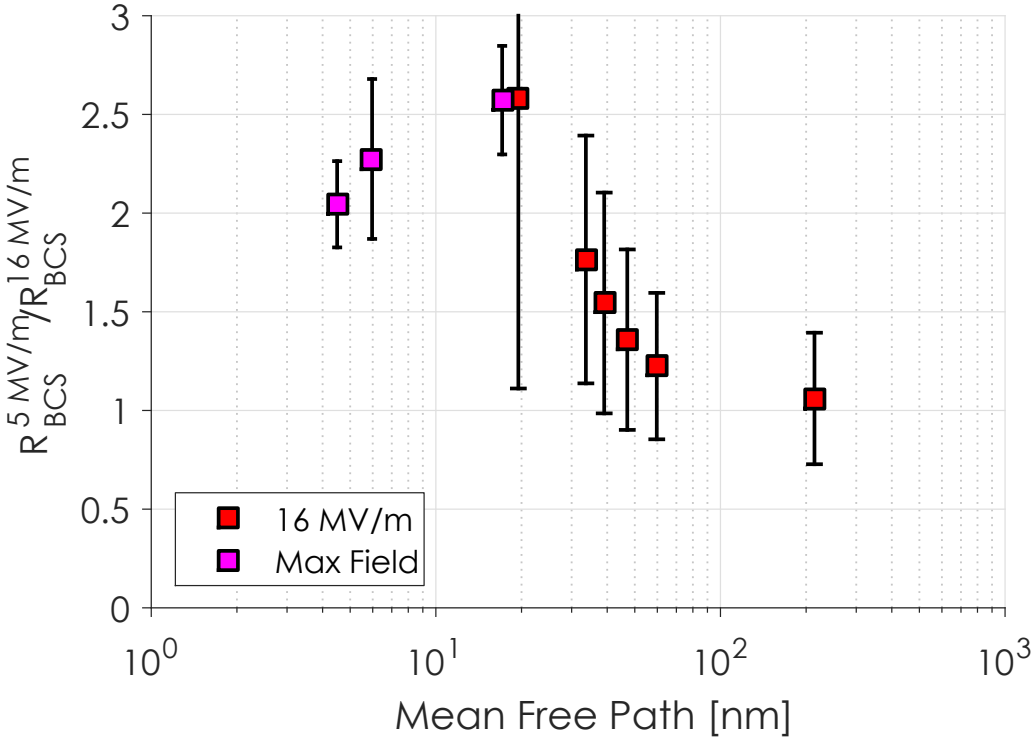

Figure 5.6: R_{BCS} (5 MV/m)/R_{BCS} (16 MV/m) at 2.0 K for the ten doped cavities representing the relative strength of the anti-Q slope. For three of the cavities that did not reach 16 MV/m, R_{BCS} at the maximum obtainable field was used. The anti-Q slope generally is stronger at lower mean free paths..

Recall from Equation 2.43 that the surface resistance can be broken into two field dependent components:

$$R_s(T, B) = R_{BCS}(T, B) + R_{res}(B). \tag{5.11}$$

An example of this deconvolution for the cavities LT1-3 (first preparation) and LT1-4 are shown in Figure 5.7 and Figure 5.8 at 2.0 K. Both cavities show a relatively unchanging R_{res} in the medium field region (5-20 MV/m) while R_{BCS} decreases in the same region. For LT1-3 this decrease is about 3 nΩ while in LT1-4 is is about 4 nΩ.

This behavior of decreasing R_{BCS} is consistent across all nitrogen-doped cav-

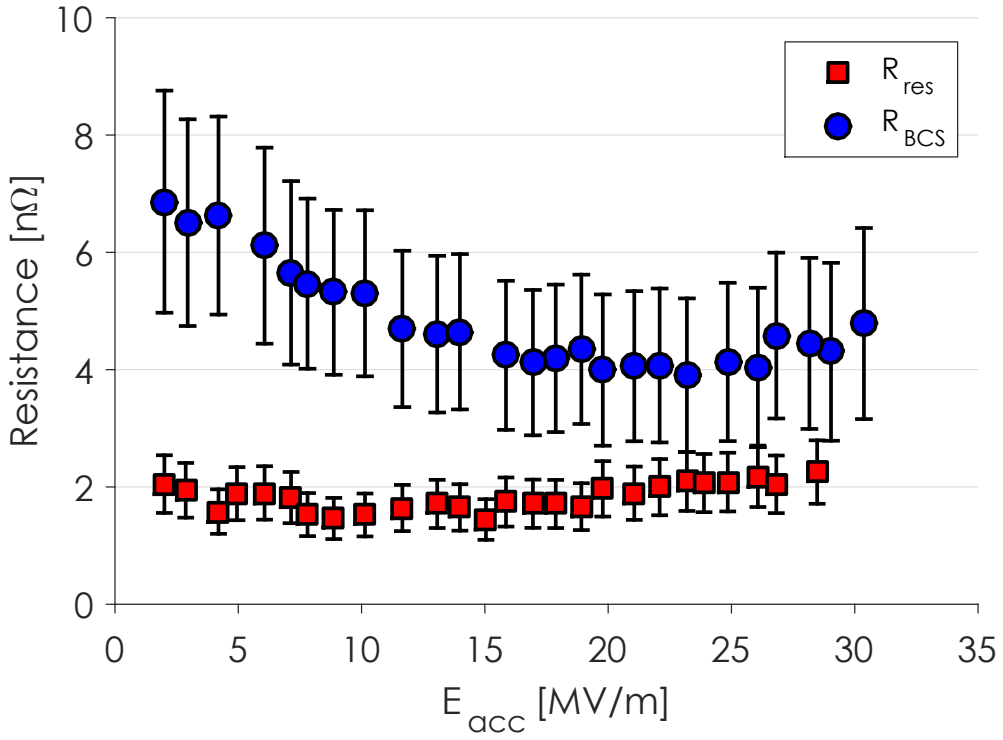

Figure 5.7: Deconvolution of 2.0 K surface resistance into R_{BCS} and R_{res} versus accelerating field for LT1-3, preparation 1. R_{res} is fairly constant with E_{acc} while R_{BCS} decreases in the medium field region.

ities tested for this dissertation. The changing R_{BCS} directly leads to the anti-Q slope: increasing Q_0 between 5 and 20 MV/m is a result of a decreasing BCS resistance in this region. Because R_{BCS} (described by BCS theory) depends on material properties, it is likely that this change is due to a change of one or multiple material properties of the niobium during nitrogen-doping. The next few sections will quantify this changing R_{BCS} with field and compare the observed field dependence with theoretical predictions. For the following analysis, the two cavities shown here (LT1-3 and LT1-4) will be analyzed.

In order to quantify the goodness of fitting, a normalized χ^2 will be discussed; smaller χ^2 meaning better fits (normalized to the number of points). For

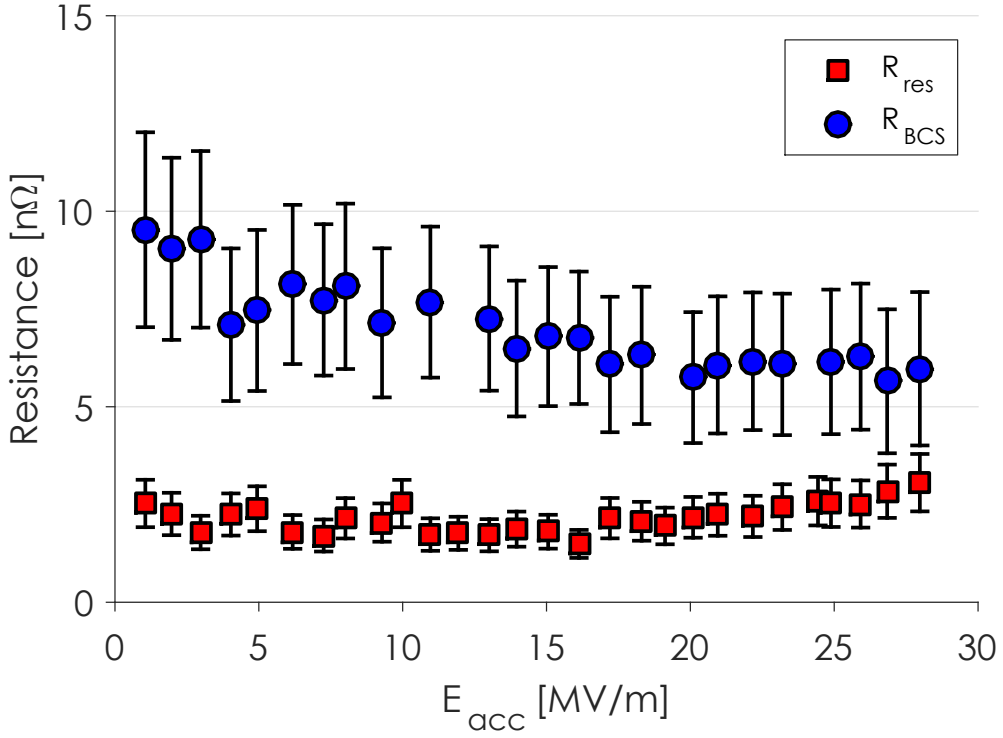

Figure 5.8: Deconvolution of 2.0 K surface resistance into R_{BCS} and R_{res} versus accelerating field for LT1-4. R_{res} is fairly constant with E_{acc} while R_{BCS} decreases in the medium field region.

reference, χ^2 is defined as

$$\chi^2(\theta) \equiv \frac{1}{N}\sum_{i=1}^{N}\frac{(y_i - f(x_i,\theta))}{\sigma_i^2}, \tag{5.12}$$

where (x_i, y_i) is a measured data point, N is the number of points, σ_i is the error for point i, f is the fitting function, and θ is a set of fitting parameters.

Logarithmic Anti-Q Slope Fitting

Previous work at Cornell and TJNAF have shown that the anti-Q slope has an approximate logarithmic dependence on the peak magnetic field (in the medium field region: ~5 – 20 MV/m) in nitrogen-doped and titanium-doped cavities [CDG14, GL14b]. This method provides a "quick and dirty" way of

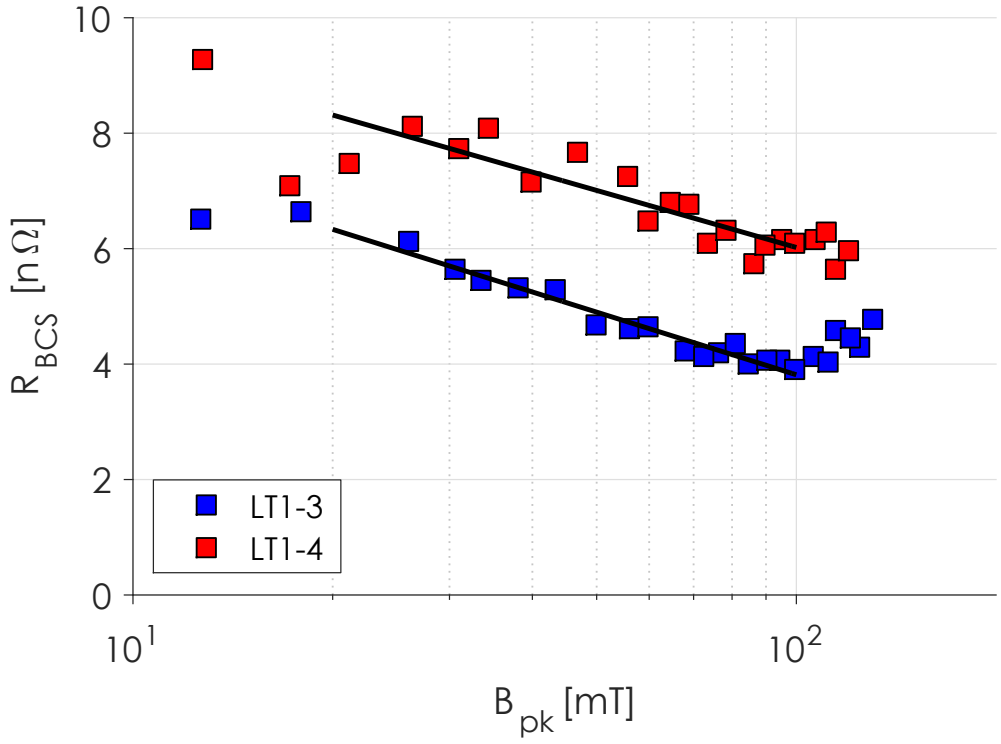

Figure 5.9: R_{BCS} versus B_{pk} for LT1-3 and LT1-4 at 2.0 K. Also shown is a logarithmic fit in the medium field region (corresponding to 5 to 20 MV/m).

quantifying the anti-Q slope in the large number of doped cavities tested for this dissertation. The function being fit (only valid in the anti-Q slope region) is

$$R_{BCS} = A \log B_{pk} + C. \tag{5.13}$$

An example of this fitting for LT1-3 and LT1-4 at 2.0 K is shown in Figure 5.9. It is clear that for these two cavities, a logarithmic fit provides a good estimate of the field dependence of R_{BCS} in the anti-Q slope region.

The normalized anti-Q slope is not dependent on temperature. Figure 5.10 shows the slope of logarithmic fitting normalized to R_{BCS} at low fields versus temperature for the six cavities given the 800°C 20+30 recipe. There are a few important conclusions to draw from this data. Firstly, the normalized anti-Q slope is mostly temperature independent for all of the cavities tested. Secondly,

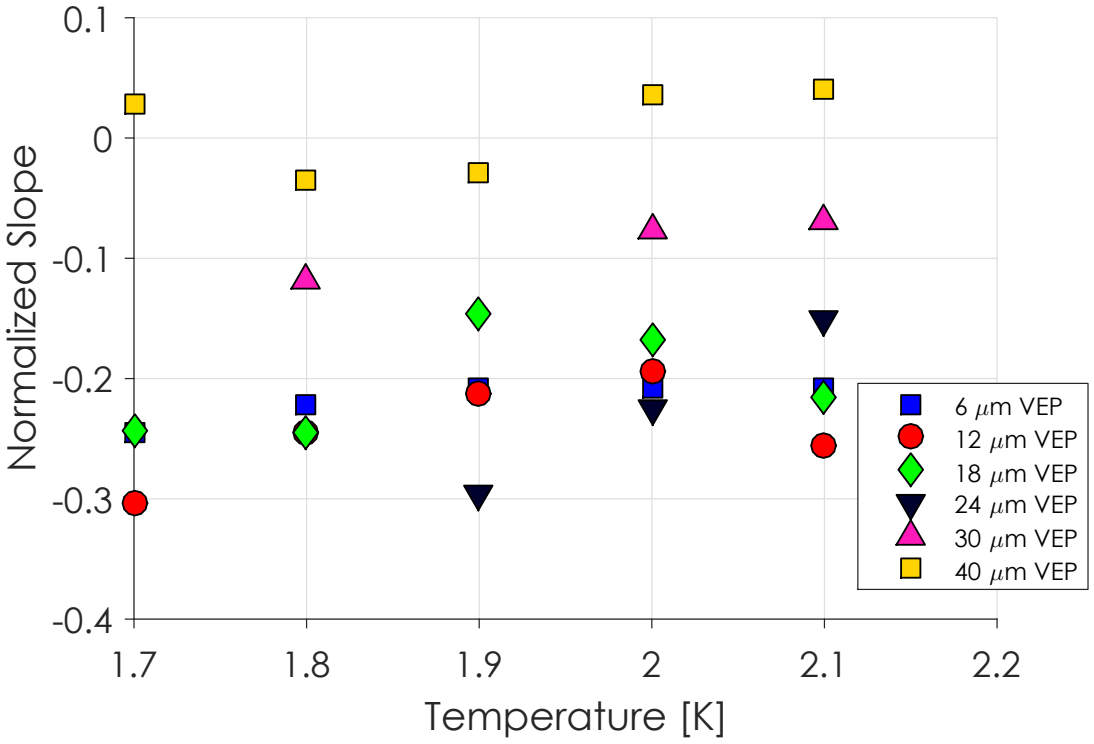

Figure 5.10: Slope of logarithmic fitting to the anti-Q slope normalized to the low field R_{BCS} versus temperature for the six cavities doped at 800°C. The relative anti-Q slope is mostly temperature independent.

there is a strong dependence of the slope on the doping level. Lastly, as more material is removed, the slope at a given temperature decreases. This confirms that as the nitrogen-doped layer is removed, the benefits of the anti-Q slope begin to disappear.

This last point can be more concretely seen in Figure 5.11 which shows the slope of the logarithmic fit at 2.0 K for all nitrogen-doped cavities tested versus their extracted mean free path. This shows a clear trend in which stronger doping (lower mean free path) leads to a stronger anti-Q slope. The dependence on mean free path is roughly logarithmic in the mean free path range studied here. As the doping level decreases, the anti-Q slope becomes less prevalent, eventu-

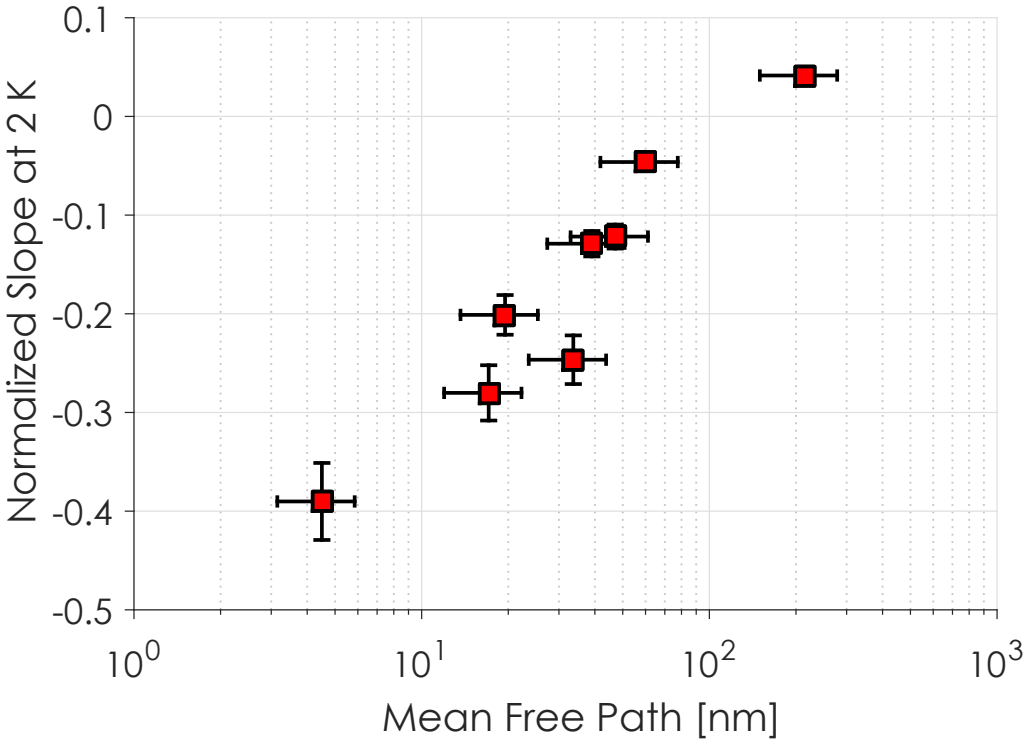

Figure 5.11: Slope of logarithmic fitting to the anti-Q slope (at 2.0 K) normalized to R_{BCS} at low fields versus mean free path for the nitrogen-doped cavities. Larger mean free path leads to a weakening of the anti-Q slope, eventually disappearing as the medium field Q slope (positive slope) returns.

ally completely disappearing as the medium field Q slope (MFQS) returns.

In addition to being a quick and dirty method for quantifying the anti-Q slope, logarithmic fitting can provide an estimate on how R_{BCS} will continue decreasing beyond a low field quench such as those seen in strongly doped cavities. Since it is difficult to compare the highest Q_0's obtained in cavities that quench at significantly different fields, the logarithmic fitting provides a method for estimating how high Q_0 would reach if a low field quench didn't occur. This method will be used in a later section during a discussion on the optimal doping level.

Fitting with Field Dependent Parameters

A good place to start for understanding the underlying physics in the field dependence of R_{BCS} is fitting R_{BCS} versus E_{acc} data to the generic form of a thermally activated resistance (for $T < T_c$), also assuming a field dependence:

$$R_{BCS}(E,T) = \frac{A(E)}{T} e^{-\Delta(E)/k_B T}, \tag{5.14}$$

with A and Δ the fit parameters which can depend on E_{acc}, T the temperature, and k_B the Boltzmann constant. Δ is the quasi-particle activation energy, typically normalized to $k_B T_c$ and expressed as $\Delta/k_B T_c$. A is the pre-exponential factor which represents a conglomeration of other material parameters such as mean free path and has units of $\Omega \cdot$ K.

Fitting to R_{BCS} versus E_{acc} data is done at constant E_{acc} and fitting to Equation 5.14 using least squares fitting. Unfortunately, allowing Δ and A to vary together leads to sloppy fitting [KGLM15]. Therefore fitting was done independently with two different models:

$$R_{BCS}(E,T) = \frac{A(E)}{T} e^{-\Delta/k_B T}, \tag{5.15}$$

holding Δ constant and varying A and

$$R_{BCS}(E,T) = \frac{A}{T} e^{-\Delta(E)/k_B T}, \tag{5.16}$$

holding A constant and varying Δ.

Figure 5.12 shows R_{BCS} versus E_{acc} for LT1-3 along with fits to Equation 5.15 and Equation 5.16 at temperatures between 1.6 and 2.1 K. There are two main conclusions to draw from these fits: first, both models fit the data fairly well, and second, the quality of the fits are virtually identical. Unfortunately, it is not

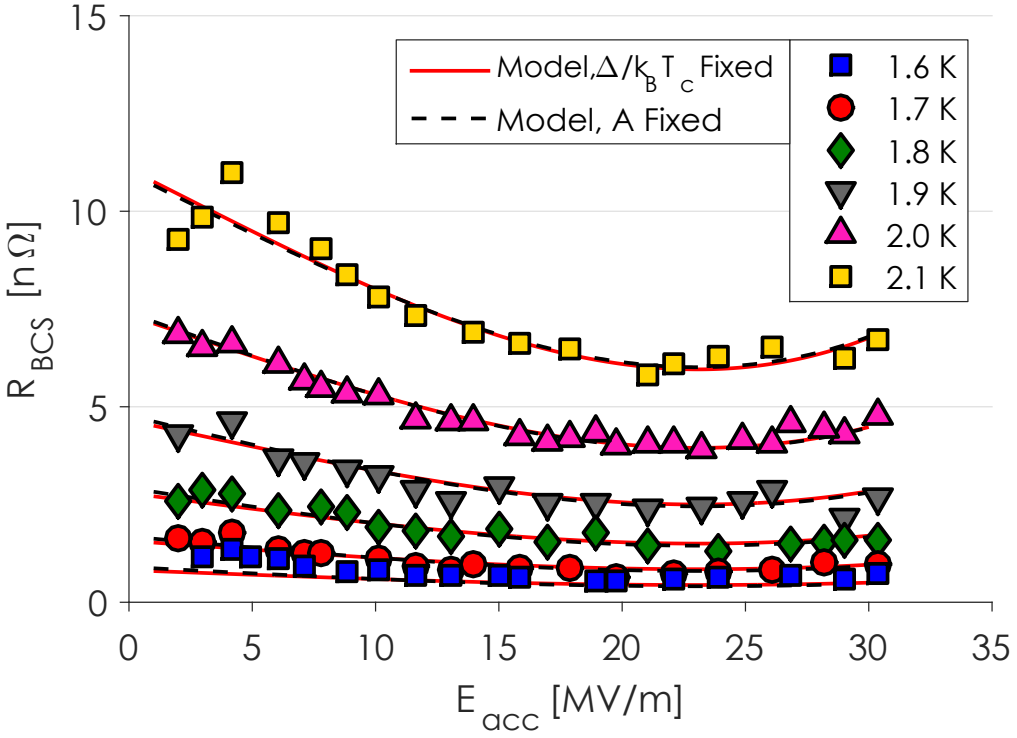

Figure 5.12: Exponential fitting to R_{BCS} versus E_{acc} data for cavity LT1-3. Both models fit the data similarly.

easy to differentiate between the goodness of fits between the two models. The normalized χ^2 for the two models at each temperature is shown in Table 5.3. The average normalized χ^2 for the temperatures measured is 0.0435 for the model with A varying and 0.0398 for the model with Δ/k_BT_c varying with field. This suggests that varying Δ/k_BT_c with E_{acc} fits the data a bit better than the model with A varying, however the two are very close.

Figure 5.13 shows R_{BCS} versus E_{acc} for LT1-4 along with fits to Equation 5.15 and Equation 5.16 at temperatures between 1.6 and 2.1 K. Again the same conclusions can be drawn, both models fit the data fairly well and they are difficult to tell apart. Specifically, the normalized χ^2 values for each temperature are given in Table 5.4. The average χ^2 for the model with A varying is 0.1900 and

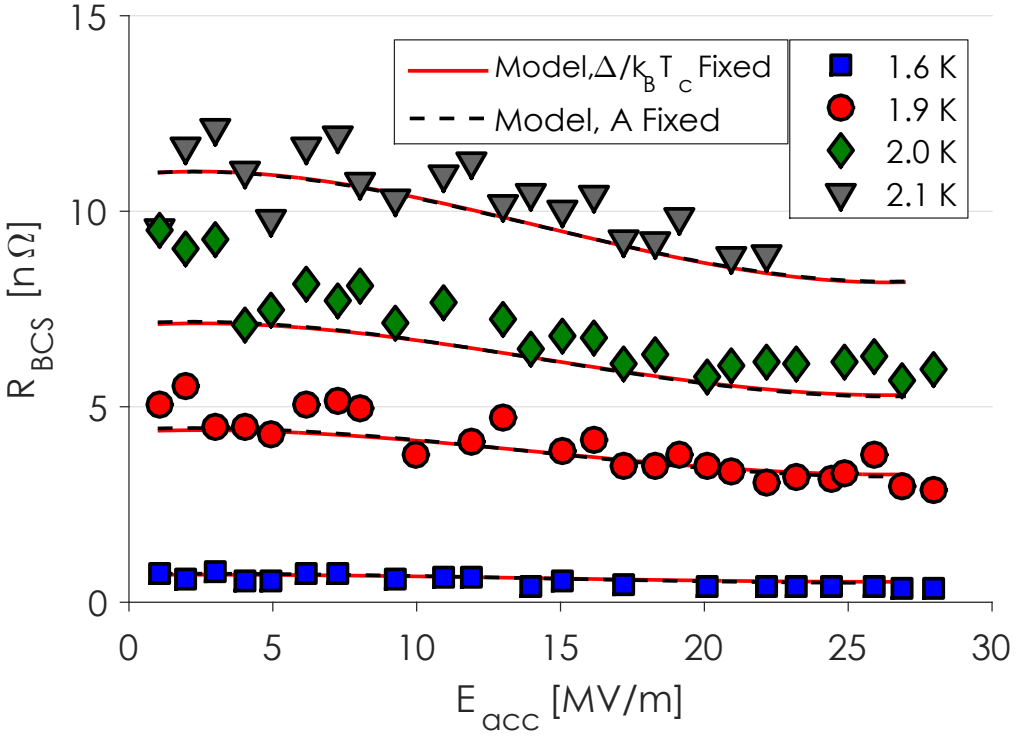

Figure 5.13: Exponential fitting to R_{BCS} versus E_{acc} data for cavity LT1-4. Both models fit the data similarly.

0.2184 for the model with Δ/k_BT_c varying. This would suggest that the A varying model fits the data slightly better than the Δ/k_BT_c varying model.

Figure 5.14 shows the extracted A parameters versus E_{acc} for the two cavities. The anti-Q slope can be explained by a decreasing A parameter in the medium field region. Likewise, Figure 5.15 shows the extracted Δ/k_BT_c versus E_{acc} for the two cavities. In this case, the anti-Q slope can be explained by an increasing Δ/k_BT_c in the medium field region. Because of the relative similarity in fits, it is not clear which model more accurately predicts the data.

In summary, 5.14 can be used to accurately fit R_{BCS} vs E_{acc} data in the anti-Q slope region. Allowing A or Δ/k_BT_c to vary produce similar fits. This leads to the interpretation that the anti-Q slope in nitrogen-doped cavities is caused by

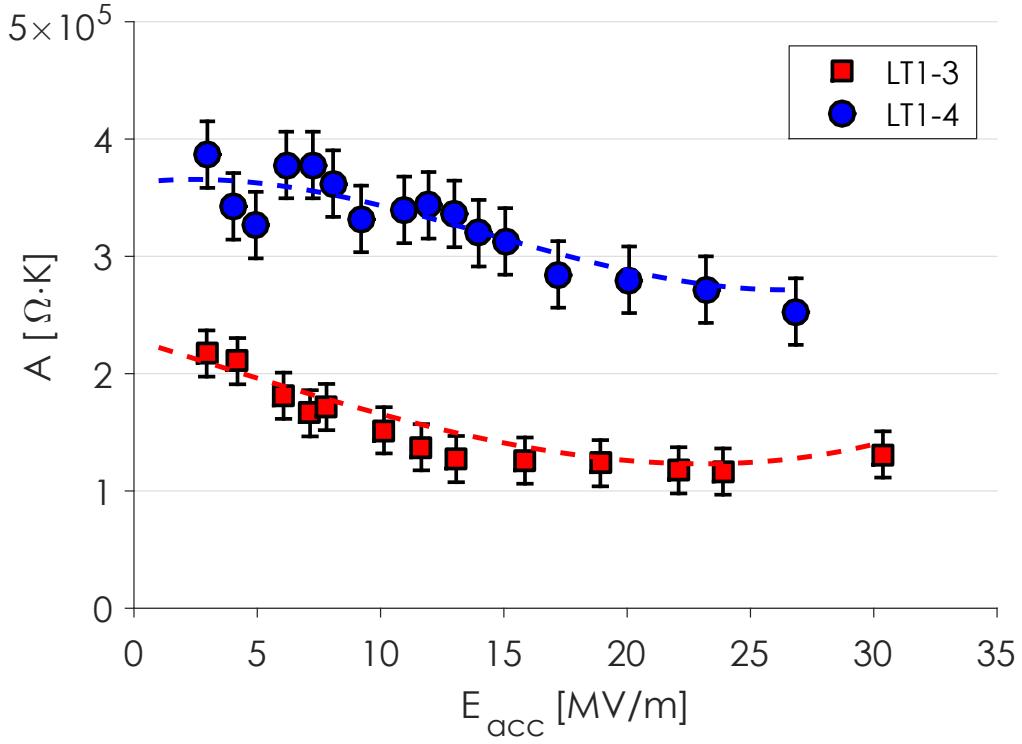

Figure 5.14: Pre-exponential factor, A, versus E_{acc} for both LT1-3 and LT1-4. Decreasing R_{BCS} can be explained by a decreasing A parameter in the medium field region.

either a decreasing A parameter or an increasing Δ/k_BT_c which makes sense intuitively since larger energy gap leads to a lower R_{BCS} in BCS theory. Exponential fitting provides an intuition for how material properties might be changing with E_{acc}. The next sections will dive into more complicated theories to more deeply study the field dependence.

BCS Fiting with SRIMP

As was discussed in Chapter 3, SRIMP, a code written by Halbritter [Hal70] can be used to calculate R_{BCS} at a given temperature from a set of material parameters. This code has been modified to allow for fitting to material parameters

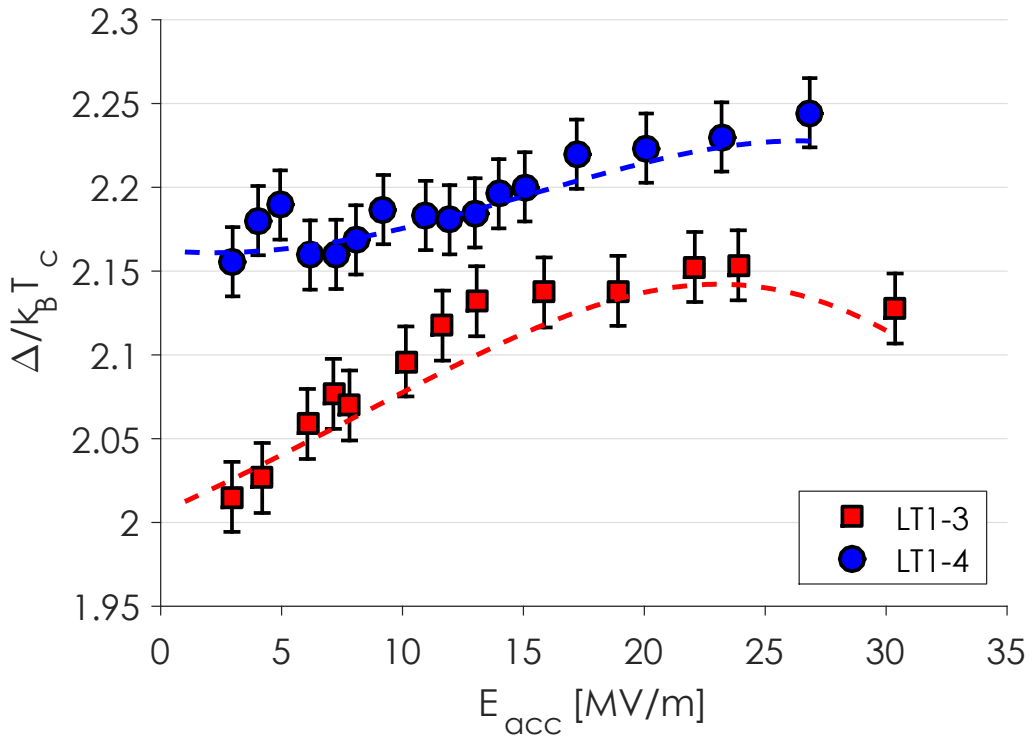

Figure 5.15: Δ/k_BT_c versus E_{acc} for both LT1-3 and LT1-4. Decreasing R_{BCS} can be explained by an increasing Δ/k_BT_c in the medium field region.

Fit	1.65 K	1.7 K	1.8 K	1.9 K	2.0 K	2.1 K
Exponential - A Varying	0.0180	0.0244	0.0317	0.0608	0.0254	0.1008
Exponential - Δ Varying	0.0124	0.0168	0.0260	0.0567	0.0264	0.1003
SRIMP	0.0588	0.0290	0.0395	0.1063	0.0557	0.1429
Xiao Theory	0.0324	N/A	0.06698	0.1055	0.2402	0.5561
Gurevich Theory	0.01892	0.0347	0.0375	0.1906	0.1729	0.3912

Table 5.3: Normalized χ^2 for R_{BCS} of LT1-3.

based on measured R_{BCS} data [Val13, MPL14]. This fitting method can be applied to field dependent cavity data as was done in the previous section to see if it can provide insight to the observed field dependence of R_{BCS}. Unfortunately a limitation of this method is that the BCS solution used inherently assumes zero field, so the exact results of fitting will be more qualitative rather than quan-

Fit	1.6 K	1.9 K	2.0 K	2.1 K
Exponential - A Varying	0.0169	0.01416	0.4768	0.2523
Exponential - Δ Varying	0.0151	0.1324	0.4725	0.2535
SRIMP	0.1689	0.2250	0.1389	0.3127
Xiao Theory	1.2795	N/A	0.7959	3.3005
Gurevich Theory	0.0190	0.2703	0.4030	1.1615

Table 5.4: Normalized χ^2 for R_{BCS} of LT1-4.

titative. Nevertheless, it provides insight to the field dependence and is more advanced than fitting with a simple exponential behavior as done in the previous section.

SRIMP takes as input the following material parameters: T_c, Δ/k_BT_c , ξ_0 (clean coherence length), λ_L (London penetration depth), and ℓ (mean free path). While T_c, Δ/k_BT_c , and ℓ can be changed for niobium based on doping with impurities, ξ_0 and λ_L are specifically the clean values of coherence length and penetration depth. Therefore they are unaffected by doping. SRIMP uses ℓ to calculate the dirty coherence length and penetration depth values. T_c was measured directly by tracking the resonance frequency of the cavities and ℓ was extracted from penetration depth fitting as discussed in Chapter 3. A changing mean free path cannot lead to the anti-Q slope, as will be discussed in detail in the coming pages. This inherently leaves Δ/k_BT_c to change with field. Recall that exponential model fitting resulted in an increasing Δ/k_BT_c in the medium field region.

Fitting with SRIMP was done for all nitrogen-doped cavities tested, however for simplicity only LT1-3 and LT1-4 will be discussed here. Figure 5.16 shows R_{BCS} versus E_{acc} for LT1-3 along with fits via SRIMP while allowing Δ/k_BT_c to

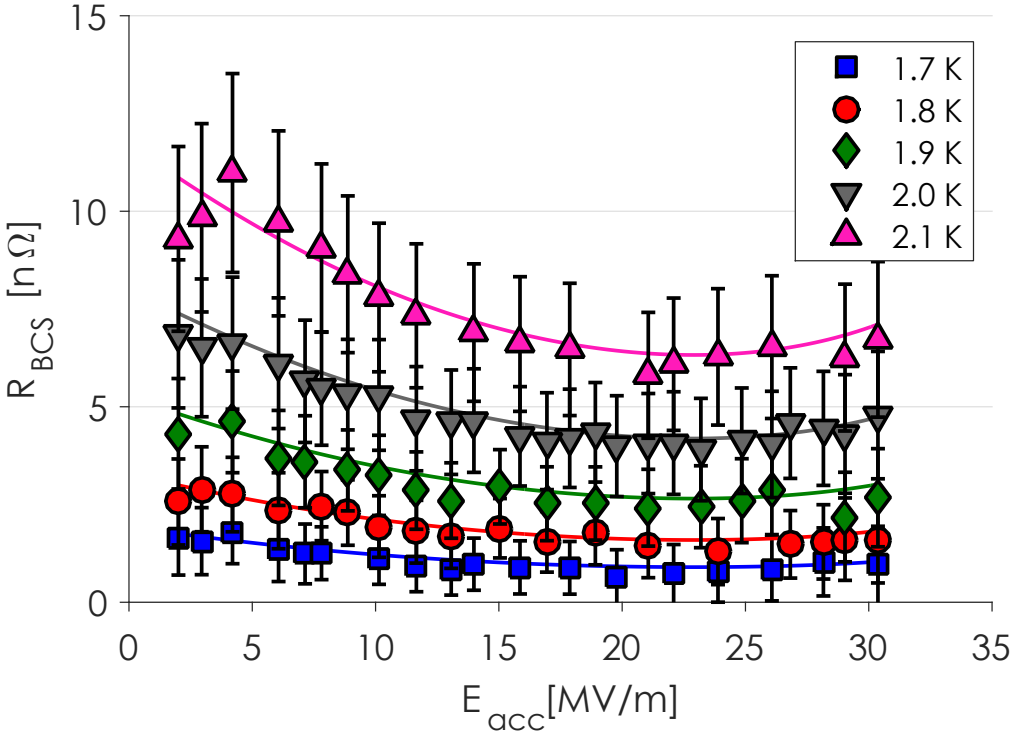

Figure 5.16: R_{BCS} versus E_{acc} for LT1-3 at temperatures below the λ point with fits to the data done via SRIMP and varying Δ/k_BT_c .

vary with field. Figure 5.17 shows the same analysis for LT1-4. Normalized χ^2 for LT1-3 is given in Table 5.3 and for LT1-4 in Table 5.4. The average χ^2 for LT1-3 under SRIMP fitting was 0.0720 and for LT1-4, 0.2114. Clearly BCS fitting was better for LT1-3 in which more data sets at different temperatures were available for fitting, leading to less sloppy fits.

Fitting with SRIMP showed a similar behavior for both cavities' Δ/k_BT_c in the medium field region. Figure 5.18 and Figure 5.19 show the Δ/k_BT_c and R_{res} versus E_{acc} for LT1-3 and LT1-4, respectively. As expected, R_{res} is relatively unchanged in the medium-field region in which the anti-Q slope is present for both cavities. Δ/k_BT_c however strongly increases in that same region, similar to what was observed in exponential fitting. This again suggests that a field

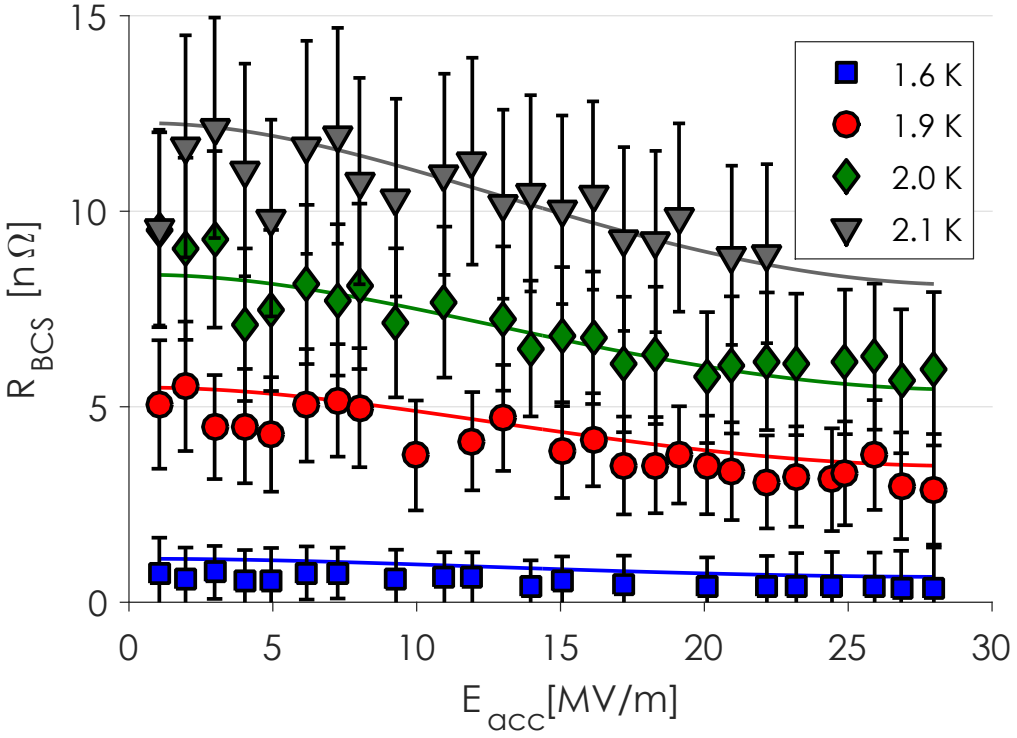

Figure 5.17: R_{BCS} versus E_{acc} for LT1-4 at temperatures below the λ point with fits to the data done via SRIMP and varying Δ/k_BT_c .

dependent energy gap could play a role in the anti-Q slope.

While varying Δ/k_BT_c with E_{acc} produces reasonable fits, it is possible that a changing mean free path could also be responsible for the anti-Q slope. If a mechanism was present to change the effective mean free path by raising the accelerating field, R_{BCS} could be "pushed" closer to the minimum in R_{BCS} versus ℓ as predicted by theory (minimum being located at $\ell \approx \xi_0/2$). Figure 5.20 shows the SRIMP prediction of R_{BCS} versus ℓ along with indicating the mean free path values of the nitrogen-doped cavities tested. It is clear that the cavities lie on either side of the R_{BCS} minimum, implying that a changing mean free path cannot solely explain the anti-Q slope. Cavities on the left side of the minimum would need an increasing mean free path to lower R_{BCS} while cavities

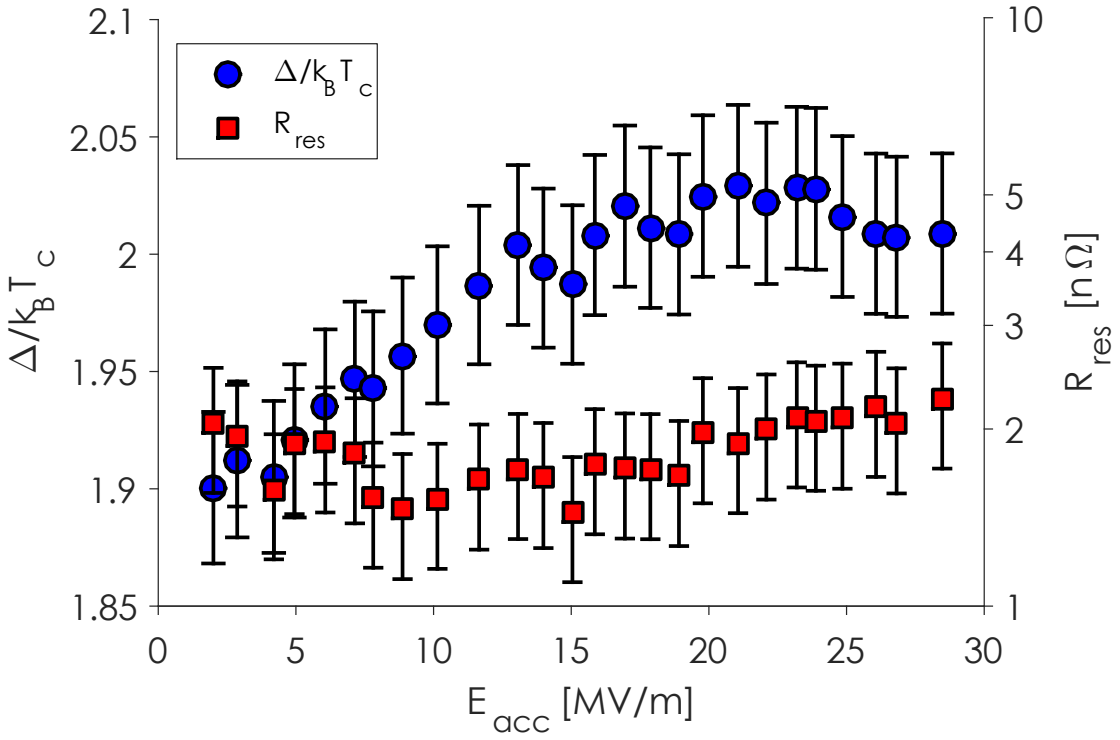

Figure 5.18: Δ/k_BT_c and R_{res} versus E_{acc} for LT1-3 as extracted from SRIMP fitting. Δ/k_BT_c increases in the medium field region while R_{res} is relatively unchanging. Anti-Q slope can be explained by an increasing Δ/k_BT_c in SRIMP fitting.

on the right would need a decreasing mean free path to lower R_{BCS}. Therefore a changing mean free path can be eliminated as a likely cause for the anti-Q slope.

Fitting with Xiao Theory

The previous three sections have discussed fitting measured data using a variety of models. This fitting was done with least squares fitting without much consideration of the physical assumptions going into each model. Now instead consider the ultimate goal in understanding the field dependence of R_{BCS}: from some material properties at zero field, predict the field dependence of R_{BCS} at any temperature. This problem is inherently more difficult and requires further

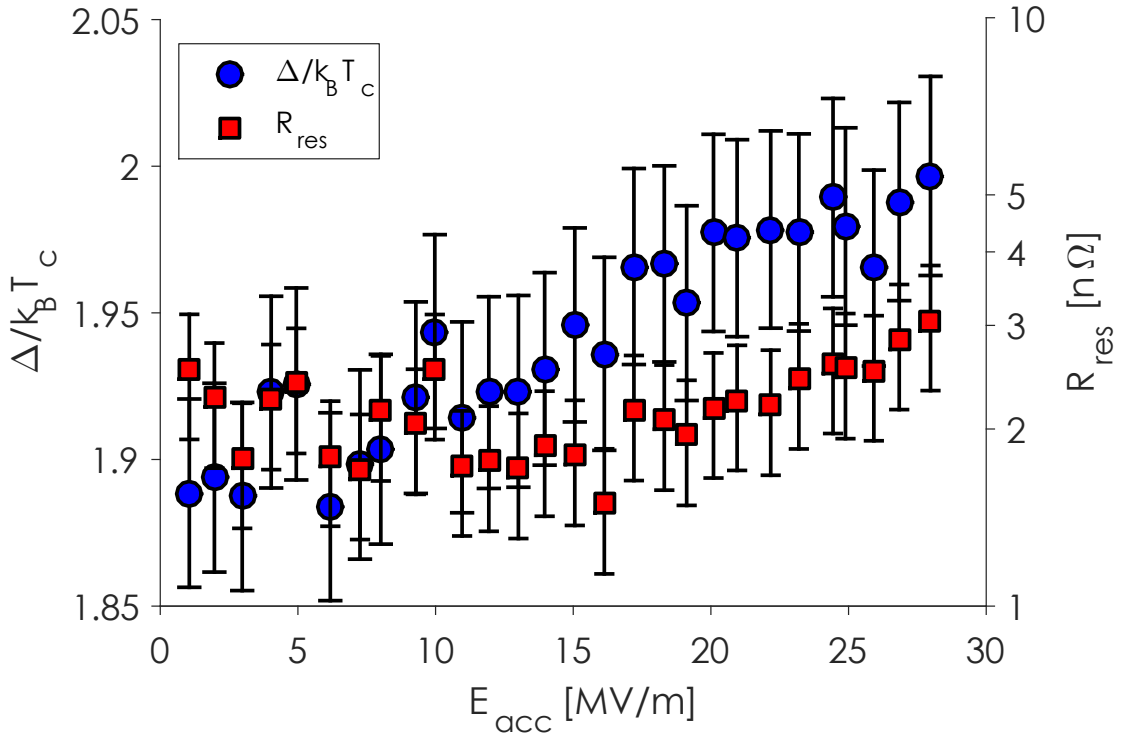

Figure 5.19: Δ/k_BT_c and R_{res} versus E_{acc} for LT1-4 as extracted from SRIMP fitting. Δ/k_BT_c increases in the medium field region while R_{res} is relatively unchanging between 5 and 20 MV/m. Anti-Q slope can be explained by an increasing Δ/k_BT_c in SRIMP fitting.

theoretical development. Two models have been proposed in literature to answer this question, the first of which is discussed in this section and the second in the following section.

In 2013, Xiao et. al. developed a model with hopes of explaining the field dependence of R_{BCS} for SRF cavities in general [XRK13]. In the development of the model, Xiao calculated the the dependence of the surface impedance of superconductors on the magnitude of the RF field. The calculation began with Mattis-Bardeen and BCS theory and extended the principles in the presence of a non-zero RF field. Most interestingly is that the theory predicts a decreasing R_{BCS} with increasing Cooper pair velocity (proportional to the strength of the

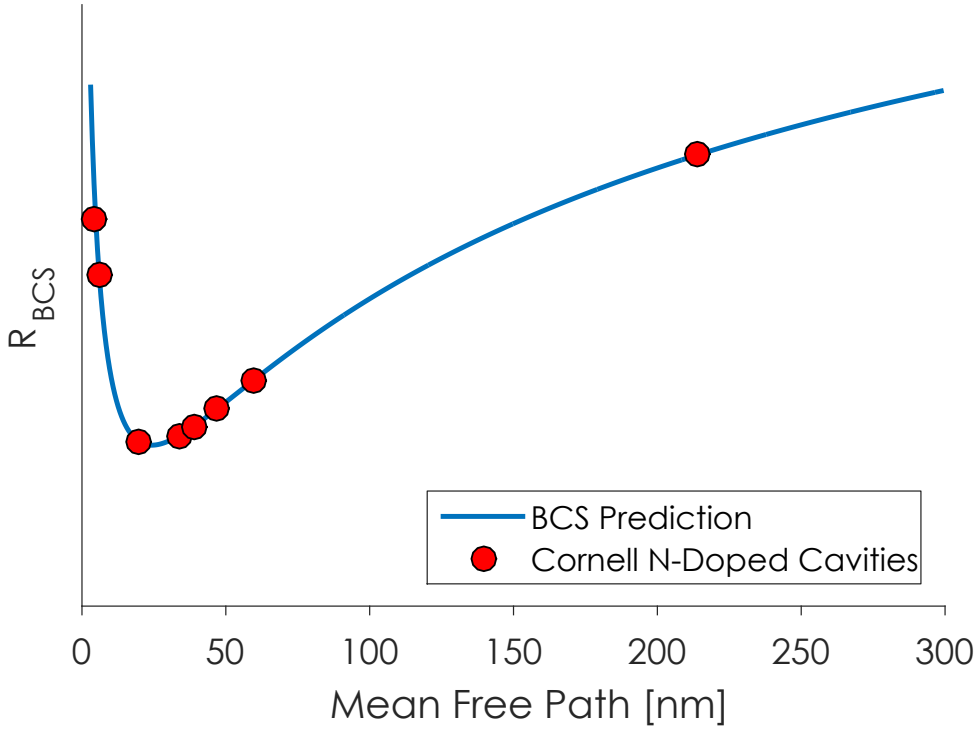

Figure 5.20: Calculated R_{BCS} versus mean free path for nitrogen-doped cavities from BCS theory. The cavity points serve as indications of where they would lie on the curve based on their extracted mean free path values. Cavities lie on either side of the R_{BCS} minimum implying that a changing mean free path cannot solely explain the anti-Q slope. Cavities to the left of the minimum would need an increasing mean free path with field to lower R_{BCS} while the opposite would be required for cavities on the right side of the minimum.

RF field) just as is observed in nitrogen-doped cavities. Initial comparison with experimental data at TJNAF showed good agreement between the theoretical predictions and measurements on nitrogen-doped cavities [XR14].

Based on this theory, a Mathematica code was developed by Xiao and modified at Cornell [KGLM15] to calculate R_{BCS} as a function of RF field magnitude based on zero field material parameters such as mean free path, energy gap, coherence length, and penetration depth. At zero field, the Mathematica code reproduces R_{BCS} as predicted by SRIMP, as one would expect. Using the values

for the material properties extracted using SRIMP fitting, R_{BCS} versus E_{acc} was calculated for LT1-3 and LT1-4.

Figure 5.21 shows R_{BCS} versus E_{acc} at different temperatures for LT1-3 with predictions from the Xiao theory. There is good agreement in the medium field region where the anti-Q slope is strongest however the theoretical prediction deviates from the measured values both at high field and low field. Specifically, the theory does not predict that R_{BCS} would begin to increase again after the peak of the anti-Q slope at as low of a field (~20 MV/m) as was observed experimentally. Additionally, the theory predicts a very strong increase in R_{BCS} as E_{acc} approaches zero. While a low field Q slope is typically observed in both doped and un-doped cavities, it is not nearly as strong as predicted by the Xiao theory and in fact has been shown to be due to a decreasing R_{res} rather than R_{BCS} [RG13]. χ^2 at each temperature is given in Table 5.3 and the average is 0.2002. While this is significantly worse than for either exponential or SRIMP fitting, this is to be expected since these predictions were made from low field material properties rather than fits to the R_{BCS} versus E_{acc} data. Also it is important to note that χ^2 is significantly lower at low temperatures suggesting better agreement between experimental data and the Xiao model.

Figure 5.22 shows R_{BCS} versus E_{acc} at various temperatures for LT1-4 with predictions from the Xiao theory. Immediately it is clear that there is significantly less agreement between the experimental data and the Xiao prediction. While there is fairly good agreement at 2.0 K (χ^2 = 0.7959), 1.6 and 2.1 K have large disagreement between the model and experimental data. An average χ^2 of 1.7920 was found for the temperatures measured compared with 0.2002 for LT1-3. Again, strongest disagreement occurred at low and high fields.

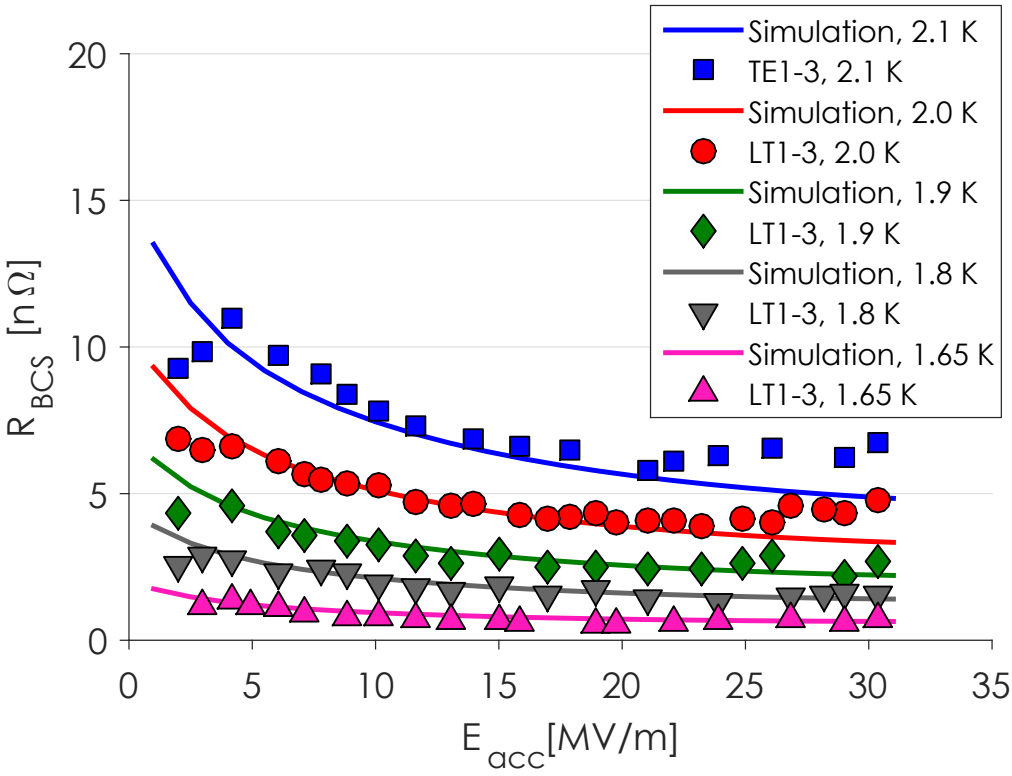

Figure 5.21: R_{BCS} versus E_{acc} at different temperatures for LT1-3 compared with predictions from Xiao theory. R_{BCS} was calculated from theory using low field material parameters extracted with SRIMP fitting (Δ/k_BT_c =1.91 ± 0.01, ℓ = 34 ± 10 nm, T_c =9.3 ± 0.1 K).

The Xiao theory made reasonable predictions for LT1-3's field dependence however was significantly worse for LT1-4. It is likely that this theory can only be thought of as an approximation and does not fully explain the anti-Q slope. Specifically, the prediction of dramatically increasing R_{BCS} at low fields is inconsistent with experimental data. At high fields, thermal effects might play an important role, which are not considered in the Xiao theory. These thermal effects are included in the following theory by Gurevich via an overheating parameter, α.

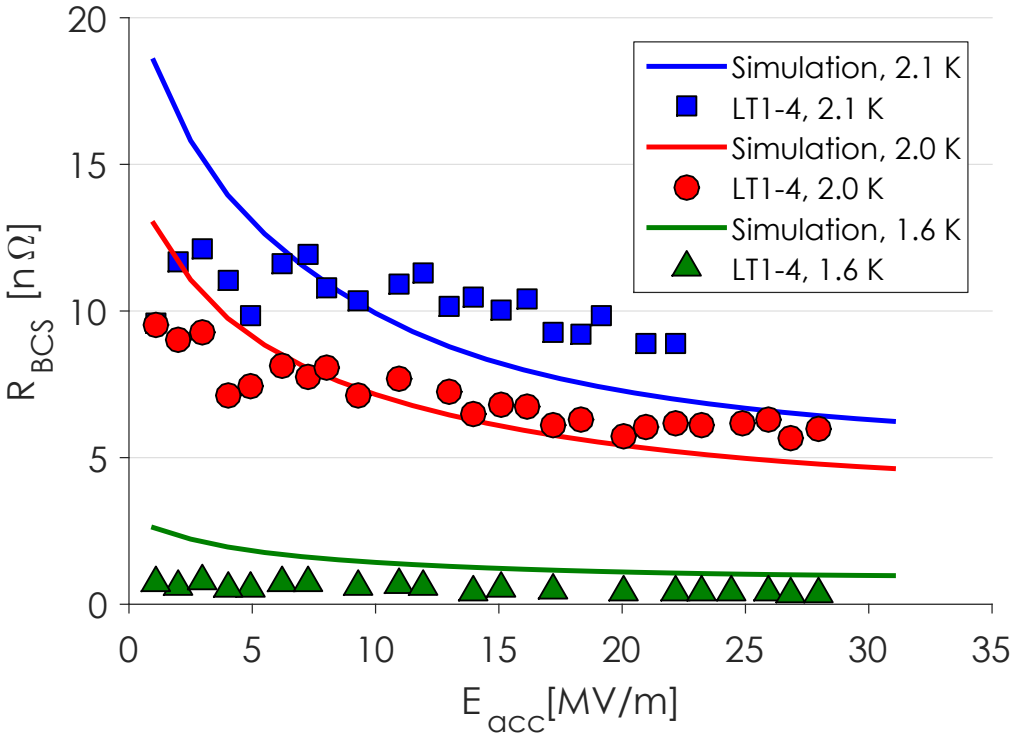

Figure 5.22: R_{BCS} versus E_{acc} at different temperatures for LT1-4 compared with predictions from Xiao theory. R_{BCS} was calculated from theory using low field material parameters extracted with SRIMP fitting (Δ/k_BT_c =1.89 ± 0.01, ℓ = 47 ± 14 nm, T_c =9.2 ± 0.1 K).

Fitting with Gurevich Theory

The last theoretical model for the field dependence of R_{BCS} that will be discussed in this dissertation is a model proposed by Gurevich [Gur14]. The theory studies dissipative nonlinear conductivity of superconductors in the presence of strong RF fields at low temperatures. In the presence of magnetic fields, screening currents form on the surface of a superconductor to screen the bulk from the external field. These screening currents can have enough energy to facilitate the breaking of Cooper pairs (quasi-particles). Because of the presence of these quasi-particles the density of states changes which can lower the normal conducting conductivity of the superconductor. This changing normal conducting

conductivity does not affect the Cooper pairs since they are superconducting but does impact the motion of the quasi-particles. As the RF field is increased, the normal conducting resistivity is increased which in turn leads to a lower RF surface resistance.

The theory is dependent on material properties such as T_c, energy gap, coherence length, and the thermodynamic critical field, B_c. It is also dependent on the mean free path and is only valid in the dirty limit. In addition to these material parameters, the theory is also heavily dependent on α, the over heating parameter. This α depends on material properties (thermal conductivity, kapitza resistance) and relates the experimental liquid helium temperature to the quasi-particle temperature. This quasi-particle temperature is an effective temperature that is higher for the quasi-particles than ambient liquid helium bath temperature due to their motion and dissipation under RF fields. In addition to depending on material parameters, α also is temperature dependent. In the following it is assumed that $\alpha \propto 1/T$ which agrees well with the experimental data.

Figure 5.23 shows R_{BCS} versus B_{pk} for LT1-3 compared with the prediction from the Gurevich theory. Material parameters extracted from low field fitting with SRIMP were used and α was fit to the 2.0 K data. The other temperature curves were generated using the assumed $1/T$ dependence of α on temperature. All temperatures have very good agreement between the theoretical prediction and experimental data in the medium field region. At low fields, the agreement with experimental data is about as good as the Xiao theory. There is disagreement at high field most likely due to vortex penetration leading to additional losses above B_{c1}, which is not accounted for in the theory. The average χ^2 for

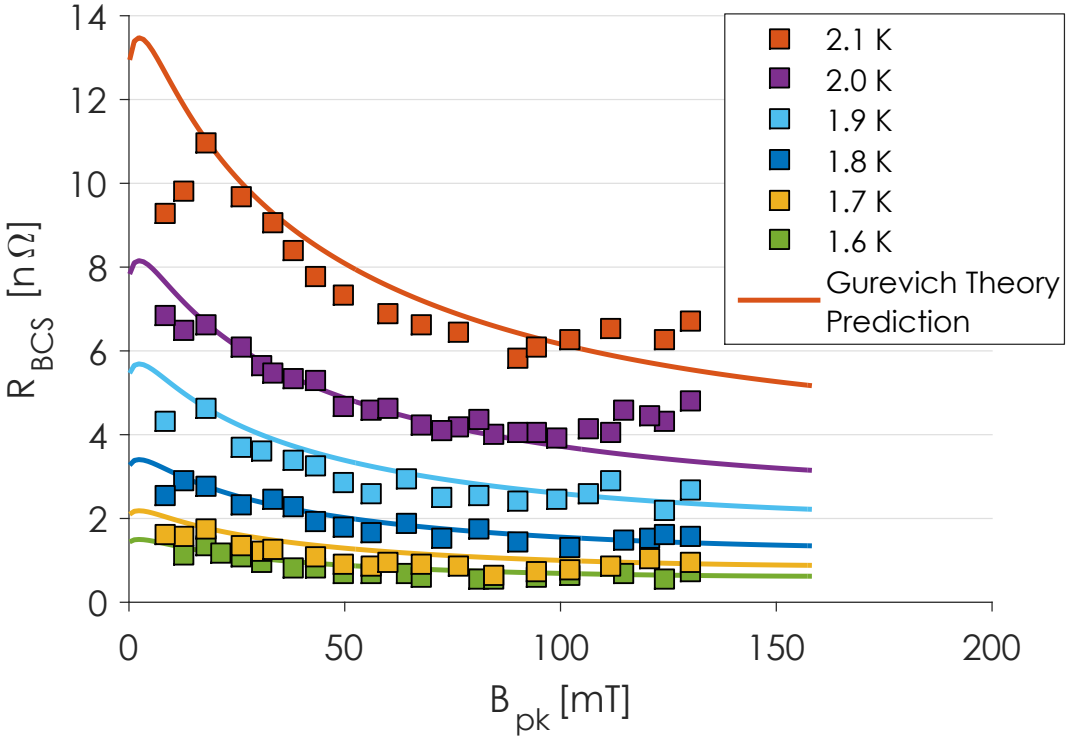

Figure 5.23: R_{BCS} versus B_{pk} at different temperatures for LT1-3 compared with predictions from the Gurevich theory. Low field material parameters from SRIMP fitting were used (Δ/k_BT_c =1.91 ± 0.01, ℓ = 34 ± 10 nm, T_c =9.3±0.1 K) and α was fit to the 2.0 K data (α(2 K) = 0.25). Other curves were created assuming the $1/T$ dependence of α on temperature.

LT1-3 is 0.1410, significantly less than the χ^2 for the Xiao theory with the same data set. This signifies that the Gurevich theory has better agreement with the experimental data.

Figure 5.24 shows R_{BCS} versus B_{pk} for LT1-4 compared with the prediction from the Gurevich theory. Material parameter extraction and fitting for α was done in the same manner as with LT1-4. Again there is very good agreement at all temperatures at low and medium fields. The average χ^2 for LT1-4 is 0.4635, worse than for LT1-3, but still significantly better than the χ^2 for the Xiao theory.

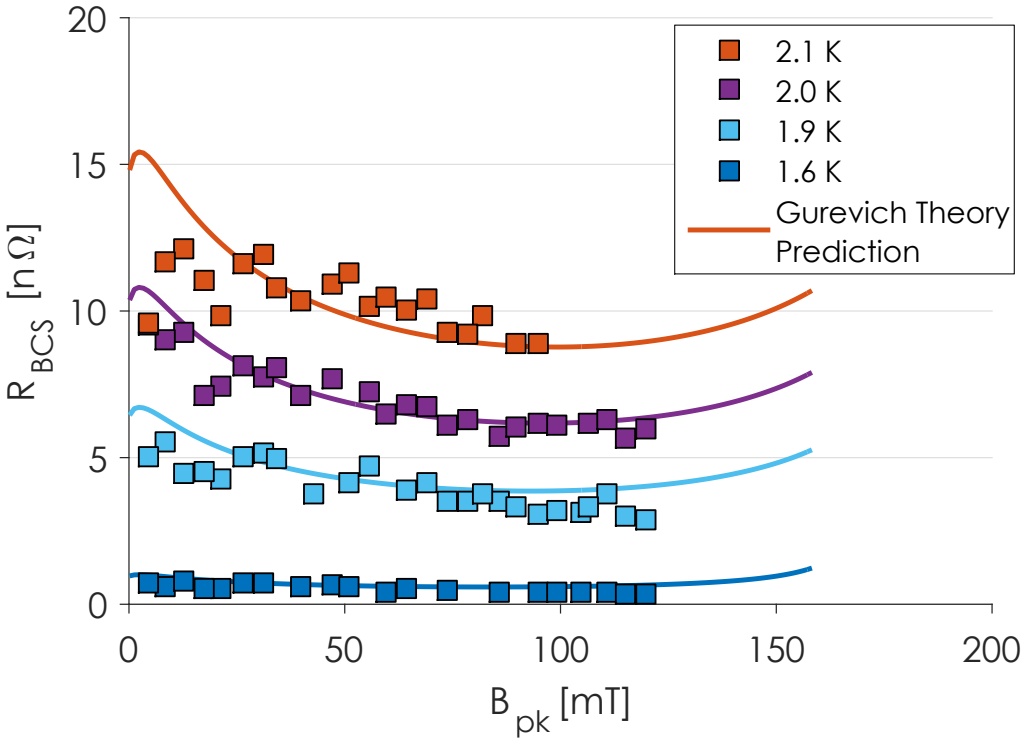

Figure 5.24: R_{BCS} versus B_{pk} at different temperatures for LT1-4 compared with predictions from the Gurevich theory. Low field material parameters from SRIMP fitting were used (Δ/k_BT_c =1.89 ± 0.01, ℓ = 47 ± 14 nm, T_c =9.2±0.1 K) and α was fit to the 2.0 K data (α(2 K) = 0.68). Other curves were created assuming the $1/T$ dependence of α on temperature.

An interesting feature of the Gurevich theory prediction is that at very low fields R_{BCS} decreases as the RF field is lowered. Unfortunately as of yet this behavior has not been experimentally verifiable due large uncertainties in the measured R_{BCS} at low fields. Future work may focus on studying this region for a further check on the theory. Also, while the Gurevich theory produces good agreement with experimental data, there is no explicit dependence of the anti-Q slope on the mean free path and the theory is only valid in the dirty limit. It would be desirable to extend the theory to the clean limit to check if the anti-Q slope disappears at higher mean free paths.

Summary of Fitting

In the previous sections, four methods have been presented to provide insight into the field dependence of R_{BCS}. Exponential fitting and BCS fitting were done with least squares fitting to the R_{BCS} versus E_{acc} data to extract field dependent material parameters. Fitting to the Xiao theory was done by calculating the field dependent R_{BCS} from low field material parameters extracted from fitting using SRIMP. These low field material parameters were also used with the Gurevich theory, however fitting of the α parameters was necessary at one temperature and used to generate the field dependence at other temperatures.

A comparison of all the fitting methods with the field dependent R_{BCS} for LT1-3 at 2.0 K is shown in Figure 5.25. The two least squares fitting methods show good agreement at all fields, as one would expect since they are directly fitting to the experimental data. The Xiao and Gurevich theory show a larger deviation at low and high fields, however they are rooted more deeply in theoretical calculations. Figure 5.26 shows the normalized χ^2 for all of the fitting methods as a function of temperature for LT1-3. Exponential and SRIMP fitting shows significantly better fitting at all temperatures, while the Gurevich theory shows better agreement with the experimental data than the Xiao theory. For all fitting methods, higher temperatures lead to worse fitting (the Gurevich theory being an exception since α fitting was done at 2.0 K).

Figure 5.27 shows the comparison of fitting methods to R_{BCS} versus E_{acc} data at 2.0 K for LT1-4. The fits for LT1-4 were in general worse than for LT1-3 however similar conclusions can be drawn. Figure 5.28 shows the normalized χ^2 versus temperature for all the fitting methods for LT1-4. Again, the Gurevich theory shows better agreement with the experimental data than the Xiao theory.

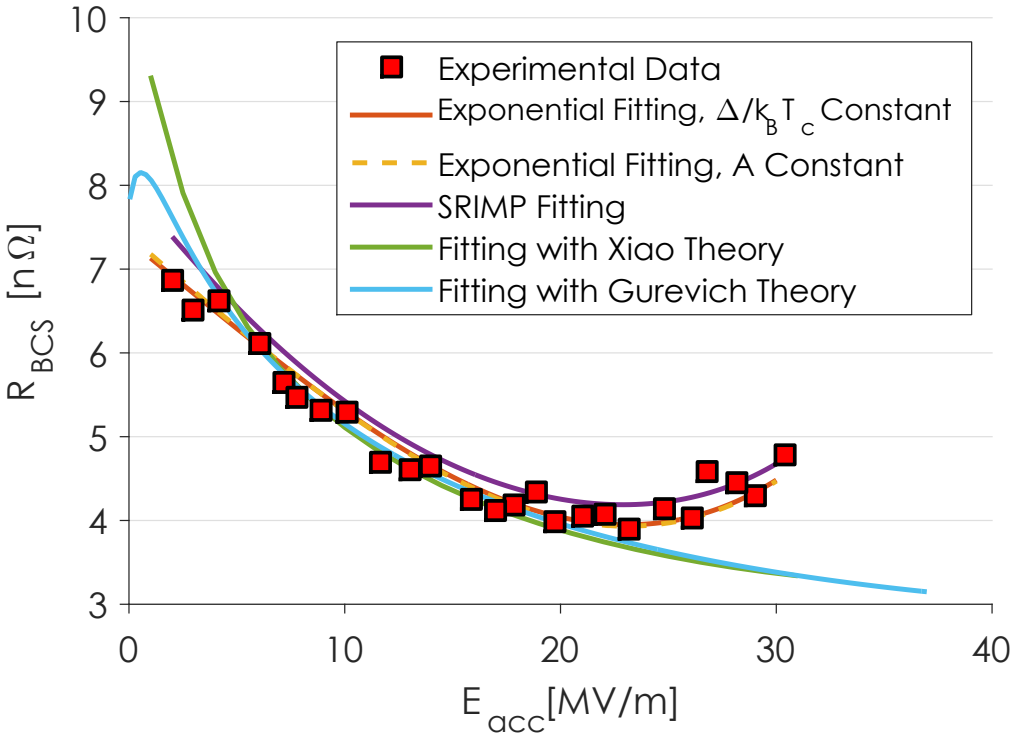

Figure 5.25: A comparison of all fitting methods with R_{BCS} versus E_{acc} data for LT1-3 at 2.0 K.

Also, as with LT1-3, higher temperatures had worse fitting than lower temperatures.

The field dependence of R_{BCS} and the anti-Q slope is characteristic of nitrogen-doped cavities. Several theories have been proposed to explain the anti-Q slope observed which has led to new unprecedented high Q_0's in doped cavities. The anti-Q slope roughly decreases as the logarithm of the magnitude of the RF field and can be explained by an increasing $\Delta / k_B T_c$ in exponential and BCS fitting or a decreasing A parameter in exponential fitting. It is however impossible for a changing mean free path to lead to the decreasing R_{BCS} since low field mean free path values lie on either side of the R_{BCS} versus ℓ curve.

In addition to fitting with low field BCS theory, two models have been pro-

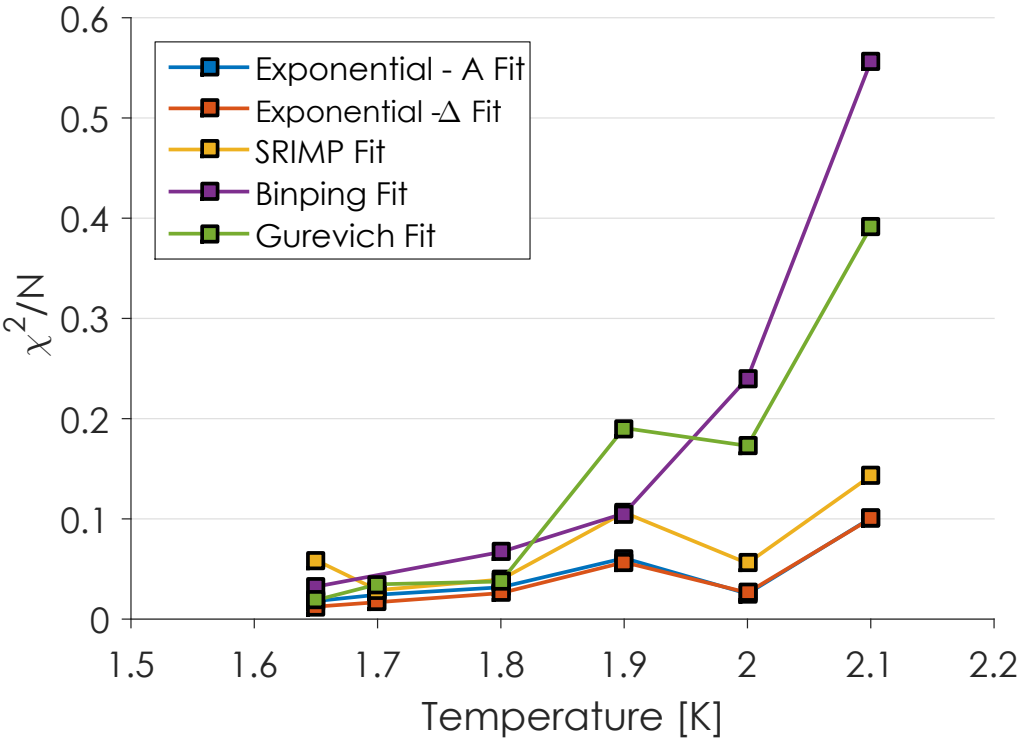

Figure 5.26: Normalized χ^2 versus temperature for the four fitting methods for LT1-3.

posed to extend superconducting theory to explain the field dependence of R_{BCS}. Xiao developed a theory extending Mattis-Bardeen theory to the case of high RF fields. While this theory's predictions show good agreement with experimental data in the medium field region, it fails to predict behavior at low and high fields. Gurevich also proposed a theory to explain the field dependence based on the theory of quasi-particles being generated by screening currents. This theory generally shows better agreement at low and medium fields with experimental data but does not inherently have a mean free path dependence of the strength of the anti-Q slope, which should be necessary to separate the performance of doped cavities with un-doped cavities. While examples from only two cavities were presented here, the behavior discussed is consistent across all nitrogen-doped cavities tested for this dissertation.

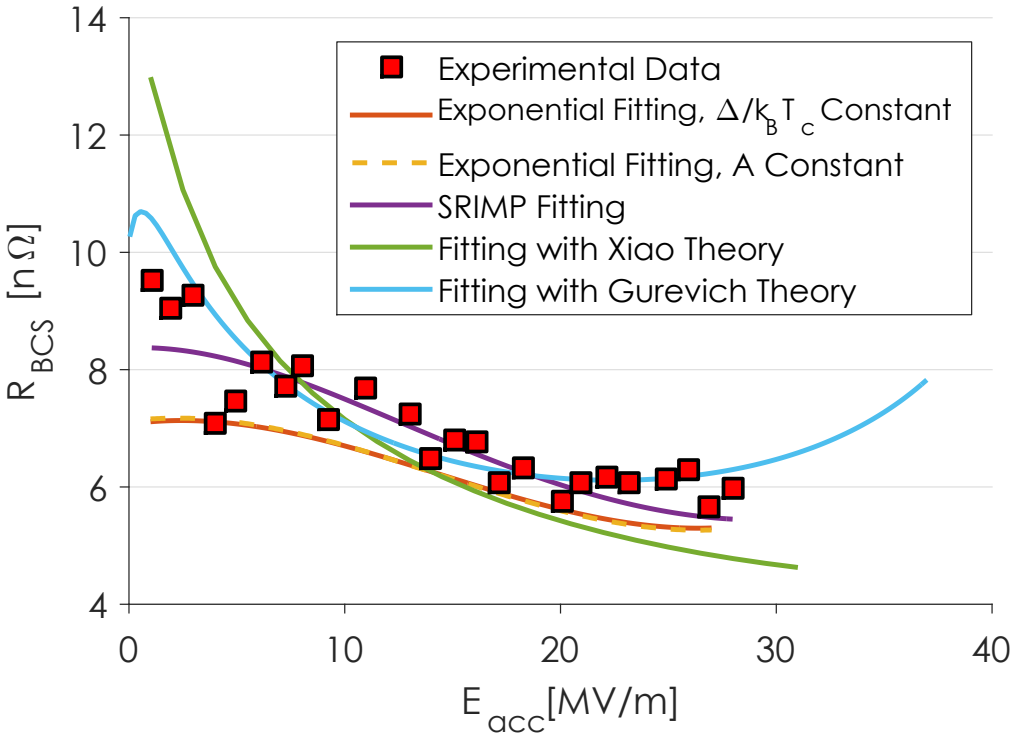

Figure 5.27: A comparison of all fitting methods with R_{BCS} versus E_{acc} data for LT1-4 at 2.0 K.

5.4 Optimal Doping

With a better understanding of how R_{BCS} is affected by nitrogen-doping, it is reasonable to start to craft a picture of an optimal doping level. Ultimately for machines such as LCLS-II, the Q_0 at 16 MV/m is the fundamental parameter that should be maximized. Therefore the optimal doping level in terms of BCS resistance is the point at which R_{BCS} (16 MV/m) is minimized.

Figure 5.29 shows R_{BCS} (16 MV/m) versus mean free path for the nitrogen-doped cavities tested. For the two cavities with $\ell < 10$ nm which quenched below 16 MV/m, the logarithmic dependence of R_{BCS} on E_{acc} was assumed to approximate how the anti-Q slope would continue beyond the quench point.

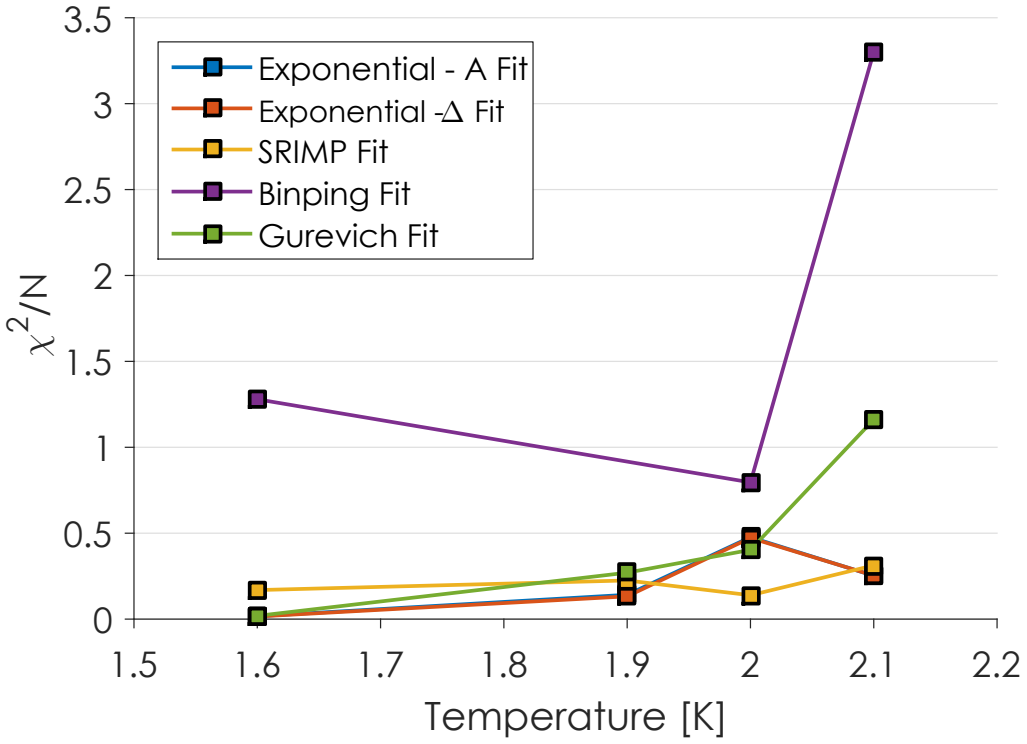

Figure 5.28: Normalized χ^2 versus temperature for the four fitting methods for LT1-4.

Also shown in Figure 5.29 is the low field prediction from BCS theory. In the clean limit, when the anti-Q slope is not very strong, the low field prediction agrees well with the medium field experimental data. In the dirty limit however, there is a deviation as the anti-Q slope allows for R_{BCS} to decrease further than can be predicted by low field BCS theory. However, applying an adjustment to the low field theory using the anti-Q slope's dependence on mean free path as in Figure 5.11 shows good agreement with the experimental data. This shows a clear minimum for R_{BCS} (16 MV/m) at mean free paths of ~10 nm. This means that to reach the minimum R_{BCS} at 16 MV/m, a mean free path of 10 nm would be ideal. For reference this was achieved with a doping at 800°C for 20 minutes with a 30 minute anneal and 6 μm final EP. This optimization of R_{BCS} will be combined with an optimization of R_{res} in the next chapter to predict a

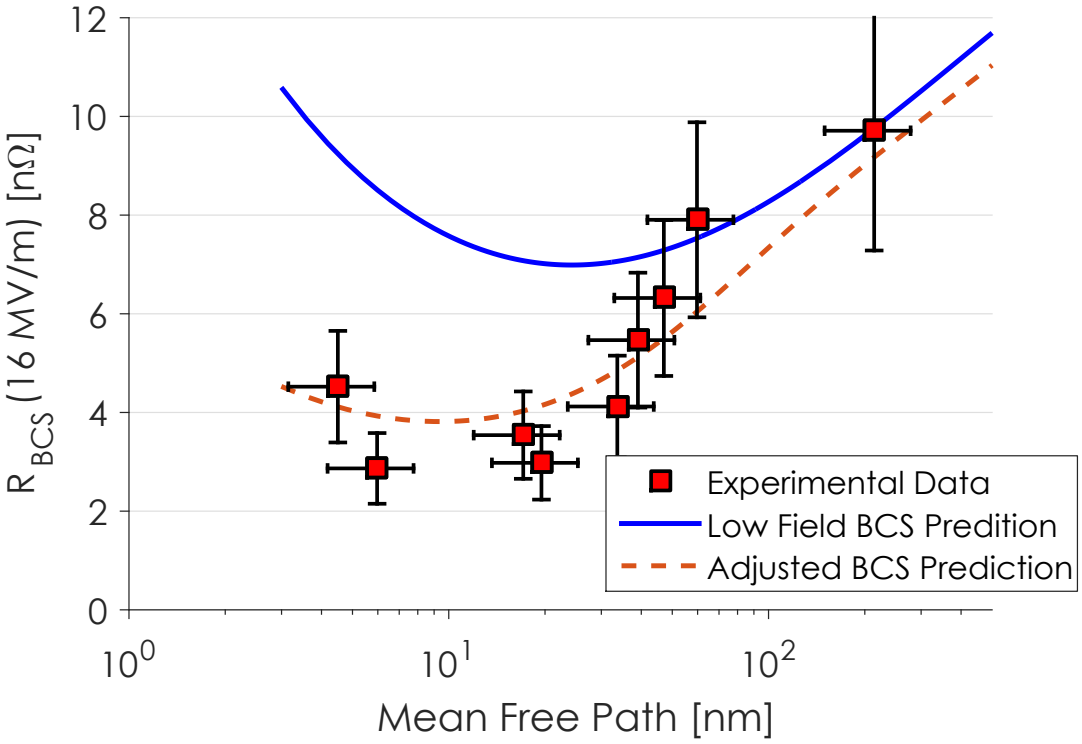

Figure 5.29: R_{BCS} at 16 MV/m versus mean free path for the nitrogen-doped cavities tested. Also shown is the low field prediction of BCS theory and an adjustment to this prediction based on the anti-Q slope as analyzed in Figure 5.11. R_{BCS} was approximated for those cavities that quenched below 16 MV/m by assuming a logarithmic dependence on the magnitude of the RF field. A minimum in R_{BCS} (16 MV/m) is present at $\ell \approx 10$ nm suggesting an optimal doping level to minimize R_{BCS}.

true optimized doping level for achieving the highest Q_0 at 16 MV/m and 2.0 K.

CHAPTER 6

RESIDUAL RESISTANCE STUDIES

This chapter focuses on residual resistance, the temperature independent component of the surface resistance. Specifically, the impact of external magnetic field on the residual resistance is discussed in detail. It begins with a discussion of the impact of ambient magnetic field on surface resistance in general. Next an introduction to trapped magnetic flux in SRF cavities is presented. Following the introduction, two theoretical models are presented to predict how the trapped magnetic flux and its impact on residual resistance depend on material properties. Next a discussion on the impact of cool down dynamics on the amount of trapped magnetic flux is presented based on work at Cornell, FNAL, and KEK. Next a discussion on an experiment to understand how residual resistance is affected from trapped flux for cavities of differing preparation methods. Specifically this will focus on how certain material parameters impact the sensitivity of residual resistance to trapped magnetic flux. Finally, this chapter will conclude with a discussion of the optimal doping level by combining the BCS resistance studies in the previous chapter with the results here.

6.1 Impact of Ambient Magnetic Field on Surface Resistance

For ambient magnetic fields below B_{c1}, a perfect superconductor will completely expel magnetic flux when it transitions from normal to superconducting. However, in reality SRF cavities are not perfect superconductors. Impurities and defects can lead to pinning sites for magnetic flux. When a cavity enters the Meissner state, some ambient DC magnetic field will be expelled while some will remain trapped in the material [Tin04]. This "trapped flux"

can cause additional losses in RF fields and lead to a higher surface resistance, R_s. Figure 6.1 shows R_s versus temperature for one single-cell cavity cooled with different amounts of trapped magnetic flux. At high temperatures (near 4 K), R_s is unchanged by the trapped flux, however at low temperatures there is a large spread in R_s. By separating R_s into its two components, the temperature dependent BCS resistance can be extracted versus temperature. This is shown in Figure 6.2 for the same cool downs shown in Figure 6.1. It is clear that R_{BCS} is unaffected by the trapped flux in the full temperature range Q_0 was measured. This implies that the only component of R_s affected by trapped flux is the residual resistance, R_{res}.

Several mechanisms have been shown to contribute to the residual resistance such as normal conducting inclusions, hydrides, oxides, and trapped magnetic flux [PKH98]. However, in well prepared cavities, the majority of residual resistance has been shown to be due to magnetic flux trapped in the cavity's walls. Therefore great care needs to be taken in order to minimize the ambient magnetic fields present during a cavity's cool down.

Understanding the dependence of sensitivity of residual resistance to RF losses from trapped flux is crucial now as Q_0 performance and specifications keep increasing. Nearly all modern cavity preparation techniques use niobium that has an surface RF layer with a lower mean free path than the bulk niobium. However the impact of these new cavity preparations on the residual surface resistance due to trapped flux was not well understood prior to the research work presented in the following. Previous measurements have highlighted that the sensitivity of residual resistance to ambient magnetic field can strongly vary. Specifically, Weingarten et. al. showed that cavities constructed of niobium

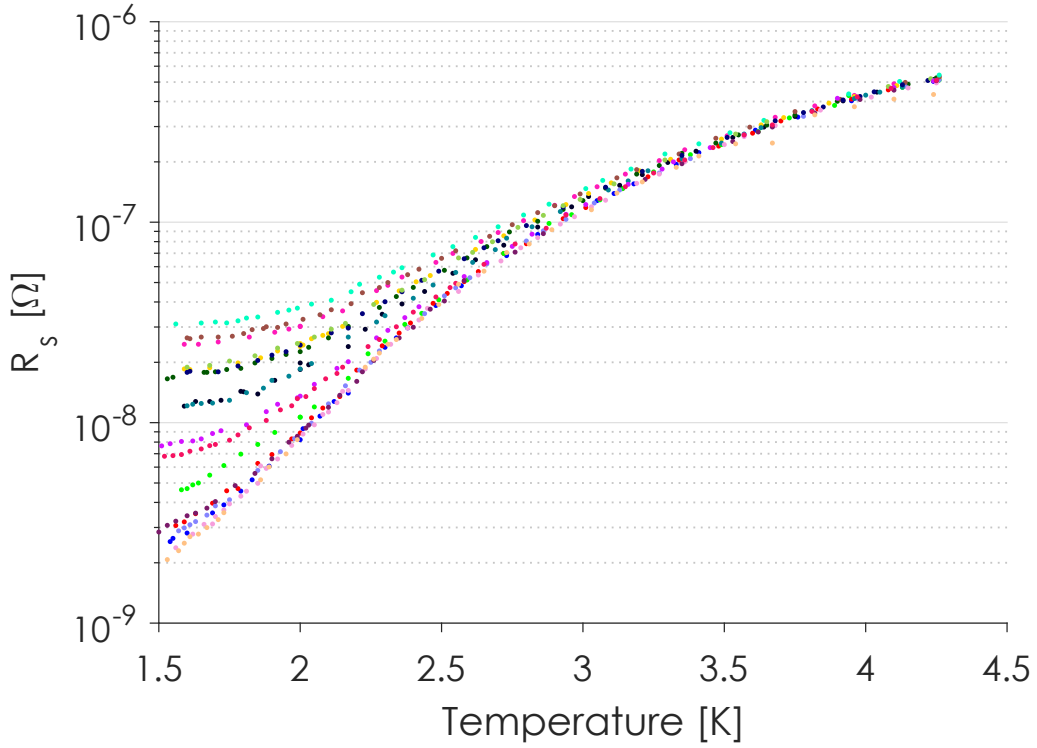

Figure 6.1: Surface resistance versus temperature at low fields ($E_{acc} < 5$ MV/m) for a single 1.3 GHz SRF cavity over many cool downs with different amounts of trapped magnetic flux between 0 and 10 mG. Each color represents a different cool down. High temperature surface resistance is unchanged by the amount of trapped flux while low temperature surface resistance is strongly affected. This is suggestive of the trapped flux affecting only the residual resistance component, not the BCS resistance component.

sputtered on copper (much smaller mean free path than high RRR (residual resistance ratio) bulk niobium) had less sensitivity to ambient field [Wei95] using a similar method to what will be discussed later in this chapter. Additionally, they showed that residual resistance scales linearly with ambient magnetic field. Now with nitrogen-doping, the mean free path of the material can be finely tuned in order to fully study this sensitivity's dependence on the full material parameter space.

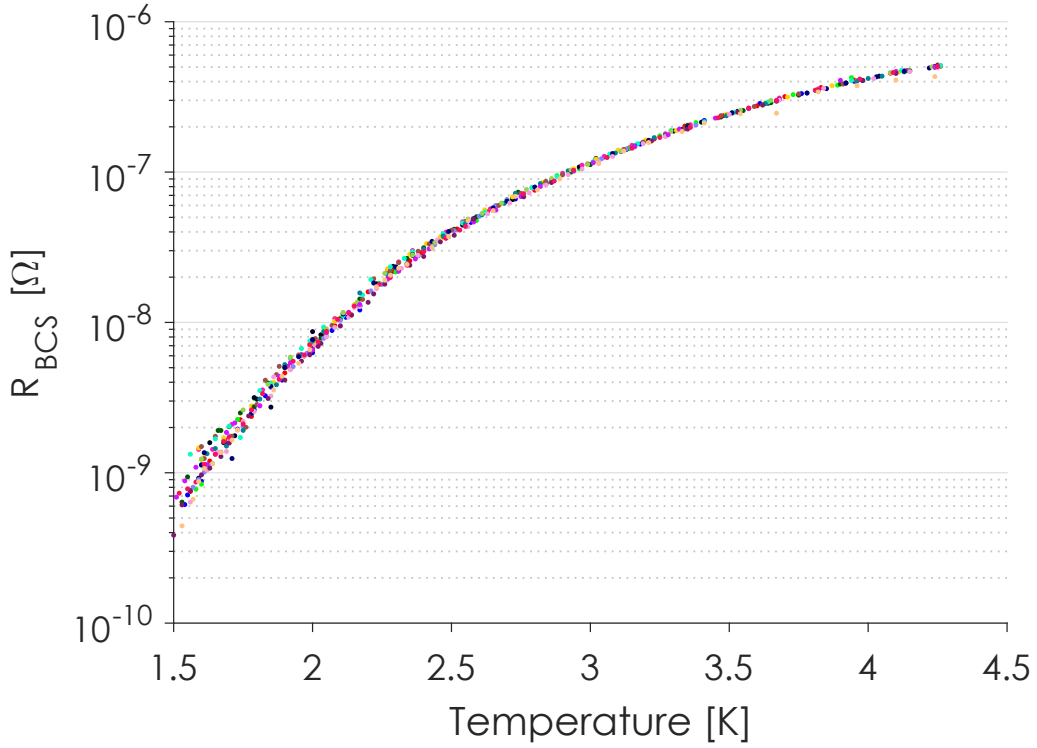

Figure 6.2: BCS resistance versus temperature for the same cavity and cool downs as in Figure 6.1. It is clear that R_{BCS} is unaffected by the amount of trapped flux at all temperatures. This implies that the change in R_s observed in Figure 6.1 is due only to a changing R_{res}.

6.2 Theoretical Considerations

6.2.1 Simple Theory of Losses from Trapped Magnetic Flux

Vallet et. al. discuss the dependence of residual resistance from trapped ambient magnetic field in SRF cavities based on a phenomenological result [VBB+92]. It can be shown that the residual surface resistance, R_s, increases linearly with trapped DC magnetic field. A trapped magnetic field, $B_{trapped}$ in a wall surface area A breaks up into N fluxoids each with a quantum of flux, ϕ_0, (see Figure 6.3)

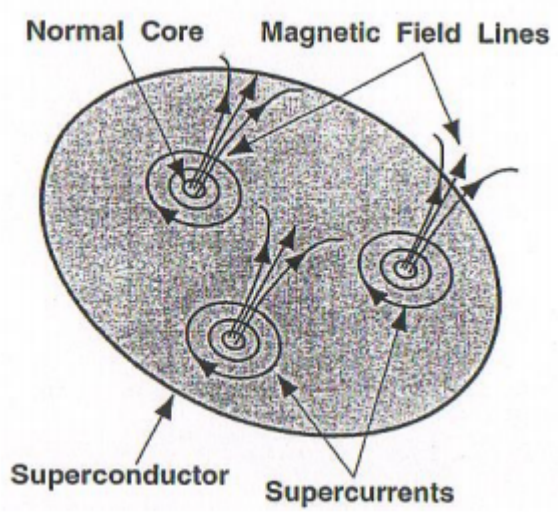

Figure 6.3: Magnetic field lines and supercurrents for trapped magnetic flux in a superconductor. Image from [PKH98].

so that

$$AB_{trapped} = N\phi_0. \tag{6.1}$$

The size of these normal conducting cores is directly related to the coherence length, ξ. The additional residual resistance from the trapped magnetic flux, $R_{\mathrm{res,B}}$, can be estimated by the following simple model. The contribution to surface resistance from the normal conducting vortex cores can be estimated by multiplying the number of fluxoids times the normal conducting resistance, R_n, times the fraction of the normal conducting area.

$$R_{\mathrm{res,B}} = NR_n\frac{\pi\xi^2}{A} = \frac{\pi\xi^2 R_n}{\phi_0}B_{trapped}. \tag{6.2}$$

Using the upper critical field, B_{c2},

$$B_{c2} = \frac{\phi_0}{2\pi\xi^2}, \tag{6.3}$$

equation 6.2 can be rewritten as

$$R_{\mathrm{res,B}} = \frac{B_{trapped}}{2B_{c2}}R_n. \tag{6.4}$$

Figure 6.4 shows the form that Equation 6.4 takes, normalized to the amount of trapped flux. As mean free path, ℓ, decreases (resulting in B_{c2} increasing and $R_N \propto 1/\sqrt{\ell}$), sensitivity of residual resistance to trapped magnetic flux would decrease in the dirty limit ($\ell \ll \xi_0$) as $\ell^{3/2}$ [PKH98]. In the clean limit ($\ell \gg \xi_0$), as B_{c2} changes more slowly, this sensitivity would decrease as mean free path is increased. This is consistent with previously mentioned results on copper cavities coated with very low RRR niobium ($\ell \approx 2$ nm, $R_{\text{res,B}}/B_{\text{trapped}} \approx 0.01$ nΩ/mG for 1.5 GHz cavities) [Wei95, BBF+]. For 1.3 GHz cavities made out of clean niobium with a B_{c2} of 240 mT and a normal state resistance R_n of 1.5 mΩ (typical for clean niobium [PKH98]), this model suggests an additional $\sim$ 0.3 nΩ/mG of ambient magnetic field. This is in good agreement with experimental results on clean bulk niobium cavities in which a sensitivity of residual resistance to trapped magnetic flux was found to be 0.35 nΩ/mG [VBB+92].

6.2.2 Gurevich's Theory of Losses from Trapped Magnetic Flux

Gurevich and Ciovati developed a more advanced theoretical model studying the impact of vortices on surface resistance for fields perpendicular to the surface [GC13]. By modeling oscillations of vortex lines (Figure 6.5) between pinning sites the additional surface resistance as a function of mean free path (ℓ) can be computed beginning from London theory. The dissipated power from a single vortex line is [GC13]

$$P = \frac{H_p^2 \phi_0^2 \left(\sinh\sqrt{2\nu} - \sin\sqrt{2\nu}\right)\sqrt{\nu}}{2^{3/2}\eta\ell_p\left(\cosh\sqrt{2\nu} + \cos\sqrt{2\nu}\right)}, \tag{6.5}$$

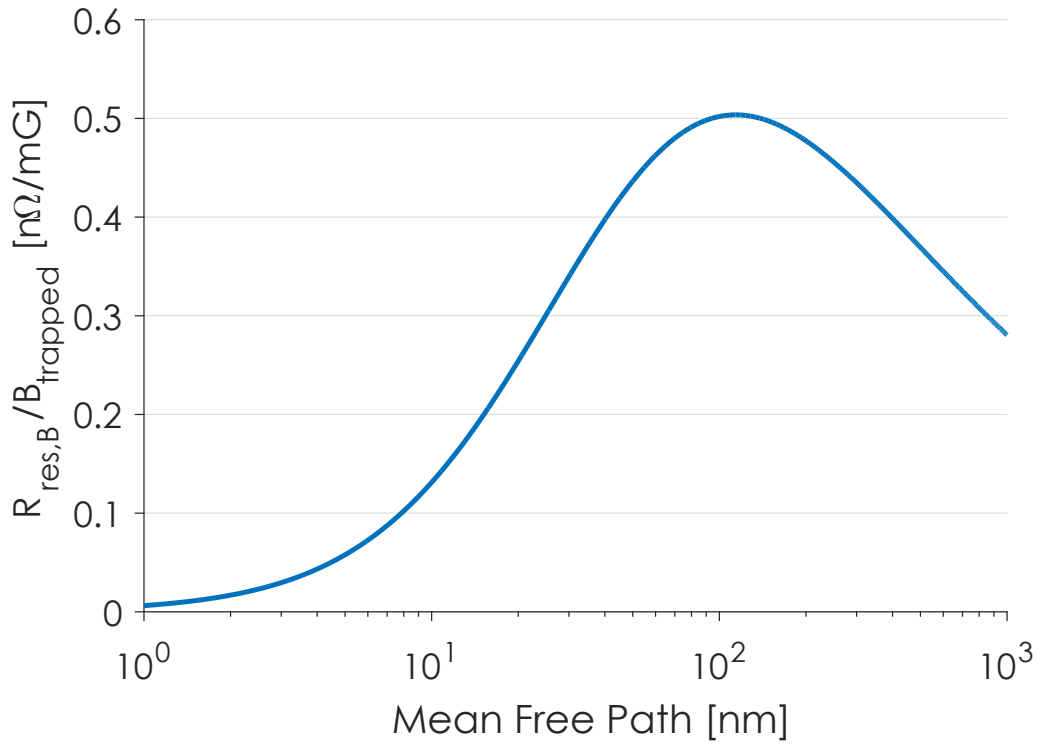

Figure 6.4: Sensitivity of residual resistance to trapped magnetic flux versus mean free path based on the simple theory in Equation 6.4 assuming $\xi_0 = 38$ nm and $f = 1.3$ GHz.

where H_p is the RF peak magnetic field, ϕ_0 is the flux quantum and ℓ_p is the mean spacing between pinning centers, with

$$\nu = \omega\eta\ell_p^2/\epsilon, \quad \epsilon = \frac{\phi_0^2 g}{4\pi\mu_0\lambda^2}, \tag{6.6}$$

$$\eta = \phi_0 B_{c2}/\rho_n, \quad g = \ln\kappa + \frac{1}{2}. \tag{6.7}$$

The mean spacing must be much greater than the coherence length in order for the theory to be valid. Here λ is the penetration depth, κ is the Ginzburg-Landau parameter, ρ_n is the normal conducting resistivity, ω is the RF frequency multiplied by 2π, and B_{c2} is the upper critical field of the superconductor defined by equation 6.3. ρ_n is proportional to $1/\ell$ with a constant of proportionality of $0.37\times10^{-15}\ \Omega\,\mathrm{m}^2$ for niobium[GK68] (Somewhat different values have been re-

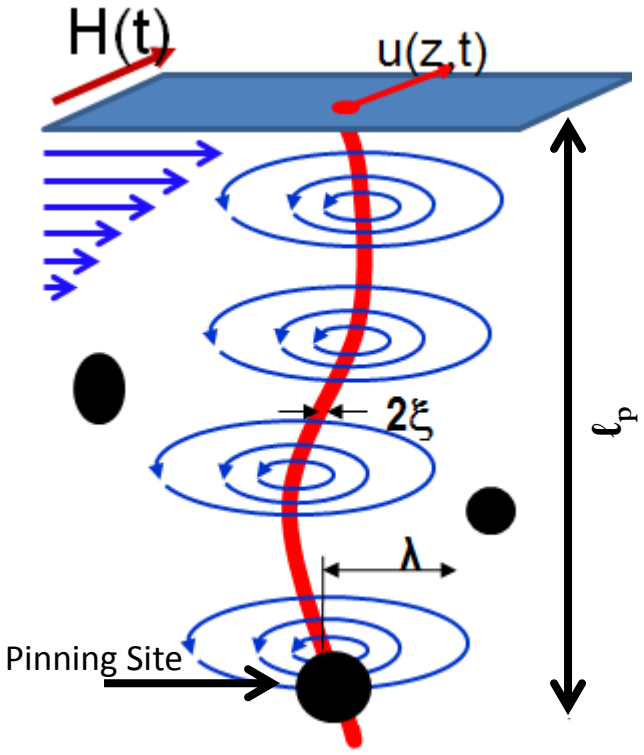

Figure 6.5: Oscillations of vortex lines between pinning sites resulting in additional residual losses. Image from [GC13].

ported elsewhere [SES10].) The penetration depth and the coherence length can be calculated as a function of the mean free path by Equation 2.24 and Equation 2.22.

From the dissipated power per flux line (equation 6.5), the total additional residual resistance from a trapped DC magnetic field of magnitude $B_{trapped}$ can be computed by the relation

$$R_{\text{res,B}} = \frac{2PB_{trapped}}{\phi_0 H_p^2}, \tag{6.8}$$

This prediction is heavily dependent on material parameters, specifically the mean free path, penetration depth, and coherence length along with the frequency. The mean pinning spacing between pinning sites is also important. Figure 6.6 shows residual resistance from trapped flux (normalized to the amount

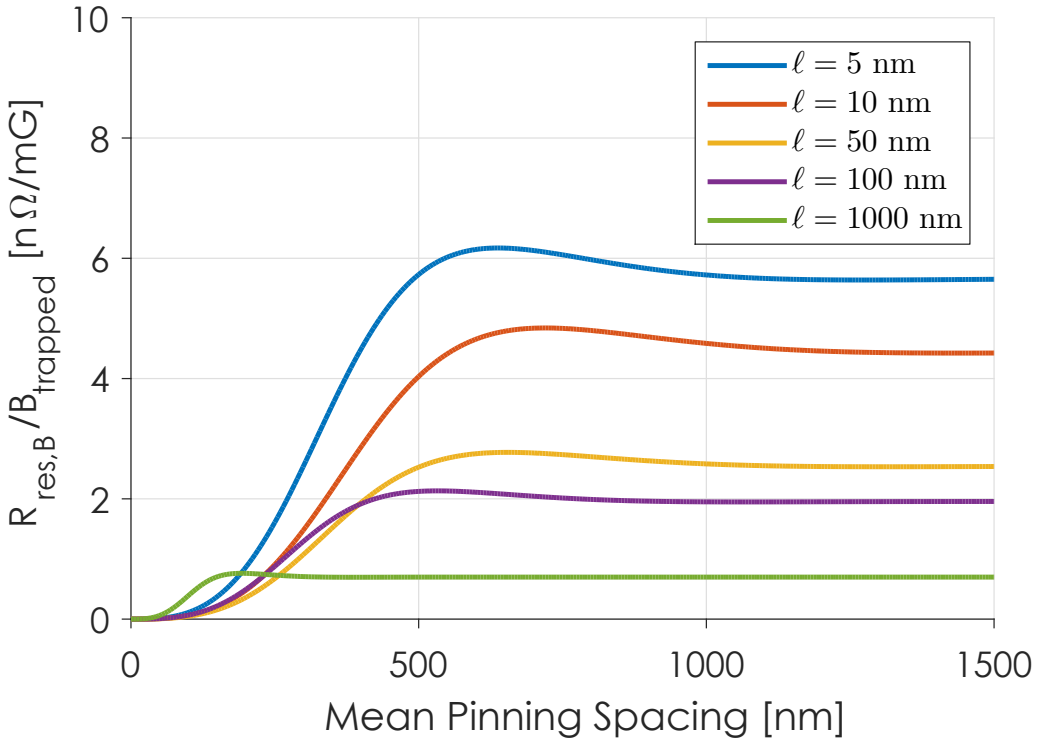

Figure 6.6: Residual resistance from trapped magnetic flux normalized to the trapped flux versus the mean spacing between pinning sites shown for different mean free paths assuming f = 1.3 GHz, λ_L = 39 nm, and ξ_0 = 38 nm. This is based on Gurevich's theory of losses from vortex oscillations [GC13].

of trapped flux) versus the mean spacing between pinning sites as predicted by Equation 6.8 for different values of mean free path. At long pinning spacings, the additional residual resistance from trapped flux is constant with increasing ℓ_p. At short pinning spacings, increasing pinning length leads to a higher residual resistance from trapped flux.

Equation 6.8 shows two distinct regions with very different behavior. Figure 6.7 shows residual resistance from trapped flux (again normalized to the amount of trapped flux) versus the mean free path for different interpretations of the mean spacing between pinning sites. In the clean limit ($\ell \gg \lambda_L$), the spacing between pinning centers, ℓ_p, does not impact the surface resistance. In this

region, losses decrease with longer mean free paths as $1/\sqrt{\ell}$. In the very dirty limit ($\ell \ll \lambda_L$), the dependence is strongly impacted by ℓ_p. If ℓ_p is a constant significantly larger than the penetration depth, losses decrease as the mean free path increases like $1/\sqrt{\ell}$ for all values of ℓ. If ℓ_p is a constant on the order of the penetration depth, larger mean free paths again lead to lower losses however there is an intermediate region where losses do not change significantly as mean free path is changed. If however, one assumes that there is a direct relationship between mean free path and the mean spacing between pinning sites, very different behavior is predicted outside of the clean limit. It is reasonable to assume that vortex lines will be pinned at defects. Therefore a linear relationship between the mean spacing and the mean free path is a reasonable assumption:

$$\ell_p = C\ell, \tag{6.9}$$

with constant of proportionality, C. In this case the surface resistance will decrease with shorter mean free paths in the dirty limit ($\ell \ll \lambda_L$). In the clean limit ($\ell \gg \lambda_L$) the surface resistance decreases with longer mean free paths. The turning point between these two regions is heavily dependent on the constant of proportionality chosen.

This behavior is qualitatively similar to the simple model discussed in subsection 6.2.1 and explains experimental results in which cavities constructed of niobium sputtered on copper (with much lower mean free paths and thus also lower mean spacing between pinning centers) showed less sensitivity to trapped ambient magnetic field than cavities made of bulk high RRR niobium (with higher mean free paths) [Wei95]. The overall shape of the curve is also similar to that given in Figure 6.4, however the sensitivity of residual resistance to trapped flux in the intermediate mean free path regime is predicted to be

significantly higher in the Gurevich theory. Equations 6.4 and 6.8 take on the form

$$R_{\text{res,B}} = F(\omega, \text{material properties}) \times B_{\text{trapped}}, \tag{6.10}$$

where F is a function of material properties and is independent of the amount of magnetic field trapped. It is therefore useful to normalize the residual resistance obtained from a given amount of trapped magnetic flux by defining the sensitivity of residual resistance to trapped magnetic flux as $R_{\text{res,B}}/B_{\text{trapped}}$. This parameter will be used often in the rest of this chapter to characterize the amount of additional residual resistance a cavity will gain for a given amount of trapped magnetic flux. It is important to note that according to Gurevich's theory, the only material properties F is dependent on are mean free path, the clean values of penetration depth and coherence length, and the mean spacing between pinning centers.

6.3 Impact of Cool Down Dynamics on Magnetic Flux Trapping

As was mentioned in Chapter 4, cavities generally performed worse after cooling slowly than after cooling fast i.e. showed a larger residual resistance [RGMS14a]. Furthermore, this effect was strongest in nitrogen-doped cavities compared with cavities prepared with standard methods (EP+120°C bake). A significant amount of work at various labs around the world has been devoted to studying and understanding this phenomenon.

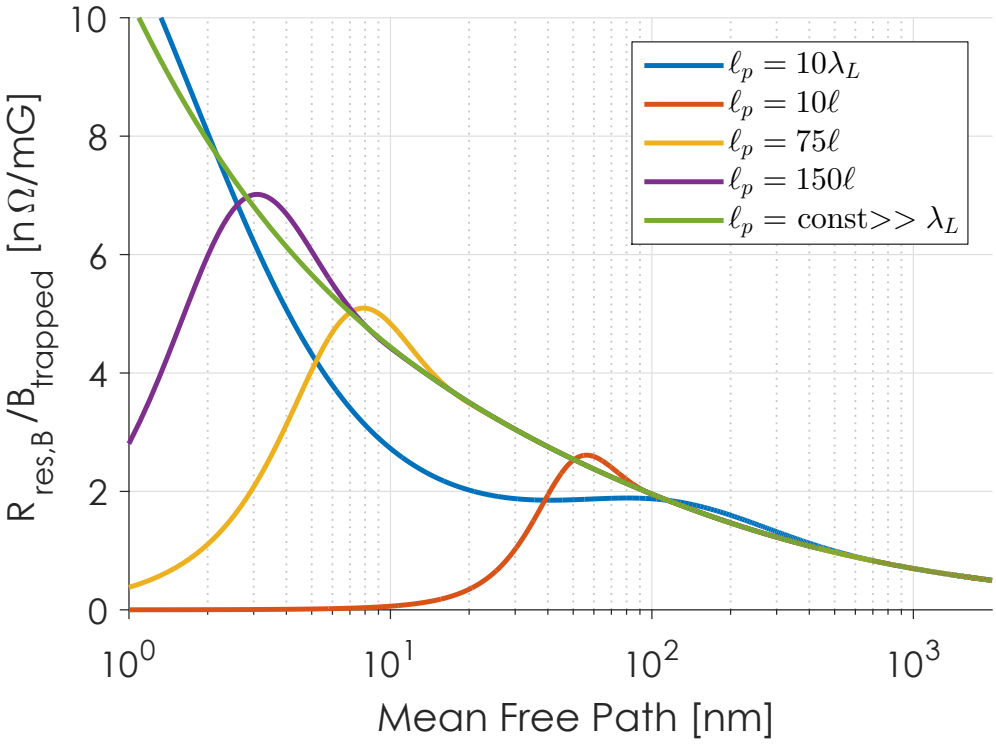

Figure 6.7: The residual resistance from trapped flux, normalized to the amount of trapped flux, versus mean free path for different interpretations of the mean spacing between pinning sites in Gurevich's theory of vortex oscillations. In blue ℓ_p a constant on the order of the penetration depth, in green ℓ_p a constant much longer than the penetration depth, and in purple, yellow, and red is ℓ_p proportional to the mean free path with different constants of proportionality. This assumes f = 1.3 GHz, ξ_0 = 38 nm, and λ_L = 39 nm.

6.3.1 Work at Fermilab

At FNAL, Romanenko et. al. assembled a single-cell cavity surrounded by a Helmholtz coil to apply a uniform external magnetic field parallel to the cavity axis. They placed temperature sensors on the two irises and the equator to measure cool down rates and gradients and fluxgate magnetometers at the equator to measure the magnetic field. It was found that in fields as high as 190 mG, high Q_0 could still be reached in some cases by optimizing the cool down con-

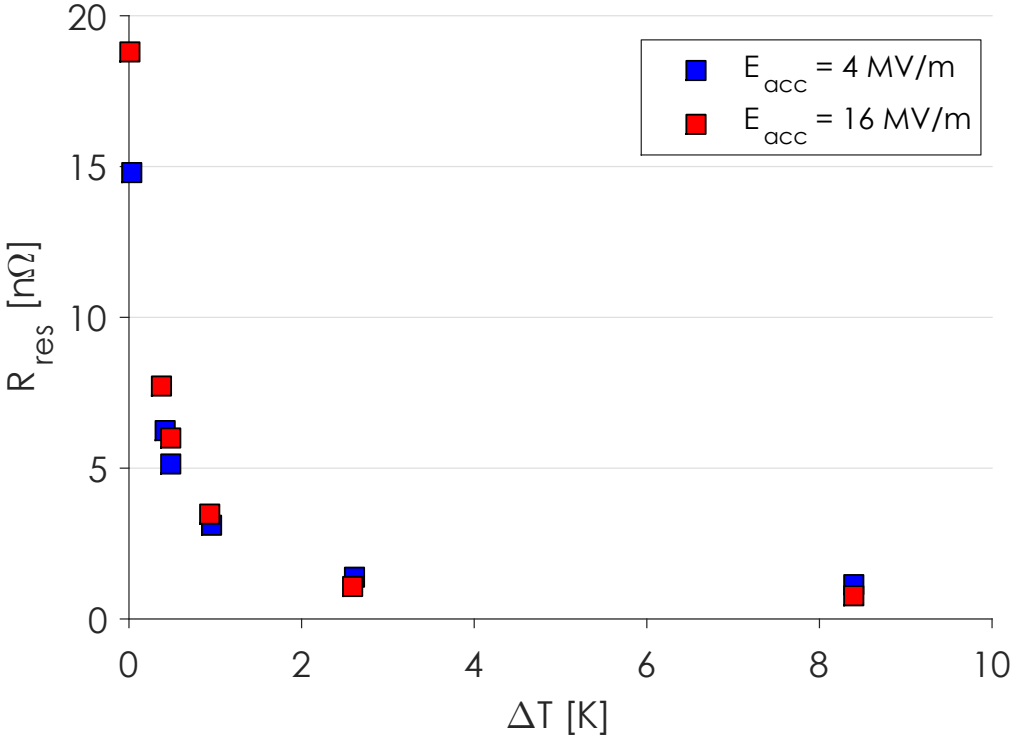

Figure 6.8: R_{res} versus temperature gradient over a 1.3 GHz TESLA shaped nitrogen-doped single-cell cavity cooled in a constant applied magnetic field at FNAL. Larger spatial temperature gradients lead to more efficient flux expulsion and thus lower residual resistance. ΔT is the spatial temperature gradient between the cavity irises. Data courtesy of FNAL [RGC+14].

ditions. Specifically, larger spatial temperature gradients led to lower residual resistance as seen in Figure 6.8. This behavior was attributed to large spatial temperature gradients leading to more efficient flux expulsion - better flux expulsion means less trapped flux and thus less residual resistance from trapped flux. This is consistent with earlier measurements that suggested that fast cool down rates led to better flux expulsion [RGMS14a, GL14a]. Typically faster cool downs carry with them larger spatial temperature gradients. It is difficult to decouple the two effects.

Furthermore, Posen continued specific flux expulsion measurements at

FNAL to measure how flux expulsion depended on cavity preparation [Pos15a]. By using a setup similar to Romanenko's mentioned above, the ratio of superconducting to normal conducting magnetic field at the surface was found as a function of spatial temperature gradient during cool down. As some magnetic flux is expelled, the magnetic field lines around the cavity will be distorted (see Figure 2.1). This can be observed on a fluxgate magnetometer located at the cavity surface as the reading of magnetic field will change after the cavity becomes superconducting. A simple model [RGMS14a] predicts that at the equator, full flux expulsion would lead to a ratio $B_{SC}/B_{NC} = 1.8$. At 100% flux trapping, this ratio is 1 (as the field is not perturbed). Posen found that the surface preparation of cavities did not have an impact on the efficiency of flux expulsion. Rather he found that the bulk material properties were far more important. Figure 6.9 shows this ratio as a function of spatial temperature gradient during cool down for three different cavities. For all of the cavities, it is clear that larger spatial temperature gradient leads to a higher B_{SC}/B_{NC}, and thus better flux expulsion. Additionally, the fine grain cavities (in blue and green) showed significantly worse flux expulsion than the large grain cavity (in red). In fact, the fine grain cavities never reached 100% flux expulsion even with very large temperature gradients of $<$20 K. Lastly, it was found that heat treatment of a fine grain cavity at 1000°C for 4 hours dramatically improved the cavity's flux expulsion (green compared with red). High temperature heat treatment typically is associated with grain growth in niobium. It is likely that large grains lead to more efficient flux expulsion.

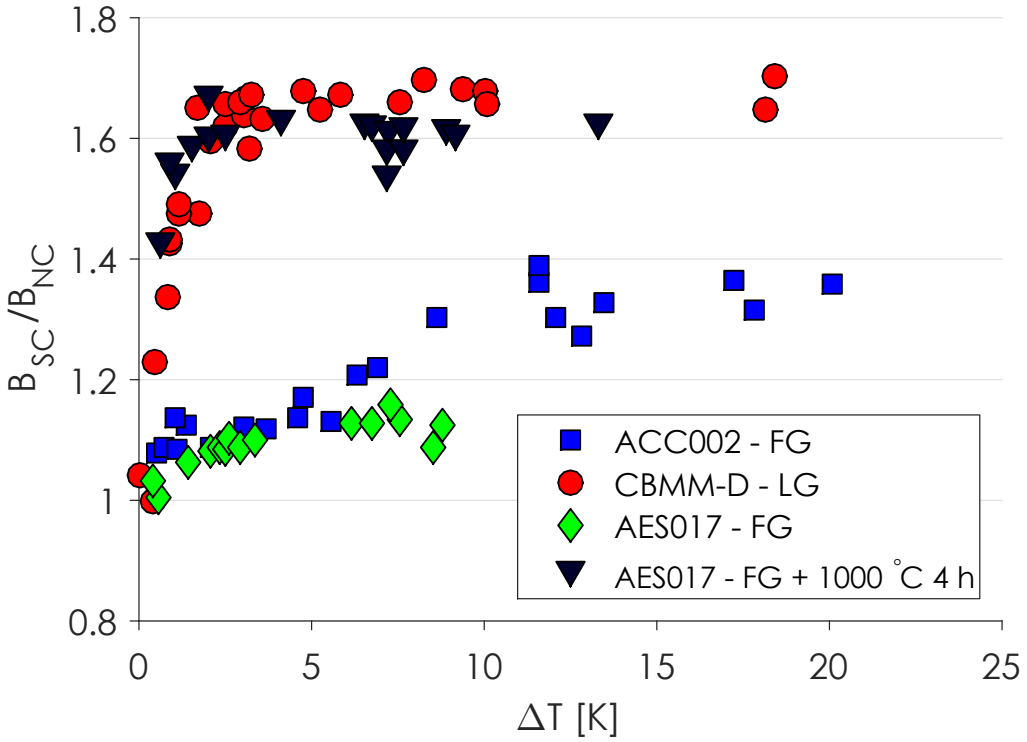

Figure 6.9: Ratio of superconducting to normal conducting reading on the fluxgate magnetometers versus temperature gradient during cool down at FNAL. Fine grain cavities showed poor flux expulsion while large grains showed better. A fine grain 1.3 GHz cavity's expulsion improved after a high temperature heat treatment at 1000°C for four hours. ΔT is the spatial temperature gradient across the cell. Data courtesy of FNAL [Pos15a].

6.3.2 Work at Cornell

Similar measurements to the ones discussed in subsection 6.3.1 were conducted at Cornell. A single-cell cavity's flux expelling efficiency was first measured after 800°C heat treatment and then remeasured after an additional 3 hours at 900°C. These results are shown in Figure 6.10. The cavity showed poor flux expulsion after the 800°C heat treatment, never reaching 100% expulsion even at large temperature gradients. After 3 hours at 900°C, flux expulsion improved dramatically, reaching 100% expulsion with relatively small gradients of ~4 K

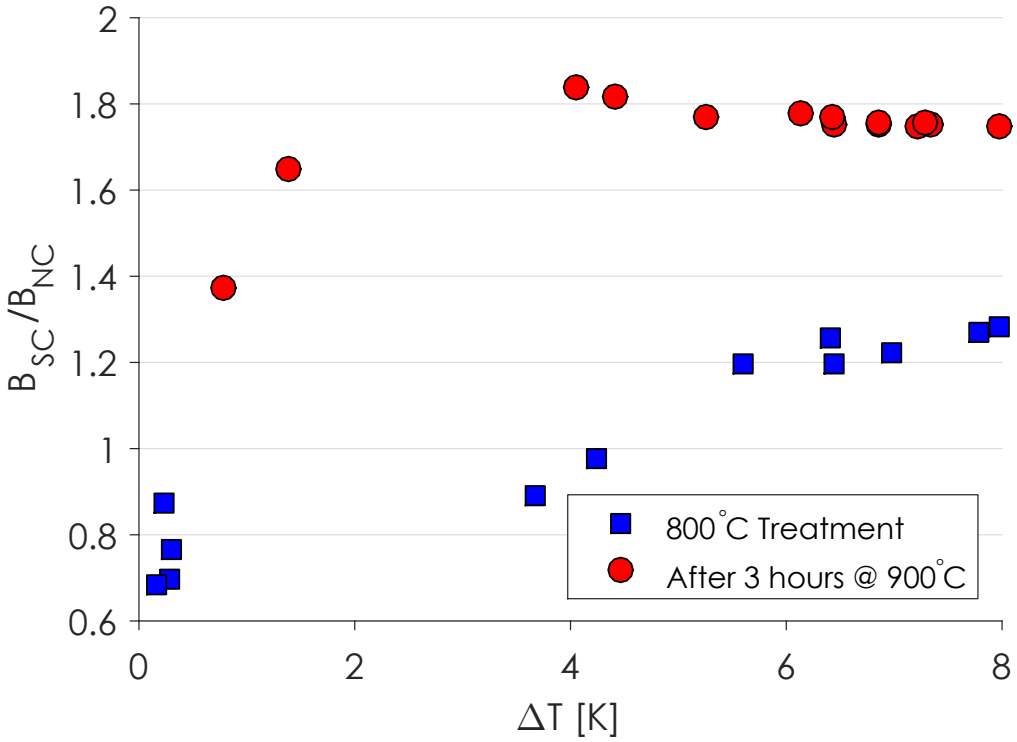

Figure 6.10: Ratio of superconducting to normal conducting reading on the fluxgate magnetometers versus temperature gradient during cool down at Cornell on a 1.3 GHz fine grain cavity. Larger temperature gradients led to better flux expulsion. Flux expulsion improved after heat treatment for 3 hours at 900°C. ΔT is the spatial temperature gradient across the cell.

across the cavity cell.

Additionally, flux expulsion measurements were carried out in the Cornell Horizontal Test Cyromodule (HTC) on a 9-Cell nitrogen-doped cavity (the full details of these measurements will be discussed in Chapter 8). A solenoid was placed around the 9-cell cavity to apply a magnetic field parallel to the cavity axis. In a field of 20 mG, the cavity was cooled five times with different vertical spatial temperature gradients. These results can be seen in Figure 6.11. It is clear that larger temperature gradients lead to lower residual resistance, most likely due to more efficient flux expulsion and less trapped magnetic flux. These

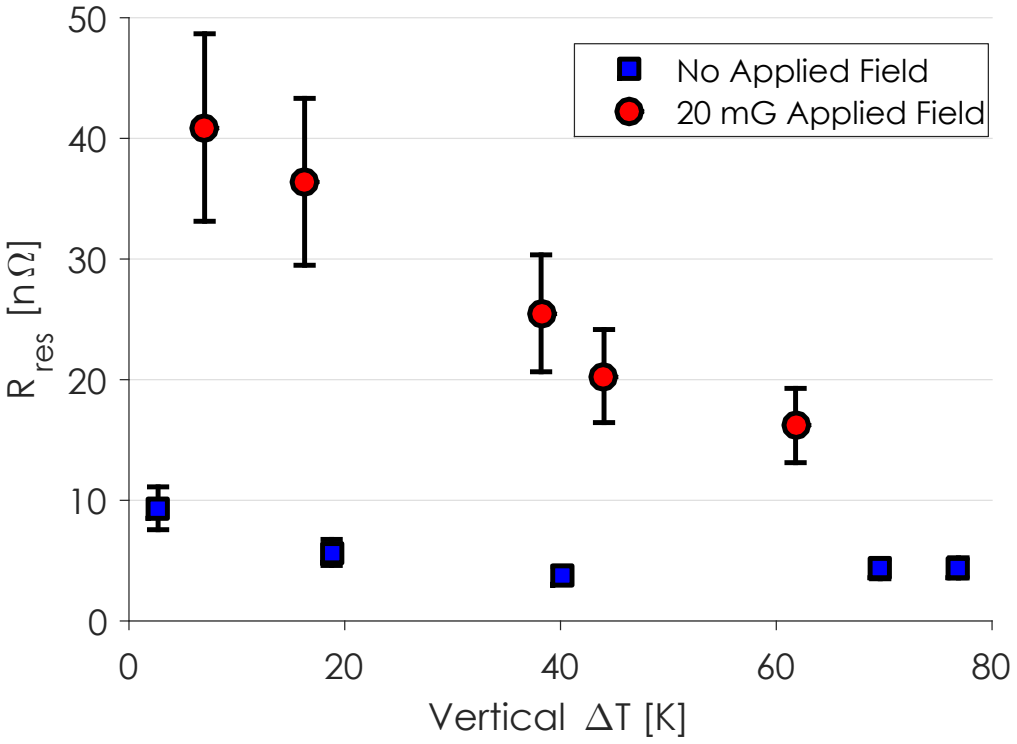

Figure 6.11: R_{res} versus vertical spatial temperature gradient in the Cornell HTC on a 1.3 GHz nitrogen-doped 9-cell cavity. Vertical ΔT is the spatial temperature gradient between the bottom and top of the cell when the cavity is in the horizontal orientation. Larger ΔT led to better flux expulsion and lower residual resistance.

measurements are consistent with measurements on single-cell cavities both at Cornell and at FNAL.

6.3.3 Theoretical Work on Flux Expulsion at KEK

Kubo developed a theoretical model for flux trapping and its dependence on the spatial temperature gradient based on Ginzburg-Landau theory [Kub15]. If one looks at the superconducting boundary (where $T \leq T_c$), the region surrounding the boundary will have strongly suppressed critical fields B_{c1} and B_{c2}. Because

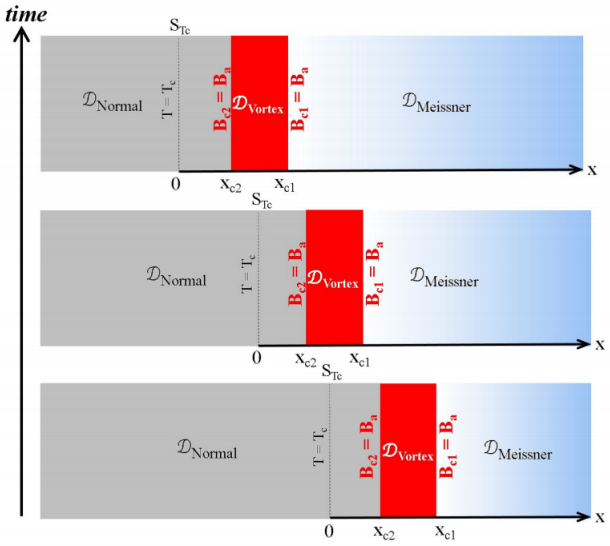

Figure 6.12: Schematic view of a material during transition between the normal and superconducting states from [Kub15]. Three regions exist: the normal conducting state ($B_a \geq B_{c2}$), the vortex state ($B_{c1} \leq B_a < B_{c2}$), and the meissner state ($B_a \leq B_{c1}$)

of this suppression, the critical fields may be on the same order or less than the ambient field B_a. This leads to three distinct regions with x the position variable along the temperature gradient (as seen in Figure 6.12):

1. $\mathcal{D}_{\text{Normal}}$: $x \leq x_{c2}$
2. $\mathcal{D}_{\text{Vortex}}$: $x_{c2} < x \leq x_{c1}$
3. $\mathcal{D}_{\text{Meissner}}$: $x > x_{c1}$

These regions represent the normal conducting state ($B_a > B_{c2}$), the vortex state ($B_{c1} \leq B_a \leq B_{c2}$), and the meissner state ($B_a < B_{c1}$). The boundaries between these regions, x_{c2} and x_{c1}, are the positions where the applied field is equal to the critical fields respectively ($B_{c2}(x = x_{c2}) = B_a$ and $B_{c1}(x = x_{c1}) = B_a$). S_{T_c} represents the boundary where $T = T_c$.

Now following the derivation presented in [Kub15] and starting with GL theory, define

$$t \equiv \frac{T}{T_c}. \tag{6.11}$$

The coherence length is temperature dependent as

$$\xi(T) \equiv \xi^*(1-t)^{-\frac{1}{2}}, \tag{6.12}$$

with $\xi^* \equiv \sqrt{\gamma\hbar^2/|\alpha_0|}$, related to the coherence length from BCS theory, $\xi_{\text{BCS}} = \hbar v_F/\pi\Delta(0)$ and the penetration depth

$$\lambda(T) = \frac{\lambda^*}{\sqrt{1-t}}, \tag{6.13}$$

with $\lambda^* = \sqrt{\beta/8\mu_0 e^2\gamma|\alpha_0|}$. α_0, γ, and β are constants derived from BCS theory. This leads to the Ginzburg-Landau parameters

$$\kappa = \frac{\lambda(T)}{\xi(T)} = \frac{\lambda^*}{\xi^*}, \tag{6.14}$$

which is temperature independent. The upper critical field then can be written as

$$B_{c2}(T) = \frac{\phi_0}{2\pi\xi(T)^2} = \frac{\phi_0}{2\pi\xi^{*2}}(1-t). \tag{6.15}$$

The thermodynamic critical field then can be written as

$$B_c(T) = \frac{B_{c2}(T)}{\sqrt{2}\kappa} = \frac{\phi_0}{2\sqrt{2}\pi\kappa\xi^{*2}}(1-t). \tag{6.16}$$

In the dirty limit (when $\kappa \gg 1$) the lower critical field is

$$B_{c1}(T) = \frac{\ln\kappa + a}{\sqrt{2}\kappa}B_c(T) = \frac{\phi_0(\ln\kappa + a)}{4\pi\kappa^2\xi^{*2}}(1-t), \tag{6.17}$$

with $a \approx 0.5$. The remaining derivation is true in the dirty limit.

These critical fields as functions of temperature can be converted into functions of position using the temperature distribution

$$T(x) = T_c + \frac{dT}{dx}x = T_c\left(1 - \left|\frac{dt}{dx}\right|x\right). \tag{6.18}$$

Then the coherence length can be rewritten

$$\xi(T(x)) = \frac{\xi^*}{\sqrt{x}} \left| \frac{dt}{dx} \right|^{-\frac{1}{2}}. \tag{6.19}$$

leading to the position dependent critical fields

$$B_{c2}(T(x)) = \frac{\phi_0}{2\pi\xi^{*2}} \left| \frac{dt}{dx} \right| x, \tag{6.20}$$

$$B_{c1}(T(x)) = \frac{\phi_0 \left(\ln\kappa + a\right)}{4\pi\kappa^2\xi^{*2}} \left| \frac{dt}{dx} \right|^{-1}. \tag{6.21}$$

The positions of the phase fronts, x_{c2} and x_{c1} are the positions at which the applied field is equal to the two critical fields, respectively. Thus

$$x_{c2} = 2\pi\xi^{*2} \frac{B_a}{\phi_0} \left| \frac{dt}{dx} \right|, \tag{6.22}$$

$$x_{c1} = \frac{4\pi\kappa^2\xi^{*2}}{\ln\kappa + a} \frac{B_a}{\phi_0} \left| \frac{dt}{dx} \right|. \tag{6.23}$$

This coordinate system moves with the boundary of S_{T_c}.

Now consider that the phase transition fronts are at rest but the pinning centers move and collide with the vortices. This system can then be thought of as a beam-target collision with a reaction cross section σ. Since pinning centers and vortices have an effective radii ξ, and ξ is a maximum at x_{c2}, it can be assumed that the reactions between pinning centers and vortices occur mostly near $x = x_{c2}$. Then

$$\sigma \propto \xi(x_{c2})^2, \tag{6.24}$$

with

$$\xi(x_{c2}) = \frac{\xi^*}{\sqrt{x_{c2}}} \left| \frac{dt}{dx} \right|_{x=\bar{x}}^{-\frac{1}{2}} = \frac{1}{\sqrt{2\pi}} \sqrt{\frac{\phi_0}{B_a}}. \tag{6.25}$$

From this one can compute the number of vortices in the vortex domain, $\mathcal{D}_{\text{vortex}}$,

$$N_\phi^{(\delta x)} \propto \frac{B_a}{\phi_0} \Delta L_y \delta x, \tag{6.26}$$

where B_a/ϕ_0 is the density of vortex cores, ΔL_y is the thickness of the material, and δx is the thickness of $\mathcal{D}_{\text{vortex}}$ given by

$$\delta x \equiv x_{c1} - x_{c2} = 4\pi\xi^{*2} f_n(\kappa) \frac{B_a}{\phi_0} \left|\frac{dt}{dx}\right|^{-1}, \tag{6.27}$$

and

$$f_n(\kappa) \equiv \frac{\kappa^2}{\ln\kappa + a} - \frac{1}{2}. \tag{6.28}$$

Equation 6.27 and Equation 6.26 predict as $\left|\frac{dt}{dx}\right|$ increases, δx decreases and thus so does $N_\phi^{(\delta x)}$.

By introducing the total cross section $\Sigma = \sigma N_\phi^{(\delta x)}$, the reaction probability is given by $P = \Sigma/\Delta L_y \Delta L_z$ with ΔL_z the height of the material. Then the number of events is

$$N_{\text{event}} = (\rho_{\text{pin}} \Delta L_x \Delta L_y \Delta L_z) P = \rho_{\text{pin}} \Delta L_x \sigma N_\phi^{(\delta x)}, \tag{6.29}$$

with ρ_{pin} is the density of pinning centers that have strong enough pinning forces to pin vortices. Since the number of trapped vortices is proportional to N_{event},

$$N_{\text{trap}} \propto \rho_{\text{pin}} \Delta L_x \sigma N_\phi^{(\delta x)} \propto B_a \left|\frac{dt}{dx}\right|^{-1}. \tag{6.30}$$

This means that the number of trapped vortices is proportional to the applied magnetic field, B_a (which one would expect) and is inversely proportional to the temperature gradient.

Following the derivation in subsection 6.2.1, the additional residual resistance can be calculated and found to be

$$R_{\text{res}} \propto N_{\text{trap}} \propto B_a \left|\frac{dt}{dx}\right|^{-1}. \tag{6.31}$$

6.3.4 Comparison of Theoretical Work with Experiment

The Kubo model has good agreement with the flux expulsion data from FNAL [RGC+14] as shown in Figure 6.13a. There is however poor agreement with the data from the Cornell HTC as shown in Figure 6.13b. The disagreement between the theory and the Cornell HTC data highlights two significant limitations of the model:

1. Due to the $1/\Delta T$ dependence, the model predicts that as $\Delta T \rightarrow 0$, $R_{\text{res}} \rightarrow \infty$ which clearly is not realistic. This is because the model does not require that $N_{trap} \leq N_{\phi}$, i.e. that a maximum of 100% of the flux lines can be trapped.
2. The model does not predict that in some cavities very large ΔT does not result in full flux expulsion.

This second point is addressed in Figure 6.13b, in which an additional offset is added to the model to allow for a finite amount of flux to be that is always trapped (pinned), leading to better agreement with the experimental data.

6.4 Cavities Prepared and Tested at Cornell

In order to measure how cavity preparation and material properties affect $R_{\text{res,B}}/B_{\text{trapped}}$, ten SRF cavity preparations were completed on six individual cavities to vary the mean free path of the RF penetration layer. Nitrogen-doping provides a powerful tool for tuning the mean free path of the material. The construction of five of the six cavities was described in depth in Chapter 4. The sixth

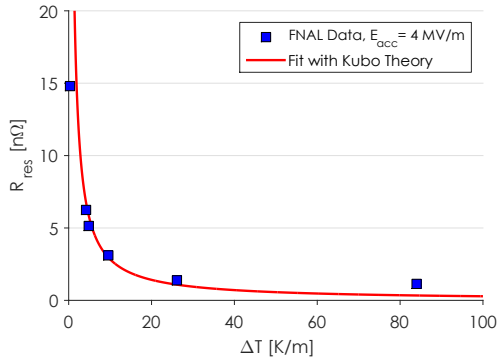

(a) Comparison of FNAL data from Figure 6.8 with the Kubo theory. There is good agreement in all regions.

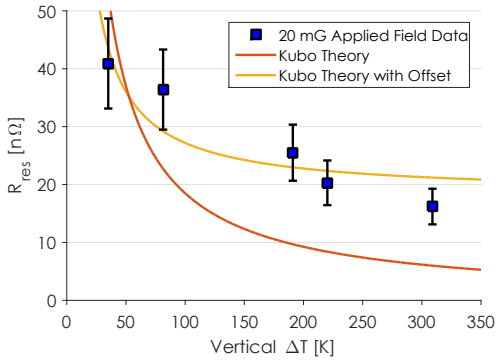

(b) Comparison of data from the Cornell HTC9-3 test as shown in Figure 6.11 with the Kubo theory. There is poor agreement unless an offset is assumed in the model, i.e. that there is a certain amount of flux that cannot be expelled.

Figure 6.13: Comparison of the Kubo theory with data from FNAL and Cornell.

cavity was fabricated by Niowave. All six were 1.3 GHz single-cell Tesla shaped cavities [ABB+00]. Six of the cavity preparations consisted of the same nitrogen-doping at 800°C followed by a different amount of final vertical electropolishing (VEP) between 6 and 40 μm. Two of these five cavities (LT1-2 and LT1-3) had their surfaces reset and were prepared with nitrogen-doping at 900°C and 990°C, respectively, to increase their doping level. As was discussed in Chapter 5, the doping is effectively constant over the RF penetration layer. The ninth and tenth preparations were standard cavity preparations: Bulk vertical electropolish (VEP) and VEP+48 hour 120°C bake, both carried out on the Niowave cavity, NR1-3. The exact details of all of these preparations are summarized in Table 6.1.

For each cavity preparation, the cavity was cooled in at least three separate cool downs leading to different amounts of trapped magnetic flux. The amount of trapped flux obtained was tuned via the applied magnetic field and the cool

Cavity Name	Preparation	T_c [K]	Δ/k_BT_c	Mean Free Path [nm]	$R_{\text{res,B}}/B_{\text{trapped}}$ [nΩ/mG]
LT1-3	990°C N-Doping[1]+ 5 μm VEP	9.1 ± 0.1	2.05 ± 0.01	4 ± 1	3.2 ± 0.5
LT1-2	900°C N-Doping[2]+ 18 μm VEP	9.1 ± 0.1	2.00 ± 0.01	6 ± 1	4.7 ± 0.6
LT1-2	800°C N-Doping[3]+ 6 μm VEP	9.3 ± 0.1	1.88 ± 0.01	19 ± 6	3.7 ± 0.9
LT1-3	800°C N-Doping[3]+ 12 μm VEP	9.3 ± 0.1	1.91 ± 0.01	34 ± 10	3.1 ± 0.5
LT1-1	800°C N-Doping[3]+ 18 μm VEP	9.3 ± 0.1	1.88 ± 0.01	39 ± 12	2.5 ± 0.6
LT1-4	800°C N-Doping[3]+ 24 μm VEP	9.2 ± 0.1	1.89 ± 0.01	47 ± 14	2.2 ± 0.2
LT1-5	800°C N-Doping[3]+ 30 μm VEP	9.2 ± 0.1	1.88 ± 0.01	60 ± 18	1.87 ± 0.08
LT1-5	800°C N-Doping[3]+ 40 μm VEP	9.2 ± 0.1	1.94 ± 0.01	213 ± 64	1.06 ± 0.02
NR1-3	100 μm VEP[4]	9.2 ± 0.1	1.81 ± 0.01	800 ± 100	0.6 ± 0.1
NR1-3	100 μm VEP[4]+ 48 hour 120°C Bake	9.2 ± 0.1	1.96 ± 0.01	120 ± 36[5]	0.88 ± 0.07

[1] 100 μm VEP, 800°C in vacuum for 3 hours, 990°C in 30 mTorr of N_2 for 5 minutes.
[2] 100 μm VEP, 800°C in vacuum for 3 hours, 900°C in 60 mTorr of N_2 for 20 minutes, 900°C in vacuum for 30 minutes.
[3] 100 μm VEP, 800°C in vacuum for 3 hours, 800°C in 60 mTorr of N_2 for 20 minutes, 800°C in vacuum for 30 minutes.
[4] After bulk VEP, cavities received an 800°C heat treatment in vacuum for three hours.
[5] The 48 hour 120°C bake has been shown to affect only the mean free path in a fraction of the RF penetration layer, especially at temperatures near the critical temperature [RGB+14]. Because our method of mean free path extraction averages over this entire layer, the exact mean free path value is difficult to extract.

Table 6.1: Extracted Properties of Cavities Tested

down rate/gradient (experimental apparatus described in the next section). For each cool down, Q_0 versus temperature was measured at low fields (2-4 MV/m) between 1.6 and 4.2 K. Additionally for each preparation, resonance frequency versus temperature was measured. From these sets of data, material properties (mean free path, T_c, $\Delta/k_B T_c$) along with R_{res} could be extracted using the method described in section 3.4. These material properties are also summarized in Table 6.1

6.5 Experimental Apparatus to Measure Effect of Ambient Magnetic Field on Residual Resistance

A Helmholtz coil was used to apply a uniform magnetic field parallel to the cavity axis. A fluxgate magnetometer located at the iris of the cavity and parallel to the applied magnetic field was used to measure both applied field and trapped magnetic flux. Three cernox temperature sensors were used to measure temperature cooling rates and spatial gradients during the cool downs. A picture of the experimental setup is shown in Figure 6.14. A typical cool down is shown in Figure 6.15. First the cavity is above its critical temperature, T_c, with the coil off (in a very small ambient magnetic field B_{amb}). Then the coil is turned on to generate a DC magnetic field which is much larger than the ambient magnetic field and the cavity is cooled. When the cavity transitions to the superconducting state, there is a small jump in the measured magnetic field as some flux is expelled. After cooling, the coil is turned off and the magnetic field drops to B_{left}, a value significantly higher than the initial ambient field B_{amb}. The

difference between B_{left} and B_{amb} is the amount of trapped flux:

$$B_{trapped} = B_{left} - B_{amb}. \tag{6.32}$$

The trapped flux is the amount of magnetic field that is not expelled when the material becomes superconducting. The exact fraction of applied external magnetic field trapped depends strongly on the cool down mechanics: larger spatial temperature gradients giving less flux trapping, as discussed in the previous sections.

6.6 Residual Resistance vs Trapped Magnetic Flux

For each cavity the residual resistance at low RF field (< 5 MV/m) was found as a function of the trapped flux. Figure 6.16 shows R_{res} versus trapped flux for all ten cavity preparations along with linear fits to the data. It is clear that R_{res} increases linearly with trapped flux which is consistent with the theoretical predictions in section 6.2 (see Equation 6.4 and Equation 6.8) since each additional flux line should provide a quantized amount of additional resistance and doubling the trapped magnetic flux doubles the number of trapped vortices. It is also clear that there is a large spread in the slopes for the ten cavity preparations. The slope of the linear fits is defined as the sensitivity of residual resistance to trapped magnetic flux, $R_{\text{res,B}}/B_{\text{trapped}}$,

$$R_{\text{res,B}}/B_{\text{trapped}} \equiv \frac{dR_{res}}{dB_{trapped}}. \tag{6.33}$$

In addition to the extracted penetration layer material properties, $R_{\text{res,B}}/B_{\text{trapped}}$ for each cavity preparation is summarized in Table 6.1.

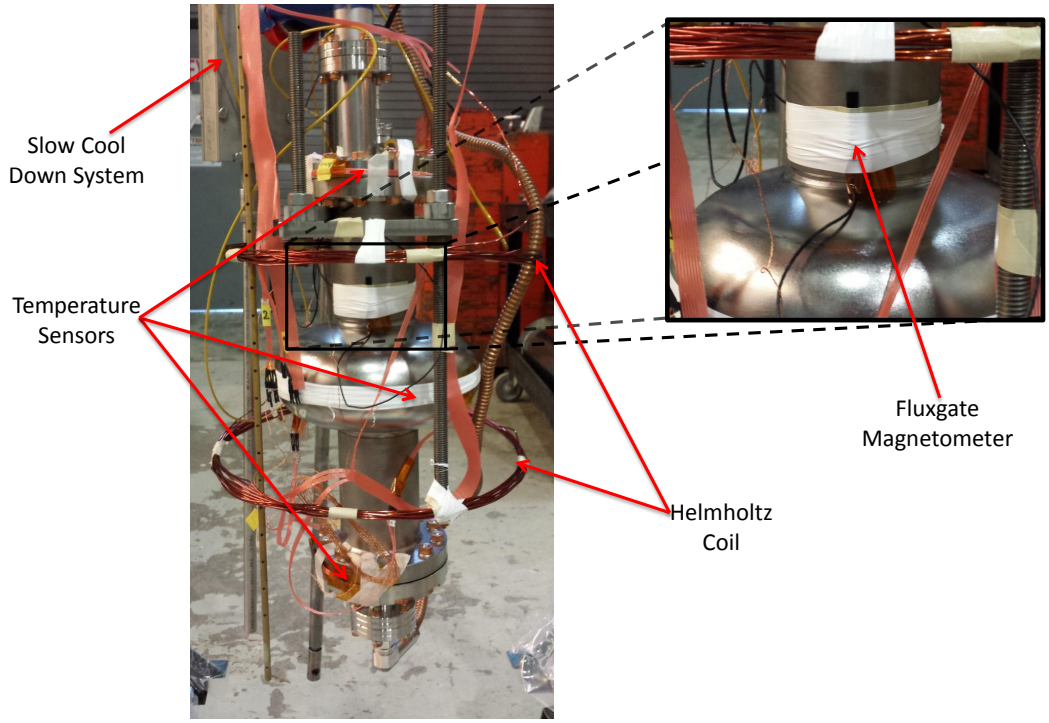

Figure 6.14: Experimental setup to measure the effects of ambient magnetic field on cavity performance. A single-cell cavity is surrounded by a Helmholtz coil to apply a uniform external magnetic field parallel to the cavity's axis. Three cernox temperature sensors are placed on the equator and each cavity flange to measure cool down rates and gradients during cool down. A fluxgate magnetometer is placed at the iris to measure applied magnetic fields and trapped magnetic flux. A slow cool down system is used to control the rate of cool down.

Figure 6.17 shows R_{res} versus trapped flux for three specific cavity preparations: a heavy doping at 900°C, a light doping at 800°C, and the EP+120°C preparation. Stronger doping may lead to a higher slope and thus a larger $R_{res,B}/B_{trapped}$. Additionally, even the lightly doped cavity yielded a $R_{res,B}/B_{trapped}$ larger than the EP+120°C cavity. The nitrogen doped cavities had $R_{res,B}/B_{trapped}$'s in the range of 2-5 times higher than the EP+120°C cavity depending on the doping strength. This is a critical discovery with major implications for future

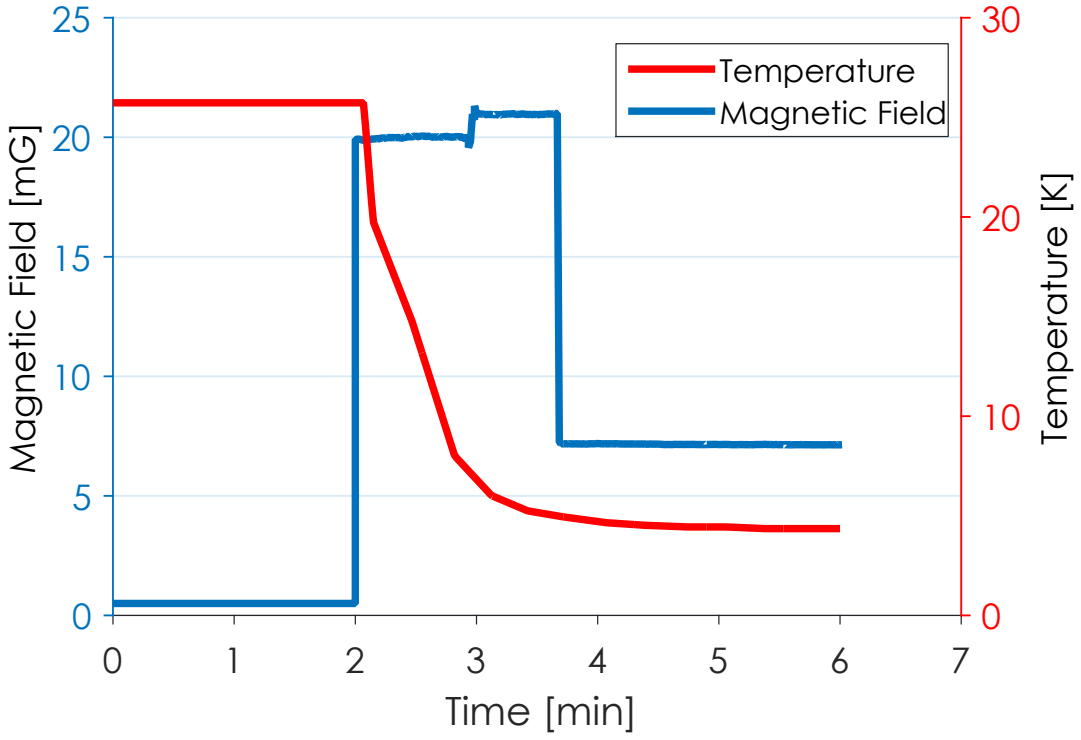

Figure 6.15: A typical cool down. The cavity is sitting at 25 K with the coil off. The ambient magnetic field $B_{amb} \approx 1$ mG. The coil is turned on to 20 mG and cooling begins. As the cavity passes through T_c, there is a bump on the fluxgate reading as some of the magnetic field is expelled. After cooling the coil is turned off and the fluxgate reading drops to the amount of trapped magnetic flux, $B_{trapped}$.

machines such as LCLS-II which plan to employ high Q_0 nitrogen-doped cavities.

From Table 6.1 and discussions in Chapter 5, it can be seen that nitrogen-doping gives significantly smaller mean free paths than the undoped VEP preparation. It is important to note that in the case of the VEP+120°C bake cavity, the mean free path extracted will not be accurate. This is due to the 120°C baking only affecting a small fraction of the RF penetration layer [RGB+14]. Our method for extracting mean free path effectively averages over the whole penetration depth. This issue is not present in the VEP only and nitrogen-doped

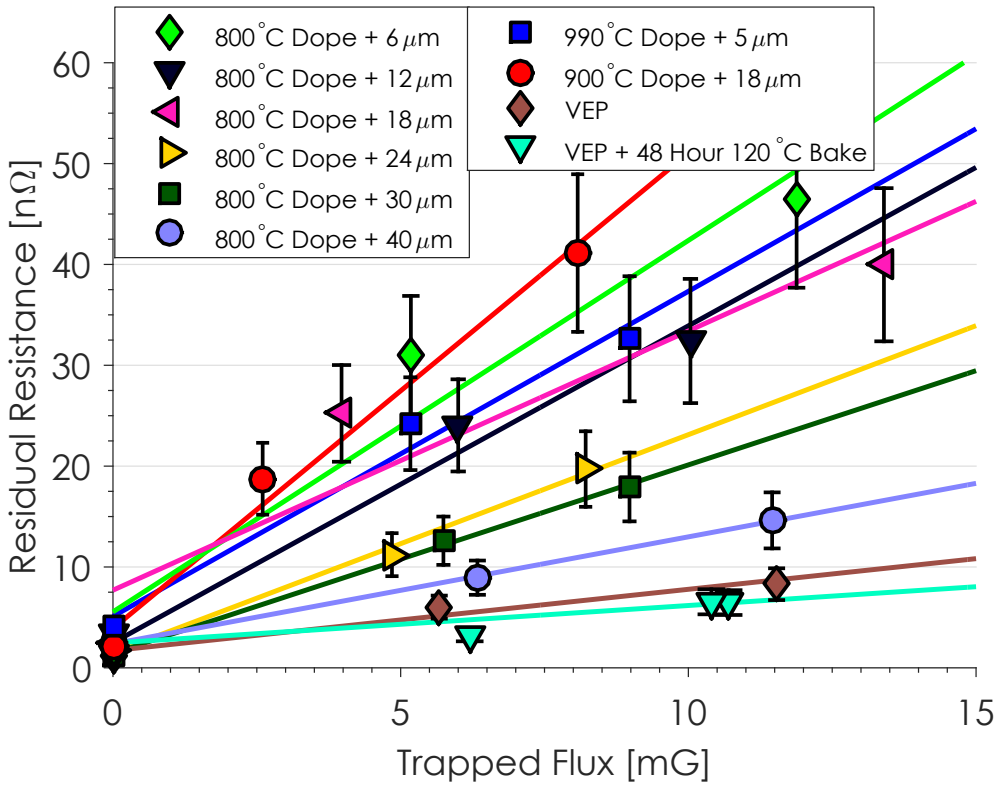

Figure 6.16: R_{res} versus trapped magnetic flux for all ten 1.3 GHz cavity preparations listed in Table 6.1. R_{res} increases linearly with trapped flux. There is a large spread in the slopes suggesting that different material preparations lead to different sensitivities of residual resistance to trapped magnetic flux.

cavities however since their surface layer is very uniform over several microns. The lowering of the mean free path in the doped preparations shows that the doping causes the niobium to become "dirtier." This change is consistent with SIMS measurements on nitrogen-doped samples (see subsection 5.2.2). We also see that for the same nitrogen-doping protocol (cavities doped at 800°C), more material removal increases the mean free path of the material since the nitrogen-doping level decreases.

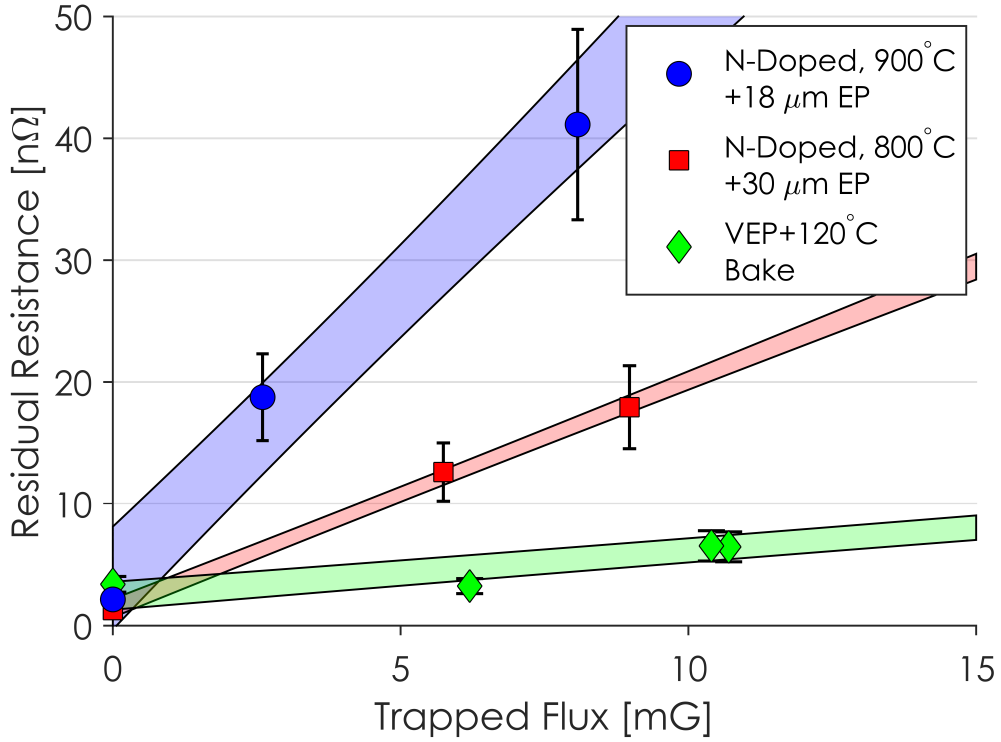

Figure 6.17: R_{res} versus trapped magnetic flux for three specific 1.3 GHz cavity preparations: a heavily doped cavity (LT1-2), a lightly doped cavity (LT1-5), and the EP+120°C baked cavity (NR1-3). Stronger doping results in a larger slope.

6.6.1 Field Dependence of R_{res} from Trapped Flux

It is important to understand if additional residual resistance from trapped magnetic flux changes with increasing accelerating field. Figure 6.18a shows a typical R_{res} versus E_{acc} for one of the cavities tested at three different values of trapped magnetic flux, 0, 3, and 7 mG. With no trapped flux, R_{res} was fairly flat in the medium field region (low field Q slope up to 7 MV/m has been attributed to a decreasing R_{res} [Pad09]). Above the low field Q slope region, additional amounts of trapped flux leads to a very weak field dependence. Figure 6.18b shows the change in R_{res} due to trapped flux versus E_{acc} for different amounts of trapped flux. On this scale it can be seen that R_{res} shows a slight increase as

E_{acc} is increased. Fits to this data is also shown assuming the form

$$R_{\text{res,B}} = \left(\frac{R_{\text{res,B}}}{B_{\text{trapped}}}\right) B_{\text{trapped}} + cB_{\text{trapped}}E_{acc}, \tag{6.34}$$

with c constant for all four curves. This suggests that increasing amounts of trapped flux lead to larger R_{res} at higher fields, however this dependence is very weak in nitrogen-doped cavities ($c = 0.015 \frac{\text{n}\Omega\cdot\text{m}}{\text{mG}\cdot\text{MV}}$ in Figure 6.18). This weak dependence on E_{acc} is quantitatively different to the behavior in niobium-coated copper cavities in which a very strong field dependence of residual resistance from trapped magnetic flux was observed [Wei95].

6.7 Sensitivity of Residual Resistance to Trapped Magnetic Flux

From Figure 6.16 and Table 6.1, we can see that all eight nitrogen-doped surfaces had a higher sensitivity of residual resistance to trapped magnetic flux, $R_{\text{res,B}}/B_{\text{trapped}}$, than the VEP and VEP+120°C baked cavities. $R_{\text{res,B}}/B_{\text{trapped}}$ for the VEP preparation is similar to the previously predicted value of 0.3 nΩ/mG as discussed in [VBB+92, PKH98]. For the same amount of trapped flux, a nitrogen-doped cavity will have a higher residual resistance and thus a lower Q_0 at very low temperatures. We also can see that there is a large spread in $R_{\text{res,B}}/B_{\text{trapped}}$ for the nitrogen-doped cavities. Stronger doping leads to larger $R_{\text{res,B}}/B_{\text{trapped}}$ to a certain point, after which $R_{\text{res,B}}/B_{\text{trapped}}$ begins to decrease with even stronger doping.

It is useful to compare the extracted material properties in Table 6.1 with $R_{\text{res,B}}/B_{\text{trapped}}$ to see if a correlation can be found. There is clearly no trend be-

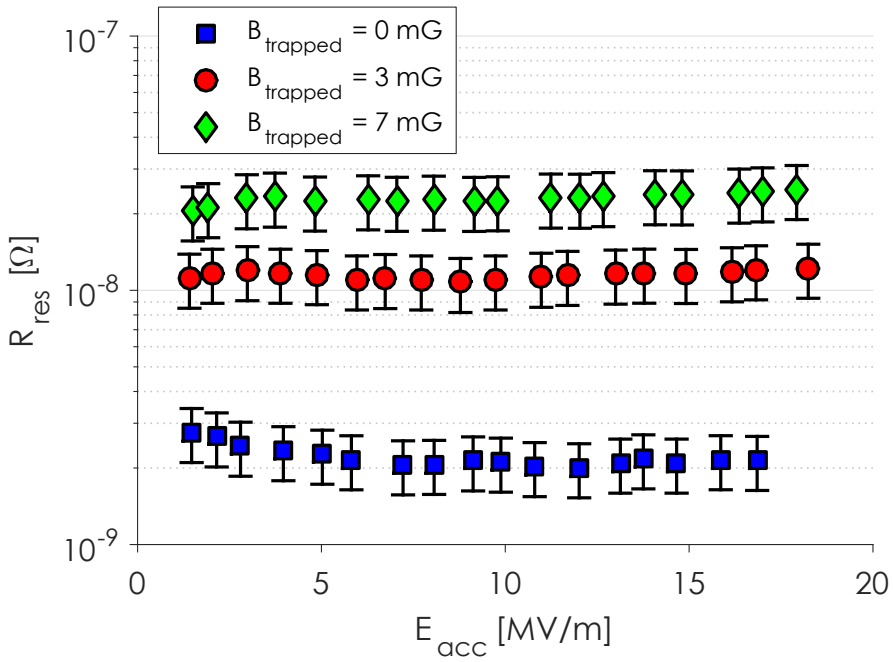

(a) R_{res} versus E_{acc} for one of the 1.3 GHz single-cell cavities tested with different amounts of trapped flux.

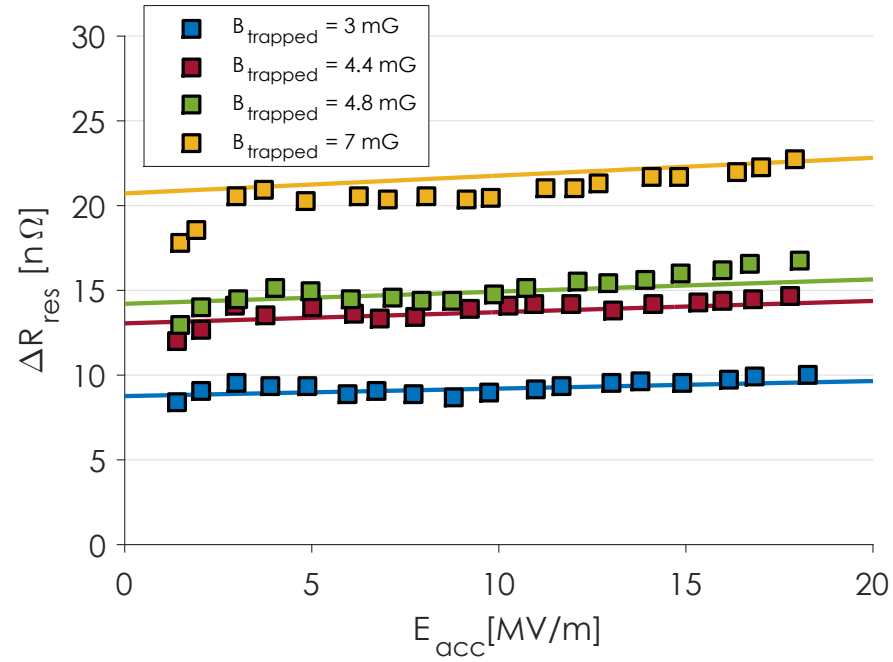

(b) Change in R_{res} from 0 mG trapped versus E_{acc} for different amounts of trapped flux for one of the cavities tested. Above 8 MV/m, there is a small field dependence in which R_{res} increases with increasing E_{acc} as Equation 6.34.

Figure 6.18: Field dependence of R_{res} from trapped flux for one of the 1.3 GHz single-cell cavities tested. A fit to Equation 6.34 is also shown.

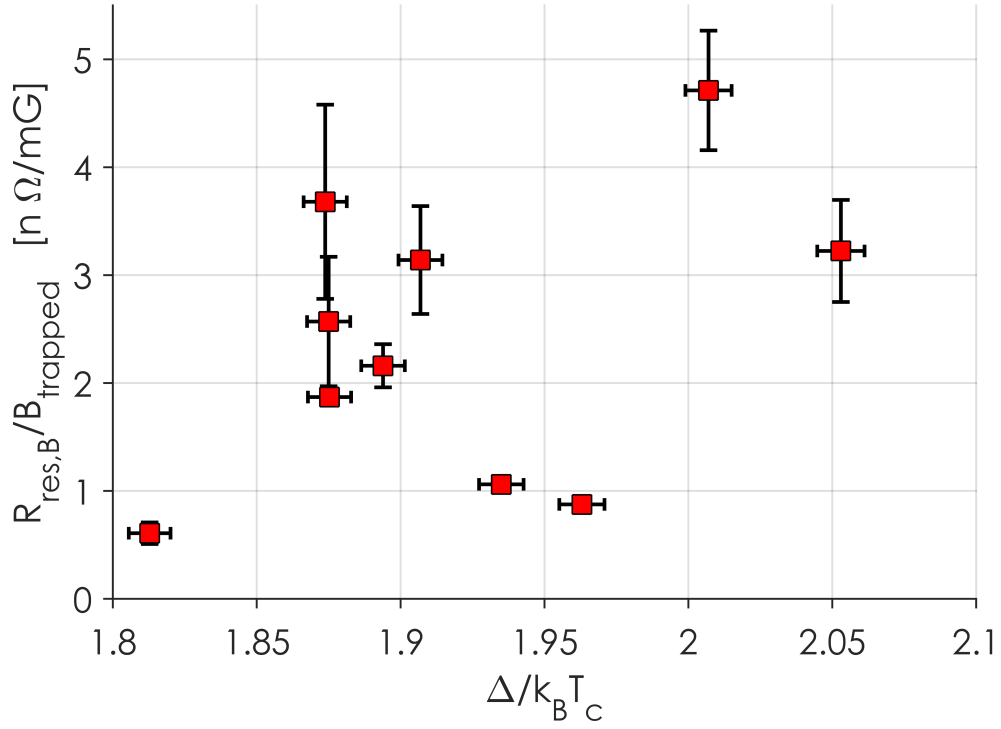

Figure 6.19: $R_{res,B}/B_{trapped}$ versus Δ/k_BT_c for the cavities tested. There is no clear trend between $R_{res,B}/B_{trapped}$ and Δ/k_BT_c suggesting that Δ/k_BT_c does not directly impact $R_{res,B}/B_{trapped}$.

tween T_c and $R_{res,B}/B_{trapped}$. Figure 6.19 shows the sensitivity of residual resistance to trapped magnetic flux, $R_{res,B}/B_{trapped}$ (slope of Figure 6.16), versus energy gap (Δ/k_BT_c) for the ten cavity preparations tested. It is clear that there is no significant correlation between Δ/k_BT_c and $R_{res,B}/B_{trapped}$. This is consistent with the theories presented in section 6.2.

There is however a clear correlation with the mean free paths of the preparations. This makes sense since doping effectively is changing the mean free path of the niobium by baking in impurities which act as scattering sites. Figure 6.20 shows the sensitivity of residual resistance to trapped magnetic flux, $R_{res,B}/B_{trapped}$, versus mean free path for all of the cavity preparations except the VEP+120°C bake cavity. Due to the previously mentioned complications

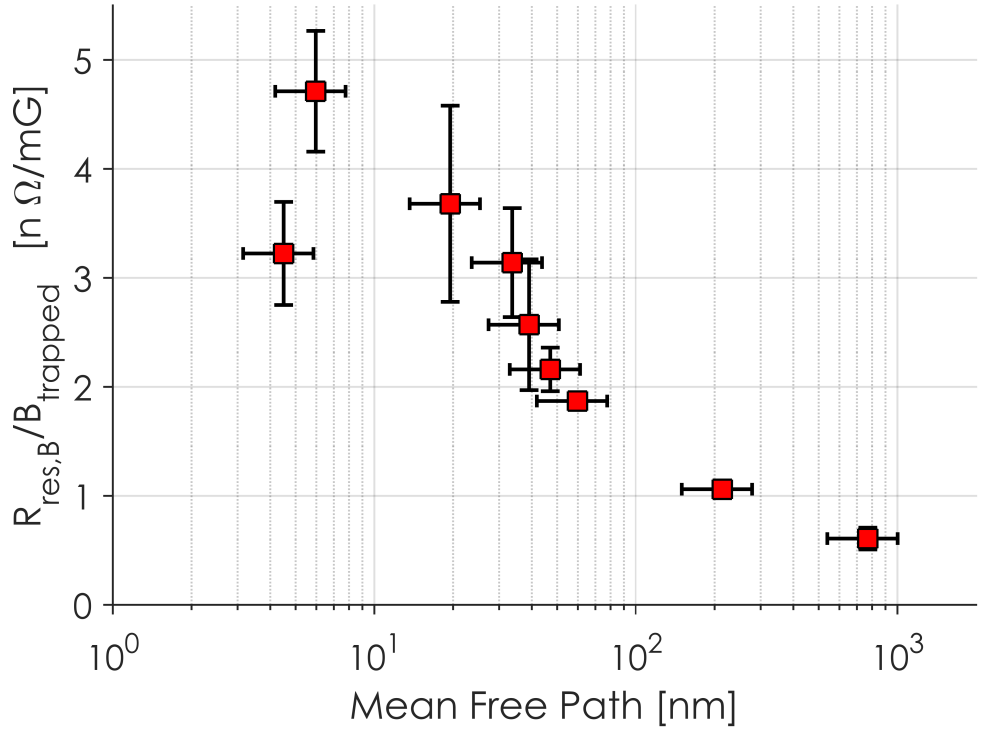

Figure 6.20: $R_{\text{res,B}}/B_{\text{trapped}}$ versus mean free path for the cavities tested. In the cleaner range ($\ell \geq 20$ nm), longer mean free path leads to lower $R_{\text{res,B}}/B_{\text{trapped}}$ while in the dirty limit ($\ell < 10$ nm) shorter mean free paths lead to lower $R_{\text{res,B}}/B_{\text{trapped}}$.

with the mean free path measurement for the VEP+120°C bake preparation, this data point was omitted from Figure 6.20. We can see that for mean free paths above ~10 nm, larger mean free path led to lower sensitivity of residual resistance to trapped magnetic flux, $R_{\text{res,B}}/B_{\text{trapped}}$. Below mean free paths of 6 nm, $R_{\text{res,B}}/B_{\text{trapped}}$ decreased with smaller mean free path. While this shape is similar to the prediction made by the simple model shown in Figure 6.4, $R_{\text{res,B}}/B_{\text{trapped}}$ is significantly larger outside the very dirty and very clean limits than Equation 6.4 predicts. Comparing with the full Gurevich theory leads to much better agreement.

Referring back to Equation 6.8, we can compare the experimental results

with the full theoretical prediction. Figure 6.21 shows the sensitivity of residual resistance to trapped magnetic flux prediction from the Gurevich theory for a mean spacing of pinning sites $\ell_p = 75\ell$. This value was found by fitting Equation 6.8 to the experimental data varying the constant of proportionality, C, between the mean free path and the mean spacing between pinning sites. It can be seen from Figure 6.21 that the theoretical model fits the data well in all regions thus supporting the assumption of a linear relationship between mean free path and mean spacing of pinning centers. These results show a maximum sensitivity at $\ell \approx 8$ nm. It is likely that the constant of proportionality, C, depends on properties of the niobium used in cavity fabrication, for example, grain size. Also shown is a least squares fit of $1/\sqrt{\ell}$ to the data with mean free paths above 20 nm, following the mean free path dependence predicted by the Gurevich theory in the clean limit. It is clear that for this region, the sensitivity does indeed change as $1/\sqrt{\ell}$.

6.8 Residual Resistance Conclusions

As discussed in Chapter 4, there were two main concerns regarding cool down of SRF cavities: first, slow cool down resulted in worse performance than fast cool down, and second, that this effect was much stronger for nitrogen-doped cavities. The work presented in the previous sections shows a concrete understanding of both of these phenomena.

Large spatial temperature gradients, which are usually associated with fast cool down rates, lead to more efficient flux expulsion. This means that less ambient magnetic field is trapped in the cavity walls during the cool down which

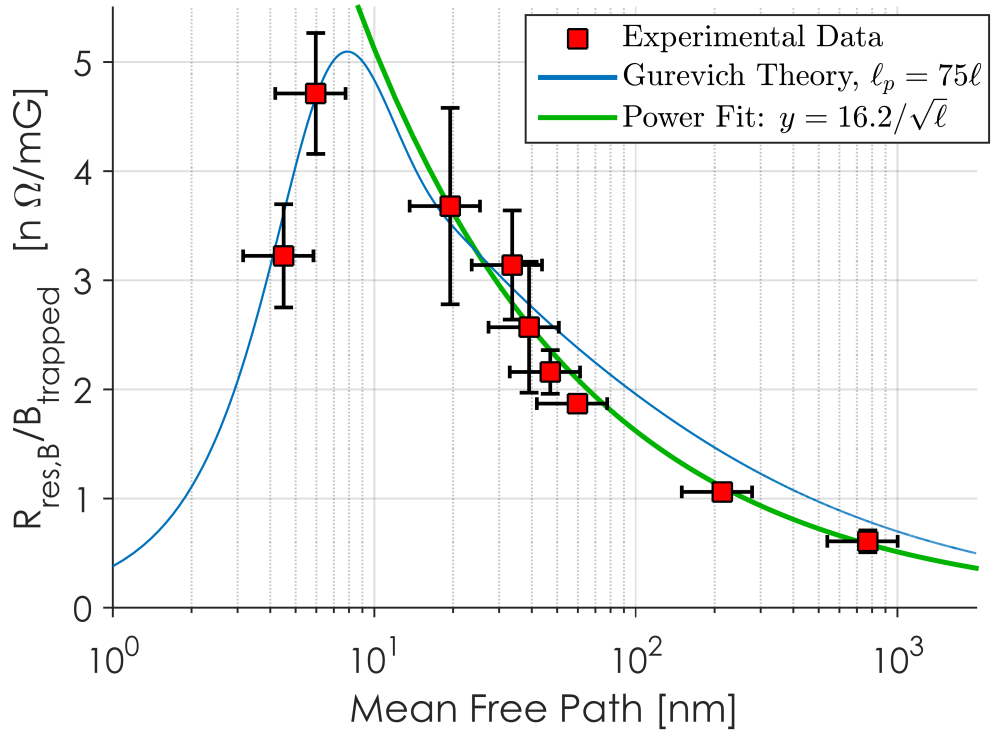

Figure 6.21: $R_{\text{res,B}}/B_{\text{trapped}}$ versus mean free path for the 1.3 GHz cavities tested compared with predictions from Gurevich's theory of vortex oscillations as discussed in subsection 6.2.2. For this prediction, the mean spacing of pinning sites was assumed to be proportional to the mean free path. The constant of proportionality was found by fitting to the experimental data (the constant of proportionality between ℓ_p and ℓ was the only fit parameter). For the relation between normal conducting resistivity and mean free path, 0.37×10^{-15} was used [GK68]. Also used were the London penetration depth, λ_L = 39 nm and the clean coherence length, ξ_0 = 38 nm [MS69, PFC99]. Also shown is a $1/\sqrt{\ell}$ fit to the data in the region of $\ell > 20$ nm. According to theoretical predictions, $R_{\text{res,B}}/B_{\text{trapped}}$ should fall as $1/\sqrt{\ell}$ in the clean limit.

directly leads to less residual resistance from trapped flux. This is supported by evidence at Cornell and FNAL [RGC+14, GEF+15].

The sensitivity of residual resistance to trapped magnetic flux, $R_{\text{res,B}}/B_{\text{trapped}}$, is highly dependent on the mean free path of the RF penetration layer. Nitrogen-doping lowers the mean free path into the region that was found to have significantly higher sensitivities of residual resistance from trapped flux. This results in larger residual resistance for the same cool down conditions and the same trapped flux in nitrogen-doped cavities than in EP+120°C baked cavities.

6.9 Optimal Doping Level

The last chapter and this one have been focused on understanding what leads to changes in the surface resistance when material properties, specifically the mean free path is changed. Chapter 5 focused on the temperature dependent R_{BCS} portion of R_s, while this chapter focused on the temperature independent R_{res}. R_{BCS} can be minimized by reaching an optimal doping level, such that $\ell \approx \xi/2 \approx 20$ nm, corresponding to a similar minimum as predicted by BCS theory (Figure 5.29). R_{res} is more complicated as it is made up of many components. However, as has been discussed previously, in well-prepared cavities trapped magnetic flux is the most significant contribution to R_{res}. Experimental data, consistent with theoretical predictions from Gurevich et. al., show a maximum sensitivity of residual resistance to trapped flux, $R_{\text{res,B}}/B_{\text{trapped}}$, at $\ell \approx 10$ nm.

Ultimately the important figure of merit for accelerator application is the Q_0 at the operating field such as 16 MV/m for LCLS-II. It is therefore useful to discuss the strength of the anti-Q slope caused by nitrogen-doping and its

impact of Q_0 at the operating gradient and temperature. Therefore it is useful to look at the ratio of R_{BCS} (5 MV/m) to R_{BCS} (16 MV/m) at 2.0 K. Due to the low quench fields of the more strongly doped cavities (specifically the cavities doped at 900 and 990°C), an adjustment to the Q_0 at maximum fields was needed for comparisons with other cavities to judge the strength of the anti-Q slope. This adjustment was done assuming a logarithmic dependence on E_{acc} (as described in section 5.3.2). Figure 6.22a shows the sensitivity of residual resistance to trapped magnetic flux versus the low field R_{BCS}. Lowering of the mean free path due to nitrogen-doping to lower R_{BCS} at 5 MV/m also brings with it a larger $R_{res,B}/B_{trapped}$. Figure 6.22b shows the sensitivity of residual resistance to trapped flux, $R_{res,B}/B_{trapped}$, versus the strength of the anti-Q slope, R_{BCS} (5 MV/m)/R_{BCS} (16 MV/m). There is a clear trend suggesting that stronger anti-Q slope comes at the cost of having higher $R_{res,B}/B_{trapped}$. Lowering of the mean free path via doping that optimizes the anti-Q slope unfortunately brings with it a stronger sensitivity of residual resistance to trapped magnetic flux. This implies that the true optimal doping level is heavily dependent on the amount of trapped flux achievable, i.e. it depends on the spatial temperature gradients achieved during cool down and the ambient magnetic field in the vicinity of the cavity..

By combining R_{BCS} (16 MV/m, 2.0 K) (from Figure 5.29), with $R_{res,B}/B_{trapped}$ from the Gurevich model (Figure 6.21), the total surface resistance at 16 MV/m can be computed for different amounts of trapped flux. Figure 6.23 shows R_s (16 MV/m, 2.0 K) versus mean free path for different amounts of trapped flux. At low amounts of trapped flux, there is a clear minimum near $\ell \approx 10 - 20$ nm, corresponding to the minimum in R_{BCS} versus ℓ. This is due to the benefits of the anti-Q slope at low ℓ outweighing the negatives from increased

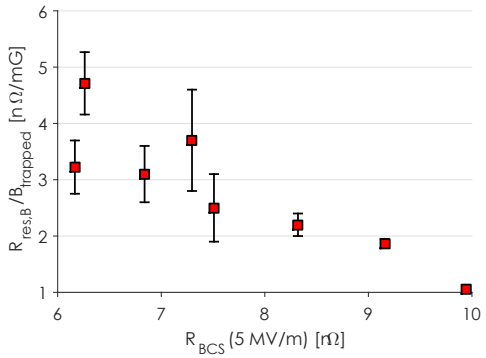

(a) $R_{\mathrm{res,B}}/B_{\mathrm{trapped}}$ versus 2 K R_{BCS} (5 MV/m) for the 1.3 GHz cavities tested. Lower R_{BCS} at low fields (due to lowering of the mean free path) comes at the cost of larger $R_{\mathrm{res,B}}/B_{\mathrm{trapped}}$.

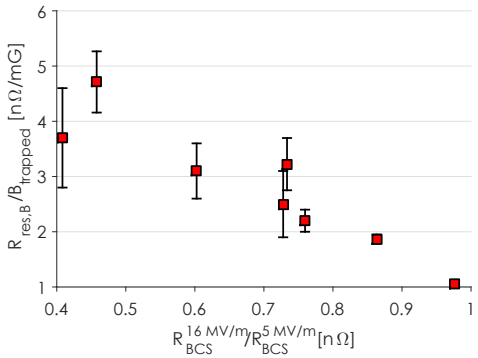

(b) $R_{\mathrm{res,B}}/B_{\mathrm{trapped}}$ versus 2 K R_{BCS} (16 MV/m)/R_{BCS} (5 MV/m) for the 1.3 GHz cavities tested. Stronger anti-Q slope comes at the cost of having a higher sensitivity of residual resistance to trapped flux, $R_{\mathrm{res,B}}/B_{\mathrm{trapped}}$. For cavities quenching below 16 MV/m, a fit to R_{BCS} (5) and R_{BCS} (E_{quench}) was used to approximate R_{BCS} (16 MV/m).

Figure 6.22: $R_{\mathrm{res,B}}/B_{\mathrm{trapped}}$ versus R_{BCS} (5 MV/m) and R_{BCS} (16 MV/m)/R_{BCS} (5 MV/m).

$R_{\mathrm{res,B}}/B_{\mathrm{trapped}}$ at low values of trapped flux. As the amount of trapped flux is increased, this minimum in R_s is located at increasingly higher mean free paths. At high enough values of trapped flux, there is no longer an absolute minimum in the standard doping region and the lowest R_s is at mean free paths significantly higher than for doped niobium. This transition happens around 4 mG of trapped flux. At very low mean free paths, it is possible to reach lower R_s due to lower $R_{\mathrm{res,B}}/B_{\mathrm{trapped}}$ in very strongly doped cavities, however this region of mean free paths is typically plagued with low quench fields and thus is not useful for accelerator applications. A full discussion of quench limitations in strongly doped cavities will be presented in Chapter 7.

Figure 6.23 provides clear guidance for the optimal doping level based on the achievable amount of trapped flux in a cryomodule. With a specification of

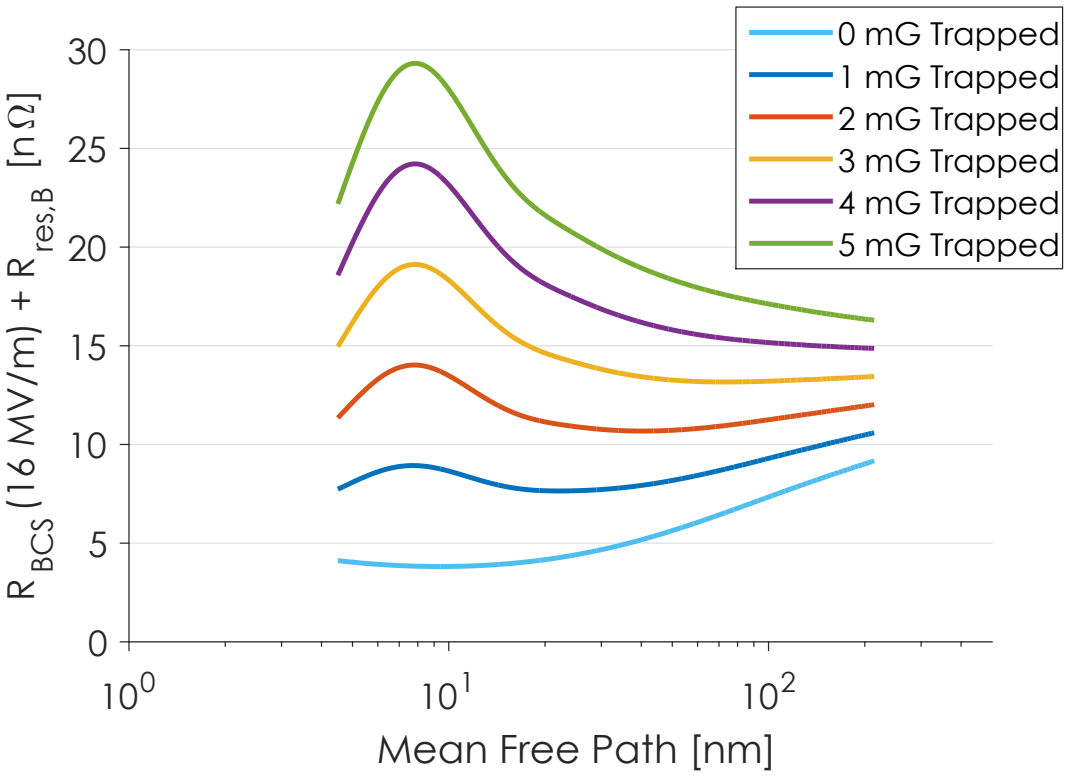

Figure 6.23: An estimate of the optimal doping level by combining R_{BCS} (16 MV/m, 2.0 K) from studies on BCS resistance (Figure 5.29) and the theoretical prediction from Gurevich's theory of vortex oscillations (Figure 6.21) for different values of trapped magnetic flux (R_{res} from trapped flux is independent of E_{acc}). With low trapped flux, moderate doping produces the smallest R_s while for high doping, R_s is minimized at mean free paths significantly larger than nitrogen-doping produces.

5 mG ambient magnetic field such as that for LCLS-II, ~50% flux expulsion is necessary to reach the Q_0 specification of 2.7×10^{10} at 16 MV/m.

CHAPTER 7

HIGH FIELD LIMITS

This chapter discusses the fundamental field limitations of doped cavities. It begins with an introduction to the theory of critical fields for superconductors. Then a summary of how quench field has been shown to be reduced in doped cavities is presented. Next is a discussion on lowering of the lower critical field, B_{c1}, by doping and lowering of the mean free path. Next is a discussion on the pulsed measurements experimental setup at Cornell, using a 1.5 MW klystron to reach the fundamental field limits of SRF cavities and the first pulsed measurements conducted on nitrogen-doped cavities. Finally, this chapter concludes with a study of the quench location in two nitrogen-doped cavities.

7.1 Introduction to Critical Fields

Recall from Chapter 2 that superconductors can be broken into two types based on the Ginsburg-Landau parameter, κ_{GL},

$$\kappa_{GL} \equiv \frac{\lambda_{GL}}{\xi_{GL}}, \tag{7.1}$$

with λ_{GL} and ξ_{GL} the Ginsburg-Landau penetration depth and coherence length, respectively. Materials with $\kappa_{GL} < 1/\sqrt{2}$ are Type-I superconductors, others are Type-II. In general, Type-I superconductors exist either in the superconducting or normal conducting state, while Type-II can also exist in a mixed state where normal conducting vortices are present in the superconducting bulk.

7.1.1 Critical Fields in Type-I Superconductors

[Tin04] provides a derivation of the necessary critical fields to be referenced in this chapter. Type-I superconductors have a single critical field, known as the thermodynamic critical field, B_c, given by

$$B_c = \frac{\phi_0}{2\sqrt{2}\pi\lambda_{GL}\xi_{GL}}, \tag{7.2}$$

with λ_{GL} the penetration depth, ξ_{GL} the GL coherence length, and ϕ_0 the flux quantum. Below B_c, the material is purely superconducting and above B_c, it is purely normal conducting.

7.1.2 Critical Fields in Type-II Superconductors

While Type-I superconductors have one intrinsic critical magnetic field, B_c, the situation is more complicated in Type-II superconductors which possess two important critical fields: the lower critical field, denoted B_{c1}, and the upper critical field, denoted B_{c2}. Below B_{c1}, the material is purely superconducting as in a Type-I below B_c. The lower critical field, B_{c1}, is the field at which the Gibbs free energy is equivalent whether a magnetic flux line is inside or outside the superconductor. Above B_{c1}, flux can be inside the material. This is the lowest field at which the superconductor enters the mixed state. While there is no closed form solution for B_{c1} based on κ_{GL}, an approximation can be obtained for $\kappa_{GL} \gg 1$ based on [Hei99],

$$B_{c1} = \frac{\phi_0}{4\pi\lambda_{GL}^2}\left(\ln\kappa_{GL} + 0.5\right). \tag{7.3}$$

Additionally, the exact value of B_{c1} has been calculated numerically from the Ginsburg-Landau equations for various κ_{GL} [HA63]. These results are shown in

κ_{GL}	$\mathbf{B_{c1}/B_c}$ **via GL**	$\mathbf{B_{c1}/B_c}$ **via Equation 7.3**
0.3	1.68	-
$2^{-1/2}$	1.00	0.150
1	0.817	0.351
2	0.547	0.421
5	0.315	0.298
10	0.201	0.198
20	0.124	0.123
50	0.0622	0.0624

Table 7.1: B_{c1} versus κ_{GL} computed from Equation 7.3 and calculated from GL theory.

Table 7.1.

While it is energetically favorable for a flux line to be inside the superconductor above B_{c1}, there is an energy barrier to its entry, meaning that flux lines do not necessarily enter exactly at B_{c1}. This energy barrier keeps the superconductor flux free in a metastable state up to the superheating field, B_{sh}. The superheating field can be estimated from [TCS11]:

$$B_{sh} = B_c\left(\frac{\sqrt{20}}{6} + \frac{0.5448}{\sqrt{\kappa_{GL}}}\right). \tag{7.4}$$

Under RF, normal conducting vortex flux lines can be detrimental to performance since they will be oscillating billions of times per second (in the case of 1.3 GHz cavities for example), causing excessive heat dissipation. Therefore once flux lines begin to enter, it can be expected that performance will dramatically decrease as the dissipated power increases and Q_0 decreases. Therefore the superheating field is generally considered to be the fundamental limit for a superconductor above which it will quench and transition to normal conducting. Empirically, the temperature dependence of the critical fields follows $1-(T/T_c)^2$

[Tin04]. The superheating field can be written as

$$B_{sh}(T) = c(\kappa_{GL})B_c(T=0)\left[1-\left(\frac{T}{T_c}\right)^2\right], \tag{7.5}$$

where $c(\kappa_{GL})$ is a function that depends on material properties and may depend on temperature [TCS11]. Measurements of the superheating field near T_c can lead to a calculation of $c(\kappa_{GL})$ as shown in [Val13].

As the field is increased above B_{sh}, flux lines will continue to enter the superconductor. This state is known as the vortex state and is characterized by flux lines forming a lattice in the superconductor. Above the upper critical field, B_{c2}, the material is purely normal conducting just as a Type-I superconductor above B_c. B_{c2} can again be calculated from GL theory as in [Tin04]

$$B_{c2} = \frac{\phi_0}{2\pi\xi_{GL}^2}. \tag{7.6}$$

While there is no physical meaning to the thermodynamic critical field in Type-II superconductors, it can be thought of as an average between the two critical fields. It can be useful to express the other critical fields in terms of this thermodynamic critical field as in Equation 7.4.

In a perfect cavity with no defects, the fundamental limit is B_{sh}. However, in reality, defects in the material may alter the superconductivity of the defect location, effectively lowering the energy cost required for a flux line to enter at the defect. This can lead to earlier vortex penetration prior to B_{sh}. Experimentally, this can be characterized by a quench field that follows the $1-(T/T_c)^2$ behavior one would expect from a critical field, but at $B_{c1} \leq B < B_{sh}$. If normal conducting defects are present on the other hand, excessive heating can occur in the vicinity of the defect leading to thermal runaway above a certain field value leading to a similar deviation from the $1-(T/T_c)^2$ dependence of the quench field.

7.1.3 Critical Field Dependence on Mean Free Path

As can be seen from the equations in the previous section, the critical fields are heavily dependent on penetration depth, coherence length, and κ_{GL}. As was shown in Chapter 2, these three parameters are strongly dependent on the mean free path. Also, Chapter 5 showed a significant impact on the mean free path due to doping with nitrogen, resulting in much lower mean free paths than for clean niobium. It is therefore useful to calculate the critical fields for different mean free paths in order to understand how they may be affected by nitrogen-doping.

Figure 7.1 shows the critical fields B_{c1}, B_c, B_{sh}, and B_{c2} of niobium versus mean free path. For reference, lower mean free path leads to higher κ_{GL}. There are a few important things to take away from this:

- The thermodynamic critical field, B_c, is relatively unchanged by changes in ℓ.
- The superheating field, B_{sh}, decreases slightly as ℓ is decreased.
- The lower critical field, B_{c1}, is significantly lowered at low values of mean free path - this could lead to earlier vortex penetration than in clean niobium if defects are present.
- The upper critical field, B_{c2}, is significantly increased at low values of mean free path.

For completeness, Table 7.2 shows the corresponding critical fields for each of the cavities tested for this dissertation calculated from their mean free paths.

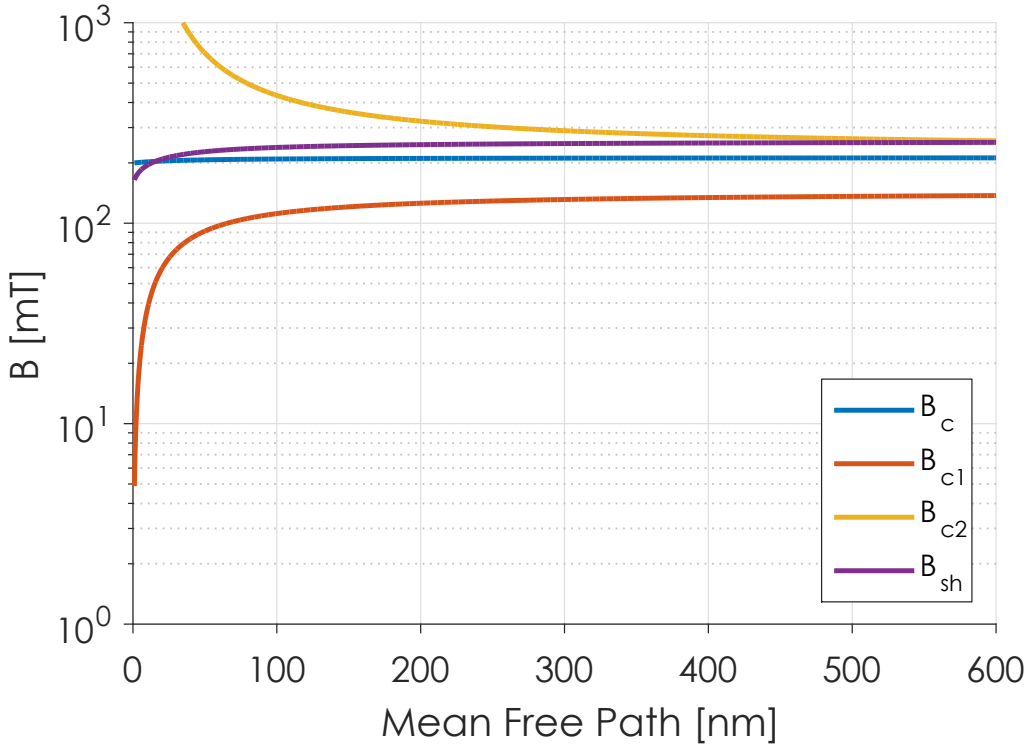

Figure 7.1: Critical fields of niobium predicted from GL theory versus mean free path. Low mean free path (high κ_{GL}) leads to significantly lower B_{c1} and higher B_{c2}. B_c is relatively unchanged from changes in ℓ and B_{sh} decreases slightly with lower mean free paths. For this calculation ξ_0 = 38 nm and λ_L = 39 nm were used.

Given are B_{c1}, B_c, and B_{sh}. B_c was calculated with Equation 7.2, B_{c1} from Table 7.1, and B_{sh} from Equation 7.4.

7.2 Reduction in Quench Field Due to Doping

7.2.1 Quench Field Reduction in 9-Cell Cavities

In addition to improvement in Q_0, nitrogen-doping can bring with it a reduction in the quench limit of a cavity. For example, a 1.3 GHz 9-cell cavity (AES030)

Cavity	Preparation	Mean Free Path [nm]	B_{c1} [mT]	B_c [mT]	B_{sh} [mT]	Quench Field [mT]
LT1-3	990°C N-Doping[1]+ 5 μm VEP	4 ± 1	26 ± 9	201 ± 0.3	179 ± 3	40 ± 2
LT1-2	900°C N-Doping[2]+ 18 μm VEP	6 ± 1	37 ± 8	202 ± 0.3	186 ± 2	64 ± 4
LT1-2	900°C N-Doping[2]+ 12 μm VEP	13 ± 4	64 ± 24	203.1 ± 0.8	200 ± 5	51 ± 4
LT1-2	900°C N-Doping[2]+ 6 μm VEP	17 ± 5	76 ± 26	203.9 ± 0.8	206 ± 5	36 ± 2
LT1-2	800°C N-Doping[3]+ 6 μm VEP	19 ± 6	81 ± 30	204 ± 1	208 ± 5	68 ± 4
LT1-3	800°C N-Doping[3]+ 12 μm VEP	34 ± 10	107 ± 33	206 ± 1	220 ± 5	141 ± 13
LT1-1	800°C N-Doping[3]+ 18 μm VEP	39 ± 12	113 ± 35	206 ± 1	223 ± 5	77 ± 9
LT1-4	800°C N-Doping[3]+ 24 μm VEP	47 ± 14	121 ± 34	207 ± 1	226 ± 5	146 ± 13
LT1-5	800°C N-Doping[3]+ 30 μm VEP	60 ± 18	131 ± 33	208 ± 1	231 ± 4	111 ± 9
LT1-5	800°C N-Doping[3]+ 40 μm VEP	213 ± 64	165 ± 20	211 ± 0.5	247 ± 2	77 ± 9

[1] 100 μm VEP, 800°C in vacuum for 3 hours, 990°C in 30 mTorr of N_2 for 5 minutes.
[2] 100 μm VEP, 800°C in vacuum for 3 hours, 900°C in 60 mTorr of N_2 for 20 minutes, 900°C in vacuum for 30 minutes.
[3] 100 μm VEP, 800°C in vacuum for 3 hours, 800°C in 60 mTorr of N_2 for 20 minutes, 800°C in vacuum for 30 minutes.

Table 7.2: Calculated Critical Fields of Cavities Tested

prepared at Cornell was tested prior to nitrogen-doping and found to quench at ~30 MV/m. The cavity was then given two different nitrogen-dopings with a surface reset of 40 μm in between:

1. 800°C for 20 minutes in 60 mTorr of N_2, 30 minute anneal, 26 μm VEP.
2. 800°C for 6 minutes in 30 mTorr of N_2, 6 minute anneal, 14 μm VEP.

Although the dopings were quite different, differences in final amount of VEP led to similar mean free paths (as predicted by the nitrogen-diffusion simulation, see subsection 5.2.1), with preparation one having a slightly lower mean free path than preparation two. These three Q_0 versus E_{acc} curves at 2.0 K are shown in Figure 7.2. The first doping resulted in a reduction in quench field from 30 MV/m to ~16 MV/m. After the surface reset and second doping, the quench field improved to ~20 MV/m. Both cases of nitrogen-doping resulted in a significant drop in the quench field of the cavity. This behavior is consistent with a lowering of B_{c1} due to nitrogen-doping lowering the mean free path of the niobium. The differences in the quench fields of the two doping preparations could be attributed to more total chemistry eroding a defect further between the two tests. Also because the first preparation had a slightly lower mean free path than the second, B_{c1} would be further reduced which could lower the quench field.

A second 1.3 GHz 9-cell cavity was tested in a similar fashion to AES030. AES022 was given a baseline test and found to quench at 21 MV/m. The Q_0 versus E_{acc} of the cavity is shown in Figure 7.3. The quench location was found via temperature mapping and found to be centered at a single location, most likely a defect on the surface. After a nitrogen-doping at 800°C for 2 minutes

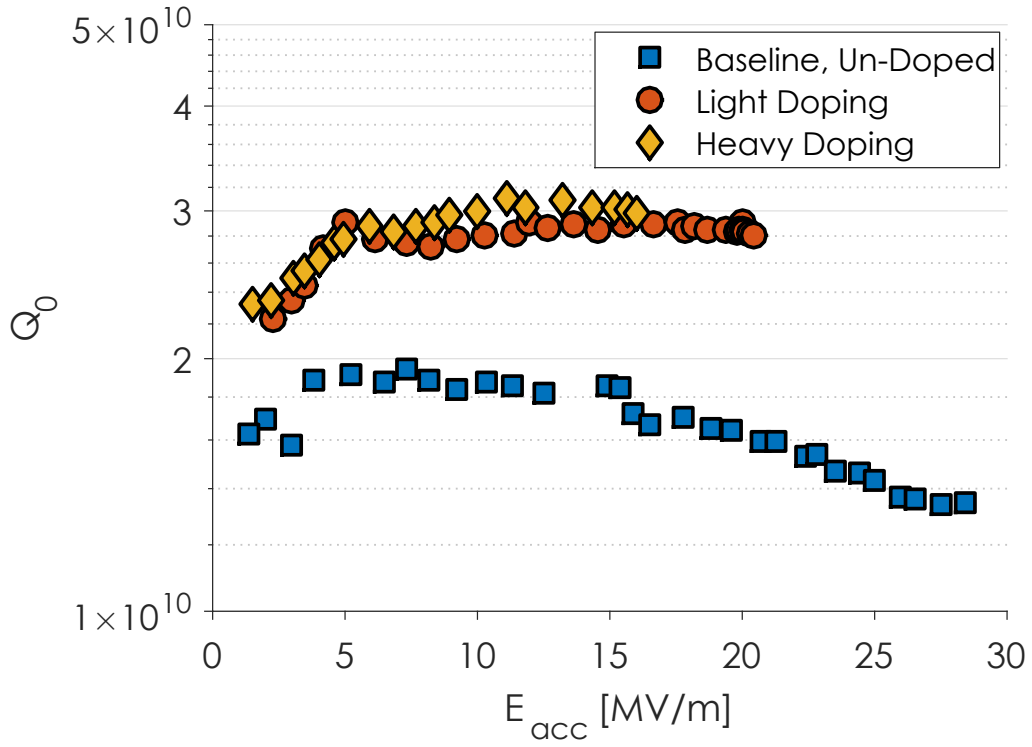

Figure 7.2: Q_0 versus E_{acc} for AES030 (9-cell cavity tested at Cornell) at 2.0 K. Cavity quenched at ~30 MV/m prior to nitrogen-doping. Following a heavy doping, the quench field was reduced to ~15 MV/m. After a surface reset and a light doping, the quench field was improved to ~20 MV/m. After a reset and Errors on Q_0 are ~20% and on E_{acc} are ~10%.

followed by a 2 minute anneal and a final VEP of 5 μm, the quench field was reduced to 15 MV/m. Again the quench spot was located and found to be in the same location as before nitrogen-doping.

The quench location in AES022 was studied using optical inspection and a visible bump was found on the surface as shown in Figure 7.4. This bump will have led to magnetic field enhancement at that location and thus higher local fields. This forces the cavity to quench at a lower field than if the defect was not present. This shows that while the cavity quenched due to the same defect in both cases, nitrogen-doping significantly lowered the field at which

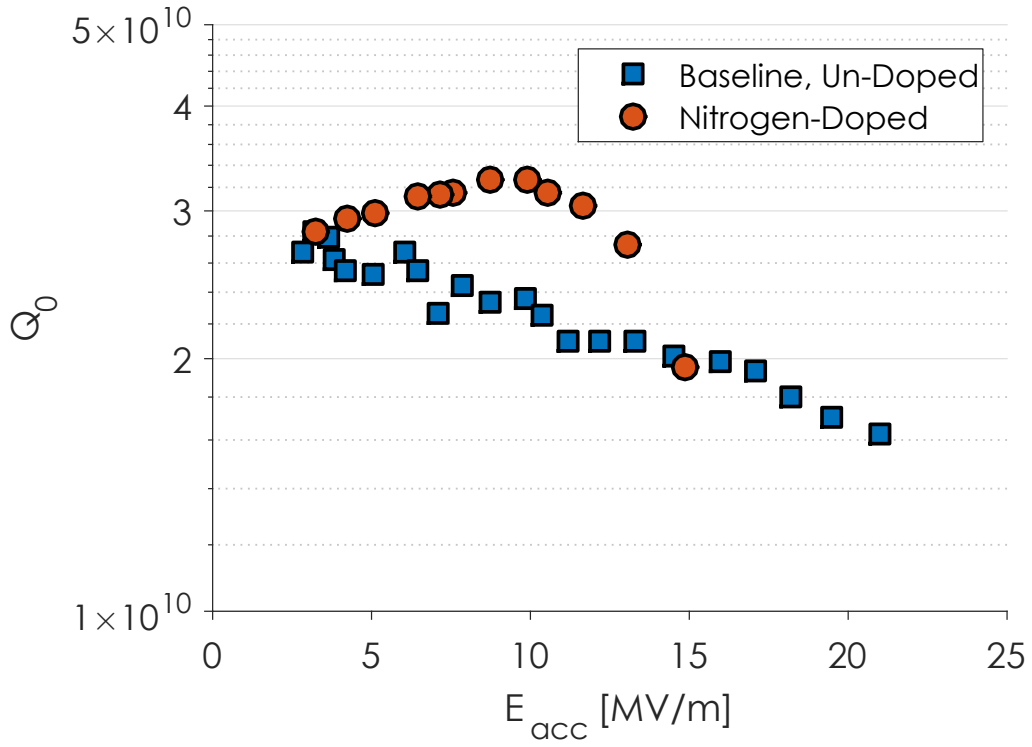

Figure 7.3: Q_0 versus E_{acc} for AES022 (9-cell cavity tested at Cornell) at 2.0 K. Cavity quenched at ~21 MV/m prior to nitrogen-doping. Following a light nitrogen-doping, the quench field was reduced to 15 MV/m. Errors on Q_0 are ~20% and on E_{acc} are ~10%.

the quench would occur. This data along with the measurements on AES030 suggest that increasing the level of doping leads to a lowering of the quench field via a reduction in B_{c1} and earlier flux entry at defects and is consistent with heavily doped cavities at FNAL and TJNAF [GRS+13].

7.2.2 Quench Field Reduction in Single-Cell Cavities

Additionally, two single-cell cavities were tested with moderate and heavy dopings and a significant impact on quench field was observed. Cavities LT1-2 and

Figure 7.4: A defect (bump) at the quench location in AES022 obtained via optical inspection.

LT1-3 were given the same moderate doping[1] and given 6 (ℓ = 19 ± 6 nm) and 12 μm (ℓ = 34 ± 10 nm) VEP, respectively. After this moderate doping, their quench fields were 30 and 16 MV/m, respectively. Then after a surface reset, they were then given heavy dopings:

- LT1-2: 900°C in 60 mTorr of N_2 for 20 minutes followed by a 30 minute anneal and 6 μm VEP (ℓ = 6 ± 1 nm).
- LT1-3: 990°C in 20 mTorr of N_2 for 5 minutes followed by a 5 μm VEP (ℓ = 4 ± 1 nm).

Following the heavy dopings, both cavities quenched at ~9 MV/m. Their Q_0 versus E_{acc} performance is shown in Figure 7.5 and their mean free paths and quench fields are listed in Table 7.2.

It is clear that doping can lead to lower quench fields and stronger doping leads to an even more drastic reduction in E_{quench}. Understanding the mechanism behind this effect is vitally important for future accelerators which may need to operate in the high field regime such as the ILC but would also benefit from the high Q_0 achievable with nitrogen-doping. The rest of this chapter

[1] 800°C in 60 mTorr of N_2 for 20 minutes followed by a 30 minute anneal.

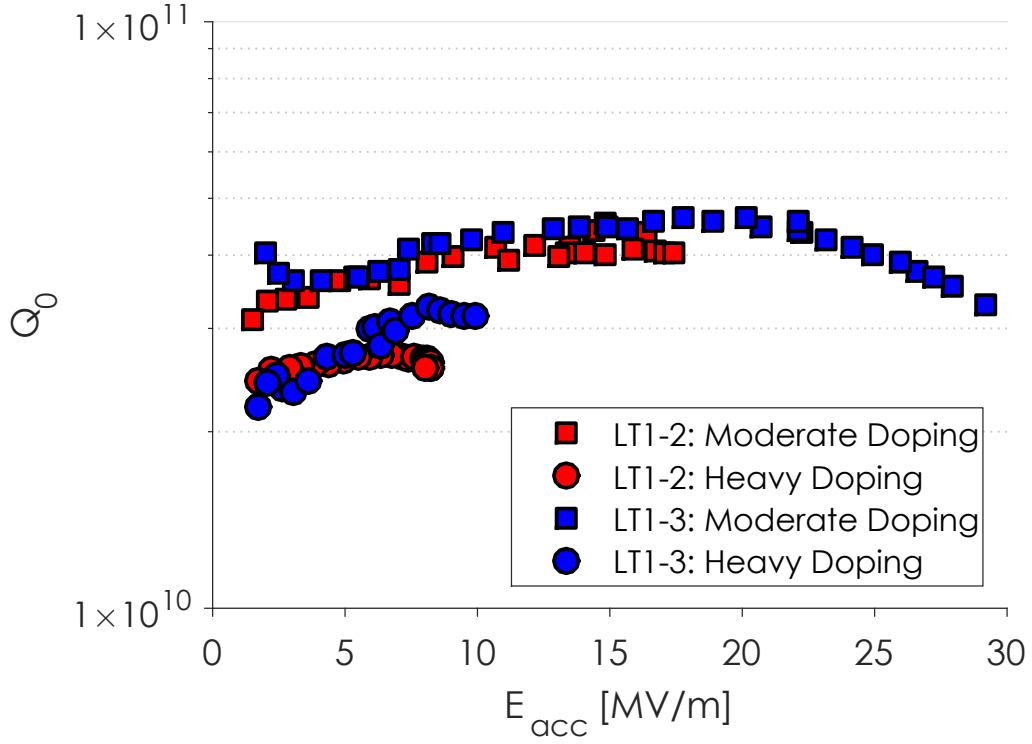

Figure 7.5: Q_0 versus E_{acc} for LT1-2 and LT1-3 (single-cell cavities) at 2.0 K. Stronger doping resulted in lower quench fields on the same cavities. Errors on Q_0 are ~20% and on E_{acc} are ~10%.

will focus on understanding this reduction in quench field in the context of the cavities' critical fields.

7.3 Lower Critical Field Reduction from Doping

As has been discussed in detail in the previous chapters, doping of SRF cavities with nitrogen causes a significant decrease of the mean free path of the RF penetration layer. Due to the change in mean free path, the critical fields will also be severely impacted as discussed in subsection 7.1.3. It is possible that these changing critical fields could directly lead to the lowering of the quench field

that is typically observed in nitrogen-doped cavities if defects are present that lower the energy barrier to flux entry. Additionally, if normal conducting defects are present, thermal runaway could lead to lower quench fields. It is likely that poor phases of niobium-nitride which are normal conducting at operating temperatures are present even after significant chemistry due to deep diffusion at the grain boundaries [TGMR15].

Figure 7.6 shows the theoretical prediction from Ginzburg-Landau theory of B_{c1} as a function of mean free path in the region of mean free paths for the nitrogen-doped cavities tested as outlined in Table 4.2. As predicted by Equation 7.3 and Table 7.1, B_{c1} decreases as the material gets dirtier (ℓ decreases). Also shown in Figure 7.6 are the single-cell cavities tested[2]. It is clear that lowering of the mean free path from doping causes a significant reduction in the lower critical field, B_{c1}. For the strongest doped cavities, B_{c1} is as low as 20 mT, corresponding to ~5 MV/m.

Reduction of B_{c1} does not necessarily mean that the cavity quench field will be lowered to B_{c1}. As discussed above, at fields greater that B_{c1}, it becomes energetically favorable for a normal conducting vortex to be inside the bulk, however there is an energy barrier to flux entry, delaying the flux entry. Figure 7.7 shows the quench field versus mean free path for the single-cell cavities along with the predicted B_{c1} from GL theory. From this there are few things that can be observed. First, there is a clear correlation between longer mean free paths leading to higher average quench fields. Second, all but two of the cavities quench at approximately B_{c1} or greater than B_{c1}. This means that 80% of the cavities tested operate in the metastable regime! In fact three of the ten cavities quench at fields near or above two times B_{c1}. Two of the cavities quenched at

[2] B_{c1} for the cavities is calculated from their extracted mean free paths, not measured.

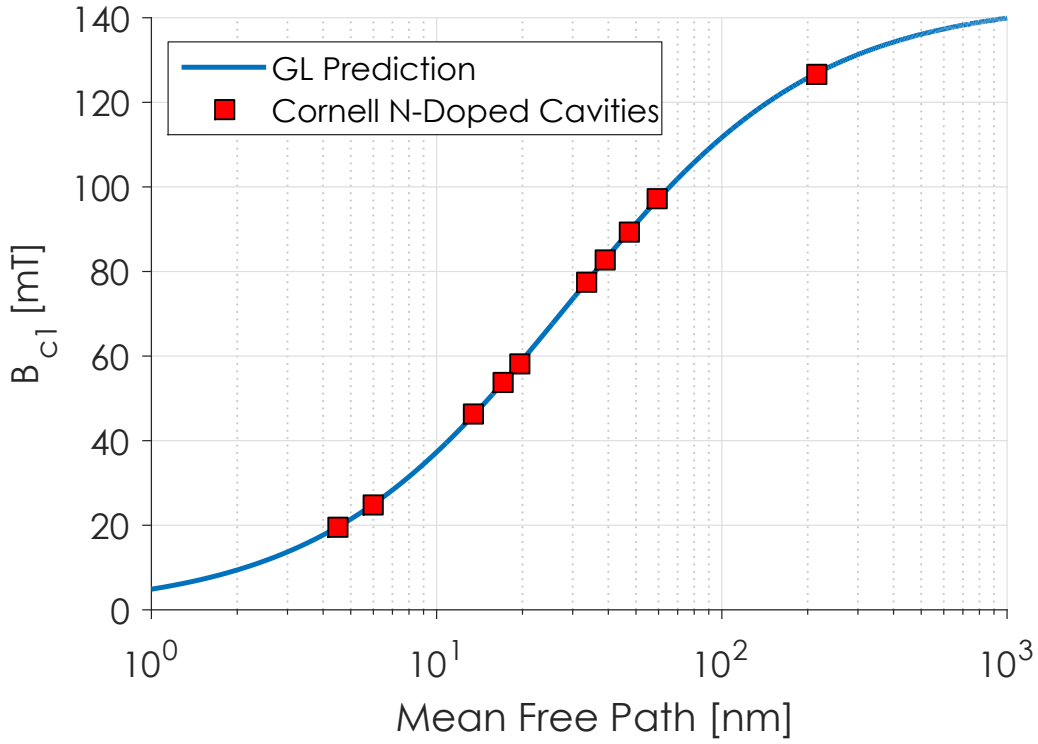

Figure 7.6: Predicted B_{c1} from GL theory versus mean free path. Also shown are the single-cell cavities tested for this dissertation (B_{c1} for the cavities is calculated from their extracted mean free paths, not measured).

lower fields but this may have been due to other factors lowering the quench field such as defects (pits) leading to magnetic field enhancement or normal conducting niobium-nitride which diffused through the grain boundaries. LT1-5, the one cavity which quenched significantly below B_{c1} is likely to have been limited by a multipacting barrier that was insurmountable. In conclusion, it is likely that lowering of B_{c1} has a role to play in the lower average quench fields observed in the doped cavities.

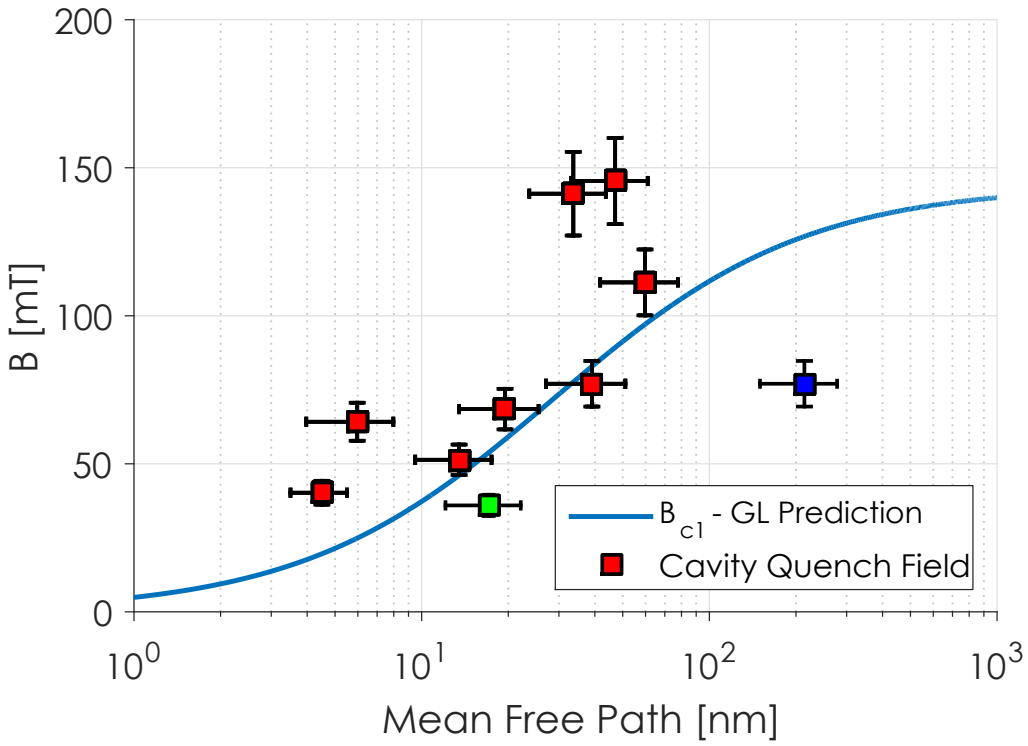

Figure 7.7: Predicted B_{c1} from GL theory versus mean free path and the single-cell cavity quench fields (converted to the peak magnetic field on the cavity surface, B_{pk} from CW testing. The point in blue is most likely limited by multipacting and the point in green by normal conducting NbN on the surface due to only a small amount of final VEP after nitrogen-doping.

7.4 Pulsed Measurements Experimental Setup

In order to further explore the mechanisms behind the early quench in nitrogen-doped cavities, two strongly doped cavities (LT1-2, preparation 2 and LT1-3, preparation 2 as outlined in Table 4.2) were tested using the high power pulsed test setup at Cornell (for a full description of the methods of this experiment see [Val13]). A 1.5 MW klystron is used to pulse high RF power at ~1 Hz rate into a cavity. This allows for thermal effects that usually manifest in CW operation to be reduced. This can lead to reaching higher fields than in CW if defects are

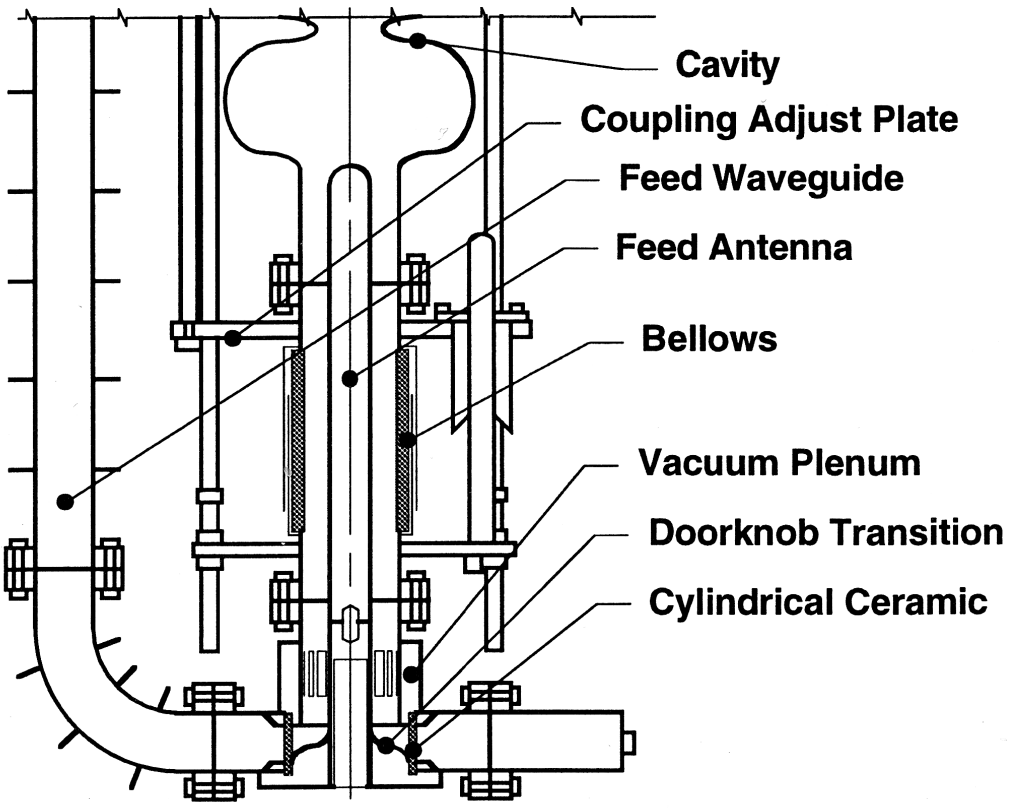

Figure 7.8: Schematic of the high power klystron insert at Cornell. Image from [PKH98].

present and potentially to reaching the fundamental field limit of the cavity. A schematic of the test insert for high power measurements is shown in Figure 7.8. RF power is input through a waveguide which couples into the antenna via a doorknob transition. The cavity rests on a bellows that has approximately 4 inches of travel allowing the input coupling to be adjusted between $Q_{ext} \approx 1 \times 10^4$ and 1×10^{10}.

An example of a typical pulse is shown in Figure 7.9. Forward power is turned on for approximately 100 μs to ~900 kW. When the power is turned on the field in the cavity ramps up until the quench point is reached, which in this case occurs at a peak surface magnetic field of $B_{pk} \approx 65$ mT. After the quench power drains out of the cavity. The peak magnetic field is the maximum surface

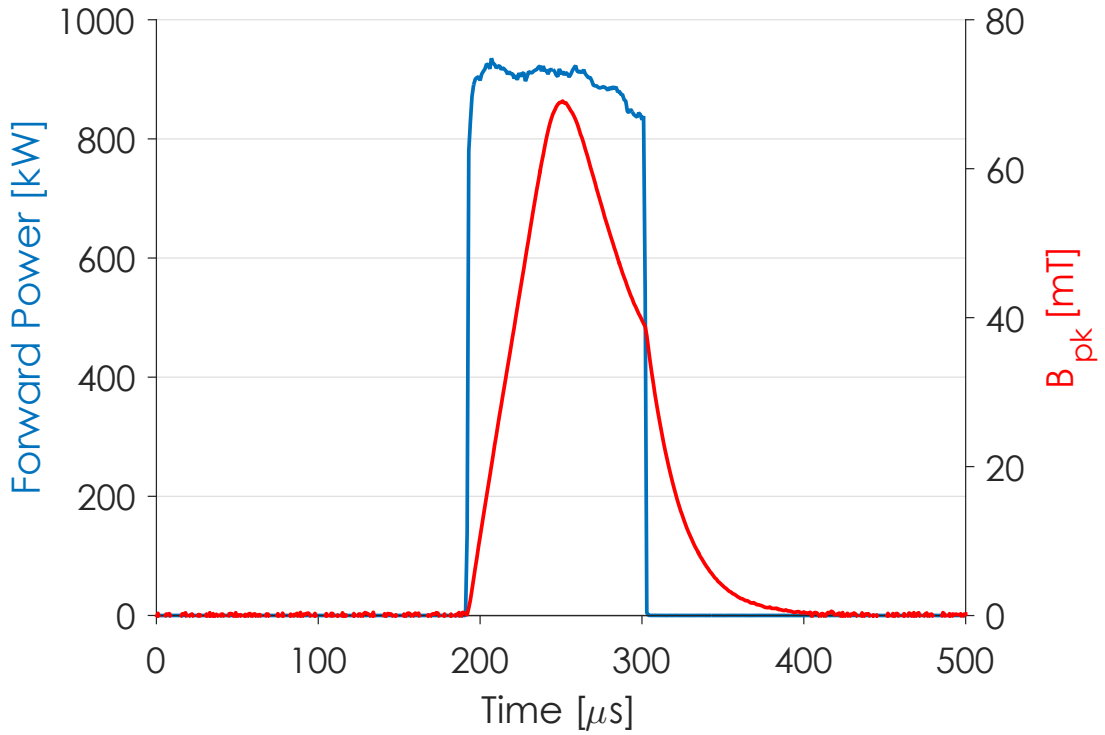

Figure 7.9: An example of a single pulse measurement. Pulse length was ~100 μs and the forward power was ~900 kW. Cavity field increases when the power is on until quench shown at ~65 mT.

field reached on the cavity wall.

7.5 Pulsed Measurements

Two nitrogen-doped cavities were tested with pulsed measurements to understand the nature of their quench. The first cavity tested was LT1-2, preparation 2 (doping at 900°C for 20 minutes in 60 mTorr of N_2, 30 minute anneal, 18 μm VEP) which had a CW quench field of 15 MV/m. The second cavity tested was LT1-3, preparation 2 (doping at 990° for 5 minutes in 20 mTorr of N_2, 5 μm VEP) which had a CW quench field of 9 MV/m. These cavities were selected

since they had been given heavy dopings and quenched at significantly lower quench fields than un-doped cavities. For reference, under preparation 1 with a moderate doping, LT1-3 quenched at 35 MV/m. For both cavities, the quench field field was measured in short pulse operation as a function of temperature and quench field at 4.2 K was measured as a function of forward power (lower forward power led to longer times to quench).

Cavity LT1-2 quenched at 15 MV/m during CW operation at 2.0 K corresponding to B_{pk} = 64 mT. Short high power pulses resulted in a significantly higher quench field at the same temperature. Figure 7.10 shows $\mu_0 H_{pk}$ versus $(T/T_c)^2$ for LT1-2 between 2.0 K and T_c with pulses of ~1 MW. Also shown is the superheating field, B_{sh}, and the lower critical field, B_{c1} versus temperature as calculated from superconducting theory for the extracted mean free path from CW RF results. Near T_c, the quench field of the cavity closely follows the superheating field. However, at lower temperatures, the quench field deviates from the superheating field and settles to a lower quench field, albeit higher than the CW quench field. This behavior of a transition between following B_{sh} at high temperatures and deviating at low temperatures is indicative of a quench at a defect [Val13]. Above B_{c1}, it is energetically favorable for flux to be inside the superconductor however there is an energy barrier to its entry. If there is a defect on the surface, the energy barrier could be lowered, leading to flux entry below B_{sh} and resulting in a quench. A normal conducting defect could also lead to the same behavior due to thermal runaway causing excessive heating on the surface leading to a quench. The behavior shown in Figure 7.10 is consistent with both flux entry above B_{c1} and a normal conducting defect.

Also shown in Figure 7.10 is the result of a simulation of quench by a defect

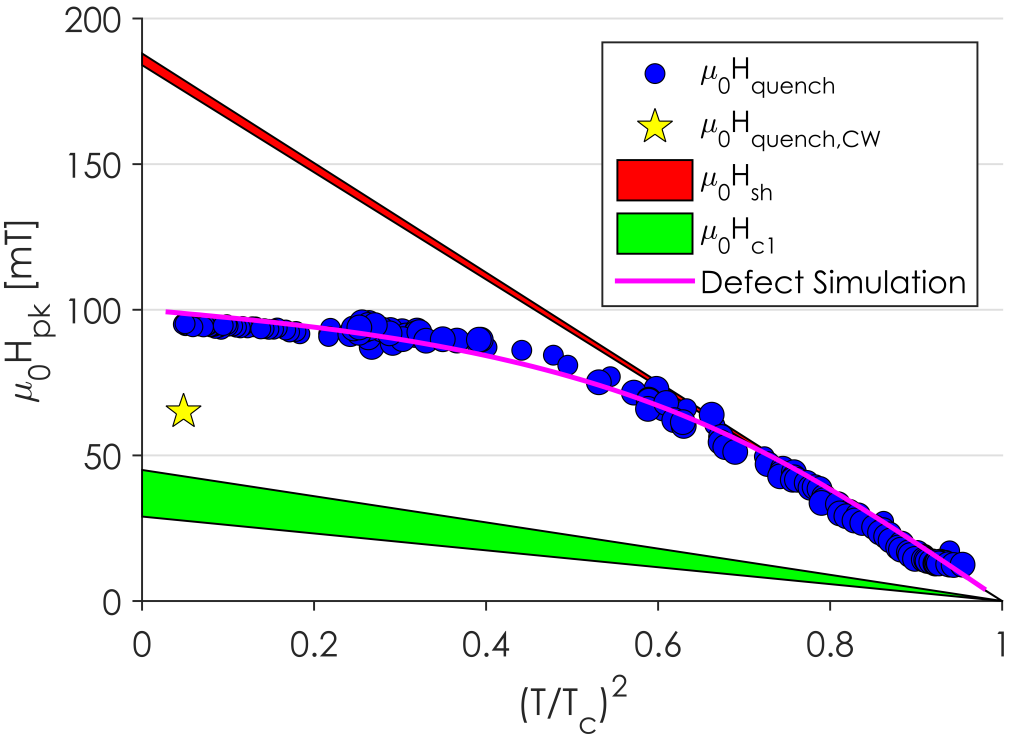

Figure 7.10: B_{pk} vs $(T/T_c)^2$ for LT1-2. Near T_c, quench field follows the superheating field. However at lower temperatures, quench field is significantly lower than B_{sh} but still well above B_{c1}, consistent with a quench at a defect. CW quench field is also shown and can be seen to be significantly higher than B_{c1}. B_{c1} and B_{sh} were calculated from extracted mean free path values obtained from CW RF measurements.

on the surface leading to flux entry. This simulation approximates the heating from a flux line entering above B_{c1}. The simulation also predicts how quench field would be affected by heating due to a normal conducting defect and finds that the behavior is identical to the case with flux entry. This means that the results shown in Figure 7.10 do not allow one to differentiate between the two cases.

Another measurement to understand the nature of a quench is to study how the quench field changes as the time to reach quench in pulsed operation is

increased. The amount of forward power directly affects the time it takes for the cavity to fill with field and reach quench. By lowering the forward power of the klystron (at constant temperature), the cavity will take longer to reach the quench field, and thermal heating effects will thus be increased. At high powers, the quench will occur faster and thermal effects will be reduced. The results from this measurement is shown in Figure 7.11 for cavity LT1-2. Also shown is the CW quench field and a simple defect thermal model:

$$\mu_0 H_{quench} = A + \frac{B}{\sqrt{t}}, \tag{7.7}$$

which is valid for $H_{quench} < H_{sh}$. It is clear that there is a strong relationship between the quench field and the time to quench: as the time to quench is increased, the quench field decreases. At long times to quench, the pulsed quench field approaches the CW quench field. This trend also follows the simple thermal model closely and is again indicative of a quench at a defect. Also note that even at the highest powers used, thermal effects still limit the maximum field reachable in the cavity.

Cavity LT1-3 had a CW quench field of 9 MV/m corresponding to 38 mT at 2.0 K. The same measurements completed on LT1-2 were conducted on LT1-3. Quench field versus $(T/T_c)^2$ is shown in Figure 7.12 along with the calculated values for B_{c1} and B_{sh}. Similar behavior was observed to cavity LT1-2, at high temperatures the quench field followed the superheating field and at low temperatures it deviated from B_{sh} and settled at a much lower field. Again the CW quench field was just above B_{c1}. It is therefore likely that LT1-3 also quenched at a defect.

In addition to measuring the temperature dependence of the quench field on LT1-3, the quench field versus time to quench was also measured, just as in

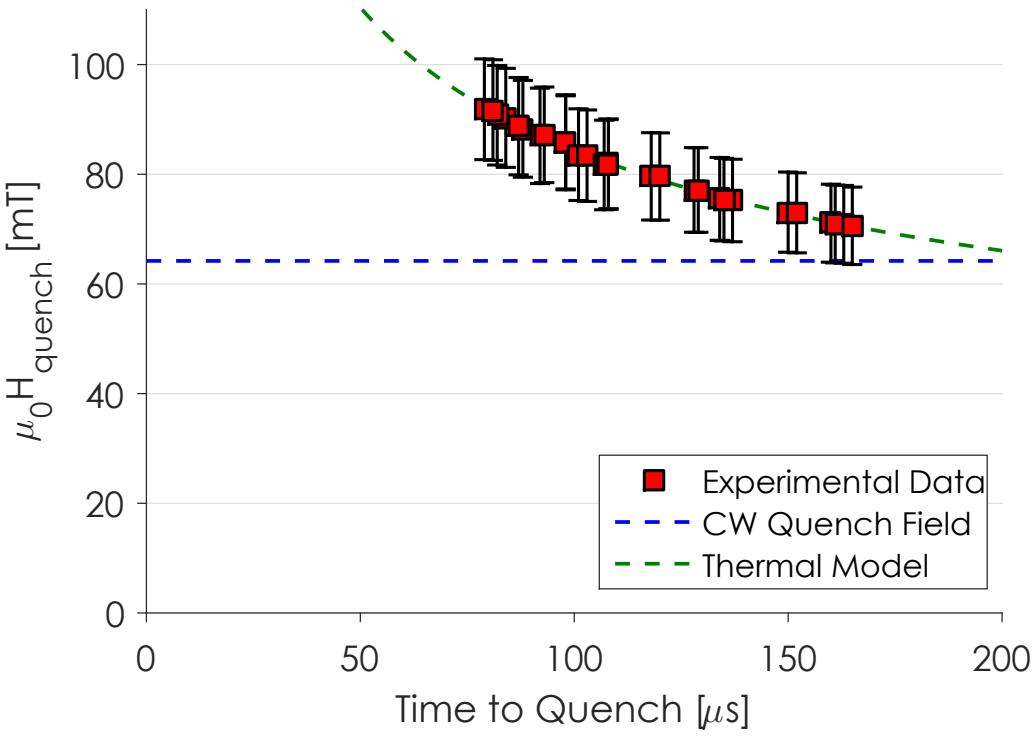

Figure 7.11: Quench field versus time to quench for LT1-2 at 4.2 K. Time to quench was adjusted by changing the forward power of the kylstron. For longer times to quench, the quench field decreased and approached the CW quench field at long times to quench, again indicative of a quench at a defect. Also shown is a simple thermal model which fits the data well. Even at the highest powers used, the time to quench is not short enough to avoid thermal effects and reach the fundamental limit.

LT1-2. The result from this measurement is shown in Figure 7.13. Again, longer times to quench led to a lower quench field and at long times to quench, the quench field approached the CW quench field.

In conclusion, both nitrogen-doped cavities tested with pulsed power displayed quenches characteristic of a quench at a defect. Additionally, the quenches at high temperature are in very good agreement with the superheating field predicted by the measured mean free path and lend insight to the value of the superheating field. Indeed, these two heavily doped cavities had super-

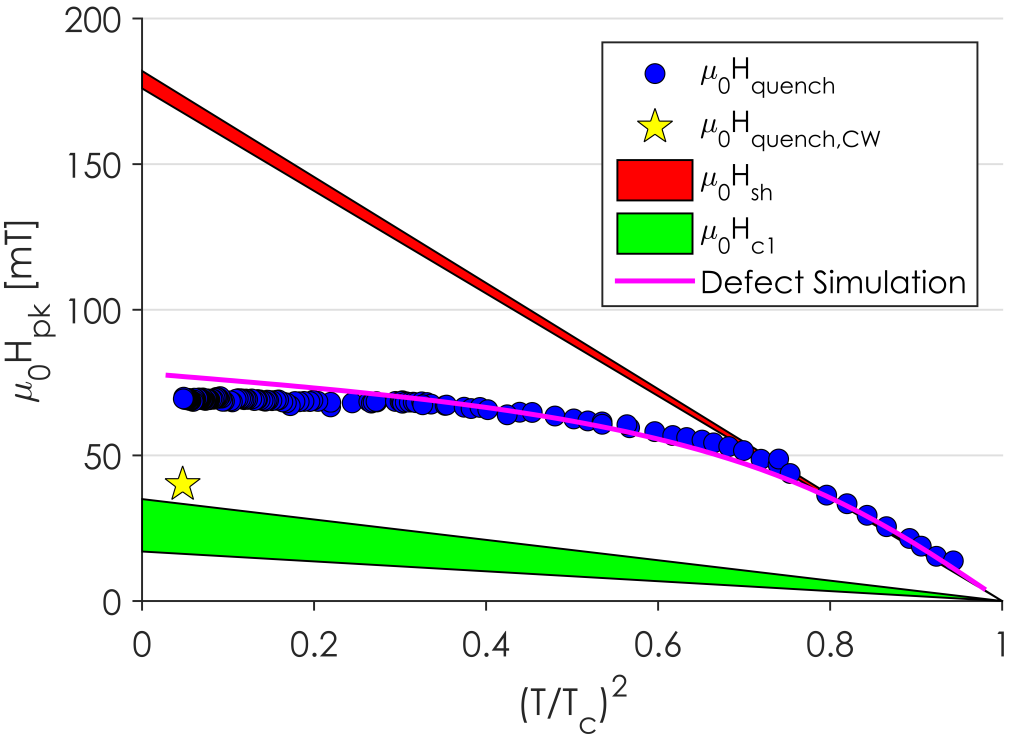

Figure 7.12: B_{pk} vs $(T/T_c)^2$ for LT1-3. Near T_c, quench field follows the superheating field. However at lower temperatures, quench field is significantly lower than B_{sh} but still well above B_{c1}, consistent with a quench at a defect. CW quench field is also shown and can be seen to be significantly higher than B_{c1}. B_{c1} and B_{sh} were calculated from extracted mean free path values obtained from CW RF measurements.

heating fields significantly lower (~25%) than that of clean niobium. The degree to which the high temperature data follows the predicted temperature dependence for B_{sh} lends further legitimacy to the method of calculating critical fields from the extracted mean free path.

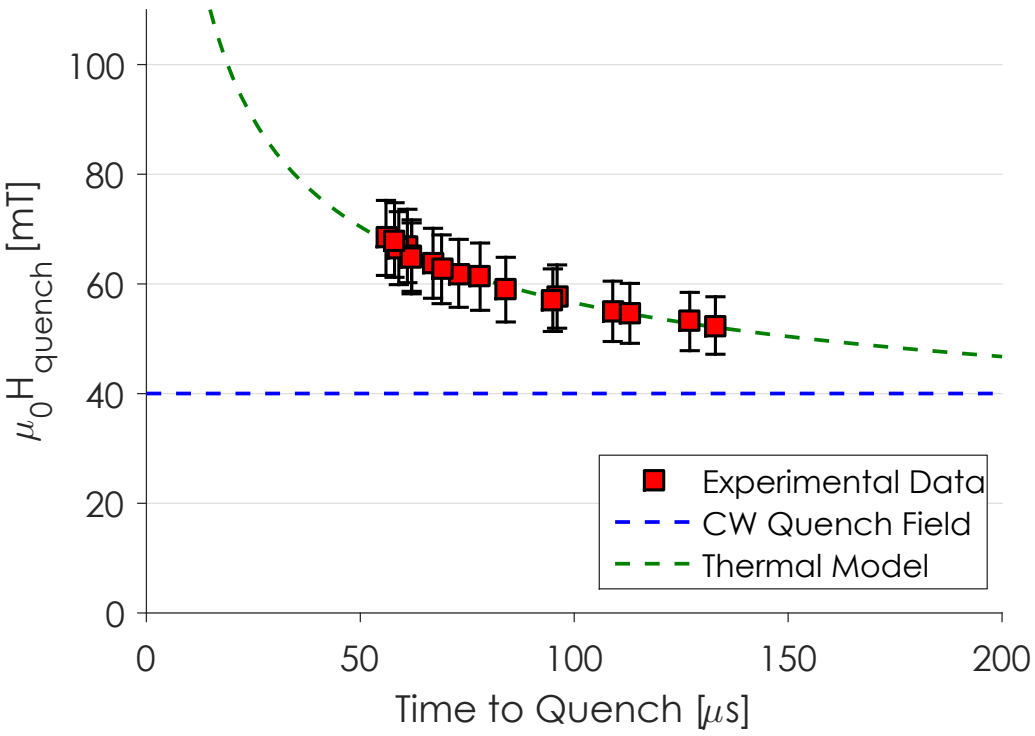

Figure 7.13: Quench field versus time to quench for LT1-3 at 4.2 K. Time to quench was adjusted by changing the forward power of the kylstron. For longer times to quench, the quench field decreased and approached the CW quench field at long times to quench, again indicative of a quench at a defect. Also shown is a simple thermal model which fits the data well.

7.6 Quench Location

If the cavities discussed in the previous section are truly quenching at a defect, a localized quench location should be able to be measured using quench detection. As discussed in Chapter 3, the Cornell Temperature Mapping (T-map) system can be used to detect a cavity's quench location.

Figure 7.14 shows a color plot of the quench location for LT1-2 at 2.0 K. Shown is a grid of the board and resistor numbers colored by the duration that a given resistor stays "warm" during the quench. Recall that each board runs

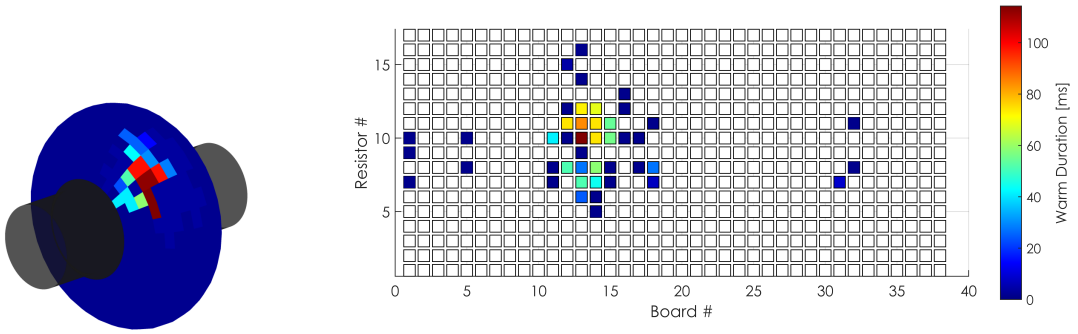

(a) Quench location on the cavity.

(b) Quench location on the temperature map.

Figure 7.14: Quench location at 2.0 K using the temperature mapping system for LT1-2. Quench was centered at one location near the equator (high magnetic field region). This region is most likely associated with a defect due to the quench behavior shown in Figure 7.10 and Figure 7.11.

from iris to iris with resistor 9 sitting on the equator. Indeed for LT1-2 a single quench location was found just above the equator. This confirms the results from pulsed testing which suggested that the quench occurred at a defect.

Since pulsed measurements were unable to decipher if the localized quench was occurring due to early flux entry or a normal conducting defect, LT1-2 (preparation 2, 6 μm VEP) was tested with temperature mapping. By studying the heating prior to quench at the quench location it can be determined if the quench is being caused by a normal conducting defect or flux entry. A normal conducting defect would result in "ohmic heating" in which the increase in temperature on the surface (ΔT) would increase quadratically with the magnitude of the RF field. On the other hand if the quench was due to flux entry, heating would be minimal until just before the quench when flux would start to enter at the defect and manifest as heating. Figure 7.15 shows the average ΔT versus B_{pk}^2 for this cavity. ΔT was averaged over the four temperature mapping resistors centered at the quench location. Indeed heating is minimal until just

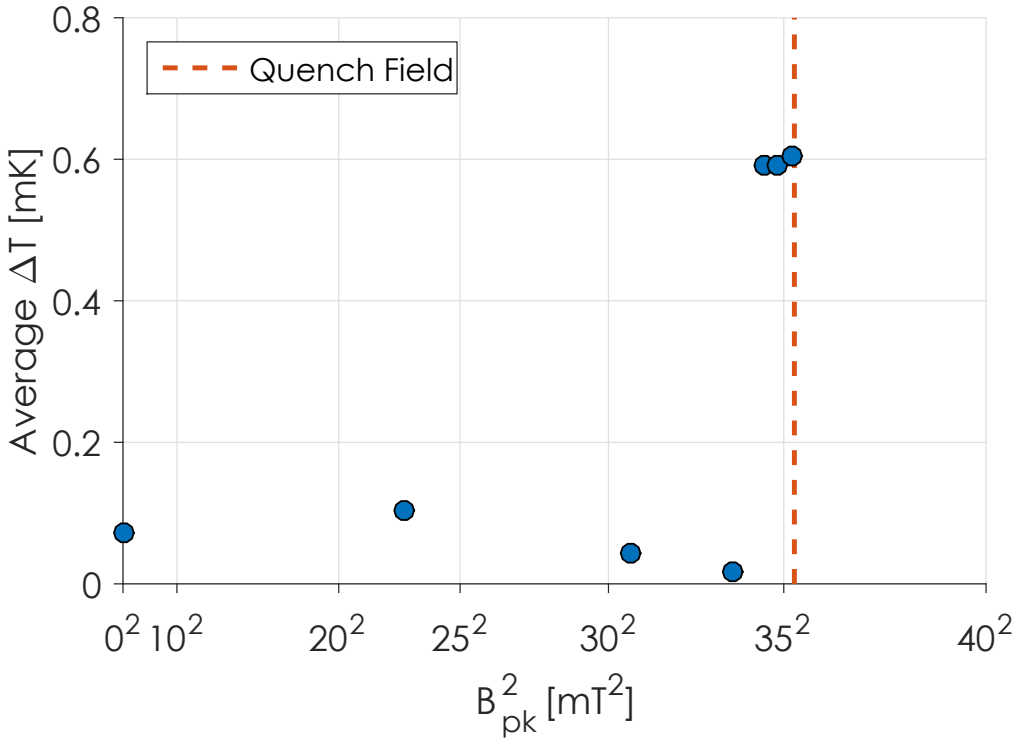

Figure 7.15: Average temperature increase at the quench location of LT1-2 (preparation 2, 6 μm VEP) versus B^2_{pk}. Very little heating is present as the field in the cavity is increased until just prior to the quench field. This is indicative of flux entry at a defect due to the energy barrier dropping to zero.

prior to the quench field at which point there is a sudden increase in the heating. This is very indicative of the quench being due to flux entry: a defect at the quench location caused a lowering of the energy barrier to flux entry and just below quench this energy barrier dropped to zero allowing flux to enter the bulk.

Figure 7.16 shows the quench detection temperature map for the quench of LT1-3 at 2.0 K. Again a single quench location was found, this time centered at resistor 13 (still located in the high magnetic field region). Furthermore, optical inspection was used to study the quench location in LT1-3. A picture of that location is shown in Figure 7.17. There was no visible defect that could be de-

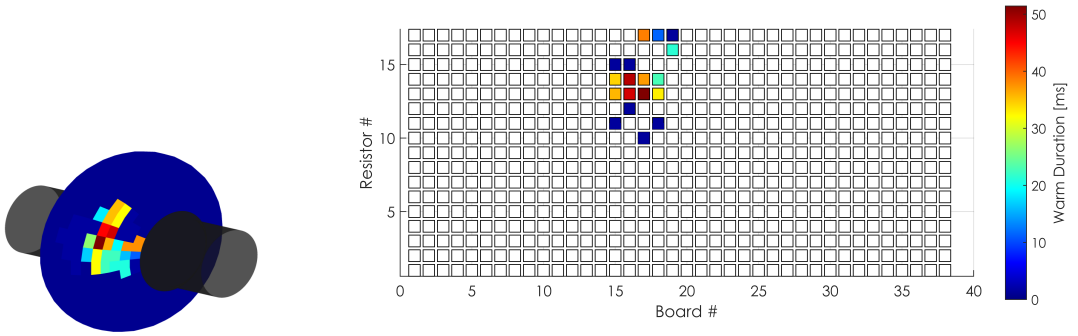

(a) Quench location on the cavity.

(b) Quench location on the temperature map.

Figure 7.16: Quench location at 2.0 K using the temperature mapping system for LT1-3. Quench was centered at one location between the equator and the iris. This region is most likely associated with a defect due to the quench behavior shown in Figure 7.12 and Figure 7.13.

tected optically. It is likely that the defect is small enough that it cannot be seen simply by an optical inspection or is not optically visible if for example the defect was NbN at a grain boundary. This may imply that it will be very difficult to predict via optical inspection if a cavity's quench field will be impacted by nitrogen-doping.

7.7 Summary of High Field Limits

Nitrogen-doping strongly impacts the material properties of niobium, especially the mean free path of the RF penetration layer. This change in mean free path will lead to a significant decrease of the lower critical field, B_{c1}, and to a smaller reduction in the superheating field, B_{sh}. Lowering of these two critical fields has been observed and correlated with quench fields. Moreover studies on both CW quenches and the fundamental quench limits under pulsed operation suggest that nitrogen-doped cavities have quench fields that are limited by

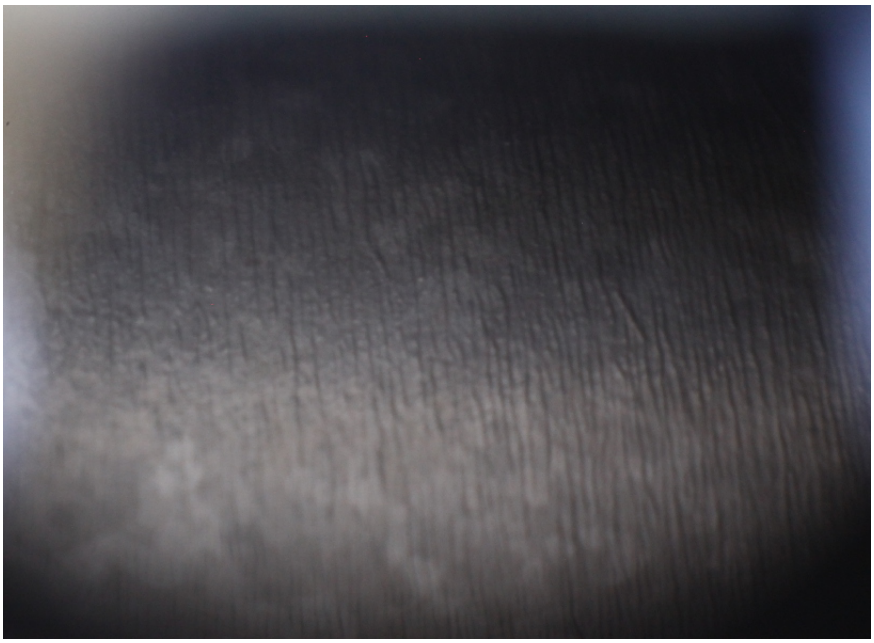

Figure 7.17: Picture of the quench location in LT1-3 as taken by optical inspection. No visible defect is present at the location suggesting that the defect is smaller than is able to be detected optically or not optically visible. Image is approximately 15x10 mm with a resolution of 2.77 μm/pixel.

defects more strongly than un-doped cavities. The quench field was shown to be localized in three single-cell cavities and one 9-cell cavity and is most likely due to early vortex penetration below B_{sh} as was evident by the absence of significant pre-heating at the quench location. The lower quench fields typically observed in moderate to heavily nitrogen-doped cavities are therefore likely a direct result of the lowering of B_{c1} and vortex penetration at the field at which the energy barrier drops to zero at the defect.

The European X-Ray Free Electron Laser (EXFEL) has conducted many cavity tests on 9-cell cavities prepared with standard (un-doped) techniques [Res15]. Figure 7.18 shows a histogram of the usable gradient from these cavities compared with a histogram of the quench fields from the single-cell nitrogen-doped cavities tested for this dissertation. The median usable gradient from the

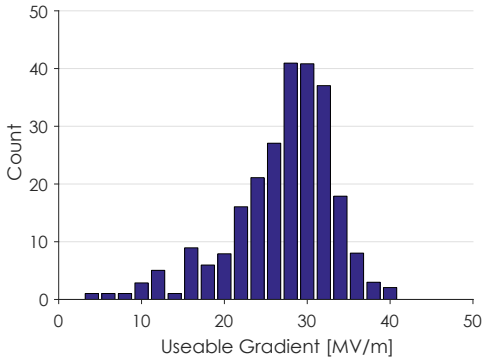

(a) Histogram of usable gradient from EXFEL production. Data from [Res15].

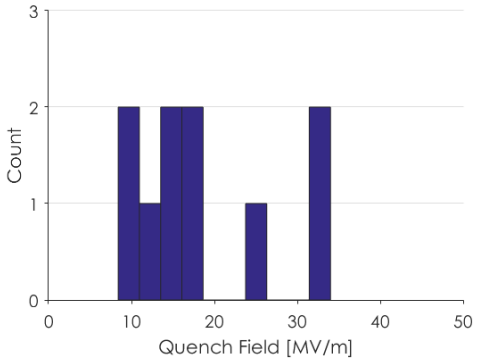

(b) Histogram of the quench field in the single-cell nitrogen-doped cavities tested.

Figure 7.18: Histograms of usable gradient from the EXFEL of 9-cell cavities and the single-cell nitrogen-doped cavities tested for this dissertation.

EXFEL is 30 MV/m compared with an average quench field of ~19 MV/m from the doped cavities. Assuming the EXFEL cavities represent the expected gradient that can be achieved with standard preparation techniques, this represents a 37% drop in quench field due to nitrogen-doping on average. Compare this with a 34% drop in average B_{c1} from clean niobium to nitrogen-doped niobium. While the statistics on nitrogen-doped cavities are limited, this is certainly in agreement with the measurements presented here which suggest that lowering of B_{c1} plays a significant role in the quench field reduction due to nitrogen-doping.

CHAPTER 8

CRYOMODULE TESTS

This chapter focuses on the performance of nitrogen-doped cavities in the Cornell Horizontal Test Cryomodule (HTC). It begins with a discussion on why horizontal testing is necessary for prototyping of large-scale SRF driven accelerators and then gives a brief introduction to the HTC and the organization of the HTC tests conducted. Next a discussion on the changes in cavity performance from vertical to horizontal test is presented for each of the HTC tests. Two important SRF application issues are then discussed, the dependence of Q_0 on the cavity beam tube temperature, and conditioning of field emission by using a different TM010 mode than the fundamental. Next a study of the cool down mechanics and their impact on cavity performance in cryomodules is discussed. Following this, a further discussion of the impact of magnetic field on cavity performance is presented as an extension of the work on single-cell cavities presented in Chapter 6. Then a model for optimization of cool down based on the cryomodule ambient magnetic field conditions combined with the impact of thermoeclectric currents is presented. Finally a discussion of the impact of the high power input coupler on cavity performance is discussed.

8.1 Why Horizontal Testing?

Horizontal testing of SRF cavities is an important step during development and production of modern particle accelerators that use SRF cavities. This is especially important as machines move towards using many large cryomodules holding multiple cavities. For example, LCLS-II requires 35 cryomodules each holding eight 9-cell cavities. Due to the large scale of these cryomodules, a full

prototype test can be very expensive and time consuming. However, very important lessons can be gained by testing in a cryomodule that are not possible to be learned when testing cavities vertically. In vertical test, it is relatively easy to achieve perfect cool down conditions, minimize the ambient magnetic field due to excellent magnetic shielding, and assemble cavities cleanly due to the nature of the geometry of the vertical test system and the use of a high Q input coupler as opposed to a high power RF coupler (the assembly of which can produce significant contamination that can lead to field emission). Horizontal testing on the other hand consists of assembling the cavity in a realistic cryomodule environment and allows for a happy medium in which real cryomodule conditions can be tested without having to assemble a full cavity string with many cavities. It provides a useful tool for prototyping cryomodule parts and checking performance changes from vertical to horizontal tests along with giving the user the ability to discover issues that may arise during production of full cryomodules. While there is no fundamental reason why cavity performance should be affected by cavity orientation, data from laboratories around the world has shown consistently lower Q_0 is horizontal testing than in vertical [Hoc13]. These differences can arise from cleanliness of the cavity and coupler assemblies, cool down conditions in a cryomodule, manifestation of thermoelectric currents, and the impact of using a high power coupler.

8.2 Introduction to the Cornell HTC

The Cornell Horizontal Test Cryomodule (HTC) was originally constructed as a test bench for the Cornell ERL program using a 7-cell cavity [Val13]. It has since been modified to hold a standard 9-cell Tesla shaped cavity for prototyping of

the LCLS-II cavities. The HTC accepts a cavity that is dressed with helium tank and the cavity is suspended from the helium gas return pipe (HGRP) just as in a full cryomodule. The cross-section of the HTC is very similar to the proposed LCLS-II cryomodule and in practice represents a one-cavity section of that cryomodule. A schematic of the HTC fitted with a 9-cell cavity is shown in Figure 8.1. The main difference between the HTC and the LCLS-II cryomdoule is the use of active cooling on the high power coupler by means of an 80 K and 5 K helium gas system as opposed to thermal strapping as will be used in the LCLS-II cryomodule. This may impact the performance of the coupler by improving cooling when compared with the production system. Additionally, the HTC has an 80 K shield while the LCLS-II cryomodule has a 40 K shield, which slightly impacts the thermal static loads of the cryomodule.

In addition to an active helium gas shield, multi-layer insulation (MLI) is used to reduce the total static heat load of the cryomodule. The HTC has a stainless steel vacuum vessel with magnetic shields surrounding the 80 K shield and the cavity's helium vessel. The LCLS-II cryomodule on the other hand has a carbon steel vacuum vessel and a magnetic shield around the cavity at 4 K. Pictures of the assembly at various stages are shown in Figure 8.2. The RF system allowed for control of the cavity with either a phase lock loop or a low level RF system. During HTC9-1,2 and 3 (with high Q input coupler), a 300 W solid state amplifier was used to excite RF fields in the cavity. In HTC9-4 and 5, a 5 kW solid state amplifier was used.

Significant instrumentation was used during the HTC tests to monitor temperatures and magnetic fields during cool downs and RF operations. The cryomodule itself was assembled with Cernox temperature sensors throughout to

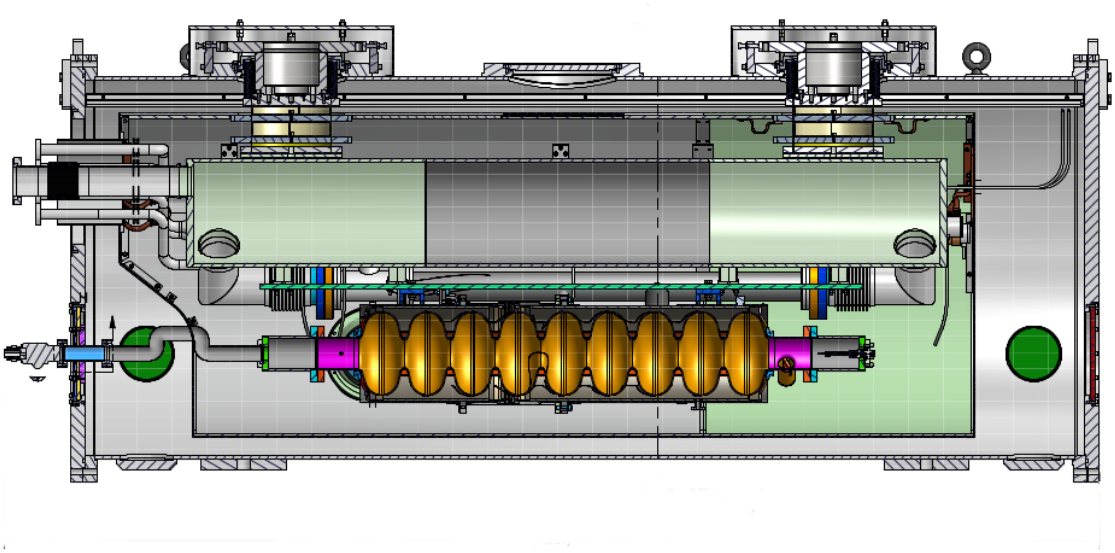

(a) A schematic of the Cornell HTC from the side.

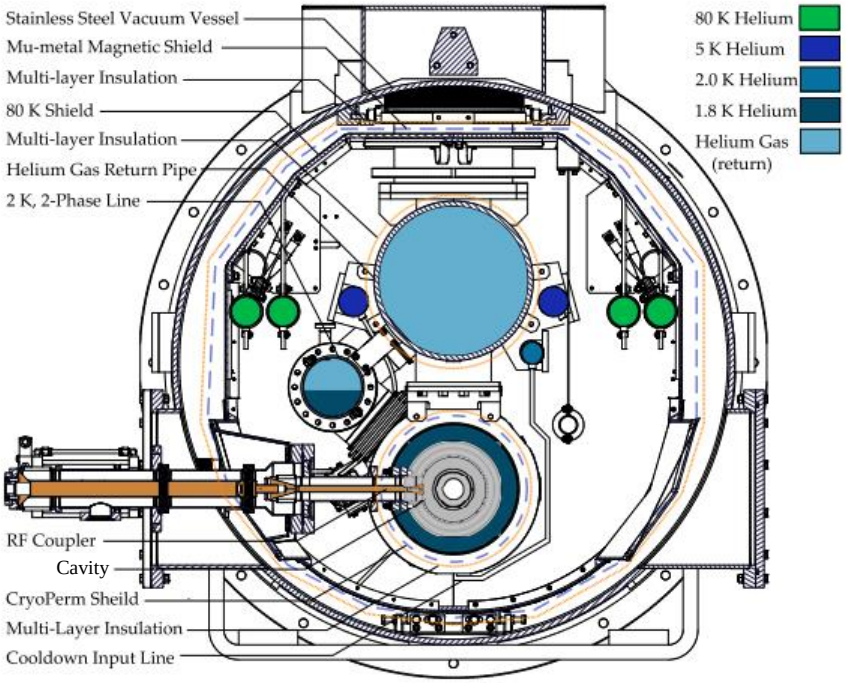

(b) A cross-sectional schematic of the HTC from [Val13] with the major components labeled.

Figure 8.1: A schematic of the Cornell HTC with a 9-cell cavity. The HTC is a close representation to a full cryomodule and is very useful for prototyping and testing prior to production.

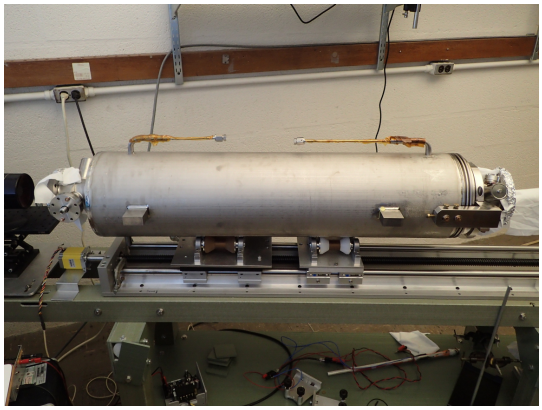

(a) A 9-cell cavity with LCLS-II helium vessel.

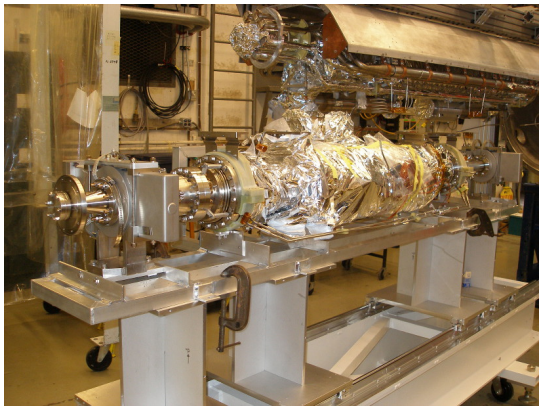

(b) The completed string just after initial MLI assembly.

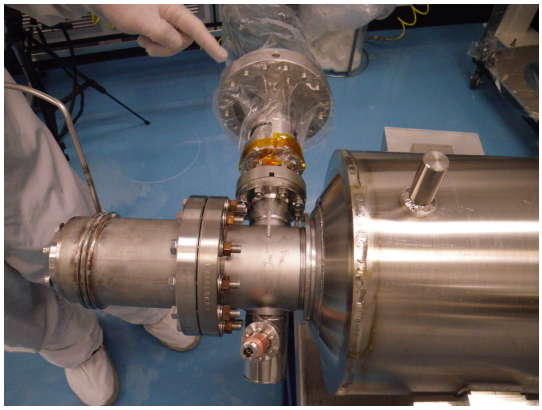

(c) The fully assembled high power coupler on HTC9-4.

(d) The completed HTC on a truck for transport to the testing area.

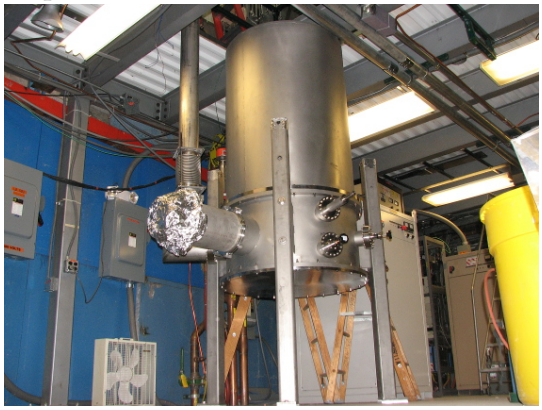

(e) The HEX can prior to connection to the HTC.

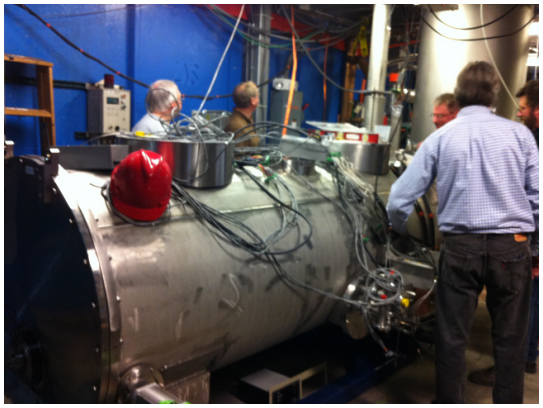

(f) The HTC being connected to the HEX can in the testing area.

Figure 8.2: The HTC during various stages of assembly

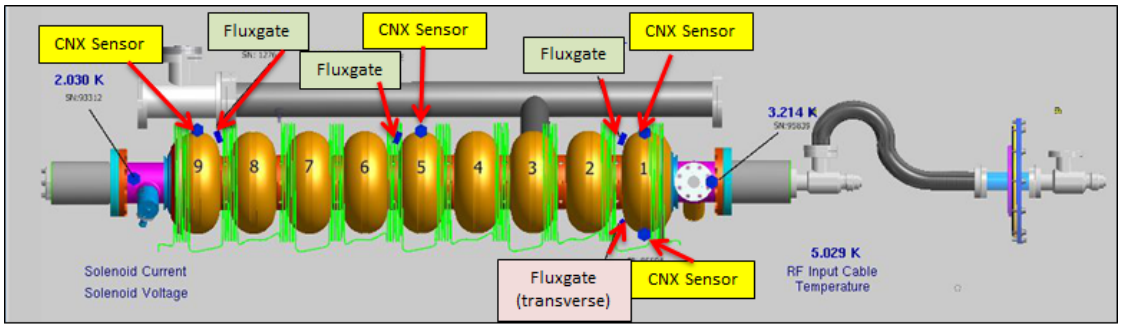

Figure 8.3: A schematic showing the instrumentation locations in HTC9-2. Cernox temperature sensors are marked with blue circles and fluxgate magnetometers with blue rectangles. Other HTC tests had similar configurations of temperature sensors and fluxgate magnetometers.

measure temperatures of the components during cool down and testing and fluxgate magnetometers to measure the ambient magnetic fields during cool down. Figure 8.3 shows the locations of the Cernox sensors and fluxgate magnetometers in the HTC9-2 test. The other HTC tests had similar instrumentation configurations. Cernox temperature sensors were typically placed on the tops and bottoms of cells 1, 5, and 9, on the coupler ports, and on both beam tubes. For HTC9-4 and HTC9-5 there were also temperature sensors placed on the 5 K and 80 K gas lines for the high power RF coupler. HTC9-5 also had temperature sensors placed on the HOM cans.

Fluxgate magnetometers measure magnetic fields parallel to their axis and were typically placed to measure fields parallel to the cavity axis (usually denoted B_{long}) and perpendicular to the cavity axis (usually denoted B_{perp}). Radiation monitors were also placed outside of the cryomodule inline with the beam tubes. In HTC9-2, a small heater was placed on one of the beam tubes in order to control the horizontal temperature gradients and measure the effects of beam tube heating on cavity Q_0.

8.2.1 Organization of the HTC Tests

In total, five tests in the HTC were conducted as part of the LCLS-II High Q Program and will be discussed here. They were organized in such a way to answer three questions:

1. Can vertical cavity performance be maintained in a cryomodule?
2. Can nitrogen-doped cavities be cooled adequately to minimize the effects of ambient magnetic field and thermoelectric currents?
3. Does the high power input coupler inherently degrade cavity performance?

A summary of the HTC tests is shown in Table 8.1. Four different cavities were tested in total. The first two HTC tests, using cavities prepared by FNAL, were meant as a proof of principle, using a high Q input coupler (making it easier to measure Q_0) and an ILC type helium vessel (see Figure 8.16a for a schematic of the ILC type helium vessel). In the second HTC test, a coil was placed around the cavity to apply an external magnetic field for studying the impact of ambient field on cavity performance and a heater was placed on one of the beam tubes to generate a large horizontal temperature gradient during cool down to induce a large thermoelectric current.

The next two tests were with the same cavity, prepared at Cornell, first with a high Q input coupler and then with the LCLS-II high power input coupler (HPC). The purpose of this test was to measure changes in Q_0 performance directly due to assembly of the coupler without changing anything else. An LCLS-II type helium vessel (see Figure 8.16b for a schematic of the LCLS-II type

Test	Cavity Name	Prepared By	RF Coupler	Helium Vessel	Other
HTC9-1	ACC012	FNAL	High Q	ILC	
HTC9-2	AES011	FNAL	High Q	ILC	Coil, Heater
HTC9-3	AES018	Cornell	High Q	LCLS-II	Solenoid
HTC9-4	AES018	Cornell	LCLS-II	LCLS-II	
HTC9-5	AES031	TJNAF	LCLS-II	LCLS-II	Tuner, HOM Couplers

Table 8.1: A summary of the completed HTC tests. "Other" column lists auxiliary parts assembled on the fully assembled cavity for further diagnostics. The high Q input coupler had a $Q_{ext} \approx 10^10$ for use with the 300 W solid state amplifier and the LCLS-II coupler was a high power input coupler with $Q_{ext} \approx 10^7$ for use with the 5 kW amplifier.

helium vessel) was also used to study cavity performance under realistic cool down conditions. A solenoid was placed around the cavity in HTC9-3 in order to apply a uniform external magnetic field parallel to the cavity axis to measure the effects of ambient magnetic field on cavity performance in a realistic accelerator environment.

The final HTC test was on a fully dressed cavity prepared at TJNAF. The cavity was assembled with LCLS-II type helium vessel and input coupler and with the tuner and HOM couplers. This allowed for a full prototype test of a cavity ready for assembly in the LCLS-II string.

Each cavity was prepared with nitrogen-doping. An exact description of the preparations for each cavity is shown in Table 8.2. In addition to these preparations, extracted material parameters for HTC9-1, 2, and 3 are given in Table 8.2. These materials were extracted using the methods described in section 3.4.

Test	HTC9-1	HTC9-2	HTC9-3/4	HTC9-5
Bulk Treatment	CBP and EP	EP	VEP	EP
Initial Heat Treatment	800°C, 3 hours	800°C, 90 minutes	800°C, 3 hours	800°C, 3 hours
N-Doping	25 mTorr, 20 minutes	60 minutes[1]	60 mTorr, 20 minutes	20 minutes
Anneal Time	30 minutes	None	30 minutes	30 minutes
Final EP	18 μm	10 μm	24 μm	26 μm
$\mathbf{T_c}$ **[K]**[2]	9.2±0.2	9.2±0.2	9.2±0.2	N/A
$\Delta/k_B\mathbf{T_c}$ [2]	1.94±0.02	1.94±0.02	2.03±0.02	N/A
Mean Free Path [nm][2]	58±17	29±9	N/A	N/A

Table 8.2: HTC Cavity Preparation and Extracted Material Parameters

[1] Mix of Argon and Nitrogen (exact amount of N_2 unknown)
[2] Material properties extracted using the methods described in section 3.4

8.3 Measuring Q_0 Cryogenically

During cavity operation, RF power is dissipated in the cavity walls and is absorbed in the liquid helium bath. The accelerating field can be measured directly via RF field pick-up signals and power meters and used to calculate the stored energy based on the constant $E_{pk}/\sqrt{U}$ which is calculated with computer codes (see Table 2.2). Likewise, the resonance frequency of the cavity can be measured directly with a frequency counter. Then a measurement of the dissipated power in the cavity walls will lead to a measurement of Q_0 based on Equation 3.1.

When a cavity is assembled with high Q input coupler ($Q_{ext} \sim Q_0$), measuring Q_0 is done exactly as outlined in Chapter 3 by measuring RF power decay. However, in a realistic cryomodule, the high power RF input coupler has a significantly stronger coupling in order to properly match beam load during operation. Because $Q_{ext} \gg Q_0, \beta \gg 1$, which would lead to significantly large errors in measurements of Q_0. Therefore Q_0 must be measured via a direct measurement of the dissipated power in the cavity walls which is absorbed in the helium bath. This method has been shown to have good agreement with RF decay measurements [Val13]. Two methods were used to measure the dissipated power cryogenically: a measurement of the total helium mass flow using a mass flow meter (effectively counting helium atoms which pass), and a measurement of the helium gas flow from boil off using a flow meter (measured in L/min of helium gas at 2 K). The helium gas boil off came directly from the helium boil off in the cavity's helium vessel. For HTC9-4 and HTC9-5 both of these methods were used and averaged to find a reliable Q_0.

The residential gas mass flowmeter measures mass of helium gas passing

and can be converted to energy via the specific heat and volume of the gas. The gas meter continuously counts energy passing, therefore the power is the slope of energy versus time on the gas meter.

The gas flow meter reads a volume of helium gas at 2 K that passes in a given amount of time. This is measured in liters of helium gas per minute. A simple relation can be used to calculate the dissipated power leading to this amount of gas flow based on the latent heat of vaporization,

$$P_{diss,gf} = \frac{f \cdot L_v}{a}, \tag{8.1}$$

where f is the gas flow in L/sec, $a = 5.9\,\mathrm{L/g}$ is the mass of helium atoms in a liter of gas at 2 K and $L_v = 23.2825\,\mathrm{J/g}$ is the latent heat of vaporization of helium.

In addition to a measurement of the total dissipated power, the static head load of the cryomodule must be known in order to accurately extract the dissipated power of just the RF fields in the cavity. For each measured Q_0 point, the static head load of the system was measured just after the total dissipated power measurement. Typically the RF was turned on in the cavity and held at constant field for ~30 minutes. Then the RF was turned off for an additional ~30 minutes. The dissipated power over each entire interval was then calculated. The dissipated power in the cavity then is the static dissipated power subtracted from the total dissipated power.

8.4 Modal Analysis for Individual Cell R_s

In HTC9-1 and HTC9-2, the Q_0 of other TM010 modes were measured in addition to the Q_0 of the π mode. From these measurements, and the knowledge of

the field distribution for each cavity mode, R_s of each cell pair can be calculated. Due to the symmetry of the cavity, it is impossible to separate into individual cells. Instead an average R_s of cells 1 and 9, 2 and 8, 3 and 7, and 4 and 6 can be found. The exact R_s of cell 5 is also obtainable. This is calculated through the use of a matrix which represents the relative stored energy (or field squared) in each of the cavity cells for a given mode:

$$\mathbf{M}(n,m) = A \cdot \frac{2}{9} \sin^2\left(\frac{n\pi}{9} \cdot \frac{(2m-1)}{2}\right), \tag{8.2}$$

with n the mode number, and m the cell number (up to 5, 1 through 4 corresponds to the cell pairs). A is either 1 when $m = 5$ or 2 when $1 \leq m \leq 4$. Then with $\vec{Q}$, a vector of Q_0's for each mode (of length 9),

$$\vec{R}_{s,avg} = \frac{G}{\vec{Q}}, \tag{8.3}$$

is the average surface resistance of each mode across the cavity with G the geometry factor. Then the surface resistance, $\vec{R}_s$, of each cell can be calculated

$$\frac{1}{\vec{R}_s} = \frac{\mathbf{M}}{\vec{R}_{s,avg}}. \tag{8.4}$$

The results of this modal analysis will be presented in subsection 8.5.2.

8.5 Changes from Vertical to Horizontal Test

It is useful to discuss the changes from vertical test (VT) to horizontal test (HT) in order to quantify any changes that may be directly related to assembly of cavities in a cryomodule. For the cavities discussed here, any changes in the total surface resistnace, R_s, have been shown to be due only to changes in the residual resistance, R_{res}, and not due to changes in the BCS Resistance, R_{BCS} [GEF+15].

Possible causes of changes in performance between VT and HT are larger ambient DC magnetic fields in the HTC compared with our vertical test dewar, less efficient magnetic flux expulsion due to imperfect cool down conditions, the presence of thermoelectric currents, and increased field emission loading due to the difficulty of assembling a cavity in a cryomodule cleanly. A summary of the changes between VT and HT are shown in Table 8.3. It is important to note that there are three steps of interest: vertical test prior to helium tank dressing, vertical test after helium tank welding (not conducted in HTC9-1 or HTC9-2), and horizontal test after helium tank welding. It is crucial to understand if changes in performance are coming directly from assembly in the cryomodule or from issues that arose during helium tank welding. From Table 8.3 it is clear that the most significant changes occurred between tank welding. On average the change in R_{res} from vertical test (after welding) to horizontal test for the four tests discussed was 1 ± 1 nΩ. This shows that there is virtually no degradation due to assembly in the cryomodule!

8.5.1 HTC9-1

In vertical test, prior to helium tank welding, ACC012 quenched at 15±1 MV/m compared with 14±1 MV/m in HTC9-1. However between these two tests, the cavity was re-tuned for field flatness which can have an impact on the quench field on the ±5% level. Therefore it is reasonable to assume that this change in quench field was a result of the tuning and not assembly in the HTC.

A comparison of the 2.0 K Q_0 versus E_{acc} performance between vertical and horizontal test for this cavity is shown in Figure 8.4. In vertical test (prior to

Test	Vertical Q_0 Un-dressed	Vertical Q_0 Dressed	Horizontal Q_0 Dressed	ΔR_{res} [3] [nΩ]	ΔR_{res} [4] [nΩ]
HTC9-1	3.5×10^{10}	N/A	3.2×10^{10}	N/A	1 ± 1
HTC9-2	3.4×10^{10}	N/A	2.7×10^{10}	N/A	2 ± 1
HTC9-3[1]	3.2×10^{10}	2.3×10^{10}	2.3×10^{10}	3 ± 1	0 ± 1
HTC9-5[2]	3×10^{10}	2.3×10^{10}	2.3×10^{10}	2 ± 1	0 ± 1

[1] HTC9-4 is not presented here since the cavity was the same as in HTC9-3. Full discussions of the change in performance due to the coupler are given in section 8.11.
[2] Q_0 presented at low fields due to excessive multipacting at high fields in the HTC.
[3] From vertical test, un-dressed to vertical test, dressed.
[4] From vertical test, dressed to horizontal test.

Table 8.3: Changes from vertical to horizontal test. All Q_0 values are for 16 MV/m and 2.0 K unless otherwise noted. Average change in residual resistance between vertical test dressed and horizontal test was ~1 nΩ. Errors on Q_0 are approximately 20%.

dressing), the cavity reached a Q_0 of $(3.5 \pm 0.7)\times10^{10}$ just prior to quench. In horizontal test the Q_0 dropped to $(3.2 \pm 0.6)\times10^{10}$. This change in Q_0 was directly attributed to a change in the residual resistance of 1 ± 1 nΩ [GEF+15]. Within uncertainties, there was no change between vertical and horizontal test, especially considering that the two measurements were done with using different test setups.

8.5.2 HTC9-2

In HTC9-2, the cavity quenched at 20 ± 2 MV/m, consistent with maximum fields during vertical test. The Q_0 versus E_{acc} performance for vertical and horizontal tests are shown in Figure 8.5. Q_0 reached $(2.7 \pm 0.5)\times10^{10}$ at 2.0 K and 16 MV/m in horizontal test, meeting the LCLS-II specification. Comparatively,

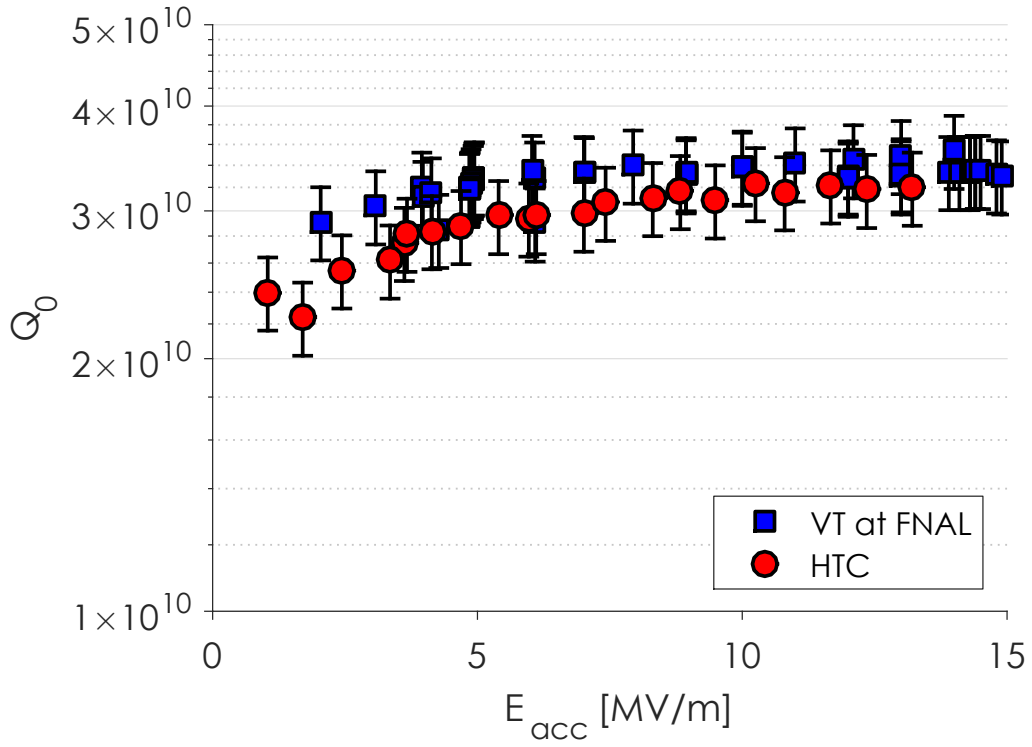

Figure 8.4: Comparison of the Q_0 versus E_{acc} performance of HTC9-1 at 2.0 K in vertical test at FNAL and horizontal test at Cornell. Vertical test data courtesy of Anna Grassellino.

in vertical test prior to tank welding, the cavity reached a Q_0 of $(3.4 \pm 0.7) \times 10^{10}$ at 16 MV/m and 2.0 K. This change again was due to an increased R_{res} of 2 ± 1 nΩ, larger than in HTC9-1. This larger degradation was likely due in part to significant field emission which could not be fully conditioned away. These results are the first proof-of-principle measurement of a 9-cell nitrogen-doped cavity to meet the LCLS-II specification in a cryomodule, a significant milestone of the R&D phase of the LCLS-II project.

As discussed in section 8.4, measurements of the other TM010 modes can be used to find the surface resistance in each cavity cell. Q_0 of these modes was measured at 1.6 and 2.0 K to extract both R_s and R_{res} for each cell. Figure 8.6 shows the residual resistance distribution for the second fast cool down

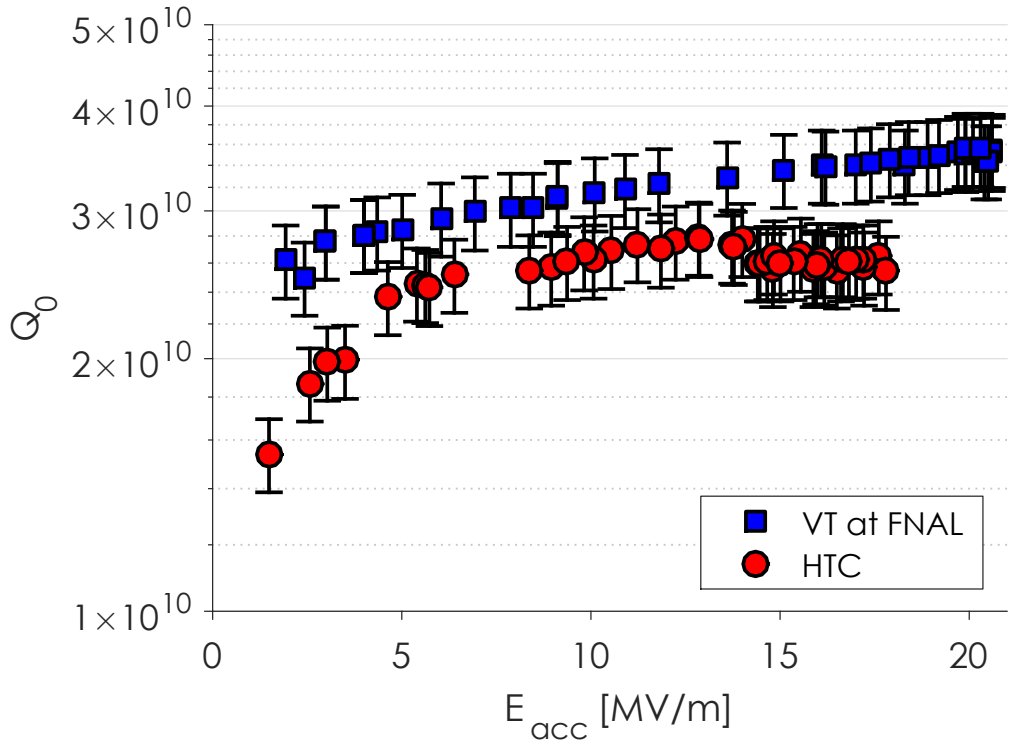

Figure 8.5: Q_0 versus E_{acc} performance of HTC9-2 at 2.0 K in vertical test at FNAL and horizontal test at Cornell. Vertical test data courtesy of Anna Grassellino.

of HTC9-2, demonstrating that residual resistance is not uniformly distributed among the cells. Cell pairs 1 and 9 and 3 and 7 are responsible for the largest contribution to the residual resistance. This non-uniformity could be due to how magnetic flux is expelled in the cavity. As a spatial temperature gradient "sweeps" the magnetic flux out of the superconductor, it is likely that it was trapped in the cells with higher R_{res}.

8.5.3 HTC9-3 and HTC9-4

In vertical test prior to tank welding, AES018 reached a quench field of 20 MV/m and a Q_0 of $(3.2 \pm 0.6) \times 10^{10}$ at 16 MV/m and 2.0 K. After tank welding

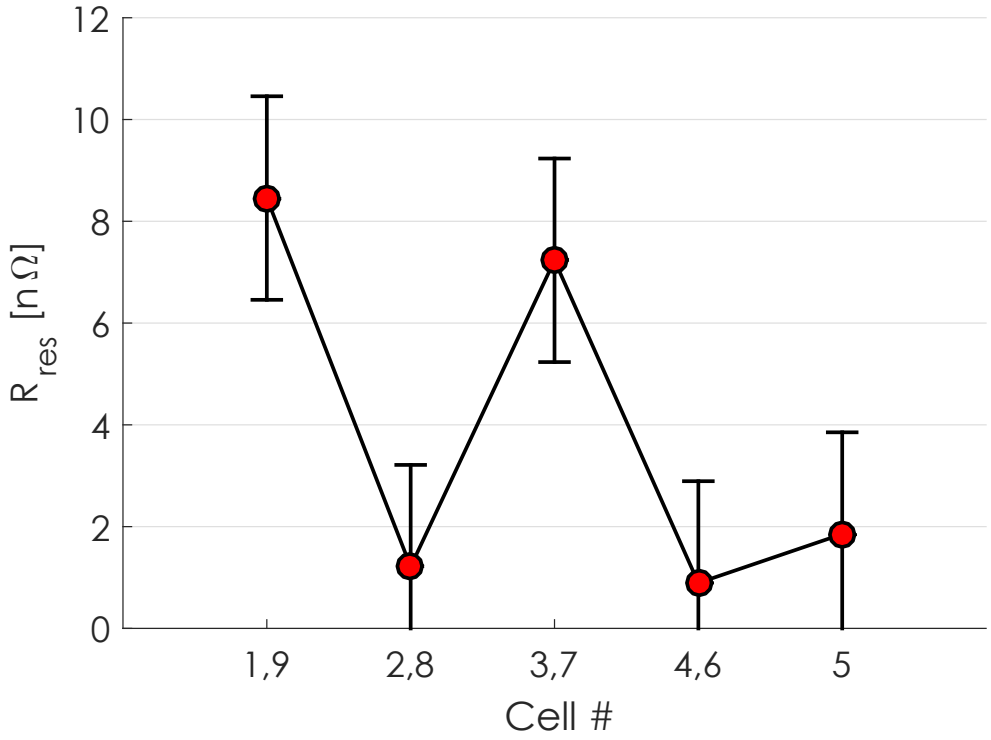

Figure 8.6: R_{res} distribution by cell in HTC9-2. Cell pairs 1,9 and 3,7 had the highest losses. Vertical test data courtesy of Anna Grassellino.

but again in vertical test, the cavity Q_0 decreased to $(2.3 \pm 0.5)\times10^{10}$ at 16 MV/m corresponding to an increase in R_{res} of 3 ± 1 nΩ. After assembly in the HTC the Q_0 was completely unchanged from the vertical test post-dressing. No degradation was observed in the cavity performance due to assembly in the cryomodule. See subsection 8.5.5 for a full discussion on the changes in R_{res} during tank welding. The Q_0 versus E_{acc} at 2.0 K for these tests along with the performance from HTC9-4 with LCLS-II input coupler are shown in Figure 8.7. A discussion on the impact of the coupler will be presented in section 8.11.

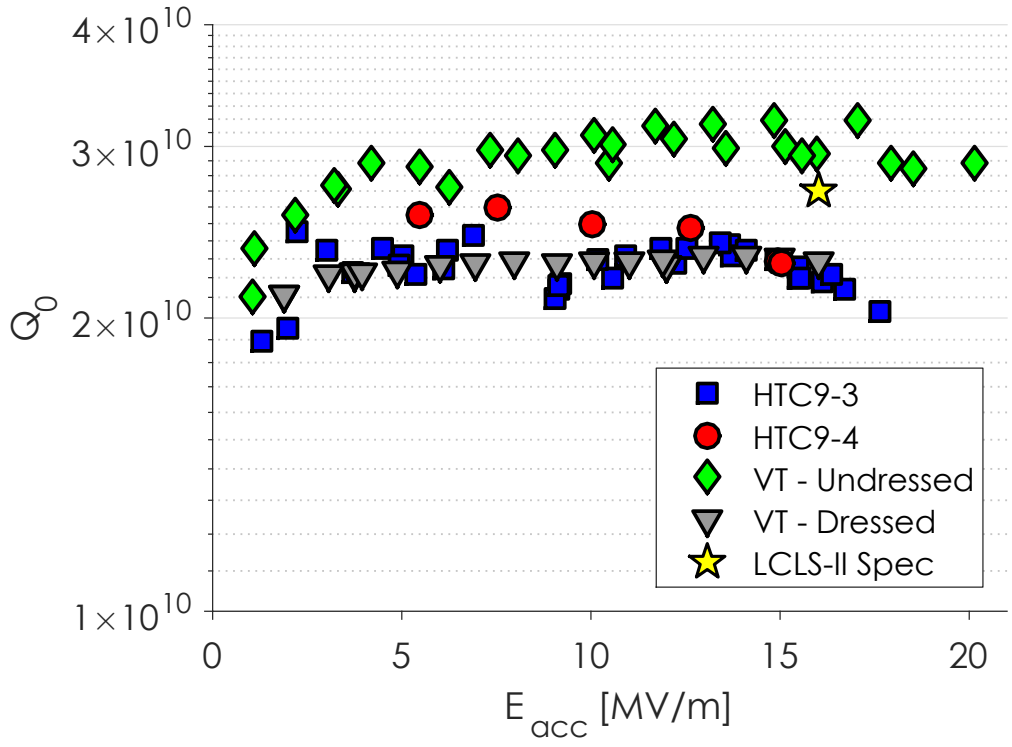

Figure 8.7: Comparison of the Q_0 versus E_{acc} at 2.0 K performance for AES018 before and after helium tank dressing in vertical test and in HTC9-3 (high Q input coupler) and HTC9-4 (LCLS-II input coupler).

8.5.4 HTC9-5

In vertical test at TJNAF, AES031 (used in HTC9-5) reached $(3 \pm 0.6)\times10^{10}$ and more than 20 MV/m at 2.0 K. After helium tank welding, the cavity Q_0 decreased to $(2.7 \pm 0.5)\times10^{10}$ at 16 MV/m and 2 K and a low field Q_0 of $(2.3 \pm 0.5)\times10^{10}$ at 5 MV/m. See subsection 8.5.5 for a discussion on this change between vertical tests. After assembly in the HTC, the low field Q_0 was unchanged, again reaching $(2.3 \pm 0.5)\times10^{10}$ at 5 MV/m. However, at higher fields a large Q slope appeared that severely limited the Q_0 of the cavity and the achievable field. It was found that this Q slope was caused by multipacting in one of the HOM couplers in which the F-part was shorted to the HOM can due to a

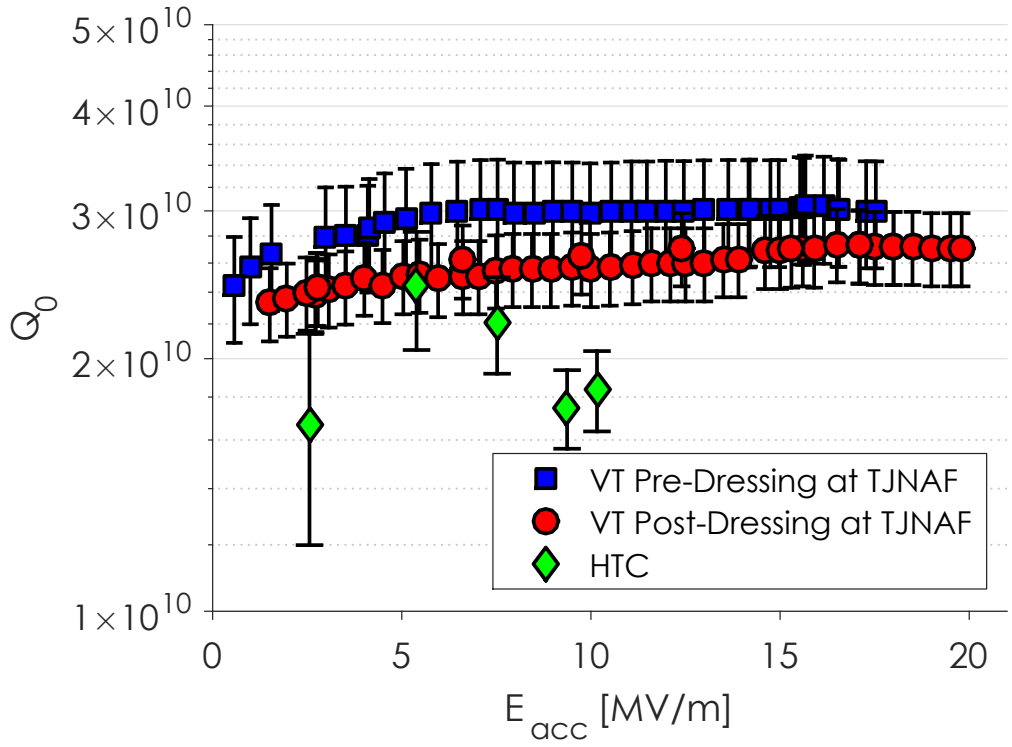

Figure 8.8: Q_0 versus E_{acc} performance for HTC9-5 at 2.0 K before and after dressing and in the HTC. There was a small degradation in Q_0 after tank welding. Low field Q_0 was unaffected by assembly in the HTC however a large Q slope manifested due to multipacting in one of the HOM couplers. Vertical test data courtesy of Ari Palczewski and Kirk Davis.

manufacturing error (see Figure 8.9a). This multipacting resulted in significant heating on the HOM can as is shown in Figure 8.9b which shows the heating on the HOM can as a function of E_{acc}^2. At fields greater than 10 MV/m, heating reached more than 40 K. It is important to note however that the Q_0 of the cavity was unaffected by the cryomodule itself. Degradation in the HTC was due to an auxillary part and machining error.

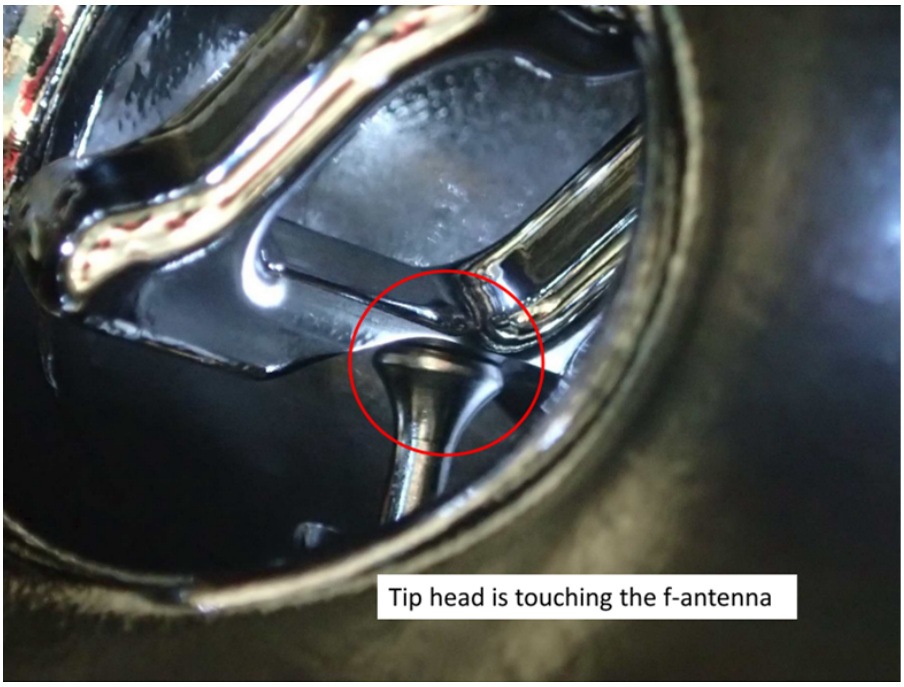

(a) A picture of the F-part touching the tip head of the HOM antenna in HTC9-5.

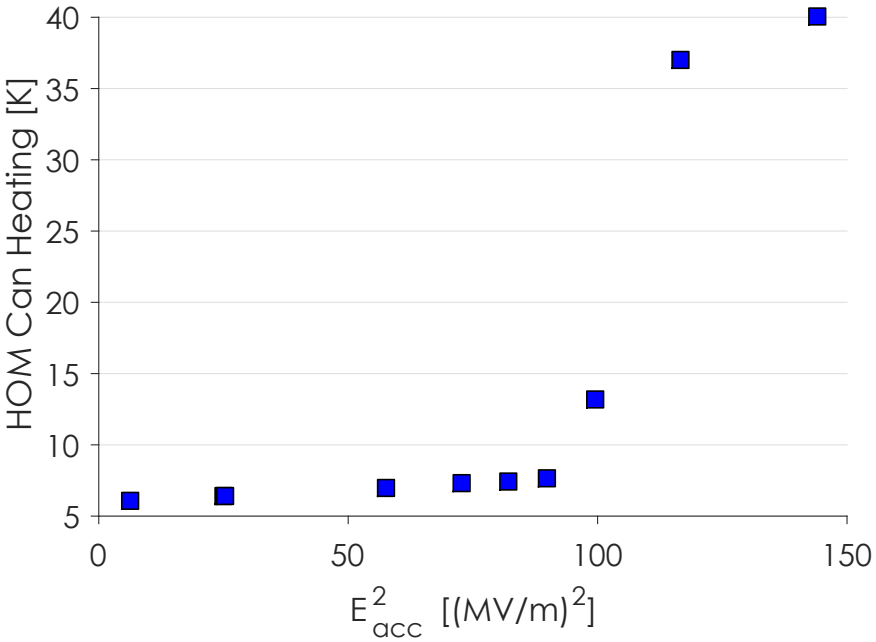

(b) Heating on the HOM can in HTC9-5 due to multipacting versus E_{acc}^2.

Figure 8.9: Short in the HOM antenna and heating on the HOM can in HTC9-5

8.5.5 Excessive HPR and Its Effect on Q_0

All four cavities showed a small increase in residual resistance (1-3 nΩ) between vertical test un-dressed and horizontal test dressed. In HTC9-3/4 and HTC9-5 it is clear that this degradation occurred during the tank welding and was not related to the cryomodule assembly itself. Additionally, it was found that during the course of the HTC program, as cavities were passed between Cornell, FNAL, and TJNAF, they received many hours of high pressure rinsing (HPR). This excessive HPR led to the growth of a lossy oxide layer on the cavity surfaces (see Figure 8.10). This oxide has been identified as the cause of the degradation in performance. It is likely that the degradation observed in HTC9-1 and HTC9-2 also occurred due to this oxide growth and was unrelated to the cryomodule assembly. This demonstrates that there is no inherent risk of degradation in cavity performance due to assembly and operation in a cryomodule: one can expect that good cavities will continue to perform well once fully assembled in a cryomodule.

8.6 Q_0 Dependence on Beam Tube Temperature

When operating a linac in CW, there is a concern that beam tube heating can cause degradation of the cavity Q_0. This is because the beam tubes sit in vacuum in a cryomodule and are only cooled via thermal conduction. This is different in vertical test in which the entire cavity including beam tubes is surrounded by liquid helium. Two studies were completed to test this phenomenon: a measurement of Q_0 vs beam tube temperature to measure when beam tube heating becomes important and a measurement of Q_0 vs time with the cavity at operat-

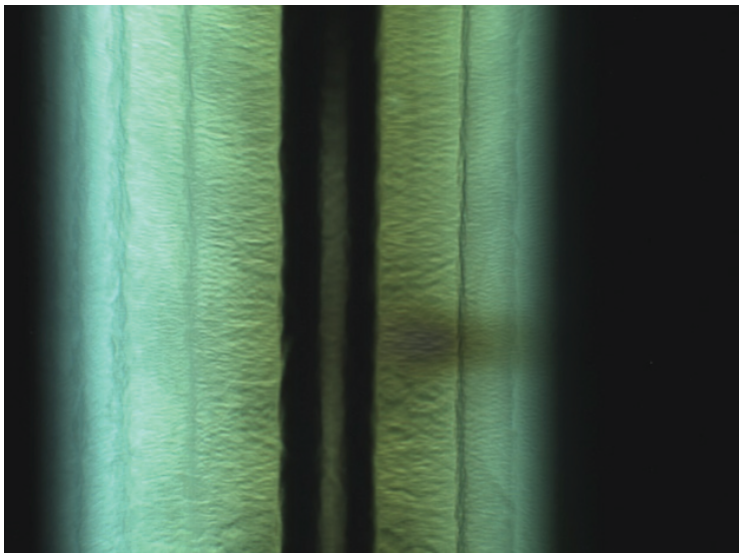

Figure 8.10: Picture of oxidation found at the irises of some of the dressed cavities at FNAL. Picture from [GRM+15].

ing temperature and gradient to see if normal operation would cause significant beam tube heating and Q_0 degradation.

During the fifth fast cool down of HTC9-2, Q_0 was measured as a function of beam tube temperature (see instrumentation locations in Figure 8.3). Using the heater attached to the beam tube on cell #9, the beam tube's temperature was increased. Q_0 at 2.0 K and 10 MV/m was measured to check the dependence of Q_0 on beam tube temperature. The results shown in Figure 8.11 demonstrate that Q_0 is unaffected by the beam tube temperature until it reaches 7 K where Q_0 begins to drop substantially.

In order to explore if this effect would have a strong impact on Q_0 during CW cavity operation in LCLS-II the Q_0 at 16 MV/m and 2.0 K (operating temperature and gradient) was measured as a function of time that the cavity was at field. These results are shown in Figure 8.12. Also shown are the two beam tube temperatures and the cavity temperature. The cavity temperature was un-

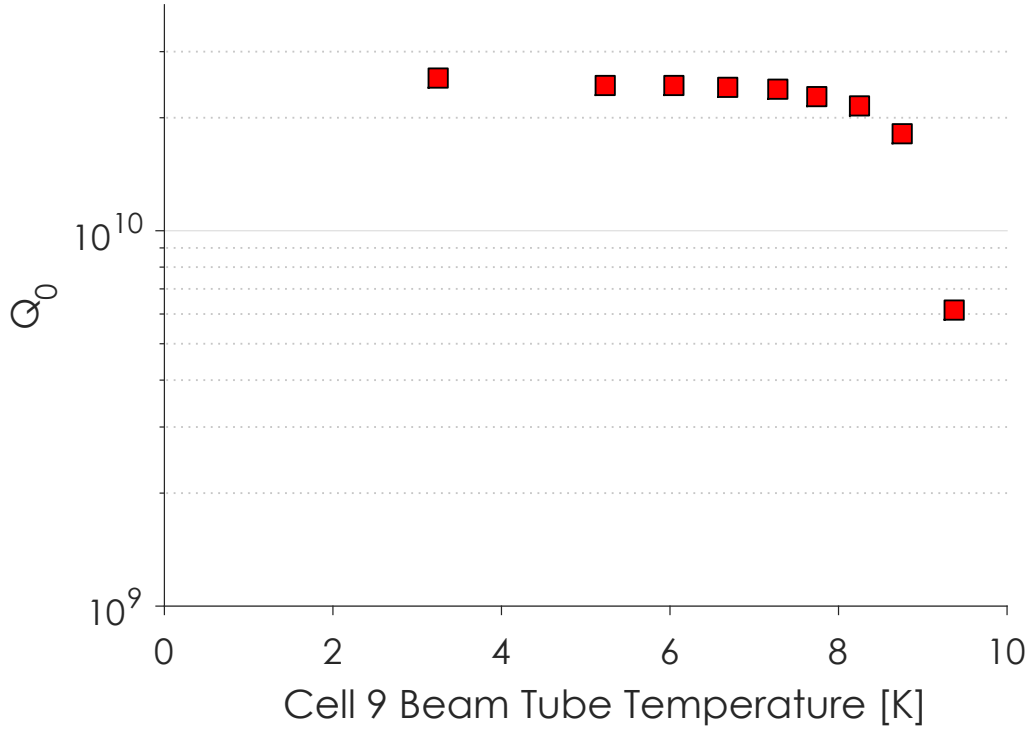

Figure 8.11: Q_0 at 2.0 K and 10 MV/m as a function of beam tube temperature in HTC9-2.

affected. Initially the beam tubes increased in temperature by ~0.5 K and then stabilized around 5 K. The data shows that Q_0 of the cavity was not significantly impacted by this temperature increase, in agreement with the results of the measurements of Q_0 as a function of beam tube temperature. These results demonstrate that end-group heating in continuous LCLS-II cavity operation can be kept low enough so as to not significantly reduce the high Q_0 of nitrogen-doped cavities.

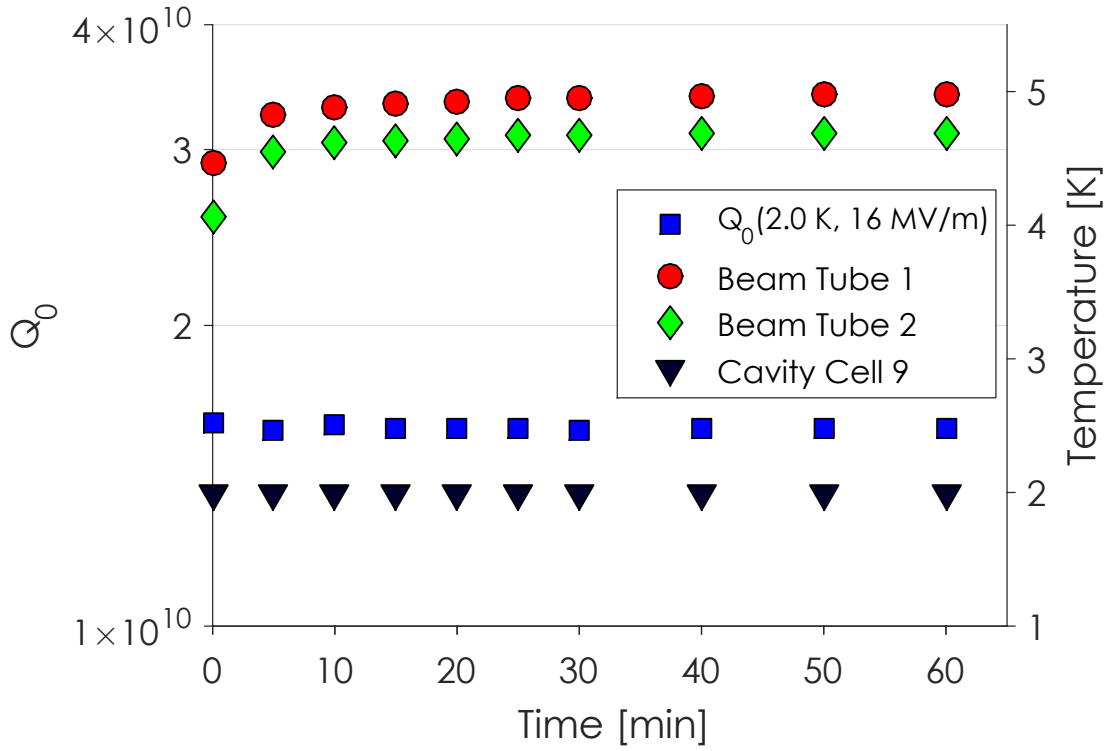

Figure 8.12: Q_0 at 2.0 K and 16 MV/m as a function of time with the cavity field on in HTC9-2. Also shown are the two beam tube temperatures and cavity temperature as a function of time.

8.7 Conditioning of Field Emission in HTC9-1

During the first test of HTC9-1, radiation was very high, ~100 R/hr at 13.5 MV/m measured at the end of the cryomodule inline with the beam axis. The field emitter was suspected to be in the end cell on the coupler side and by driving the cavity in the $8\pi/9$ mode, higher fields in the end cells could be reached than in the fundamental mode, in which fields were limited to ~14 MV/m in all cells by quench in one of the cells. The higher end-cell fields in the $8\pi/9$ mode were able to condition the field emitter. This is shown in Figure 8.13, which shows the radiation as a function of maximum accelerating field (accelerating field of the cell with the maximum E_{acc} in a given mode) for the

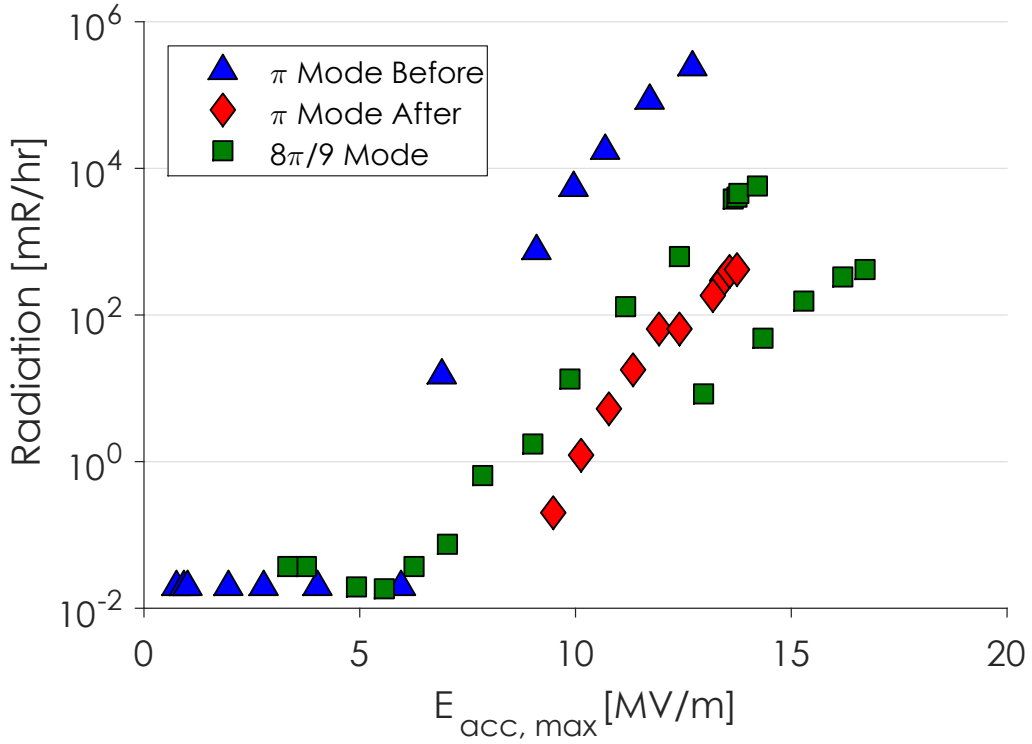

Figure 8.13: Field emission conditioning in the $8\pi/9$ mode for HTC9-1. Radiation in the π mode is also shown before and after conditioning. E_{acc} for the $8\pi/9$ mode is defined as the accelerating field of the cell which has the maximum field. Before conditioning, radiation in the π mode can be seen to reach nearly 100 R/hr. In the $8\pi/9$ mode, radiation increases as E_{acc} is increased until ~15 MV/m at which point the field emitter was conditioned and the radiation decreased by a factor of 1000.

$8\pi/9$ mode and the π mode before and after conditioning. The radiation in the π mode is reduced by a factor of 1000 after conditioning. This demonstrates a powerful method for conditioning field emission in multicell cavities by driving the cavity in a different TM010 mode. Additionally, because the quench field of the fundamental mode was unchanged after conditioning, this confirms that the quench was not caused by field emission, but by some unrelated other type of defect.

8.8 Cool Down Studies

Cool down dynamics are especially important in nitrogen-doped cavities due to the need for efficient flux expulsion to counter the effects of higher sensitivity of residual resistance to trapped magnetic flux when compared with standard prepared cavities as discussed in Chapter 6. This section will outline studies completed in the HTC to understand how cool down dynamics in a realistic cryomodule environment will impact cavity performance and whether necessary flux expulsion can be achieved to reach high Q_0.

8.8.1 Overview of Cool Downs

Due to the ease of Q_0 measurements with the high Q input coupler in HTC9-1, HTC9-2, and HTC9-3 many cool downs were conducted. HTC9-1 included a total of four cool downs. The purpose of these different cool downs was first to condition field emission, then perfect the cool down conditions to reach high Q_0. A summary of these cool downs is given in Table 8.4. HTC9-2 included a total of six cool downs. These were split into three main categories: optimal cool down conditions to reach high Q_0, studies with the solenoid on to understand ambient magnetic field dependence, and studies with the heater on to understand the effects of thermoelectric currents. A summary of these cool downs is given in Table 8.5. HTC9-3 included a total of thirteen cool downs. The purpose of these was to optimize the cool down conditions for high Q_0 and to systematically study the impact of ambient magnetic field on cavity performance, including understanding how spatial temperature gradients and helium gas flow rate during cool down impact flux expulsion. A summary of these cool downs

Parameter	Fast 1[1]	Fast 2	Slow 1	Fast 3
Starting Temp[2][K]	80	80	20	150
$\lvert dT/dt \rvert$ [K/min]	1.4	6.8	0.7	2.4
Max ΔT_{horiz} [K]	0.5	0.2	0.8	2.0
Max ΔT_{vert} [K]	7.9	2.4	0.3	14.1
$\lvert B_{long}(10\ K) \rvert$ [mG]	0.6	0.4	0.2	0.3
$\lvert B_{perp}(10\ K) \rvert$ [mG]	0.3	0.1	0.1	1.5
Q_0 (2.0 K, 14 MV/m)	2.5×10^{10}	2.8×10^{10}	2.5×10^{10}	3.2×10^{10}
R_{res} (14 MV/m) [nΩ]	5 ± 1	4.0 ± 0.8	5 ± 1	2.7 ± 0.5

[1] After field emission conditioning
[2] Starting temperature of fast cool down

Table 8.4: HTC9-1 Cool Down Parameters

is given in Table 8.6.

It is important to note how these parameters are obtained. $\lvert dT/dt \rvert$ is the rate of change in the temperature at the location where the cavity first becomes superconducting when that location is at T_c. ΔT_{horiz} and ΔT_{vert} are the maximum horizontal and vertical temperature gradients, respectively, across the cavity when the first part of the cavity becomes superconducting. $\lvert B_{long}(10\ K) \rvert$ and $\lvert B_{perp}(10\ K) \rvert$ are the longitudinal and perpendicular magnetic fields when the part of the cavity which goes superconducting first is at 10 K (locations of fluxgate magnetometers shown in Figure 8.3).

While HTC9-4 and HTC9-5 were not used for systematic studies on the impact of cool down of cavity performance, for completeness details of the two cool downs in HTC9-4 and the one cool down in HTC9-5 are shown in Table 8.7.

Parameter	Fast 1	Fast 2	Fast 3	Fast 4	Slow 1	Fast 5	Fast 6
Solenoid On	No	No	No	Yes	Yes	No	No
Heater Power[1][W]	0	0	0	0	0	50	100
Starting Temp[2][K]	150	150	80	150	20	80	80
$\lvert dT/dt \rvert$ [K/min]	1.2	1.3	2.2	1.3	0.4	4.7	4.9
Max ΔT_{horiz} [K]	5.2	6.8	9.4	5.9	0.2	21.8	29.4
Max ΔT_{vert} [K]	6.2	8.9	16.1	7.0	0.5	32.5	39.4
$\lvert B_{long}(10\ K) \rvert$ [mG]	1.2	1.2	4.4	10.1	10.6	2.5	3.1
$\lvert B_{perp}(10\ K) \rvert$ [mG]	6.3	0.3	3.1	7.2	1.0	50.3	62.8
Q_0 (2.0 K, 16 MV/m)	2.6×10^{10}	2.7×10^{10}	2.4×10^{10}	1.9×10^{10}	6.2×10^{9}	2.1×10^{10}	1.5×10^{10}
R_{res} (16 MV/m) [nΩ]	5.2 ± 1	4.5 ± 0.9	4.6 ± 0.9	9 ± 1.4	40 ± 8	7.3 ± 0.9	12 ± 2

[1] Heater power of the heater on the beam tube of cell 9 to control horizontal temperature gradients
[2] Starting temperature of fast cool down

Table 8.5: HTC9-2 Cool Down Parameters

Cool Down	**1**	**2**	**3**	**4**	**5**	**6**	**7**	**8**	**9**	**10**	**11**	**12**	**13**
Solenoid On	No	No	No	No	Yes	No	Yes	Yes	Yes	Yes	Yes	Yes	No
$\|dT/dt\|$ [K/min]	27.4	59.4	0.02	2	18.7	23.9	42.7	9.1	0.6	22.4	0.2	37.1	37.9
Max ΔT_{horiz} [K]	N/A	19.1	0.3	4.4	32.9	6.7	9.9	3.9	1.9	4.6	0.9	9.3	4.9
Max ΔT_{vert} [K]	N/A	76.9	2.7	40.1	44.0	69.6	61.8	38.2	16.3	57.1	7.0	71.3	18.8
$\|B_{long}(10\ K)\|$ [mG]	6.2	7.1	2.5	5.7	38.2	0.03	20.0	20.0	20.0	20.0[1]	20.0	20.0[1]	0.02
$\|B_{perp}(10\ K)\|$ [mG]	0.7	3.4	3.1	1.8	3.0	2.5	4.5	0.5	0.5	2.5	2.2	5.2	3.1
He Flow Rate [g/s]	4.7	4.6	0.2	0.4	2.1	1.7	1.5	0.9	0.4	4.0	0.3	3.4	2.3
Q_0 (2.0 K, 16 MV/m)$\times 10^{10}$	2.2	2.1	1.5	2.1	0.88	2.0	1.0	0.80	0.59	1.4	0.58	1.1	1.9
R_{res} (16 MV/m)[2][nΩ]	3.7	4.4	9.9	3.9	22.7	4.4	18.9	26.4	36.5	9.8	42.6	15.6	5.7

[1] Solenoid field in opposite direction compared with other cool downs.
[2] Errors on R_{res} are ~20%.

Table 8.6: HTC9-3 Cool Down Parameters

Parameter	HTC9-4 Cool Down 1	HTC9-4 Cool Down 2	HTC9-5[1] Cool Down 1
|dT/dt| [K/min]	61	23	5.5
Max ΔT_{horiz} [K]	8.2	7.9	7.1
Max ΔT_{vert} [K]	74.2	63.3	31.1
$\|B_{long}(10\ K)\|$ [mG]	10.4	22.1	6.7
$\|B_{perp}(10\ K)\|$ [mG]	1.8	3.7	2.1
Q_0 (2.0 K, 16 MV/m)	1.1×10^{10}	2.3×10^{10}	2.4×10^{10}

[1] Q_0 at 5 MV/m due to large Q slope from multipacting in one of the HOM cans.

Table 8.7: HTC9-4 and HTC9-5 Cool Down Parameters

8.8.2 Vertical vs Horizontal Cool Downs

An important aspect of understanding the effect of cool down on cavity performance is qualifying the difference between how cavities cool in a vertical test dewar and how they cool in the full cryomodule. In the vertical test dewar, liquid helium is typically input from the bottom of the dewar resulting in a temperature gradient between top and bottom of the dewar. This results in a large axially symmetric vertical temperature gradient and small horizontal temperature gradients. A schematic of this type of cool down is shown in Figure 8.14. Because of the nature of vertical testing and the lack of complicated parts in the test setup, the dewar can be cooled very quickly: from room temperature to 4.2 K in only a matter of minutes. This results in spatial temperature gradients on the order of 200 K/m.

In the HTC and in horizontal tests in general, the cavity must be welded into a helium tank. During the five HTC tests, two of the tests were completed with an ILC style helium tank which consists of one cryo-inlet on one side of the vessel and the pumping line on the same side as seen in Figure 8.16a. The other

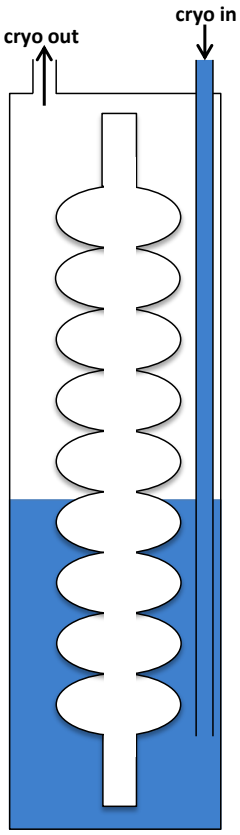

Figure 8.14: A schematic of a vertical test dewar during cool down. Liquid helium is input from the bottom leading to large vertical temperature gradients and small horizontal temperature gradients.

three tests were completed with the LCLS-II style helium vessel, a schematic of which is shown in Figure 8.16b. In the LCLS-II tank, the cryo-inlets are placed symmetrically below the cavity and the chimney is placed in the center of the vessel above cell 5. Due to the complicated nature of cryomodule assemblies, great care needs to be taken to cool the entire vessel slowly and uniformly from room temperature to ~100 K to prevent stress and strain on the vessel and helium gas return pipe (HGRP). This inherently leads to slower cool downs than can be achieved in vertical test. For the HTC cool downs that produced the best results, the vessel was cooled slowly over many hours to ~100 K and then cooled quickly through T_c. Since most thermal contraction happens at tempera-

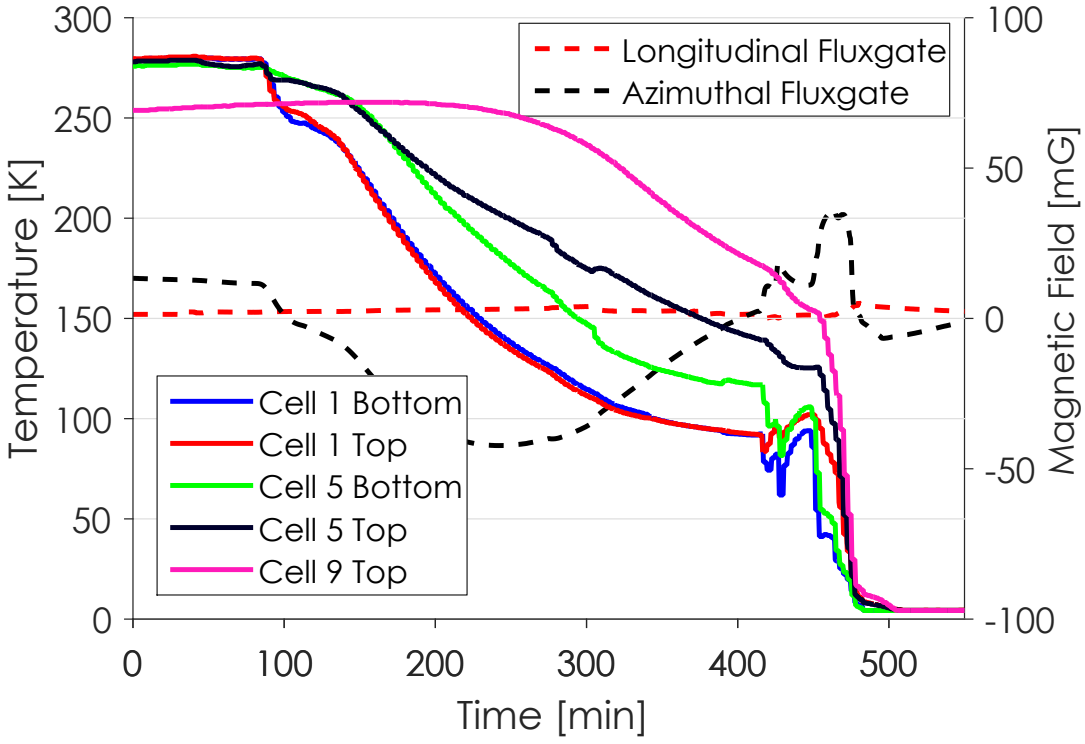

Figure 8.15: A typical cool down from room temperature to 4.2 K using the ILC type helium vessel in HTC9-1.

tures greater than 100 K it is important to cool slowly and uniformly until 100 K at which point faster cooling can be used.

8.8.3 ILC vs LCLS-II Helium Tank

In all cool downs, cooling was done by filling with liquid helium from the bottom of the liquid helium tanks. However it is important to understand the differences in cooling between the two helium vessels used.

In the ILC vessel, the cryogenic input port is located near the bottom of cell 2 on the helium jacket. As an example, the temperatures at various locations around the cavity and magnetic field values of the third fast cool down from

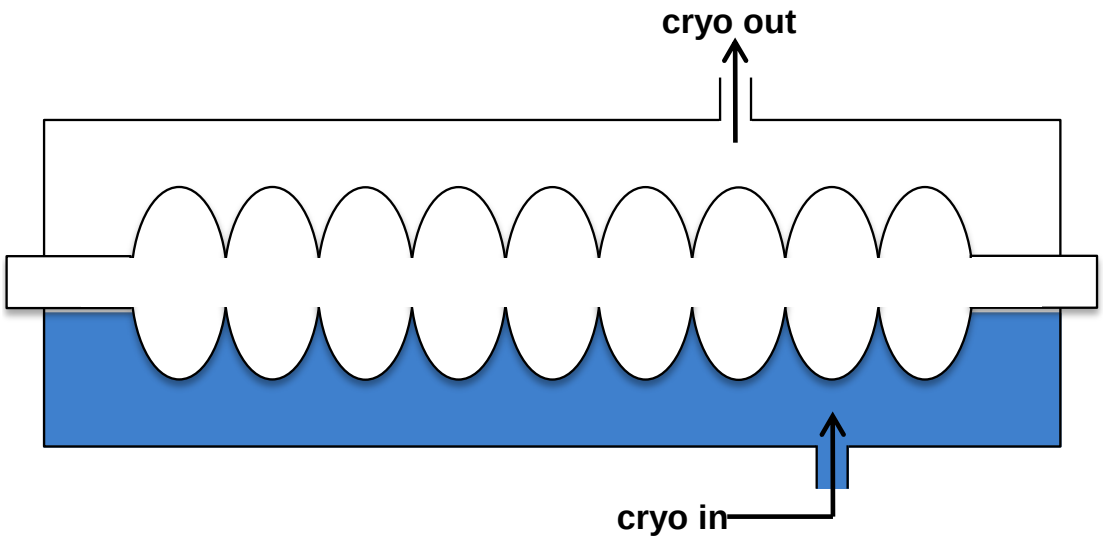

(a) A schematic of how a cavity cools with the ILC type helium vessel in a cryomodule such as the HTC. Liquid helium is input through a single cryo-inlet on the bottom of cell 2. The 2 K-2 phase line is welded to a chimney placed above cell 3.

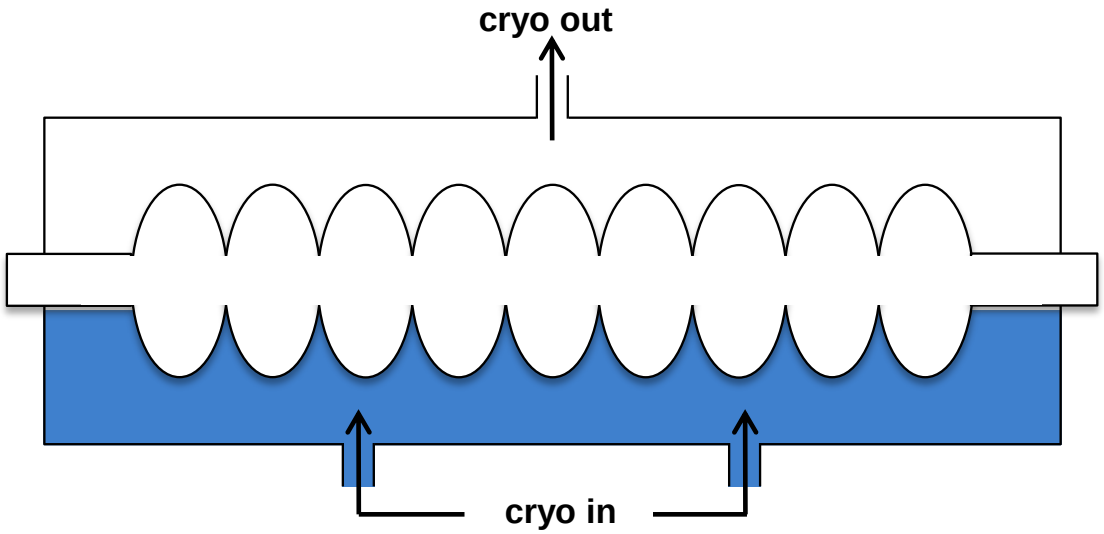

(b) A schematic of how a cavity cools with the LCLS-II type helium vessel in a cryomodule such as the HTC. Liquid helium is input through two cryo-inlets on the bottom symmetrically placed below cells 3 and 7. The 2 K-2 phase line is welded to a chimney placed in the center of the vessel.

Figure 8.16: Differences between cooling in the ILC and LCLS-II type helium vessels

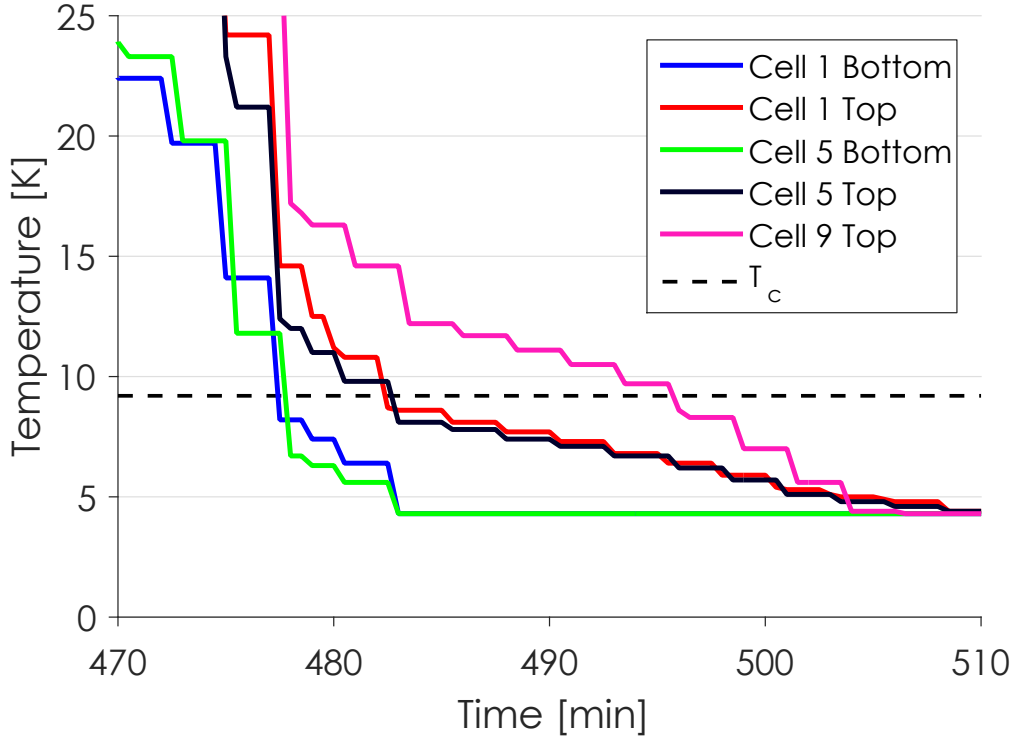

Figure 8.17: A typical cool down in the ILC helium vessel in the region around T_c in HTC9-1. The entire cavity takes about 17 minutes to cool completely from ~10 K to 4.2 K.

HTC9-1 are shown in Figure 8.15 as a function of time from room temperature to 4.2 K. The temperature profiles near T_c where dynamics are most important is shown in Figure 8.17. The cool down data from the fast cool downs consistently shows that the bottom of the cavity cools first. The top of cell 5 follows shortly after and then the top of cell 1. The top of cell 9 cools last, significantly later. Liquid begins accumulation very quickly on the bottom of the tank, resulting in the very fast cooling of the bottom. Due to the location of the chimney (the top of cell 3), gas preferentially flows towards that end, resulting in the tops of cells 1-5 cooling faster than the tops of cells 6-9.

During fast cool down in the HTC, rates on the order of 3 K/min were achieved, similar to what is typically done in fast vertical test. In the fast HTC

cool downs, vertical spatial temperature gradients achieved were 10 to 15 K (corresponding to 50 to 75 K/m), smaller than what can be achieved in vertical test where spatial gradients more than 100 K/m are typically reached in fast cool down. Horizontal temperature gradients are less than 10 K, small enough to minimize magnetic fields from thermoelectric currents, to be discussed in subsection 8.8.5.

The LCLS-II helium vessel was designed to minimize horizontal temperature gradients further and in turn minimize the effects of thermoelectric currents. As discussed above, it has two symmetrically placed cryo-inlets below cells 3 and 7 and the chimney is located in the center of the vessel above cell 5. An example cool down in the LCLS-II vessel from ~100 K to 4.2 K is shown in Figure 8.18 for a fast cool down in HTC9-5. The same cool down near T_c is shown in Figure 8.19. The bottom of cell 5 cools first followed shortly by the bottoms of cells 1 and 9. The top of the cavity cools in a similar manner. The entire cool down from when the first part of the cavity cools below T_c to when the last part does takes only ~5 minutes, significantly shorter than in the ILC tank.

Referring to Table 8.6, in fast cool downs, the vertical temperature gradients during cool down in the LCLS-II helium vessel were as high as 77 K (250 K/m, on the order of what can be achieved in vertical test). This should be sufficient for effective flux expulsion. In similar fast cool downs, the horizontal temperature gradients were as high as 19 K. Vertical temperature gradients significantly higher than in the ILC helium vessel were able to be achieved but along with them came larger horizontal temperature gradients even with the optimized helium vessel design. This could be a result of different heat loads or thermal mass

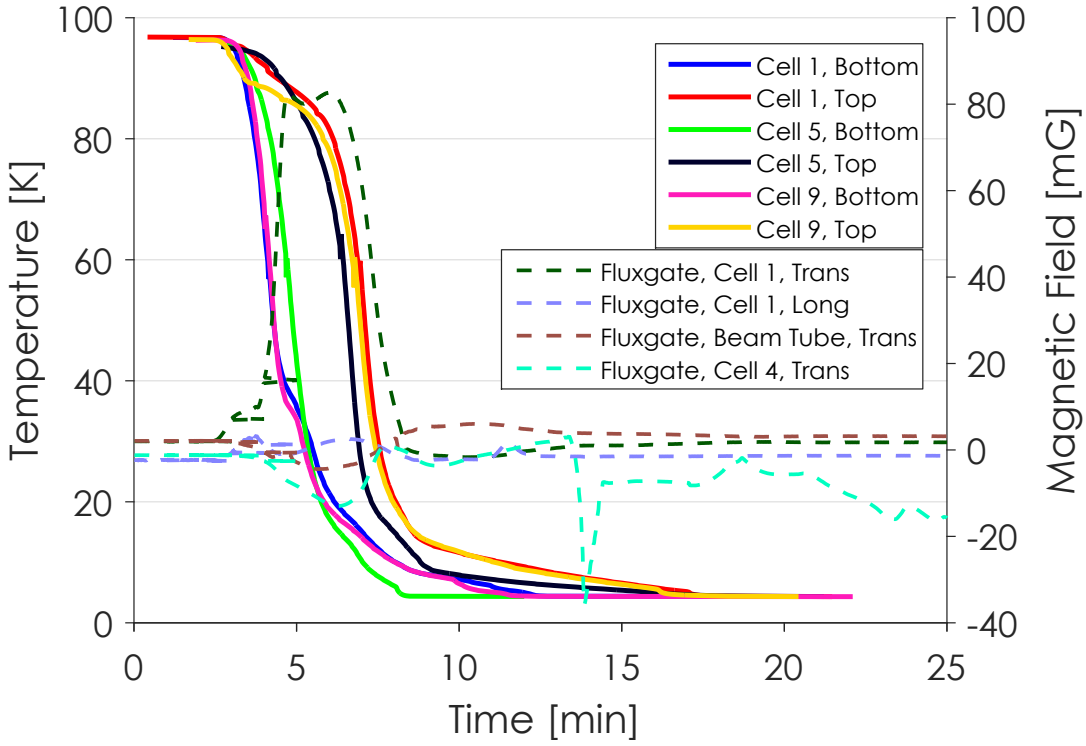

Figure 8.18: A typical cool down from room temperature to 4.2 K using the LCLS-II helium vessel in HTC9-5.

between the cavity ends due to the high power RF coupler in the tests with the LCLS-II tank which could significantly impact ΔT_{horiz}.

8.8.4 Impact of Cool Down on Cavity Performance in the HTC

HTC9-1

The Q_0 was strongly dependent on the cool down in HTC9-1, as can be seen in Figure 8.20, which shows the 2.0 K Q_0 for all four cool downs. The third fast cool down, which had the largest vertical temperature gradients, produced the best results with a Q_0 of 3.2×10^{10} at 14 MV/m and 2.0 K. Initially the 2.0 K Q_0 was

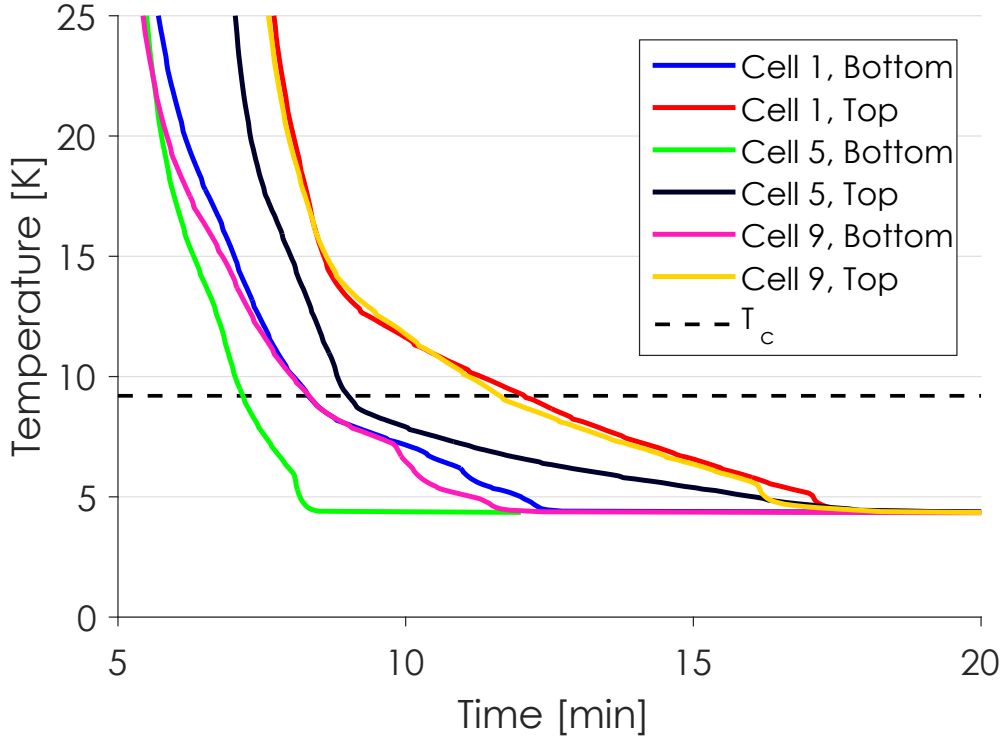

Figure 8.19: A typical cool down in the LCLS-II helium vessel in the region around T_c in HTC9-5. The entire cavity takes about 5 minutes to cool completely from ~100 K to 4.2 K.

2.5×10^{10} at maximum fields. This lower Q_0 was a result of conditioning field emission of the cavity in which the cavity was quenched many times. After a thermal cycle to release magnetic flux trapped during the quenches, and similar fast cool down, the 2.0 K Q_0 improved to 2.8×10^{10} at 14 MV/m and field emission no longer had an effect on Q_0 as the radiation dropped by a factor of 1000 due to conditioning. A slow cool down resulted in a lower Q_0 of 2.5×10^{10}, due to less efficient flux expulsion. The final fast cool down, in which larger vertical gradients were achieved than in the first two fast cool downs resulted in a 2.0 K Q_0 of 3.2×10^{10} at 14 MV/m, significantly exceeded LCLS-II Q_0 specification.

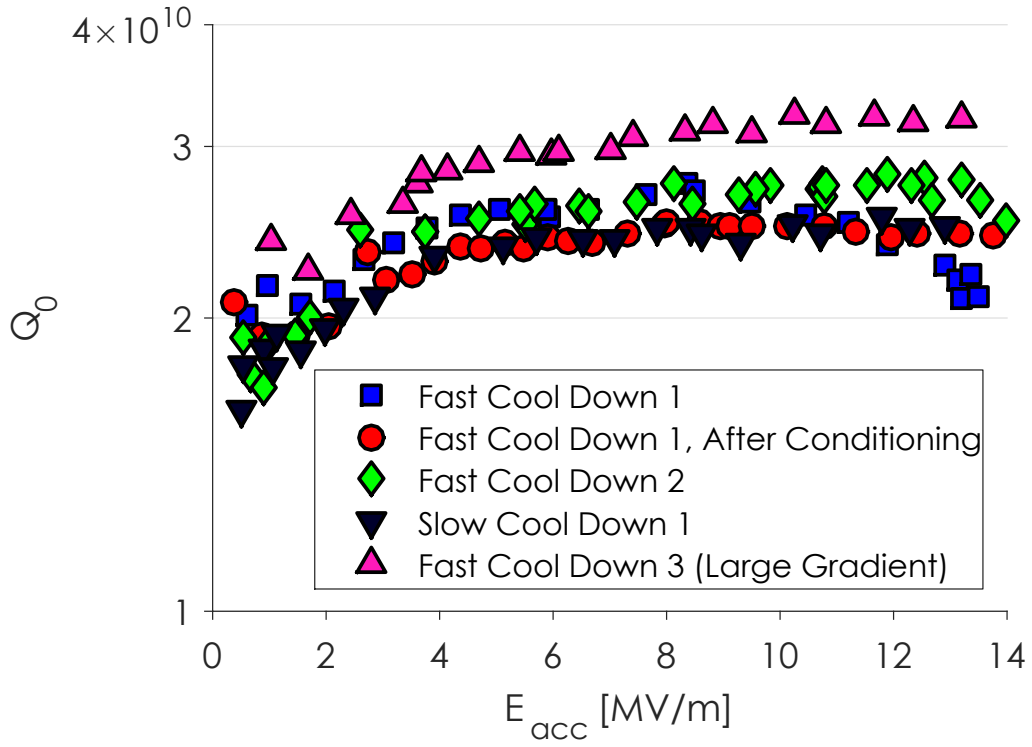

Figure 8.20: Q_0 versus E_{acc} performance at 2.0 K for all cool downs conducted on HTC9-1.

HTC9-2

As in HTC9-1, Q_0 was strongly affected by cool down conditions in HTC9-2. Figure 8.21 shows the 2.0 K performance for the cavity in all seven cool downs. The best results came from the second fast cool down which had the largest vertical spatial temperature gradient and the smallest ambient magnetic field in which the cavity reached a Q_0 of 2.7×10^{10} at 16 MV/m and 2.0 K. Cool downs with magnetic field and heater will be further discussed in later sections.

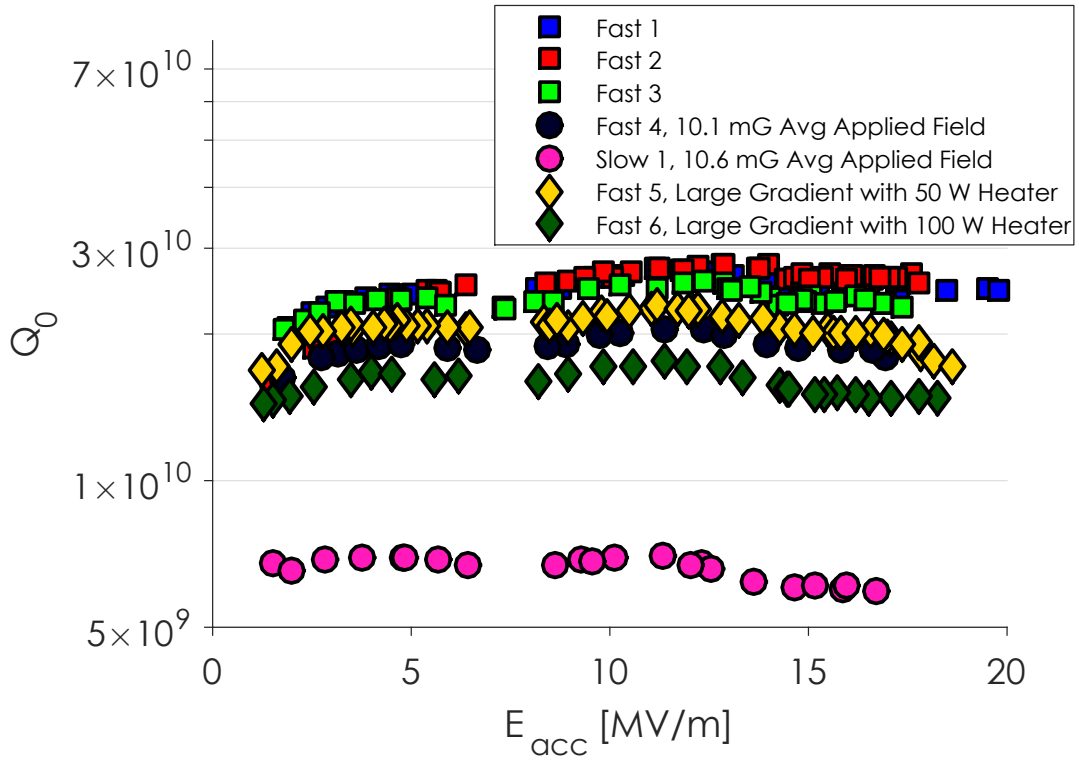

Figure 8.21: Q_0 versus E_{acc} performance at 2.0 K for all cool downs conducted on HTC9-2.

8.8.5 Thermoelectric Currents

While large spatial temperature gradients are important to improve magnetic flux expulsion, they also can lead to thermoelectric currents which can create larger magnetic fields at the cavity surface and lead to higher R_{res}. Measurements on a dressed cavity at Helmholtz Zentrum Berlin (HZB) showed that the residual resistance of a cavity increased with larger longitudinal temperature gradients across the cavity near T_c (based on the readings of temperature sensors on the beam tubes outside of the helium vessel) [KNV+09, VKK13]. This effect was attributed to the additional magnetic field generated by thermoelectric currents flowing through the bimetal loop created by the cavity and titanium helium vessel, which gets trapped during the cool down through T_c. Due

to the Seebeck effect, a spatial temperature gradient will drive a thermoelectric current,

$$\vec{J} = -\sigma(T)\left(\nabla V + S(T)\nabla T\right), \tag{8.5}$$

where σ is the conductivity and S is the Seebeck coefficient, which depends on temperature and is different for different materials. In order to generate a persistent current, a bimetal junction must be present forming a loop with the two transitions at different temperatures. Having different materials is required to have a continuous current flow. The net emf in the loop, ϵ, is related to the difference in Seebeck coefficients

$$\epsilon = \int_{T_1}^{T_2} \left[S_{Nb} - S_{Ti}\right] dT, \tag{8.6}$$

where S_{Nb} and S_{Ti} are the Seebeck coefficients of niobium (cavity) and titanium (helium tank), respectively [Cra14]. This current will lead to additional magnetic fields. Since no magnetic field probes were installed inside the helium tank during the HZB test, no direct measurements of the induced magnetic field by the thermoelectric currents were possible to support this explanation. These findings were in apparent contradiction to the data presented previously here and at FNAL in which large temperature gradients reduced R_{res}.

In addition, theoretical analysis showed that the axial symmetry of the SRF cavities leads to very small thermoelectric induced magnetic fields in the relevant RF penetration layer at the inner cavity surface [Cra14]. Therefore, in vertical cavity tests, these thermoelectric induced magnetic fields usually do not cause a significant surface resistance degradation.

To study the trade-off in horizontal cavity performance between the potential detrimental effect of thermoelectric currents generated by large thermal gradients and the benefits of large temperature gradients in reducing flux trapping,

a heater was installed on the cell #9 beam tube during the HTC9-2 test (see Figure 8.3). The heater was then used to generate large longitudinal gradients during cool down, affecting both the magnitude of the thermoelectric current and thus the induced ambient magnetic field as well as the flux trapping. As can be seen in Table 8.5, without heater the largest horizontal temperature gradient achieved was 9.4 K. With heater however, the horizontal gradient reached as high as ~30 K. Clearly the heater was successful in inducing larger gradients. In total, two fast cool downs were performed with the heater: one with the heater set to 50 W and one with it at 100 W. The magnetic field generated by the thermoelectric current is expected to be perpendicular to the cavity axis (as seen in Figure 8.24) between the cavity and tank. The measured perpendicular magnetic field versus horizontal temperature gradient (field perpendicular to the cavity axis) is shown in Figure 8.22 as measured between cells 5 and 6 (as shown in Figure 8.3) and it can be seen that larger horizontal temperature gradients did in fact lead to larger perpendicular magnetic fields. As shown in Table 8.5, the perpendicular magnetic field during the two cool downs in which the heater was used was as high as 62.8 mG at 10 K, compared with 0.3 mG during the cool down without heater that produced the best results. The fields generated by the currents in the heater itself and its current wires were negligible. Additionally, Figure 8.23 shows the residual resistance versus the perpendicular magnetic field for the same cool downs as in Figure 8.22. It is clear that the additional magnetic field directly led to larger R_{res} when the heater was used.

This experiment showed that the larger horizontal temperature gradients produced by the heater resulted in a significant degradation of the Q_0 even in fast cool downs. This can be understood by carefully analyzing the thermoelectric magnetic fields produced during cavity cool down. In vertical cavity tests,

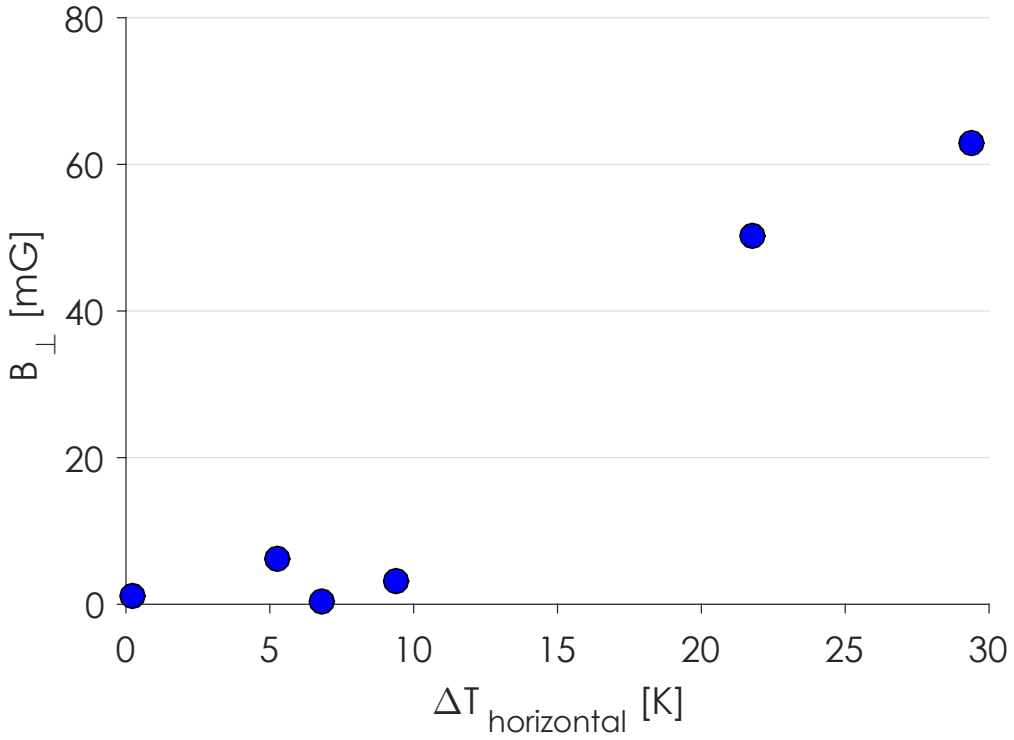

Figure 8.22: Perpendicular magnetic field versus horizontal temperature gradient in HTC9-2. Larger gradients led to larger induced magnetic field due to the generation of thermoelectric currents.

axial symmetry of the SRF cavities leads to very small thermoelectric induced magnetic fields in the RF penetration layer, and thus to no significant increase in residual resistance due to trapped flux. However, in horizontal cavity test this argument does not hold. For cavities placed horizontally with the cool down connections at the bottom of the liquid helium tanks, symmetry is broken since the cavities primarily cool from the bottom of the cells to the top of the cells. This leads to vertical temperature gradients in addition to the horizontal temperature gradients. Since the electric conductivity of niobium strongly changes with temperature, especially when it becomes superconducting, the vertical temperature gradients result in non-symmetric thermoelectric currents through the cavity (higher currents at the bottom) as shown in Figure 8.24. These non-

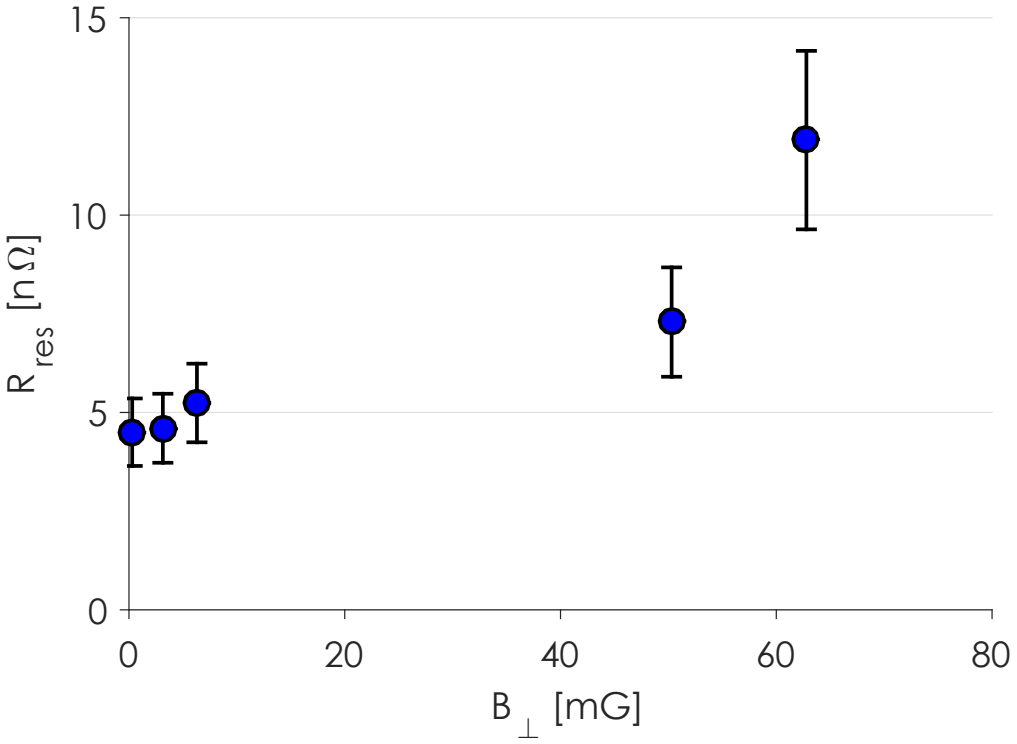

Figure 8.23: R_{res} versus perpendicular magnetic field in HTC9-2. Large magnetic fields resulting from thermoelectric currents led to larger R_{res}.

symmetric thermoelectric currents then can produce very significant magnetic fields (also shown in Figure 8.24) in the RF penetration layer at the inner cavity wall, which partly get trapped and cause increased surface resistance. The HTC9-2 tests with the heater show that the detrimental effect of the increased thermoelectric currents outweigh the reduction in the fraction of ambient field trapped when the longitudinal temperature gradients are increased, especially considering that $\Delta T_{horiz}/L$ is still less than $\Delta T_{vert}/L$ so there is not much gain in flux expulsion, resulting in higher R_{res}. Therefore, in order to achieve low residual resistance and high Q_0, horizontal cavities in cryomodules should be cooled with as small a horizontal temperature gradient as possible to reduce thermoelectric currents, while keeping vertical temperature gradient as large as possible to reduce trapping of ambient magnetic fields.

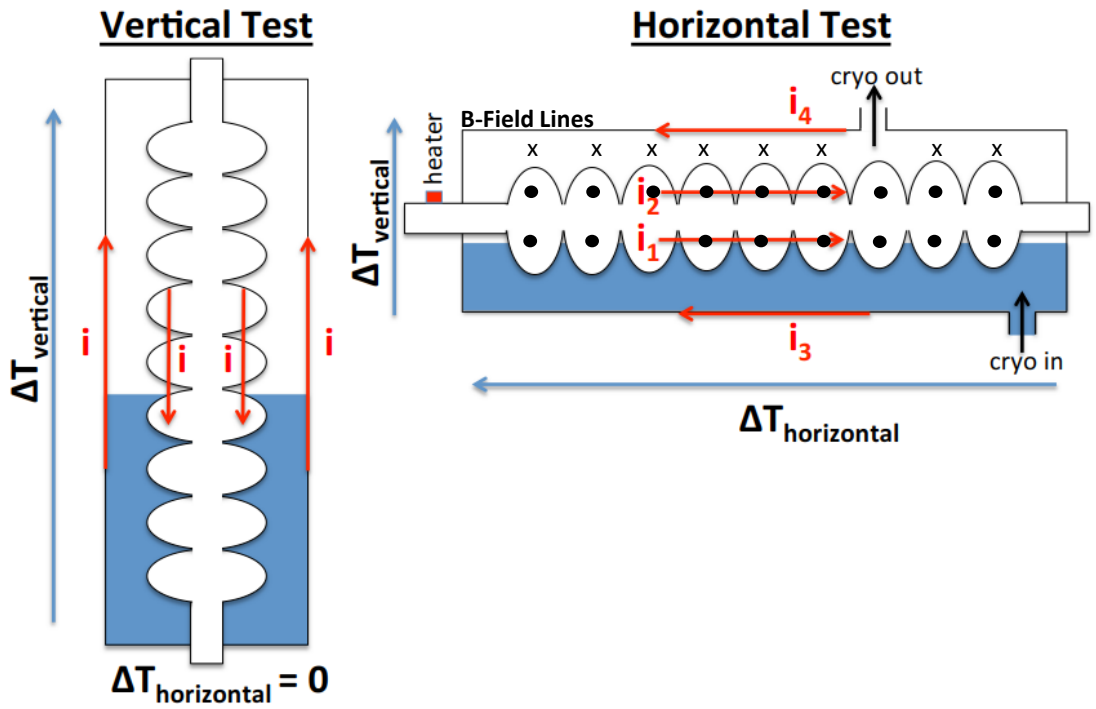

Figure 8.24: A schematic drawing of cooling in vertical test and horizontal test and the induced thermoelectric current. Cylindrical symmetry reduces the induced magnetic field at the cavity surface in vertical test. In horizontal test, vertical temperature gradients break the symmetry resulting in non-zero magnetic field at the cavity inner surface. A simple schematic of the the magnetic field lines inside the helium tank are also shown. The magnitudes of these lines is studied completely in [EDF+16].

While these findings might be concerning upon first inspection, it is important to note that in HTC9-2, the only cool downs during which thermoelectric currents were strong enough to lead to significant increases in R_{res} were when the heater was used. In all other cool downs, even with the ILC helium vessel, horizontal temperature gradients and thus thermoelectric currents were sufficiently small. Interestingly, as was discussed above, the LCLS-II tank cools with about the same horizontal temperature gradients as the ILC vessel. In practice, both helium vessels cool with small enough horizontal temperature gradients to keep the effects of thermoelectric currents small.

8.9 Magnetic Field Studies

8.9.1 HTC9-2

HTC9-2 was assembled with a solenoid wrapped around the helium vessel of the cavity (see Figure 8.25). The solenoid consisted of 10 equally spaced coils (5 Helmholtz coil pairs) in order to induce an approximately uniform external magnetic field parallel to the cavity axis. Using the coil, an average magnetic field of ~10 mG was applied across the cavity and the cavity was cooled twice, once fast (Fast 4), and once slow (Slow 1). The parameters of the cool downs are shown in Table 8.5. The purpose of these studies was to understand the sensitivity of nitrogen-doped cavities in cryomodule to ambient magnetic fields under realistic cool down conditions. Figure 8.26 shows the 1.6 K Q_0 vs E_{acc} for HTC9-2 during the second fast cool down (best cool down without applied solenoid field) for reference and the two cool downs with magnetic field (Fast 4, Slow 1). Under fast cool down ($\Delta T_{vertical} = 7$ K), residual resistance increased by 4.6 ± 0.9 nΩ due to the applied ambient magnetic field, as compared with the fast cool down that had similar vertical temperature gradients, but no additional magnetic field applied. With slow cool down in the same magnetic field, the increase was 36 ± 7 nΩ in residual resistance.

By analyzing other TM010 mode data, as discussed in section 8.4, the change in residual resistance per cell pair can be computed for the cool downs with applied ambient magnetic field. This change by cell is shown in Figure 8.27. From this data, we can make two conclusions: first that in slow cool down the largest change in residual resistance happened in the center cells of the cavity; and second, that large vertical temperature gradients result in significantly less

Figure 8.25: Picture of the solenoid around the cavity in HTC9-2.

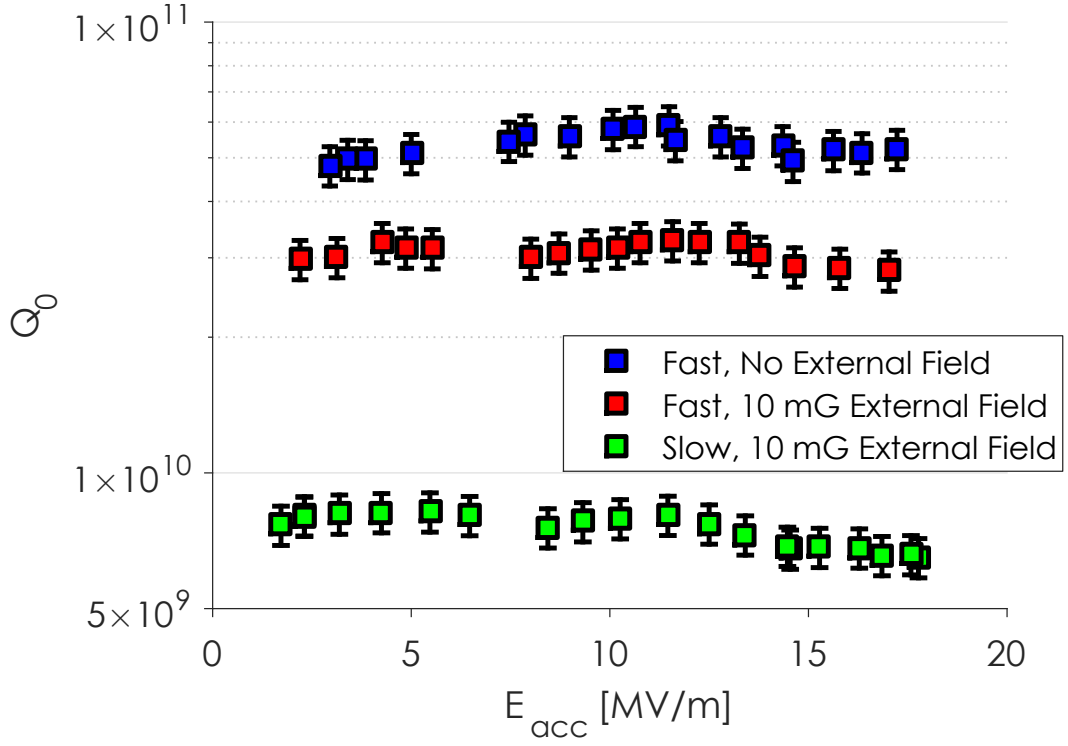

Figure 8.26: Q_0 versus E_{acc} at 1.6 K for HTC9-2 for cool downs completed in ~10 mG external magnetic field. The best fast cool down without applied solenoid field is also shown for reference.

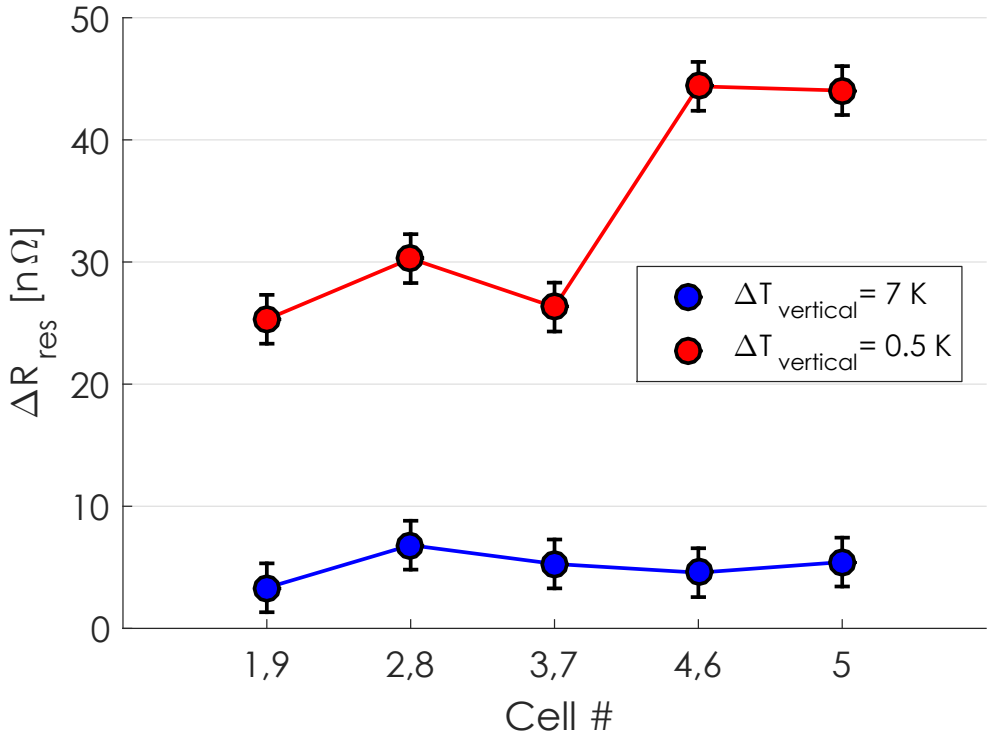

Figure 8.27: The change in residual resistance per cell between the cool downs with 10 mG applied ambient magnetic field and the best fast cool down (Fast 2) without applied field. R_{res} from trapped flux was predominantly found in the center cells.

flux trapping in all cells.

Analyzing this data leads to the following sensitivities of nitrogen-doped cavities in a cryomodule to losses from trapped ambient magnetic fields: For fast cool down ($\Delta T_{vertical}$ = 7 K) the measured change in residual resistance for a given change in magnetic field is 0.5 ± 0.2 nΩ/mG. For slow cool down ($\Delta T_{vertical}$ = 0.5 ± 0.1 K) the change in residual resistance for a given change in magnetic field is 3.8 ± 0.6 nΩ/mG. Assuming that during slow cool down there was near 100% flux trapping, this value of 3.8 ± 0.6 nΩ/mG is consistent with flux trapping measurements presented in Chapter 6. For reference, with a mean free path of 29±9 nm (measured using the methods outlined in Chapter 3) for the

cavity in HTC9-2, predictions from Chapter 6 suggest a sensitivity of residual resistance to trapped flux of 3 ± 0.4 nΩ/mG, very close to the value found from experiments.

8.9.2 HTC9-3

As was discussed in detail in Chapter 6, large spatial temperature gradients lead to more efficient flux expulsion and less trapped magnetic flux. In HTC9-3, a solenoid was again placed around the cavity to apply a uniform external magnetic field parallel to the cavity's axis. Many cool downs were completed with the solenoid on in order to study the efficiency of flux expulsion via spatial temperature gradients. Figure 8.28 shows the residual resistance versus the vertical temperature gradient. From this we can see two things: first, for the points with applied magnetic field, larger gradients result in less residual resistance (consistent with previous measurements) and second, for the points with no applied magnetic field, there is not a significant improvement in R_{res} above gradients of ~20 K (~100 K/m). This tells us that the gradients achieved in HTC9-4 were more than sufficient to maximize flux expulsion in ambient magnetic fields less than 5 mG (LCLS-II cryomodule specification). Figure 8.29 shows the residual resistance for each cool down as a function of the maximum helium gas flow during the cool down. In cool downs without applied magnetic field, flow rates greater than ~1 g/sec were sufficient to minimize residual resistance. This is an important specification for LCLS-II cryomodule and cryosystem design.

From this data, the sensitivity of residual resistance to trapped flux can be extracted. Specifically, slow cool down which results in significant flux trapping,

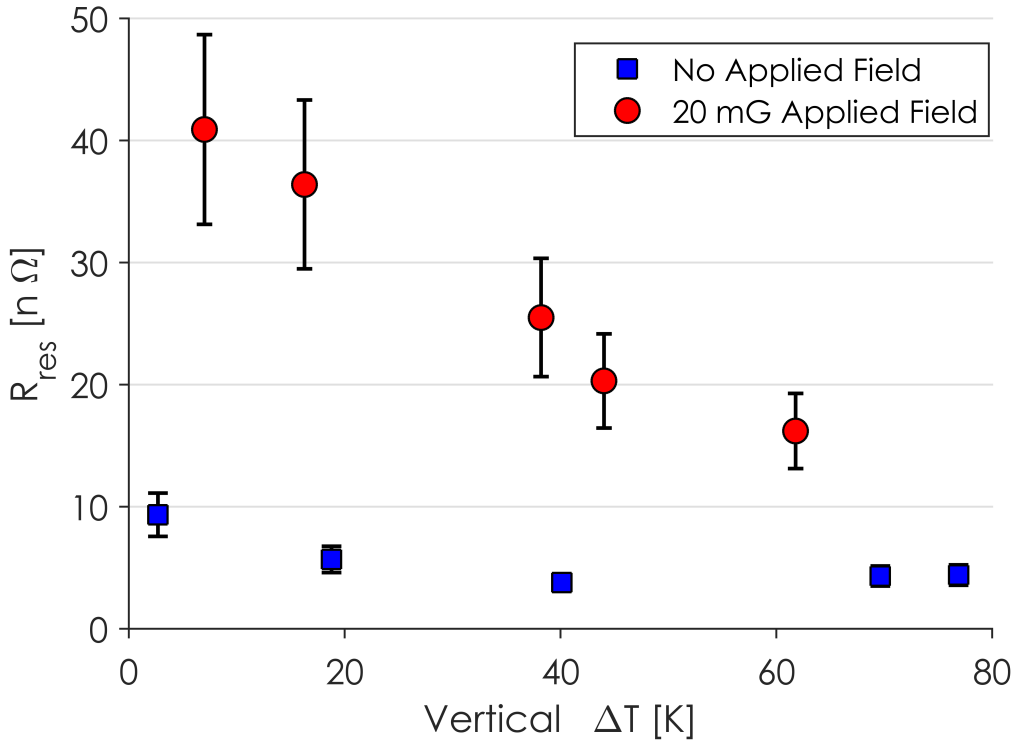

Figure 8.28: R_{res} versus vertical spatial temperature gradient (when the cavity first reaches 9.2 K) during HTC9-3 for cool downs with and without applied external magnetic field. Larger temperature gradients resulted in lower R_{res}.

gave an additional 1.8 nΩ/mG of residual resistance. Fast cool down resulted in an additional ~0.7 nΩ/mG of residual resistance corresponding to ~60% flux expulsion. For reference, a single-cell cavity with the same nitrogen-doping and subsequent final VEP had $R_{res,B}/B_{\text{trapped}} = 2.2 \pm 0.2$ (see Chapter 6), showing good agreement between measurements on the 9-cell cavity in the HTC and single-cell cavities. This flux expulsion data was compared with theoretical models in subsection 6.3.4.

These results allow for a prediction of the trapped flux contributions to residual resistance for the cavities in the LCLS-II cryomodules with fast cool down. Since the cryomodule specifications call for ambient magnetic fields at the cav-

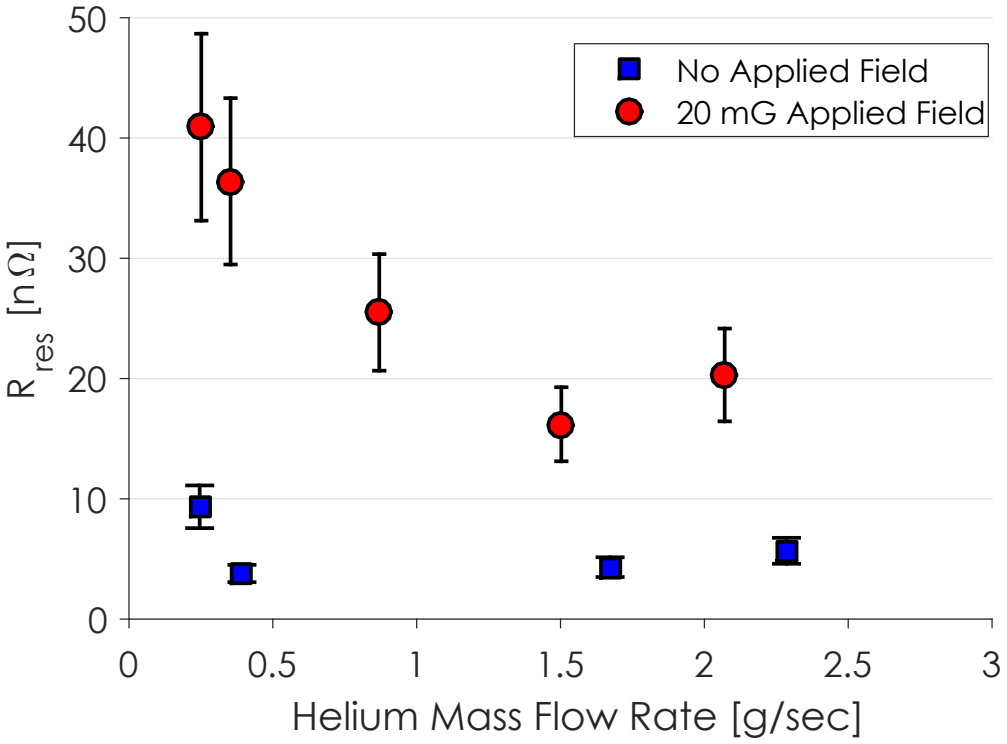

Figure 8.29: R_{res} versus helium gas mass flow for the same cool downs presented in Figure 8.28. Larger mass flow generally resulted in lower R_{res}.

ity locations of no more that 5 mG, one can expect an additional 2.5-3.5 nΩ of residual resistance with fast cool down. It is important to not however that this estimate depends on the fraction of magnetic flux that can be expelled, thus the bulk material properties of the niobium [Pos15a]

8.10 Cool Down Model

With an understanding of how flux expulsion manifests in cavities in a cryomodule environment and a theoretical basis for the generation of thermoelectric currents via large temperature gradients, it is possible to make a prediction

for the best cool down conditions based on the ambient magnetic field present in a cryomodule. When a cavity is arranged horizontally in a cryomodule, vertical temperature gradients will expel the ambient magnetic field as was illustrated in Figure 8.28. On the other hand, horizontal temperature gradients will lead to the creation of thermoelectric currents via Equation 8.5. There is a correlation between vertical and horizontal temperature gradients, i.e. larger vertical temperature gradients bring with them larger horizontal temperature gradients. The ratio between these gradients was found HTC9-3 which used the LCLS-II helium tank and was found to be $\Delta T_{horiz}/\Delta T_{vert} = 0.04$.

The thermoelectric current, I, generated by the horizontal temperature gradient can be obtained from Equation 8.6 and found to be

$$I = \frac{\left(\int_{T_1}^{T_2} [S_{Nb} - S_{Ti}]\, dT\right) \Delta T_{horiz}}{R}, \tag{8.7}$$

where R is the resistance along the path of the thermoelectric current [Cra14]. If the current is assumed to flow through the cavity and back through the liquid helium tank as shown in Figure 8.24 then the magnetic field generated from the current in between the cavity and the tank a distance r away from the axis is

$$B = \frac{\mu_0}{2\pi r} I. \tag{8.8}$$

Equation 8.8 is only true for the symmetric case with $\Delta T_{vert} = 0$. If $\Delta T_{vert} \neq 0$, the field distribution becomes much more complicated [EDF+16].

A fraction of the magnetic field from the thermoelectric current will be trapped depending on the vertical temperature gradients. Solving for the exact magnetic field for the complicated geometry of the cavity-tank system is quite complicated. Due to the complexity of the geometry with $\Delta T_{vert} \neq 0$, the R_{res} versus ΔT data from HTC9-3 was used to fit to the thermoelectric current

model and to find a scaling factor on Equation 8.8. This method allows the experimental data measured to be used in conjunction with theory to find the true average magnetic field experienced by the inner cavity surface due to the thermoelectric currents.

Figure 8.30 shows the additional residual resistance obtained in a cavity similar to HTC9-3 (in which $R_{\text{res,B}}/B_{\text{trapped}} = \sim 2$ nΩ/mG) as a function of vertical temperature gradient (in K/m) for different amounts of ambient magnetic field in the cryomodule. This model assumes that 100% of the magnetic flux can be expelled by sufficiently large temperature gradients. In a perfect cryomodule in which the ambient magnetic field is 0 mG, cooldowns with ΔT_{vert} as small as possible produce the lowest R_{res}. This is because any temperature gradient will generate a nonzero thermoelectric current. At even small ambient magnetic fields (> 2 mG), large temperature gradients lead to lower R_{res} due to the necessity of expelling the ambient magnetic field.

If however 100% of the flux cannot be expelled as has been shown in subsection 6.3.1 to occur in certain cavities, fast cool down will not necessarily lead to the lowest R_{res}. Figure 8.31 shows the additiona R_{res} from a 5 mG ambient field and the fields from thermoelectric currents for three cases: 100% of the flux can be expelled, 80% can be expelled, and only 50% can be expelled. If 80% can be expelled, large spatial temperature gradients still produce the lowest R_{res}. If however, only 50% can be expelled (which has been shown in subsection 6.3.1 to be likely) for cavities without high temperature heat treatment), cool downs with small temperature gradients always produce lower R_{res}.

This cool down model provides a guideline for how cavities should be cooled in cryomodule environments to reach the smallest possible R_{res}. If low

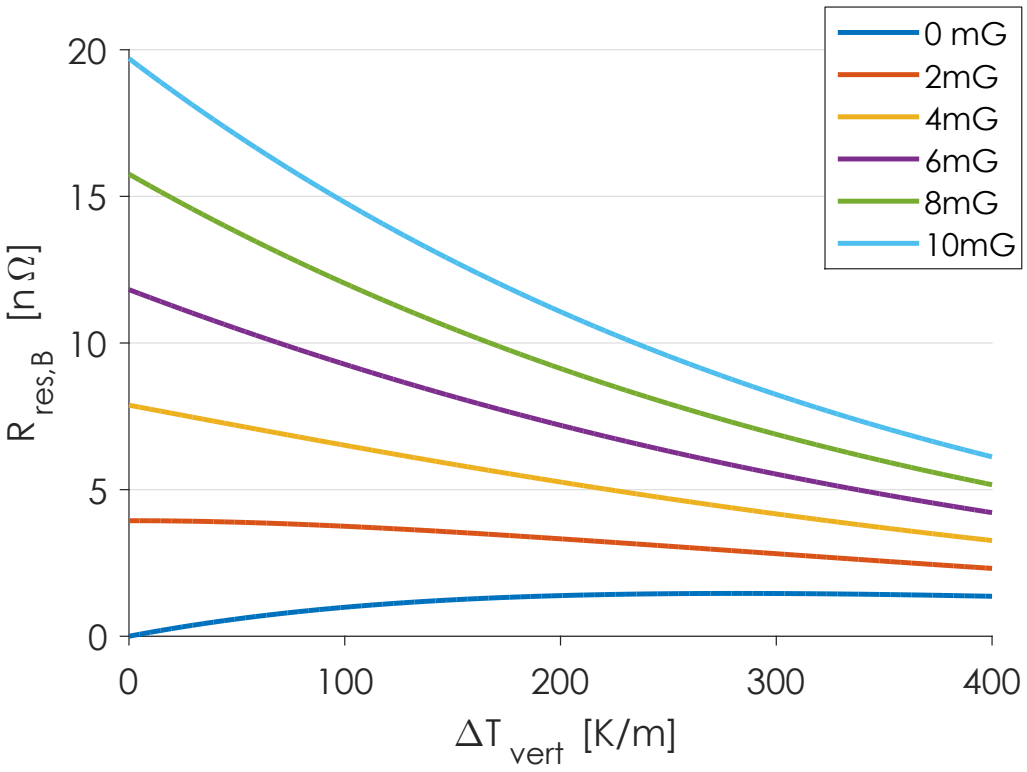

Figure 8.30: Additional residual resistance from ambient magnetic field and magnetic field from thermoelectric currents versus vertical temperature gradient as predicted by the cool down model assuming $R_{\text{res,B}}/B_{\text{trapped}}$ = ~2 nΩ/mG as in HTC9-3. Shown are curves for different amounts of ambient magnetic field. When ambient field is low, slow cool downs are better to minimize thermoelectric current fields but when ambient fields are high (> 2 mG), fast cool downs are better to maximize flux expulsion. This assumes that all magnetic flux can be expelled.

ambient magnetic fields can be achieved, cool downs with small spatial temperature gradients should be employed. However, if the ambient magnetic field is large, employing large temperature gradients during cool down is required in order to properly expel the magnetic flux. However, if less than 100% of the magnetic flux can be expelled by the material, small temperature gradients can produce better results than large temperature gradients. This emphasizes the need for great care to be taken to ensure that the material used in cavity fabrication has excellent flux expulsion properties. This model also explains why HF

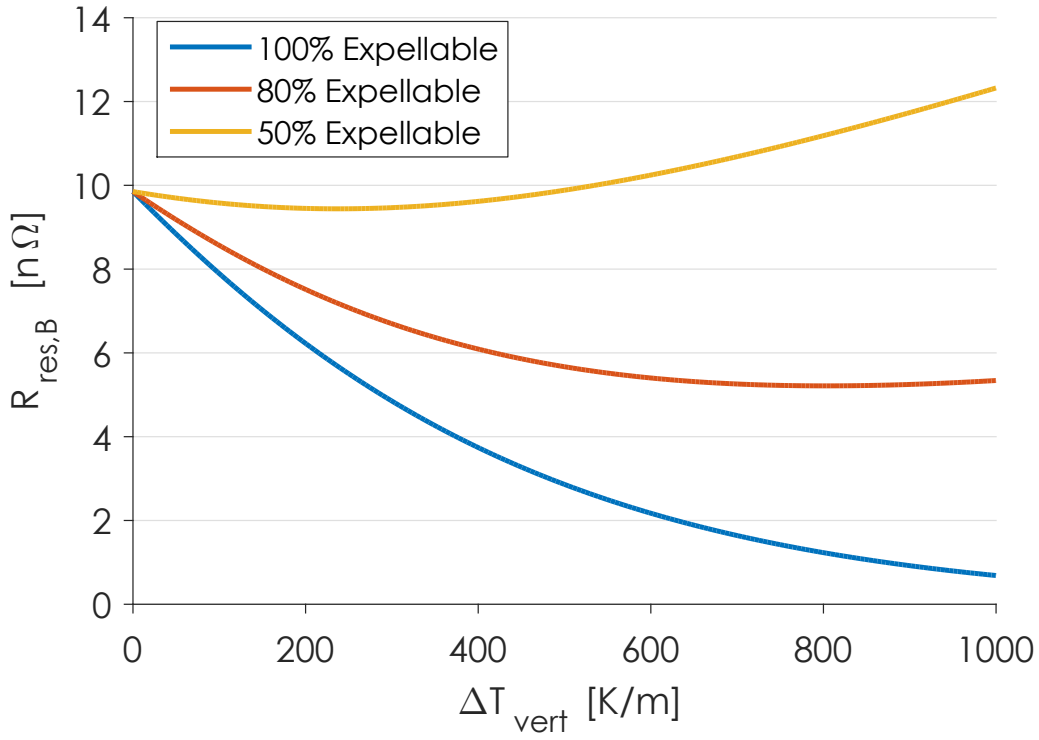

Figure 8.31: Additional residual resistance from ambient magnetic field (5 mG) and magnetic field from thermoelectric currents versus vertical temperature gradient as predicted by the cool down model for the case where less than 100% of the magnetic flux can be expelled. For the case of 80% expellable flux, cool downs with very large spatial temperature gradients still result in the lowest R_{res}. If flux expulsion is worse however and only 50% can be expelled, cool downs with small spatial temperature gradients result in the lowest R_{res}.

rinsed Cornell ERL cavities in the HTC required very small temperature gradients to produce the best results: the ambient magnetic field was quite lower in the HTC with the ERL cavity (< 1 mG) than with the LCLS-II cavities (~5 mG) [Val13].

8.11 Coupler Studies

Referring back to Figure 8.7, it is clear that there was no change in cavity performance between HTC9-3 and HTC9-4 in which the same cavity was used but with the full LCLS-II high power coupler (HPC). The coupler introduced no significant additional field emission or degradation to the cavity performance.

In order to further study the effect of operating at high RF drive power on Q_0, the cavity in HTC9-4 was tuned off resonance and then forward power was increased to maintain 10 MV/m. Q_0 was then measured. This was repeated up to 4.7 kW. The results are shown in Figure 8.32. We can see that the Q_0 is stable up to about 3 kW and then drops slightly. This drop corresponds to $\sim$ 0.3 W increase in dissipated power which would be about a 10% decrease in Q_0 at 16 MV/m. This increase in 2.0 K P_{diss} is consistent with simulations completed at SLAC and FNAL that predicted an increase of 0.2 W of P_{diss} at high power [AR14].

Since the LCLS-II coupler is adjustable, it is of interest to measure how Q_0 is affected by Q_{ext} while holding E_{acc} at a constant 15 MV/m. The coupler was adjusted between $Q_{ext} = 4 \times 10^7$ (1.8 kW for 15 MV/m) and $3{\times}10^8$ (230 W for 15 MV/m) and Q_0 was measured. These results are shown in Figure 8.33. We can clearly see that there was no significant impact of Q_{ext} on Q_0.

Also of interest is how the coupler heats up during operation. Figure 8.34 shows the temperatures of the 5 K and 80 K intercepts versus forward power up to ~4.5 kW. At the highest power levels, the 5 K intercept reached ~14 K and the 80 K intercept reached ~118 K. This is consistent with simulations at SLAC and FNAL showing that the coupler performs as predicted. Also important is

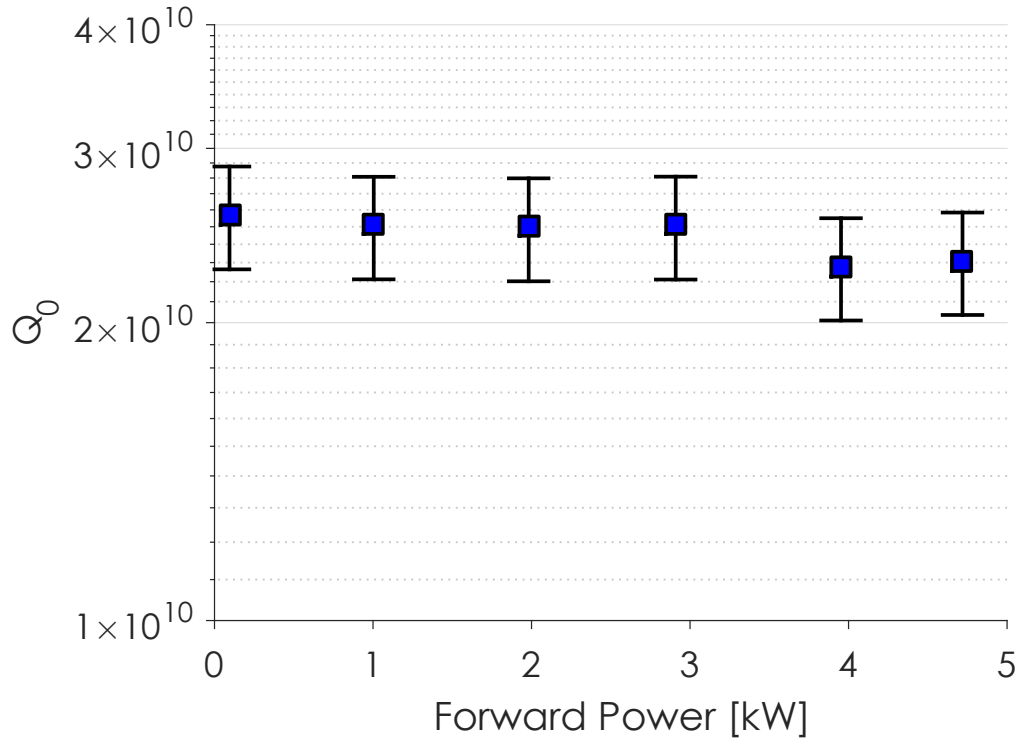

Figure 8.32: 2.0 K Q_0 versus P_f in HTC9-4. Q_0 is unaffected up to ~3 kW above which an increase of 0.2 W of dissipated power is observed.

that the heating on the coupler did not lead to a significant increase in dissipated power in the cavity.

The final coupler measurement conducted on HTC9-4 was a measurement of coupler heating and pressure while operating at high power for many hours. The cavity was tuned off resonance so that the coupler was under full reflection. Operation began at 5 kW, however approximately 3 hours into the measurement, an RF trip occurred that was unrelated to the coupler. After this trip, forward power was 4 kW. Figure 8.35 shows the results of these measurements. The 5 K intercept reached a steady state value of 14 K within ten minutes. The 80 K intercept reached a steady state value of 120 K after approximately 6 hours. The coupler vacuum reached a maximum pressure of 1×10^{-7} Torr after 3 hours

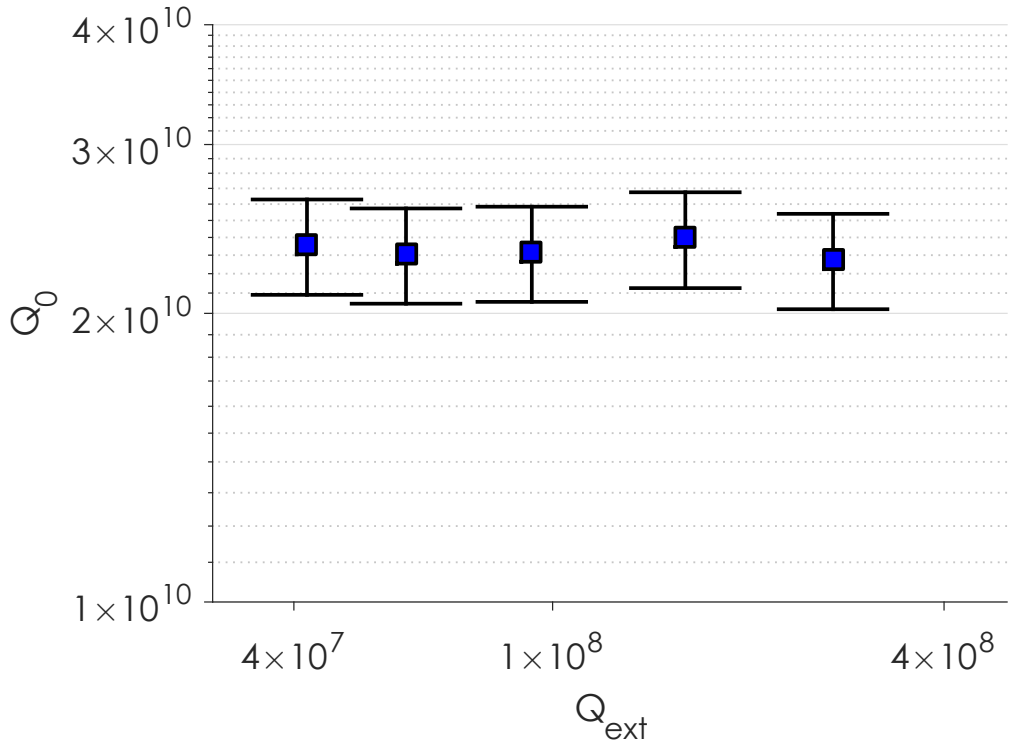

Figure 8.33: 2.) K Q_0 versus Q_{ext} for HTC9-4. Q_0 is unaffected by coupling strength of the coupler.

of operation and then began to decrease. No multipacting or vacuum events were observed in the coupler during these measurements.

Similar heating measurements were conducted during HTC9-5. Temperatures of the 5 K gas in/out along with the 80 K flanges and in/out gas is shown in Figure 8.36 while the cavity was tuned off resonance. Also shown is the forward power. Again these results are consistent with simulations and represent an important milestone for demonstrating the viability of the LCLS-II high power RF coupler.

These results on the LCLS-II coupler under realistic operating conditions represent a significant step towards demonstrating readiness for LCLS-II. The additional losses from the coupler at high power were in good agreement with

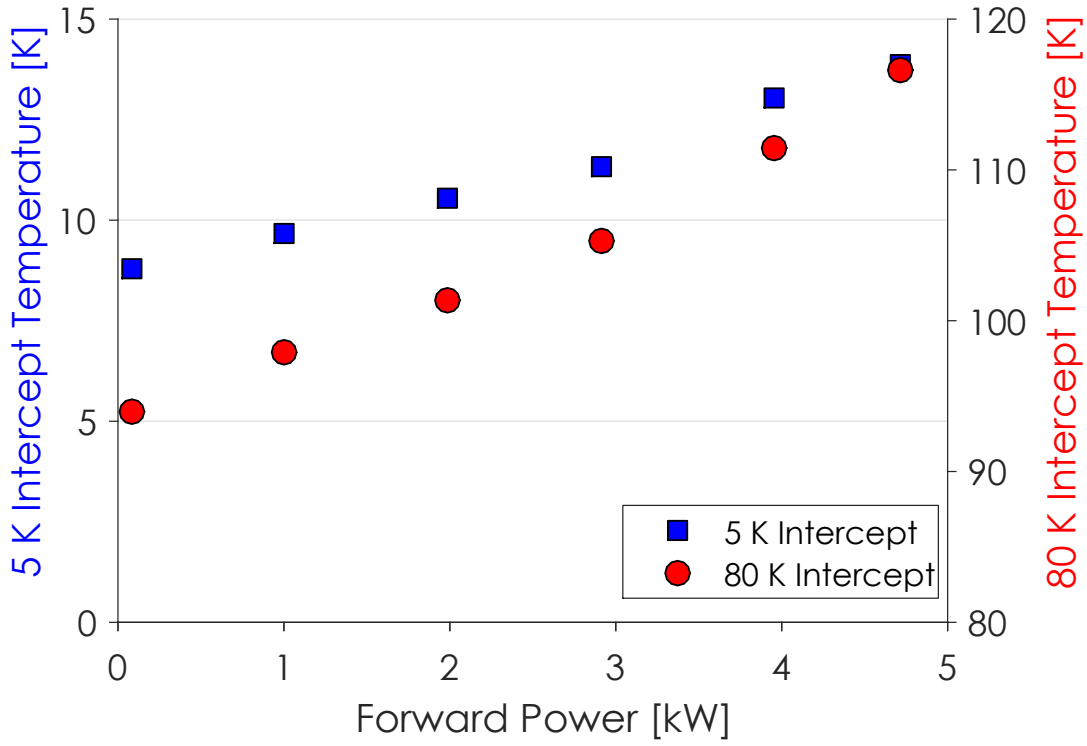

Figure 8.34: Temperature of the 5 K and 80 K intercepts versus forward power in HTC9-4.

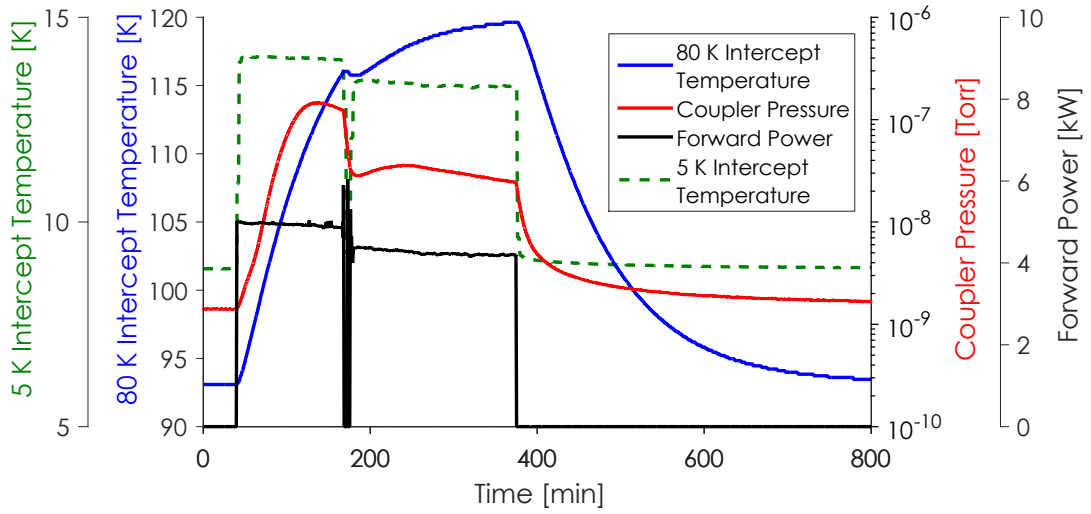

Figure 8.35: High power RF coupler pressure and temperatures of the 5 and 80 K intercepts for many hours of operation under full reflection. Also shown in the forward power.

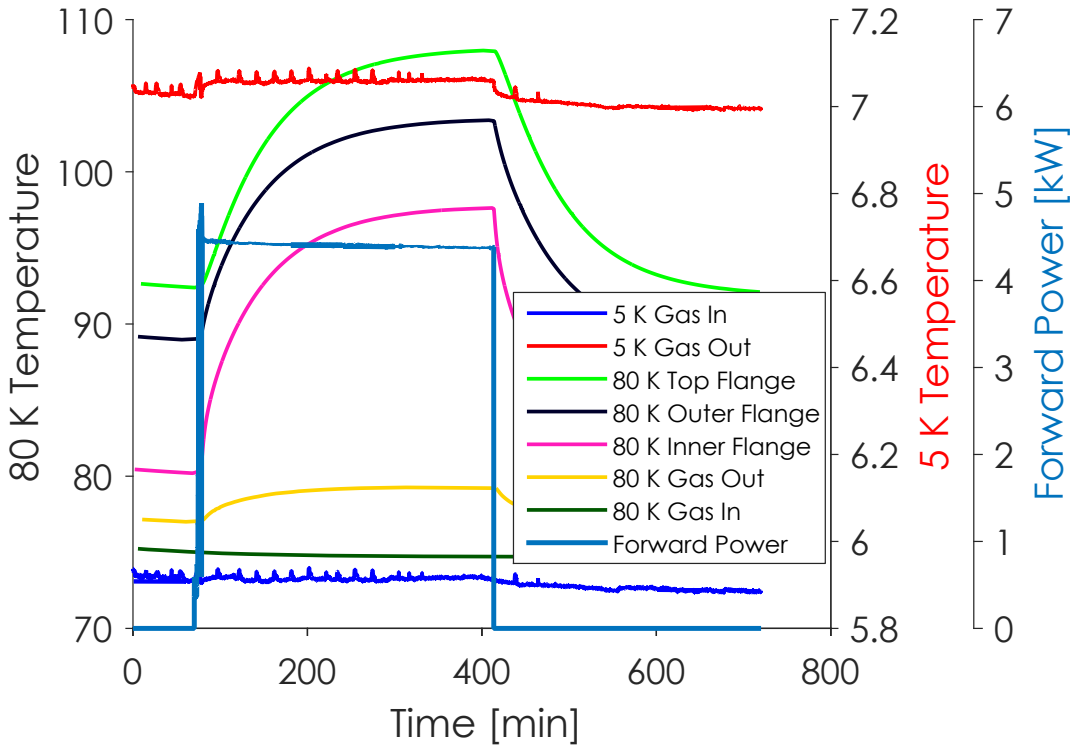

Figure 8.36: Coupler heating and forward power during HTC9-5 with the cavity tuned off resonance.

simulations. Coupler heating was well within the realm of normal operation, however it is important to note that cooling was done actively in the HTC as opposed to with thermal straps as will be done in the full LCLS-II cryomodule. Most importantly though, assembly of the coupler resulted in no degradation in cavity performance. The coupler was able to be assembled cleanly without leading to additional field emission or contaminants. This is an important proof of principle for moving forward to cryomodule production.

8.12 Horizontal Test Conclusions

The purpose of the measurements discussed in this chapter was to answer three fundamental questions about the viability of high Q_0 cavities for use in a cryomodule environment.

Can vertical cavity performance be maintained in a cryomodule?

Cavities did demonstrate a small decrease in Q_0 performance between vertical test pre-tank welding and assembly in the HTC. This degradation however was attributed to excessive HPR associated with the nature of the LCLS-II high Q program and occurred during the tank welding step. Assembly in the HTC did not lead to a significant degradation in Q_0 of the cavities tested. Likewise, there was no degradation in the maximum fields reachable in the cavities when assembled in the HTC when compared to their vertical test performance.

Can nitrogen-doped cavities be cooled adequately to minimize the effects of ambient magnetic field and thermoelectric currents?

It was found that fast cool down in the LCLS-II helium vessel was more than adequate for necessary flux expulsion in the HTC when the ambient field was less than 5 mG (the specification for the LCLS-II cryomodule). Flux expulsion during the best cool downs was ~60%, more than sufficient to reach high Q_0. Finally, thermoelectric currents did not significantly impact cavity performance with either the ILC or LCLS-II helium vessels.

Does the high power input coupler inherently degrade cavity performance?

Assembly of the high power coupler was found to have no significant impact on the Q_0 of the cavities when compared with the high Q input coupler. No additional field emission was observed and increased heat loads during high power operation were consistent with simulation predictions.

These results represent a significant milestone for demonstrating the technical readiness of nitrogen-doped cavities in a full cryomodule. It is clear that good performing cavities in vertical test can be transferred to a cryomodule without the expectation of degradation in performance.

CHAPTER 9

CONCLUSION

This dissertation has presented results from research on superconducting RF cavities doped with nitrogen. Nitrogen-doped cavities have been demonstrated to offer vast improvements in cryogenic efficiency over cavities prepared with standard methods. In order to study the effect of nitrogen-doping on cavity performance, an array of single and 9-cell cavities were prepared with various levels of nitrogen-doping to probe the entire mean free path space. The main results from this dissertation are summarized in this chapter. First, a summary of the improvement in Q_0 due to nitrogen-doping is presented. Following this is a summary of how ambient magnetic fields affect cavity performance. Next the fundamental field limits in nitrogen-doped cavities are presented followed by a discussion on the optimal doping level to maximize performance. A discussion on the readiness of this technology for use in future accelerators is then given. Finally, the chapter concludes with an outlook towards the future and a look at the questions that remain to be answered.

9.1 Understanding the Q_0 Improvement in Nitrogen-Doped Cavities

Nitrogen-doping offers two improvements over cavities prepared with standard methods: an increase in the Q_0 at low fields and an introduction of an anti-Q slope which further increases the Q_0 in the medium field region [GRS+13]. The work in Chapter 5 explained these two effects by showing that the introduction of interstitial nitrogen during nitrogen-doping lowers the mean free path

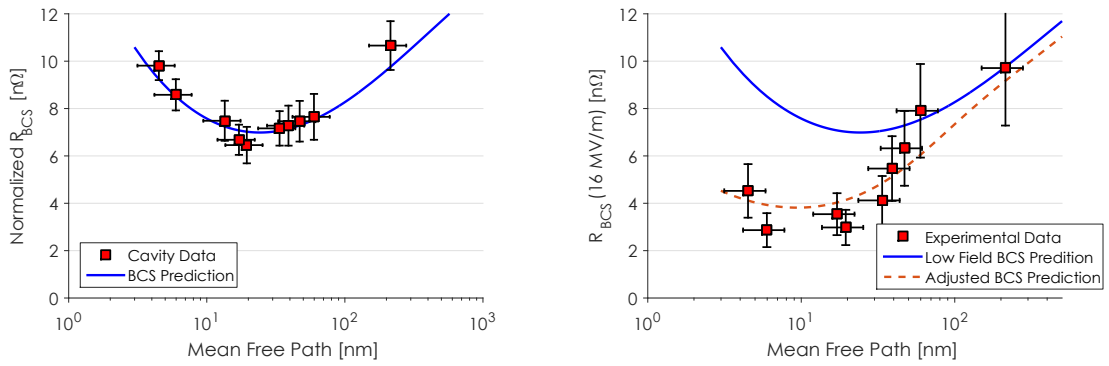

(a) Lowering of R_{BCS} at low fields at 2.0 K due to a lowering of the mean free path.

(b) Lowering of R_{BCS} at 16 MV/m and 2.0 K due to lowering of the mean free path and the anti-Q slope.

Figure 9.1: Reduction in R_{BCS} at low and high fields due to nitrogen-doping.

of the niobium. This lowering of the mean free path leads to a lowering of the temperature-dependent BCS resistance at low fields as shown in Figure 9.1a.

The anti-Q slope manifests as a decrease in R_{BCS} with RF field, and becomes stronger at smaller mean free paths. This causes a further lowering of R_{BCS} beyond the low field prediction as shown in Figure 9.1b. This anti-Q slope can be explained in a variety of ways and has been shown to have good agreement with Gurevich's theory of dissipative nonlinear conductivity [Gur14]. While this theory explains the anti-Q slope in the dirty limit, it is not valid for cavities in the clean limit and does not specifically address how nitrogen or other dopants would directly impact the strength of the anti-Q slope

9.2 Understanding the Effects of Ambient Magnetic Field on Cavity Performance

Cavities of all preparations were previously understood to suffer from worse performance after "slow" cool downs than "fast" cool downs [RGMS14b], however, this effect was significantly more pronounced in doped cavities than in cavities prepared with standard preparation techniques. This was shown to be due to two effects: large spatial temperature gradients during cool down leading to more efficient flux expulsion and nitrogen-doped cavities showing a much larger sensitivity of residual resistance to trapped magnetic flux, i.e. for the same amount of trapped flux a doped cavity will have a larger residual resistance than an un-doped cavity.

This second effect of a higher sensitivity of residual resistance to trapped flux was directly attributed to the mean free path of the material - nitrogen-doping lowers the mean free path and the losses from trapped flux are particularly sensitive to the mean free path. Figure 9.2 shows how $R_{\text{res,B}}/B_{\text{trapped}}$ changes with mean free path. Cavities with a mean free path of ~10 nm showed the highest $R_{\text{res,B}}/B_{\text{trapped}}$. These measurements also have very good agreement with Gurevich's theory of vortex oscillations which predicts this "bell-shape" behavior [GC13].

This finding represents the first systematic measurement of how trapped magnetic fields affect cavity performance. All of the nitrogen-doped cavities measured showed a higher $R_{\text{res,B}}/B_{\text{trapped}}$ than the un-doped cavities. While there is a maximum $R_{\text{res,B}}/B_{\text{trapped}}$ at $\ell \approx 10$ nm, and very strongly doped cavities have lower $R_{\text{res,B}}/B_{\text{trapped}}$, this region of very small mean free paths is typically

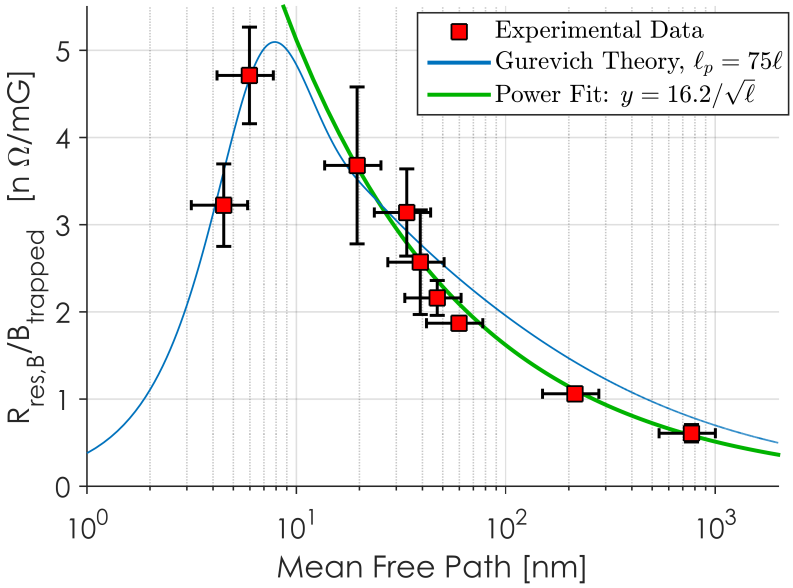

Figure 9.2: Sensitivity of residual resistance to trapped magnetic flux versus mean free path. Shorter mean free paths lead to higher sensitivity until $\ell \approx 10$ nm after which shorter mean free paths lead to a lower sensitivity.

plagued by lower quench fields and is likely not usable in accelerator applications.

9.3 Understanding the Fundamental Field Limits in Nitrogen-Doped Cavities

Nitrogen-doped cavities on average have lower quench fields than un-doped cavities [GRS+13, GGK+15]. It was shown that the reduction in quench field is most likely related to the lowering of the lower critical field, B_{c1}, due to lowering of the mean free path. A 9-cell cavity which quenched at a defect without doping quenched at the same location after doping, but at a lower field. This reduction in quench field was similar to the reduction in B_{c1} for the cavity. Low

field quenches in two single-cell nitrogen-doped cavities were studied using high pulsed power and found to be related to a defect on the surface, however it was not possible to differentiate between a normal conducting defect and early vortex penetration below the superheating field from these measurements. Measurements with temperature mapping on another nitrogen-doped cavity showed that the low field quench was a purely magnetic quench in which the energy barrier to flux entry was reduced to zero at a defect.

Lowering of B_{c1} does not necessarily mean that flux will enter prior to B_{sh} in nitrogen-doped cavities. However, in the presence of defects, the energy barrier to flux entry can be reduced and the lower B_{c1} will play a role in decreasing the quench field. Doped cavities are more susceptible to quenching at lower fields than un-doped cavities with the same defect due to this lowering of the critical fields.

9.4 Optimal Doping Level

The research presented in this dissertation allows a prediction for the optimal doping level to be made. By combining the measurements on R_{BCS} and R_{res}, a total surface resistance can be predicted as a function of mean free path for different amounts of trapped magnetic flux. This is shown in Figure 9.3. At small amounts of trapped flux (< 4 mG), moderate doping levels (mean free paths of 10-30 nm) give the lowest surface resistance at 16 MV/m and 2.0 K. At higher amounts of trapped flux however there is no longer an absolute minimum in the doping regime and the lowest surface resistance is obtained by employing standard cavity preparation techniques without the use of nitrogen-doping.

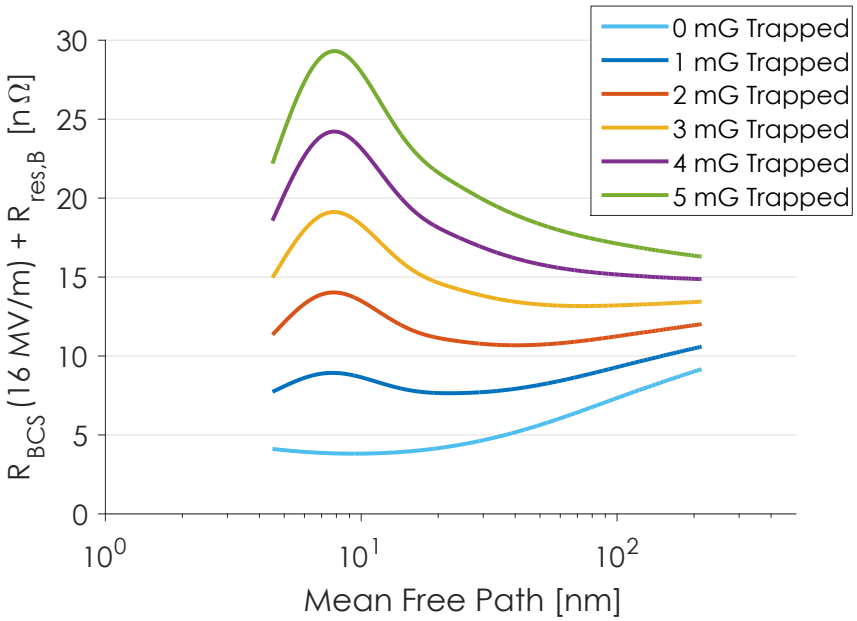

Figure 9.3: Total surface resistance for different amounts of trapped magnetic flux versus mean free path demonstrating the optimal doping level. For low amounts of trapped flux, moderate doping should be used. At high amounts of trapped flux, standard cavity preparation methods should be used to offset the effects of higher sensitivity of residual resistance to trapped magnetic flux.

This prediction allows one to determine the best cavity preparation technique based on the realistic cryomodule conditions in an accelerator. LCLS-II for example has a magnetic field specification in the cryomodule of less than 5 mG. Fast cooling will also be employed which can produce flux expulsion on the order of >50%. Therefore the use of moderate to lightly doped cavities is justified. If however flux expulsion cannot be optimized or the ambient magnetic fields in a cryomodule cannot be reduced sufficiently, standard cavity preparations should be employed.

9.5 Demonstration of Readiness for Application to Future Accelerators

A large concern with SRF cavities is the preservation of performance between vertical performance test in which it is comparatively easy to assemble cavities cleanly and quickly and test in a cryomodule. Cryomodule assembly requires significantly more time and effort to assemble and brings with it additional concerns over cleanliness due to assembly of parts such as the high power RF input coupler. Additionally, achieving the optimal cooling to maximize flux expulsion and minimize ambient magnetic fields is non-trivial. Five cryomodule tests were carried out on four nitrogen-doped cavities. Figure 9.4a shows the Q_0 versus E_{acc} performance of HTC9-3 and HTC9-4. These tests showed that assembly in the cryomodule and assembly of the high power coupler did not lead to a significant degradation to the Q_0 of the cavities. Additionally, the measurements in HTC9-2 showed for first time that LCLS-II specifications could be met by a nitrogen-doped cavity in a full cryomodule environment, as seen in Figure 9.4b.

In addition to Q_0 preservation, it was shown that flux expulsion in a cryomodule was efficient enough to still reach high Q_0 even with the higher $R_{\text{res,B}}/B_{\text{trapped}}$ present in nitrogen-doped cavities. These measurements were part of the first measurements of nitrogen-doped cavities in a full cryomodule environment and demonstrate the viability of nitrogen-doping technology's use in future accelerators.

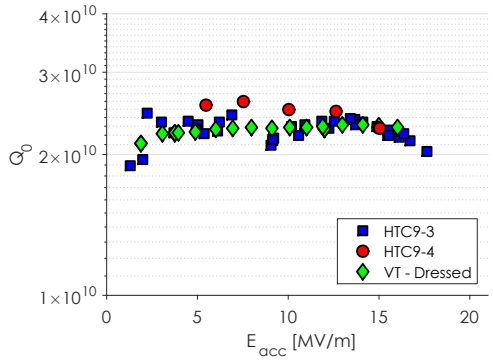

(a) Q_0 versus E_{acc} for HTC9-3 and HTC9-4 compared with vertical test results. The cryomodule environment and assembly of the high power coupler did not negatively effect the cavity performance.

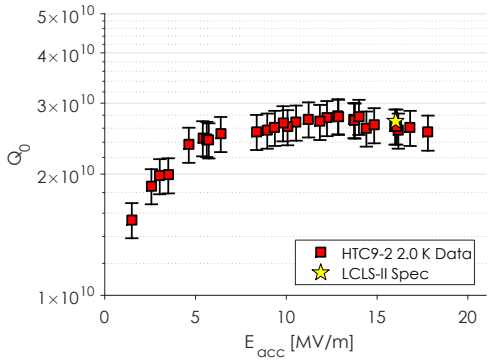

(b) Q_0 versus E_{acc} for HTC9-2 demonstrating the first nitrogen-doped cavity to meet LCLS-II specifications in a full cryomodule environment.

Figure 9.4: Q_0 versus E_{acc} at 2.0 K in the Cornell HTC.

9.6 Outlook and Open Questions

Nitrogen-doping has been shown to offer significant improvements in cryogenic efficiency over cavities of standard preparation methods. There are however limits to its viability on a large scale. The likelihood of lower quench fields in doped cavities limit the technology's potential for use in high gradient machines. Great care also needs to be taken to reduce ambient magnetic fields. As was discussed in detail in this dissertation, the benefits of nitrogen-doping can be outweighed by the downsides of higher sensitivity of residual resistance to trapped magnetic flux if the cavities cannot be cooled in such a way to enable efficient flux expulsion. Nevertheless, if flux expulsion can be optimized as was demonstrated in the Cornell HTC, nitrogen-doping has a bright future in new machines which require high cryogenic efficiency and operate in the medium field region.

This dissertation has answered many of the open questions regarding

nitrogen-doped cavities' performance, however a few open questions remain. While experimental data has been shown to fit theoretical predictions well, a unified theory which fully predicts the anti-Q slope's presence in doped cavities and absence in standard cavities has not been found. The results presented here have shown concretely that many aspects of nitrogen-doping can be explained by a lowering of the mean free path. There is no reason to expect then that similar behavior could be reached by using other dopants to lower the mean free path. Future work will focus on these studies, to try and produce similar results with other dopants without some of the downsides that nitrogen-doping brings such as lossy niobium-nitride on the cavity surface after doping. Further study of the quench using temperature mapping will also yield additional insight into the lower quench fields observed.

The results presented in this dissertation represent a significant jump forward in the understanding of the underlying physics of nitrogen-doped cavities. While there are downsides to using nitrogen-doping as a cavity preparation technique, this work has shown that these downsides can be mitigated in a cryomodule environment. This demonstrates the readiness of the technology for use in future accelerators. Thanks in part to this work, LCLS-II will fully embrace nitrogen-doping and serve as a true testament to its viability in a large scale application by preparing nearly 300 9-cell cavities with nitrogen-doping.

BIBLIOGRAPHY

[Aa12] G. Aad and et. al. Observation of a new particle in the search for the Standard Model Higgs boson with the ATLAS detector at the LHC. *Physics Letters B*, 716(1):1–29, 2012.

[ABB+00] B. Aune, R. Bandelmann, D. Bloess, B. Bonin, A. Bosotti, M. Champion, C. Crawford, G. Deppe, B. Dwersteg, D. A. Edwards, H. T. Edwards, M. Ferrario, M. Fouaidy, P. D. Gall, A. Gamp, A. Gssel, J. Graber, D. Hubert, M. Hning, M. Juillard, T. Junquera, H. Kaiser, G. Kreps, M. Kuchnir, R. Lange, M. Leenen, M. Liepe, L. Lilje, A. Matheisen, W. D. Mller, A. Mosnier, H. Padamsee, C. Pagani, M. Pekeler, H. B. Peters, O. Peters, D. Proch, K. Rehlich, D. Reschke, H. Safa, T. Schilcher, P. Schmuser, J. Sekutowicz, S. Simrock, W. Singer, M. Tigner, D. Trines, K. Twarowski, G. Weichert, J. Weisend, J. Wojtkiewicz, S. Wolff, and K. Zapfe. Superconducting TESLA cavities. *Physical Review Special Topics - Accelerators and Beams*, 3(9):092001, 2000. PRSTAB.

[AR14] Chris Adolphsen and Marc Ross. Modified TTF3 Coupler Design and Related R and D for LCLS-II. In *TTC Meeting, KEK, Japan, December 2014*, DESY, 2014. DESY.

[BBF+] Ph. Bernard, D. Bloess, T. Flynn, C. Hauviller, and W. Weingarten. Superconducting Niobium Sputter-Coated Copper Cavities at 1500 MHz. In *Proceedings of EPAC 92*, pages 1269–1271.

[BCS57] J. Bardeen, L.N. Cooper, and J.R. Schrieffer. Microscopic Theory of Superconductivity. *Physical Review*, 106:162–164, 1957.

[CDG14] G. Ciovati, P. Dhakal, and A. Gurevich. Decrease of the surface resistance in superconducting niobium resonantor cavities by the microwave field. *Applied Physics Letters*, 104(9):092601, 2014.

[Cio04] G. Ciovati. Effect of low-temperature baking on the radio-frequency properties of niobium superconducting cavities for particle accelerators. *J. Appl. Phys.*, 96(1591), 2004.

[Coo56] L.N. Cooper. Bound Electron Pairs in a Degenerate Fermi Gas. *Physical Review*, 104:1189–1190, 1956.

[CR80] James T. Clenny and Casimir J. Rosa. Nitridation kinetics of niobium in the temperature range of 873 to 1273 K. *Metallurgical Transactions A*, 11(9):1575–1580, 1980.

[Cra14] Anthony C. Crawford. A Study of Thermocurrent Induced Magnetic Fields in ILC Cavities. *arXiv*, (1403.7996), 2014.

[DCM+13] P. Dhakal, G. Ciovati, G. R. Myneni, K. E. Gray, N. Groll, P. Maheshwari, D. M. McRae, R. Pike, T. Proslier, F. Stevie, R. P. Walsh, Q. Yang, and J. Zasadzinzki. Effect of high temperature heat treatments on the quality factor of a large-grain superconducting radio-frequency niobium cavity. *Physical Review Special Topics - Accelerators and Beams*, 16(042001), 2013. PRSTAB.

[DM46] J.G. Daunt and K. Mendelssohn. *Proc. Roy. Soc.*, A185(225), 1946.

[DN61] R. Doll and M. Nbauer. Experimental Proof of Magnetic Flux Quantization in a Superconducting Ring. *Physical Review Letters*, 7(2):51–52, 1961. PRL.

[DPE05] H. Bilderback Donald, Elleaume Pascal, and Weckert Edgar. Review of third and next generation synchrotron light sources. *Journal of Physics B: Atomic, Molecular and Optical Physics*, 38(9):S773, 2005.

[EDF+16] R. Eichhorn, C. Daly, F. Furuta, A. Ganshyn, M. Ge, D. Gonnella, D. Hall, V. Ho, G. H Hoffstaetter, M. Liepe, J. May-Mann, T. OConnell, S. Posen, P. Quigley, J. Sears, and V. Veshcherevich. Thermocurrents and their role in high Q cavity performance. *Physical Review Accelerators and Beams*, 19(1):012001, 2016. PRAB.

[FHG+12] F. Furuta, G. Hoffstaetter, M. Ge, M. Liepe, and B. Elmore. Multi-Cell VEP Results: High Voltage, High Q, and Localized Temperature Analysis. In *Proceedings of IPAC 2012, New Orleans, LA, USA*, number TUPPR045, pages 1918–1920, New Orleans, LA, USA, May 2012. JaCoW.

[FSS66] D. K. Finnemore, T. F. Stromberg, and C. A. Swenson. Superconducting Properties of High-Purity Niobium. *Physical Review*, 149(1):231–243, 1966. PR.

[Fur16] F. Furuta. Discussions on Cornell VEP System, 2016.

[Gal14] J.N. Galayda. The LCLS-II Project. In *Proceedings of IPAC 2014, Dresden, Germany*, pages 935–937, Dresden, Germany, June 2014. JACoW.

[GC13] A. Gurevich and G. Ciovati. Effect of vortex hotspots on the radio-frequency surface resistance of superconductors. *Physical Review B*, 87(5):054502, 2013. PRB.

[GEF+15] D. Gonnella, R. Eichhorn, F. Furuta, M. Ge, D. Hall, V. Ho, G. Hoffstaetter, M. Liepe, T. O' Connell, S. Posen, P. Quigley, J. Sears, V. Veshcherevich, A. Grassellino, A. Romanenko, and D. A. Sergatskov. Nitrogen-doped 9-cell cavity performance in a test cryomodule for LCLS-II. *J. Appl. Phys.*, 117:023908, 2015.

[GGK+15] D. Gonnella, T. Gruber, P.N. Koufalis, M. Liepe, and J.T. Maniscalco. Fundamental Studies on Doped SRF Cavities. In *Proceedings of the 17th Workshop on RF Superconductivity, Whistler, B.C., Canada*, number MOPB042, Whistler, B.C., Canada, 2015. JaCoW.

[GK68] B.B. Goodman and G. Kuhn. Influence of Extended Defects on the Superconductive Properties of Niobium. *J. Phys. Paris*, 29(240), 1968.

[GL50] V.L. Ginzburg and L. Landau. *Zh. Eksp. Teor. Fiz.*, 20(1064), 1950.

[GL14a] Dan Gonnella and Matthias Liepe. Flux Trapping in Nitrogen-Doped and 120C Baked Cavities. In *Proceedings of IPAC 2014, Dresden, Germany*, number WEPRI063, pages 2631–2633, Dresden, Germany, June 2014. JaCoW.

[GL14b] Dan Gonnella and Matthias Liepe. New Insights into Heat Treatment of SRF Cavities in a Low-Pressure Nitrogen Atmosphere. In *Proceedings of IPAC 2014, Dresden, Germany*, number WEPRI064, pages 2634–2637, Dresden, Germany, June 2014. JaCoW.

[Gor59] L.P. Gor'kov. Microscopic derivation of the Ginzburg-Landau equations in the theory of superconductivity. *Soviet Physics JETP-USSR*, 9(6):1364–1367, 1959.

[GRM+15] A. Grassellino, A. Romanenko, O. Melnychuk, D.A. Sergatskov, G. Wu, M. Martinello, M. Checchin, A.C. Crawford, S. Posen, C. Grimm, A. Hocker, J. Ozelis, S. Aderholt, A. Rowe, N. Solyak,

R. Stanek, D. Gonnella, M. Liepe, and J. Vogt. Preservation of very high quality factors of 1.3 GHz nine cell cavities from bare vertical test to dressed horizontal test. In *Proceedings of SRF 2015*, number MOPB028, Whistler, B.C., Canada, 2015. JaCoW.

[GRS+13] A. Grassellino, A. Romanenko, D. Sergatskov, O. Melnychuk, Y. Trenikhina, A. Crawford, A. Rowe amd M. Wong, T. Khabiboulline, and F. Barkov. Nitrogen and argon doping of niobium for superconducting radio frequency cavities: a pathway to highly efficient accelerating structures. *Superconductor Science and Technology*, 26(102001), 2013.

[Gur14] A. Gurevich. Reduction of Dissipative Nonlinear Conductivity of Superconductors by Static and Microwave Magnetic Fields. *Physical Review Letters*, 113(8):087001, 2014. PRL.

[HA63] J.L. Harden and V. Arp. The lower critical field in the Ginsburg-Landau theory of superconductivity. *Cryogenics*, 3(2):105–108, 1963.

[Hal70] J. Halbritter. FORTRAN-Program for the Computation of the Surface Impedance of Superconductors. *KAROLA - OA-Volltextserver des Forschungszentrums Karlsruhe [http://opac.fzk.de:81/oai/oai-2.0.cmp.S] (Germany)*, (3/70-6), 1970.

[Hei99] Matthias Hein. *High-temperature superconducting thin films at microwave frequencies*. Springer, Berlin, New York, 1999.

[Hoc13] Andrew Hocker. High Q0 Preservation. In *Tesla Technology Collaboration on CW SRF*, Cornell Unviersity, Ithaca, NY, USA, 2013.

[HS10] Walter Henning and Charles Shank. Accelerators for america's future. Report, US Department of Energy Office of Science, 2010.

[KGLM15] P.N. Koufalis, D. Gonnella, M. Liepe, and J.T. Maniscalco. Understanding the Field Dependence of the Surface Resistance of SRF Cavities. In *Proceedings of the 17th Workshop on RF Superconductivity, Whistler, B.C., Canada*, number MOPB004, Whistler, B.C., Canada, 2015. JaCoW.

[Kno97] Jens Knobloch. *Advanced thermometry studies of superconducting RF cavities*. PhD Thesis, Cornell University, 1997.

[KNV+09] O. Kugeler, A. Neumann, S. Voronenko, J. Knobloch W. Anders, M. Schuster, A. Frahm, S. Klauke, D. Pfluckhahn, and S. Rotterdam. Manipulating the Intrinsic Quality Factor by Thermal Cycling and Magnetic Fields, 2009.

[Kub15] Takayuki Kubo. Model of Flux Trapping Cooling Down Process. In *Proceedings of the 17th Workshop on RF Superconductivity, Whistler, B.C., Canada*, number MOPB009, Whistler, BC, Canada, 2015. JaCoW.

[Lie16] Matthias Liepe. Discussions on construction costs of SRF linac machines, 2016.

[LK06] M. Liepe and J. Knobloch. Superconducting RF for energy-recovery linacs. *Nuclear Instruments and Methods in Physics Research Section A: Accelerators, Spectrometers, Detectors and Associated Equipment*, 557(1):354–369, 2006.

[LL35] F. London and H. London. *Proc. Roy. Soc.*, A149(71), 1935.

[LMN72] C. Lyneis, M. Mcashan, and V. Nguyen. Recent Measurements of S-Band and L-Band Cavities at Stanford. In *Proc. 1972 Prot. Linear Accel. Conf.*, pages 98–102, 1972.

[Mat79] R.A. Matula. Electrical resistivity of copper, gold, palladium, and silver. *J. Phys. Chem. Ref. Data*, 8(1147), 1979.

[Mei16] Wikipedia.org, 2016.

[MM65] B. Maxfield and W. McLean. Superconducting Penetration Depth of Niobium. *Phys. Rev.*, 139(5A):A1515–A1522, 1965.

[MO33] W. Meissner and R. Ochsenfeld. Ein neuer effekt bei eintritt der supraleitfhigkeit. *Naturwissenschaften*, 21(44):787–788, 1933.

[MPL14] S. Meyers, S. Posen, and M. Liepe. Analysis of Systematic and Random Error in SRF Material Parameter Calculations. In *Proceedings of Linac 2014*, number TUPP018, Geneva, Switzerland, September 2014. JaCoW.

[MS69] R. Meservey and B.B. Schwartz. *Equilibrium Properties: Comparison*

of Experimental Results with Predictions of the BCS Theory, pages 171–191. Marcel Dekker, 1969.

[Mul84] G. Muller. Diagnostic techniques and defect classification. In *Proceedings of the Second Workshop on RF Superconductivity*, pages 377–408, 1984.

[MY91] D.G. Myakishev and V.P. Yakovlev. An Interactive Code SUPERLANS for Evaluation of RF-Cavities and Acceleration Structures. In *14th IEEE Particle Accelerator Conference*, page 3002, San Francisco, CA, USA, May 1991. IEEE.

[NM75] V. Novotny and P.P.M. Meincke. Single superconducting energy gap in pure niobium. *J. Low Temp. Phys.*, 18(1-2):147–157, 1975.

[OMFB79] T. P. Orlando, E. J. McNiff, S. Foner, and M. R. Beasley. Critical fields, Pauli paramagnetic limiting, and material parameters of Nb_3Sn and V_3Si. *Physical Review B*, 19(9):4545–4561, 1979. PRB.

[Onn11] H. Kamerlingh Onnes. Further experiments with liquid helium. C. On the change of electric resistance of pure metals at very low temperatures etc. IV. The resistance of pure mercury at helium temperatures. *Commun. Phys. Lab. Univ. Leiden*, 12(120), 1911.

[Pad09] Hasan Padamsee. *RF superconductivity : science, technology, and applications*. Wiley-VCH, Weinheim, 2009.

[PFC99] C.K. Poole, H.A. Farach, and R.J. Creswick. *Handbook of Superconductivity*. Elsevier Science, 1999.

[PGH+12] S. Posen, D. Gonnella, G. Hoffstaetter, M. Liepe, and J. Oh. Residual Resistance Studies at Cornell. In *Proceedings of IPAC 2012, New Orleans, LA, USA*, number WEPPC079, pages 2393–2395, New Orleans, LA, USA, May 2012. JaCoW.

[Pie80] H. Piel. Diagnositc methods of superconducting cavities and indentification phenomena. In *Proceedings of the First Workshop on RF Superconductivity*, pages 85–118. Wiley-VCH, 1980.

[Pip53] A. B. Pippard. An Experimental and Theoretical Study of the Relation between Magnetic Field and Current in a Superconductor.

Proceedings of the Royal Society of London A: Mathematical, Physical and Engineering Sciences, 216(1127):547–568, 1953.

[PKH98] Hasan Padamsee, Jens Knobloch, and Tom Hays. *RF superconductivity for accelerators*. Wiley, New York, 1998.

[Pos15a] Sam Posen. Flux expulsion efficiency for different cavity materials and treatments. In *The Tesla Technology Collaboration Workshop, SLAC, Menlo Park, CA, USA*, SLAC, Menlo Park, CA, USA, 2015.

[Pos15b] Samuel Posen. *Understanding and Overcoming Limitation Mechanisms in Nb3Sn Superconducting RF Cavities*. PhD Thesis, Cornell University, 2015.

[RBCG13] A. Romanenko, F. Barkov, L. D. Cooley, and A. Grassellino. Proximity breakdown of hydrides in superconducting niobium cavities. *Superconductor Science Technology*, 26:5003, 2013.

[Res15] D. Reschke. Recent Progress with EU-XFEL. In *Proceedings of SRF 2015*, number MOAA02, Whistler, B.C., Canada, 2015. JaCoW.

[RG13] A. Romanenko and A. Grassellino. Dependence of the microwave surface resistance of superconducting niobium on the magnitude of the rf field. *Applied Physics Letters*, 102(25):252603, 2013.

[RGB+14] A. Romanenko, A. Grassellino, F. Barkov, A. Suter, Z. Salman, and T. Prokscha. Strong Meissner screening change in superconducting radio frequency cavities due to mild baking. *Applied Physics Letters*, 104:2601, 2014.

[RGC+14] A. Romanenko, A. Grassellino, A.C. Crawford, D.A. Sergatskov, and O. Melnychuk. Ultra-high quality factors in superconducting niobium cavities in ambient magnetic fields up to 190 mG. *Applied Physics Letters*, 105(23), 2014.

[RGMS14a] A. Romanenko, A. Grassellino, O. Melnychuk, and D. A. Sergatskov. Dependence of the residual surface resistance of superconducting radio frequency cavities on the cooling dynamics around Tc. *Journal of Applied Physics*, 115(184903), 2014.

[RGMS14b] A. Romanenko, A. Grassellino, O. Melnychuk, and D.A. Ser-

gatskov. Dependence of the residual surface resistance of SRF cavities on the cooling rate through Tc. *J. Appl. Phys.*, 115(184903), 2014.

[Sab13] Sunil Sabharwal. Electron beam irradiation applications. In *Proc. 25th North Am. Part. Accel. Conf.* JaCoW, 2013.

[Sax12] A.K. Saxena. *High-Temperature Superconductors*. Springer Berlin Heidelberg, 2012.

[Sch91] P. Schmuser. Superconducting magnets for particle accelerators. *Reports on Progress in Physics*, 54(5):683, 1991.

[SES10] W. Singer, A. Ermakov, and X. Singer. RRR-Measurement Techniques on High Purity Niobium. In *TTC-Report 2010*, 2010.

[SIM+13] W. Singer, J. Iverson, A. Matheisen, H. Weise, and P. Michelato. The Challenge and Realization of the Cavity Production and Treatment in Industry for the European XFEL. In *Proceedings of SRF 2013*, number MOIOA03, pages 18–23, Paris, France, September 2013. JaCoW.

[SML04] R.M. Scanlan, A.P. Malozemoff, and D.C. Larbalestier. Superconducting materials for large scale applications. *Proc. IEEE*, 92(10):1639–1654, 2004.

[TCS11] Mark K. Transtrum, Gianluigi Catelani, and James P. Sethna. Superheating field of superconductors within Ginzburg-Landau thoery. *Phys. Rev. B.*, 83(9):094505, 2011.

[TGMR15] Y. Trenikhina, A. Grassellino, O.S. Melnychuk, and A. Romanenko. Characterization of Nitrogen Doping Recipes for the Nb SRF Cavities. In *Proceedings of SRF 2015*, number MOPB055, Whistler, B.C., Canada, 2015. JaCoW.

[Tin04] Michael Tinkham. *Introduction to Superconductivity: Second Edition (Dover Books on Physics) (Vol i)*. Dover Publications, 2004.

[Val13] Nicholas Valles. *Pushing the Frontiers of Superconducting Radio Frequency Science: From the Temperature Dependence of the Superheating Field of Niobium to Higher-Order Mode Damping in Very High Quality Factor Accelerating Structures*. PhD Thesis, Cornell University, 2013.

[VBB+92] C. Vallet, M. Bolore, B. Bonin, J.P. Charrier, B. Daillant, J. Gratadour, F. Koechlin, and H. Safa. Flux Trapping in Superconducting Cavities. In *Proceedings of the European Particle Accelerator Conference EPAC92*, page 1295, 1992.

[VKK13] J.-M. Vogt, O. Kugeler, and J. Knobloch. Impact of cool-down conditions at Tc on the superconducting RF cavity quality factor. *Phys. Rev. ST Accel. Beams*, 16(102002), 2013.

[Wei95] W. Weingarten. Progress in Thin Film Techniques. In *Proceedings of the 1995 Workshop on RF Superconductivity, Gif-sur-Yvette, France*, page 129, Gif-sur-Yvette, France, October 1995. JP Scientific.

[XR14] Binping Xiao and Charles E. Reece. A new first-principles calculation of field-dependent RF surface impedance of BCS superconductor and application to SRF cavities, April 1, 2014 2014. 9 pages, 15 figures, an extension of SRF13 conference proceedings.

[XRK13] B. P. Xiao, C. E. Reece, and M. J. Kelley. Superconducting surface impedance under radiofrequency field. *Physica C: Superconductivity*, 490:26–31, 2013.